New Methods for Modifying Zeolites to Create Mesoporosity

A thesis submitted to The University of Manchester for the degree of

Doctor of Philosophy

in the Faculty of Science and Engineering

2020

by

Rongxin Zhang

under the supervisor of

Dr. Xiaolei Fan

Department of Chemical Engineering and Analytical Science

Table of contents

List of tables

List of figures

Abstract

Zeolites, as microporous, aluminosilicate minerals are widely used as catalysts and absorbents in industrials. In some applications (e.g., petroleum industries), the pristine micropores of zeolites limit the diffusions of bulk molecules from accessing the intracrystalline activate sites giving a low effective utilisation. The creation of hierarchical zeolites by introducing mesoporosity into microporous zeolite framework is one of the most practical ways to reduce such limitations.

The microwave-assisted chelation (MWAC) dealumination, and ultrasound irradiation desilication are both effective and efficient method for mesoporosity creation in synthetic zeolites, especially ones with low silicon to aluminium ratios (SAR) such as FAU Y. In this PhD project, development of process intensification for post-synthetic hierarchical zeolites was systematically investigated. Here, the work was carried out by: (i) demonstrating the introduction of secondary mesoporosity into microporous zeolites improves catalytic activity in heterogeneous reactions; (ii) developing the effect of ultrasound-assisted desilication for dealuminated zeolites to create mesopores; (iii) proving MWAC methods are effective in fabricating hierarchical zeolites and the degree of dealumination is related to the number coordination centres in the acidic chelating agent; and (iv) developing an insight into the mechanism of the MWAC dealumination process and understanding the interactions between the chelating agent/mineral acid (i.e., H_4EDTA and HCl) and the zeolite framework under microwave irradiation. The relevant research findings from the project on the process intensification of post-modification for hierarchical zeolites provides the guidance for the design of porous catalysts with desired properties and demonstrate the potential of applying such approaches for fabricating secondary mesoporosity into various topology zeolite frameworks, and even of applying in practical industrial utilisations.

Declaration

I declare that this research is the result of my own work except as cited in the references and no portion of the work in the thesis has been submitted in support of an application for another degree or qualification of this or any other university or other institute of learning.

Copyright

Acknowledgements

First and foremost, I would like to express my sincere thanks and deep gratitude to Dr Yilai Jiao and my main supervisor Dr Xiaolei Fan for their invaluable guidance, constant assistance, inspiration and patience throughout this PhD project.

Thank my internal examiners Dr Patricia Gorgojo and Dr Flor R. Siperstein for their kind suggestions and discussions, which helped me a lot in my work.

My great appreciation is also given to the staff at The University of Manchester for helping me a lot with laboratory work. Thanks Dr John Edward Warren and Dr Gary Harrison for their training PXRD and EDXRF. Thanks Dr Carlo Bawn for his help in NMR analysis. Thanks Mr Loris Doyle, Dr Sarayute Chansai, Mrs Shahla Khan, Miss Gemma Chapman and Mr Jordan Gaskell.

I would also like to thank my friends and colleagues in Manchester, especially Dr Huanhao Chen, who not only generously helped me with my PhD project but also taught me how to be a qualified Doctor. Thanks Mr Wei Li and Mr Yabin Chang for their considerate assistance in EM analysis.

Thanks all my friends in D39, it is joyful to have a bunch of lovely people during my PhD. And to all my dear friends around the world, I am so grateful to have you always be my side. You are the luminous things in my life, *and we swore on that night we would be friends till we die.*

Finally, I would like to thank my parents for always having my back. Thank you for supporting me to be myself and for being my sky full of stars. I would never have the whole Milky Way without your endless love. *I know that you are always with me and the way you will show. You are with me wherever I go and you both give me this feeling this everglow.*

My dear grandparents, wish you all rest in peace. Love you forever. *They say people come say people go. This particular diamond was extra special. And though you were gone and the world may not know, still I see you celestial.*

Chapter 1 Introduction

Fluid catalytic cracking (FCC) as a refinery process is primary applied to reform petroleum with high boiling point and high molecular weight fractions to value-added fuels and chemicals, such as gasoline, diesel, liquefied petroleum gas (LPG) and light olefins [1]. The global refinery catalysts market size is expected to grow from USD 4.0 billion in 2020 and USD 4.7 billion by 2025, at a compound with the annual growth rate of 2.9% during the forecast period. The growth of this market can be attributed to the rising demand for petroleum derivatives such as fuels and commodity chemicals. Additionally, demand for fuel with a high octane number is also anticipated to drive the growth of the refinery catalysts market [2]. Because the introduction of zeolite materials in the formulation of FCC catalysts has resulted in a significant increase in the yield of gasoline and downstream products (e.g. propylene) since 1970s [3], zeolites (specifically faujasite (FAU) Y and ZSM-5 (MFI type)) have been developed as the most valuable catalyst alternatives for FCC process. Recently, due to the high global demand of light olefins, modification of the FCC catalysts can improve the production of propylene up to approximately 20 wt% in a maximum petrochemical operation mode of a FCC unit [4]. Although the society demand the shift to clean and sustainable energy due to the sustainability call the relevant development of the emerging fields needs time. Therefore, as shown in Figure 1.1, in the coming 30–40 years, the world economy and energy supply will still significantly rely on fossil fuels and the petroleum refining industry and processes (including FCC).

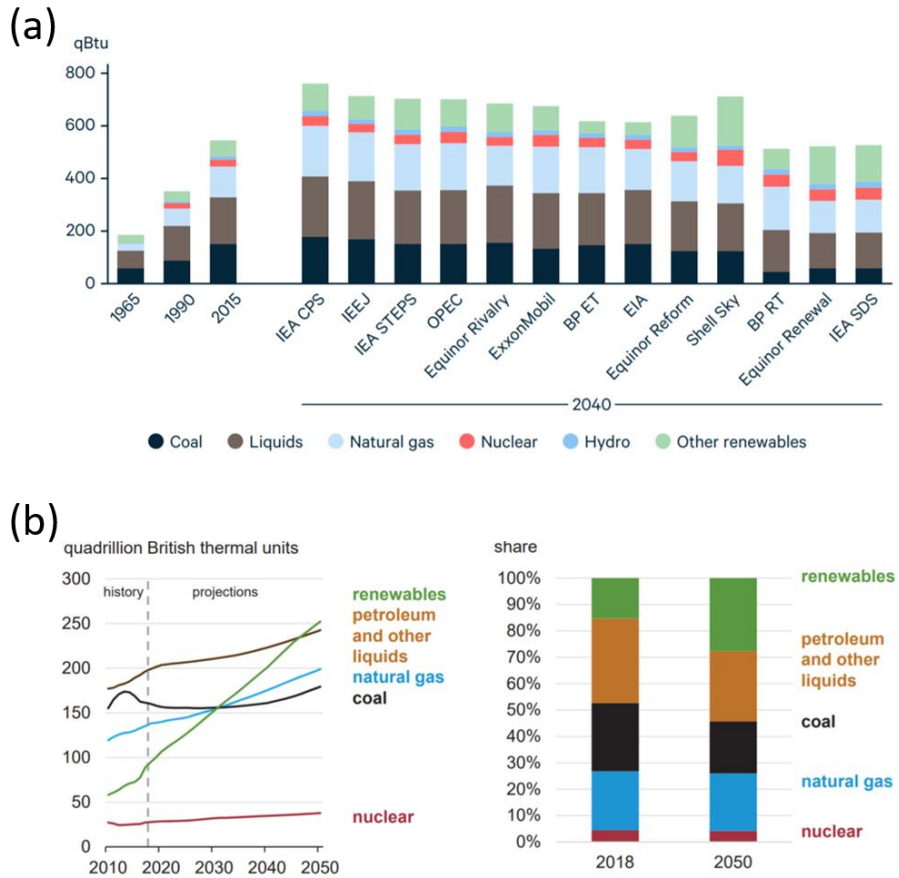

Figure 1.1 Global primary energy consumption by energy source: (a) diverse outlook by 2040 [5] and (b) outlook with projections to 2050 [6].

Since 1964, zeolites, especially FAU Y zeolites, have been being the main additives in FCC catalysts to improve catalytic activity and selectivity to the desired products in FCC process [3]. Zeolites are crystalline microporous inorganic materials (silicates, aluminosilicates, titanosilicates, aluminophosphates, etc.) with uniform channel systems and pore windows with molecular dimensions (0.3–1 nm). They are widely used as catalysts and adsorbents in the petroleum and chemical industries (e.g. oil refining (FCC) [7], esterification [8], oligomerisation of light olefins that[9] and isomerisation [10]) due to well-defined microporosity, good thermal and chemical stability, tuneable compositions, and environmental friendliness [11]. Nevertheless, the pure micropore networks (<1.2 nm) of microporous zeolites restrict molecular diffusion and mass transport within zeolite crystals and the bulky molecules are limited from accessing the intracrystalline active sites. In addition to the accessibility and diffusion issues, the selectivity to preferred bulky product molecules is also prohibited

by the micropore size in some reactions (e.g. transalkylation of toluene with trimethylbenzenes [12]). During FCC, the poor accessibility and molecular diffusion may accelerate the coke deposition which covers the active sites (i.e., Brønsted acid sites). And the continuous coke deposition can then significantly limit the access to active sites, block the porous frameworks and reduce the surface area, which lead to rapid catalyst deactivation and lifetime reduction [13-15]. In order to improve the accessibility of intracrystalline active sites and suppress the coke formation, various strategies were developed such as the development of zeolites with the reduced crystal dimensions and secondary larger pores [16]. For the latter, in addition to the intrinsic micropores, secondary mesopores and/or macropores are present in the zeolitic framework as well, which are commonly referred as hierarchical zeolites. Regarding the definition of micro-/meso-/macro-pores, generally, the IUPAC classification of pore sizes is used: micropores are pores having a pore diameter below 2 nm, mesopores are pores having a pore diameter between 2 and 50 nm and macropores are pores with a pore diameter of above 50 nm. Zeolites with hierarchical porous structures are proven to facilitate mass transport and contribute to the improved catalytic performance in FCC reactions [17, 18]. Various strategies have been developed to introduce secondary large pores in microporous zeolites, which can produce zeolitic materials with notably different hierarchical pore networks.

For example, modification of zeolite crystallisation conditions can enable the direct synthesis (i.e., bottom-up approaches) of zeolitic materials with mesoporous features. Commonly, in the bottom-up cases, additional templates are used during zeolitisation in addition to the required silica and alumina sources to scaffold secondary large pores (including both intracrystalline and intercrystalline large pores) during the synthesis, which will be rendered by subsequent templates removal step such as calcination [19]. Post-synthetic modification of pre-synthesised parent zeolites (i.e., the top-down approaches) is a different way to tune the porosity of zeolites. The post-treatments normally are based on demetalisation, such as dealumination and desilication, and/or followed with further additional treatments such as mild acid washing and steaming to create intracrystalline mesopores. Top-down methods have been practiced by relevant industries for decades and widely used not only for introducing hierarchical structures in zeolites, but also for tuning their acidic properties, as well as stability [20, 21].

Hydrothermal treatments are inevitable in traditional methods of preparing and modifying zeolites, and such methods are highly practical but can be energy intensive and less sustainable. Recent development of the fields showed the potential of alternatives to conventional conductive/convective heating, such as microwave and ultrasound irradiation, to improve the efficiency of zeolite synthesis and modification. The alternative methods based on the alternative energies may considerably reduce the preparation time with the improved process efficiency and energy saving, and thus simultaneously response to the Green Chemistry principles. Both microwave and ultrasound irradiation provide a novel way to intensify the zeolite synthesis [22, 23], however, the investigation on the process intensification of post-synthetic zeolite modification (to introduce hierarchical pores to the pristine zeolite microporous frameworks) using microwave and ultrasound irradiation is relatively lacking, which requires further investigation. Thereafter, the work presented in this thesis focuses on the application of microwave and ultrasound irradiation for process intensification of the post-synthetic modification of Al-rich zeolites for the purpose of preparing hierarchical zeolites. Firstly, the work investigates the effect of hierarchical structures on enhancing the molecules accessibility, and how it can improve the catalytic activities in liquid-phase catalysis. Secondly, the ultrasound-assisted desilication and microwave-assisted chemical treatment dealumination methods, as well as the relevant sequential treatments based on the methods, were developed to perform the modification of zeolite Y (with the silicon-to-aluminium ration, SAR = 2.6) toward hierarchical mesopore generation. The characterisation and catalytic application of the developed zeolitic materials were performed and discussed in detail. Finally, this work dedicates the effort to understand the fundamental aspects of the microwave-assisted chemical dealumination, specifically the thorough study on effect of microwave irradiation on zeolite framework, which will be beneficial to the further development of the technology toward practical applications at a large scale. As detailed discussed in 2.3.1, the efficient heat generation of microwave irradiation makes it excellent choice for aluminium-rich zeolite dealumination process as a green chemistry energy. However, for alkaline-assisted desilication procure, the microwave irradiation cannot be applied since the microwave reactor has content of SiO_2, which is easily dissolved in alkaline solution under fast thermal conduction. The results and findings achieved by the PhD project show the promising possibility of using the microwave and/or ultrasound irradiation to replace the conventional modification protocols, at least

partially, to achieve the sustainable and efficient post-synthetic treatments of zeolites for introducing mesoporous structures.

1.1 Thesis structure

The main aims of this PhD project are to explore new intensified methods based on microwave and ultrasound irradiation to enable the post-synthetic treatments of zeolites for introducing hierarchical porous structures and develop insight into the methods. The relevant findings of the PhD research has resulted in several peer-reviewed publications and conference presentations (as below in Section 1.2). Accordingly, this PhD thesis is presented with the alternative format according to the thesis submission guidelines approved by The University of Manchester[1]. Specifically, the thesis has the following chapters:

Chapter 2 reviews the state-of-the-art of the various strategies to improve accessibility to the intracrystalline voids of zeolites. Zeolites including their structure, synthesis, modification and characterisation are described briefly as well. The utilisation of microwave and ultrasound energy for intensifying zeolite modification is thoroughly discussed.

Chapter 3 comprehensively studied the porosity and acidity of three commercial FAU Y zeolites (including the original HY-2.6 and dealuminated HY-15/-30 zeolites), and revealed that HY-15 and HY-30 possess >50% open mesoporosity in the mesopores range of 5–10 nm. The acidity of the dealuminated Y zeolites has been reduced significantly in comparison to that of HY-2.6. Catalytic results of Fischer esterification of methanol with carboxylic acids and aldol condensation of benzaldehyde with 1-heptanal have evidenced that the critical role of mesoporosity of the dealuminated Y zeolites in liquid-phase reactions as compared to acidity. Results from this study allow us to explain the origin of the high activity of zeolites with mesoporosity in the liquid-phase catalysis.

In Chapter 4, the ultrasound-assisted alkaline treatment was proposed as the alternative to conventional hydrothermal alkaline treatments during the sequential chemical dealumination and alkaline desilication treatments. In comparison with the hydrothermal alkaline treatment, the ultrasonic

[1] http://documents.manchester.ac.uk/display.aspx?DocID=7420

treatment showed the comparatively enhanced efficiency in treating the dealuminated Y zeolites for creating mesoporosity. The acidic property and catalytic activity (in catalytic cracking of n-octane) of mesoporous Y zeolites obtained by the two methods were comparable. The ultrasonic desilication treatment was found to be generic.

A novel post-synthetic method combining the microwave-assisted dealumination and hydrothermal alkaline treatment for obtaining mesoporous Y zeolite catalysts is presented in Chapter 5. In the first-step microwave-assisted dealumination of the pristine Y zeolite, both the mineral acid and organic carboxylic acids were used, and their effects on the physical and chemical properties of the resulting modified zeolites are studied in detail. The hierarchical feature of the mesopores in the modified zeolites (using carboxylic acids) was probed by the model reaction of aldol condensation of 1-heptanal with benzaldehyde for the selective formation of jasminaldehyde. The normalised selectivity to jasminaldehyde (with respect to the strong acidity) was proportionally related to the specific mesopores volume of the zeolites, revealing hierarchical porous networks in the relevant modified Y zeolites and indicating the effect of hierarchical mesopores in the zeolites on their catalytic performance.

In Chapter 6, systematic investigation was performed to develop an insight into the mechanism of the microwave-assisted chelation dealumination process. Specifically, isotopic labelling Infrared and nuclear magnetic resonance analysis were performed to understand the interactions between the chelating agent/mineral acid and the zeolite framework (zeolite Y as the model zeolite) under microwave irradiation. The findings suggest that, under the microwave condition (i) chelating agent interacted with the framework directly for Al extraction, and thus creating intracrystalline mesopores without extra-framework formation; and (ii) mineral acid primarily hydrolysed the framework Al–O bond without Al removal, producing extra-framework and jeopardising pore structure and crystallinity.

Chapter 7 concludes the research findings from this PhD project and provides the recommendations for future work.

1.2 Achievements

Peer reviewed publications

1. R. Zhang, S. Xu, D. Raja, N.B. Khusni, J. Liu, J. Zhang, S. Abdulridha, H. Xiang, S. Jiang, Y. Guan, Y. Jiao, X. Fan, On the effect of mesoporosity of FAU Y zeolites in the liquid-phase catalysis, Microporous Mesoporous Mater., 278 (2019) 297–306. https://doi.org/10.1016/j.micromeso.2018.12.003

2. R. Zhang, P. Zhong, H. Arandiyan, Y. Guan, J. Liu, N. Wang, Y. Jiao, X. Fan, Using ultrasound to improve the sequential post-synthesis modification method for making mesoporous Y zeolites, Front. Chem. Sci. Eng., 14 (2020) 275–287. https://doi.org/10.1007/s11705-019-1905-1

3. R. Zhang, D. Raja, Y. Zhang, Y. Yan, A.A. Garforth, Y. Jiao, X. Fan, Sequential Microwave-Assisted Dealumination and Hydrothermal Alkaline Treatments of Y Zeolite for Preparing Hierarchical Mesoporous Zeolite Catalysts, Top. Catal., 63 (2020) 340–350. https://doi.org/10.1007/s11244-020-01285-0

Publications not included in this thesis:

1. R. Zhang, H. Chen, Y. Mu, S. Chansai, X. Ou, C. Hardacre, Y. Jiao, X. Fan, Structured Ni@NaA zeolite supported on SiC foam catalysts for catalytic CO_2 methanation, AlChE J., (2020). https://doi.org/10.1002/aic.17007

2. H. Chen, Y. Mu, Y. Shao, S. Chansai, S. Xu, C. Stere, H. Xiang, R. Zhang, Y. Jiao, X. Fan, C. Hardacre, Coupling non-thermal plasma with Ni catalysts supported on BETA zeolite for catalytic CO_2 methanation, Catal. Sci. Technol., 9 (2019) 4135–4145. https://doi.org/10.1039/C9CY00590K

3. S. Abdulridha, Y. Jiao, S. Xu, R. Zhang, A.A. Garforth, X. Fan, Mesoporous zeolitic materials (MZMs) derived from zeolite Y using a microwave method for catalysis, Front. Chem., 8 (2020). https://doi.org/10.3389/fchem.2020.00482

4. L. Lan, Y. Shao, Y. Jiao, R. Zhang, C. Hardacre, X. Fan, Systematic study of H_2 production from catalytic photoreforming of cellulose over Pt catalysts supported on TiO_2, Chin. J. Chem. Eng., (2020). https://doi.org/10.1016/j.cjche.2020.03.030

Publications under preparation:

1. R. Zhang, et al., Mechanism of mesopore formation in zeolites in post-synthetic microwave-assisted chelation treatment.

Conference presentations

1. Structured Ni@NaA Zeolite Coated SiC Foam Catalyst for Catalytic CO_2 Methanation (**Oral**), the United Kingdom Catalysis Conference 2020 (UKCC2020), Loughborough, United Kingdom (UK), January 2020.

2. A Novel Way for Creating Hierarchical Zeolites and Catalytic Applications (**Poster**), the Second Joint NSFC-RSC Symposium on Sustainable Chemistry and Processes, York, UK, September 2019.

3. Novel Methods for Making Hierarchical Zeolites: Characterisations and Catalytic Applications (**Oral**), the 26th Joint Annual Conference of the Chinese Society of Chemical Science and Technology in the UK and the Society of Chemical Industry's Chinese UK Reginal Group (CSCST-SCI 26), London, UK, September 2019.

4. Microwave-assisted post synthetic modification with different acids: a facile approach to create mesoporous zeolites (**Poster**), the United Kingdom Catalysis Conference 2019 (UKCC2019), Loughborough, UK, January 2019.

Chapter 2 Literature review

2.1 Introduction to zeolites

Zeolites, as one of the most classic alunimosilicates, have attracted lots of attention for over 260 years since 1756 discovered by Axel Fredrik Cronstedt. They are microporous crystalline polymers which consist of three-dimensional (3D) networks based on the connection between TO_4 (T = Si, Al. Where AlO_4^- is alumina and SiO_4 is silica) units. Each unit is linked by its oxygen atoms leading to a net negative charge of AlO_4 tetrahedron. Such a net negative charge is balanced by cations M which are not a part of the framework and can be exchanged by other cations. The structural formula of zeolites is generally described as $M_{m/x}^{x+}\left[\left(AlO_2\right)_m\left(SiO_2\right)_n\right]\cdot yH_2O$, where *x* is the valence of cation M, *y* is the number of moles present in the framework of inter-channel molecular water, and *n*/*m* is the silicon-to-aluminium ratio (SAR) substantially varying from 1 to infinite. From Löwenstein's rule, Al–O–Al linkage is unacceptable due to the charge restriction, meaning that 1 is the lowest SAR achievable [24].

Zeolite structures are designated by a three capital letters code according to the 6th edition of *Atlas of Zeolite Framework Types*, published by the Commission of the International Zeolite Association (IZA) [25]. Till now, the number of zeolite structures in the IZA database has been expanded to 248, and between six and seven new structures are added to the catalogue every year [26]. Finite and infinite units (i.e., chain- or layer-like) are introduced to describe zeolite framework topologies. The infinite units are found to occur in the tetrahedral units connected through their oxygen atoms to form multi-membered rings, which are called secondary building units (SBU, where the primary building units are the tetrahedra TO_4). 23 SBU symbols are presented in Figure 2.1. SBUs are invariably non-chiral (neither left- nor right-handed) and contain up to sixteen T-atoms, which suggests that only one type of SBU rather than enantiomeric pairs is needed to assemble the 3D framework. By simply applying operations such as translation and rotation to one or more SBU, the periodic building units (i.e., chains, tubes, layers, (double) rings and cages) are built up. And then the zeolite frameworks are built from periodic 0-, 1-, or 2- dimensional structurally invariant periodic building units.

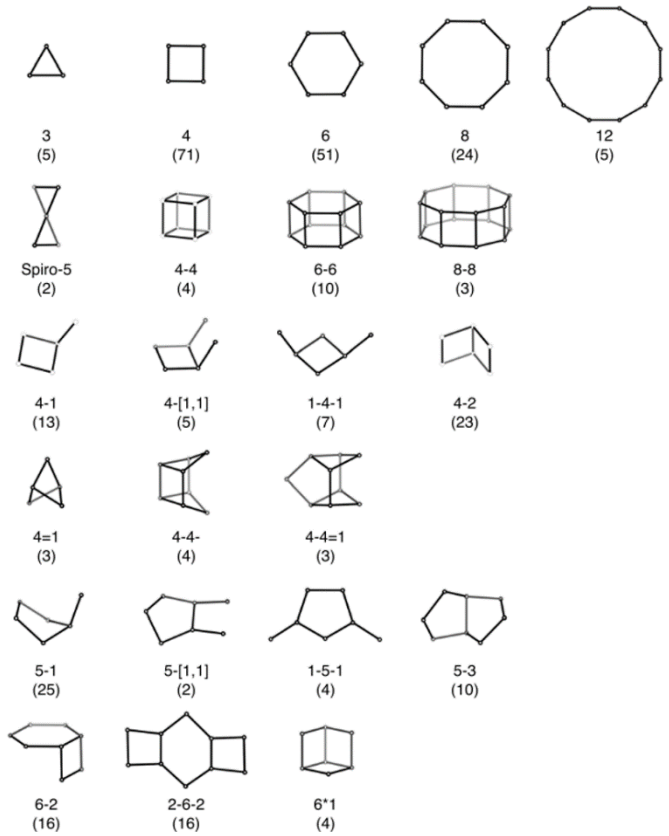

Figure 2.1 Secondary building units (SBU) and their symbols. Number in parenthesis indicates the frequency of occurrence among all identified zeolite structures [25].

2.1.1 Pore structures of zeolites

A characteristic feature of zeolites, i.e., the structural porosity, is formed within zeolite structure building units. The zeolite channels are defined by membered-rings (windows) that consist of T-atoms. Normally, only those windows with a minimum of 8 T-atoms allowing diffusion of molecules are considered for porosity characterisation. A polyhedron, whose maximum window is a 6-ring, is called a cage which is not included into zeolite channels. All other polyhedra are called cavities. Cages or cavities can be connected in several ways. Most of the zeolites can be classified into three categories by the number of T-atoms in membered-rings: zeolites containing (i) 8 membered-rings (8 T-atoms) are denoted as small pore zeolites having free diameters of 0.30–0.45 nm, (ii) ten membered-rings are referred to medium pore zeolites with the corresponding pore opening at 0.45–0.60 nm, (iii) twelve membered-rings are assigned to large pore zeolites with free diameters from 0.60 to 0.80 nm, and for those containing more than 12 T-atoms windows are assorted to ultra large pore zeolites (with the pore

opening >0.80 nm) [27]. Figure 2.2 shows two classical small pore size zeolites, CHA type (SAPO-34) and LTA type. Shorthand notations have been adopted to describe zeolite channels in various frameworks, specifically, the number in bold type indicates the number of T-atoms forming the rings controlling diffusion through the channels; the number of asterisks in the notation indicates whether the channel system is one-, two- or three-dimensional; the crystallographic free diameter of the channels presents in Angstrom units (Å); (⊥) means channel systems are perpendicular to specific crystallographic directions; interconnecting channel systems are separated by a double arrow (↔); and a vertical bar (|) means that there is no direct access from one channel system to the other. For instance, LTA type zeolite is typified by a 3D system of channels parallel to all crystallographically equivalent axes (i.e., along [100], [010] and [001]) of the cubic structure (the meaning of <100>) with circular 8-ring apertures as shown in Figure 2.2 (c) and (d). And in Figure 2.3, MFI type zeolite with medium porous structure exhibits that the channels parallel to [100] together with those parallel to [010] give rise to a 3D channel system.

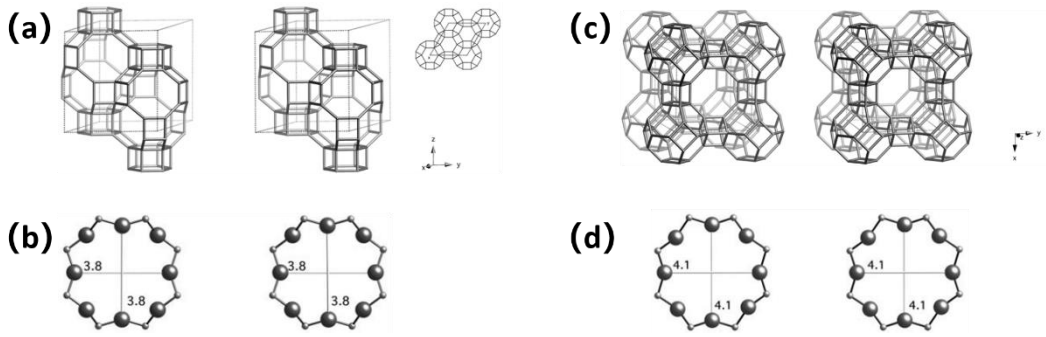

Figure 2.2 (a, b) CHA ⊥[001] **8** 3.8×3.8***, cages ∅: 6.5×11 Å, where (a) is framework viewed normal to [001] (upper right: projection down [001]), (b) is 8-ring viewed normal to [001]; (c, d) LTA <100> **8** 4.1×4.1***, cages ∅: 11.4Å, where (c) is framework viewed along [001] and (d) 8-ring viewed along <100> [25].

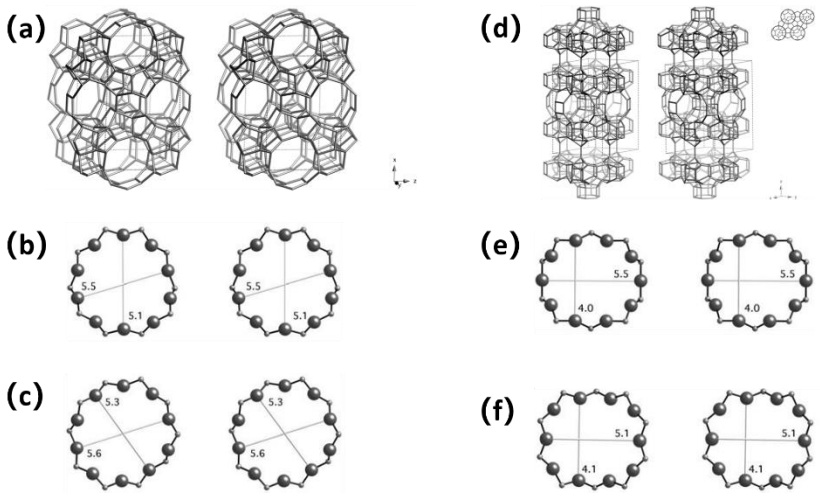

Figure 2.3 (a-c) MFI [100] **10** 5.1×5.5 ↔ [010] **10** 5.3×5.6}***, where (a) is framework viewed along [010], (b) is framework viewed along [010] and (c) is 10-ring viewed along [010]; (d-f) MWW ⊥[001] **10** 4.0×5.5** | ⊥[001] **10** 4.1×5.1**, where (d) is framework viewed normal to [001] (upper right: projection down [001]), (e) is 10-ring viewed normal to [001] between 'layers' and (f) is 10-ring viewed normal to [001] within 'layers' [25].

Large pore zeolites always attract the attention due to their practical usages in catalysis. *BEA (as shown in Figure 2.4 (a-c)) belongs to disordered type materials since in a normal synthesis the stacking of each 'layer' is random. Literally, no bulk material with ordered structure is presently known, the framework structure is given here to make a thorough description. Although three polytypes are recognised which are related to disordered structure, they do not cause any blocking of the 3-dimensional 12-ring channel system. In the framework structure, cub-octahedral units 'sodalite cage' are joined by double six-membered rings (known as hexagonal prisms) leading to the formation of supercages within 12-ring. Faujasite (FAU) as a classic of large pore zeolites with supercages and 3D channel systems has been one of the most popular materials in catalytic processes. Only 15 of the 248 framework types available today are employed as catalysts for commercial purposes. Nevertheless, only five or six among those are large pore zeolites (BEA, cancrinite (CAN), FAU, MOR, and offretite (OFF)). Although some specific processes may need large- and ultra-large-pore zeolites to contribute specific commercial applications (i.e., fluid catalytic cracking, FCC [28]), there is a clear need to explore more general avenues to develop zeolite materials with enhanced pore accessibility [29].

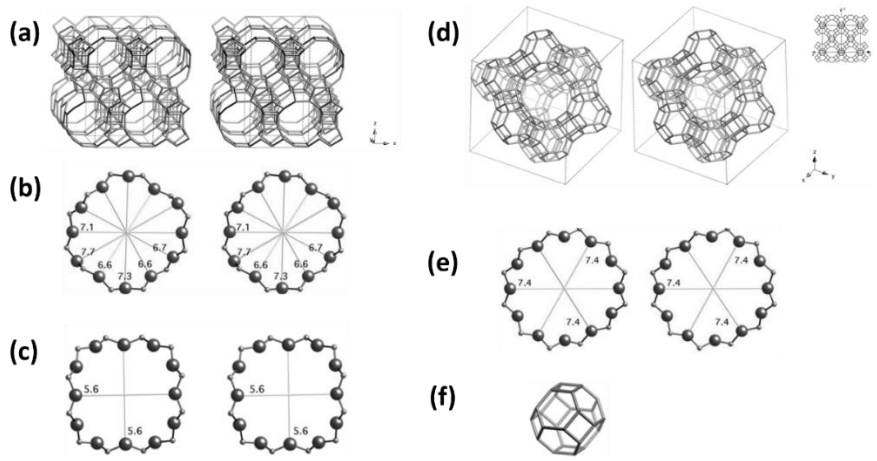

Figure 2.4 large pore zeolites: (a-c) *BEA <100> **12** 6.6×6.7** ↔ [001] **12** 5.6×5.6*, where (a) is framework viewed along [010], (b) is 12-ring viewed along <100> and (c) is 12-ring viewed along [100]; (d, e) FAU <111> **12** 7.4×7.4*** supercages ∅: 13 Å, where (d) is framework viewed along [111] (upper right: projection down [110]), (e) 12-ring viewed along <111> and (f) is the sodalite cage building unit [25].

2.1.2 Active sites

In addition to the pore structure, another characteristic feature of zeolites is the extra-framework cations, which determine the activity of zeolites. The appropriate tuning/choice of the extra-framework (EFAL) cations is one of the key factors that make zeolites versatile materials for a wide range of applications. Here we use FAU zeolite Y to facilitate the description of active sites in zeolites. In Al-containing Y zeolite, the inclusion of extra-framework cations such as metal cations and proton can be introduced during synthesis and/or after various post-synthetic treatments such as ion exchange. Regarding the location of extra-framework cations, it can be both in the inner cavities and at the external surface. Figure 2.5 shows the main locations of cation sites within zeolite Y framework. These sites include: site I located in the centre of hexagonal prims; site I′ and II″ located in sodalite cages where site II″ is about 1 Å to the centre of sodalite cage; and site II and III located in supercages. Additionally, the location depends on the type, loading and hydration state of cations.

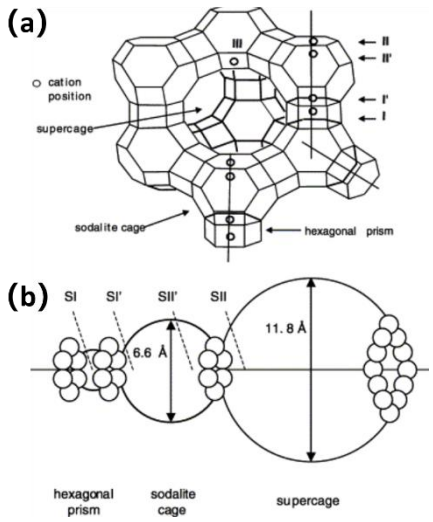

Figure 2.5 (a) Cation sites in the framework of zeolite Y, and (b) specific location of cation sites in various building units. Hexagonal prisms, sodalite cages and supercages with maximum entrances of 2.6, 2.6, 7.4 Å and diameters of 2.6, 6.6 and 11.8 Å, respectively [30].

Proton (H)-form zeolites can be employed as solid acid catalysts in which the catalytic activities are given by protonic sites, i.e., Brønsted acid sites (B). B sites are found in zeolites associated with bridging hydroxyl groups attached to framework oxygen atoms linking tetrahedral Si and Al atoms, i.e., Si–OH–Al. In this case, theoretically, the maximum number of protonic sites is equal to the number of framework aluminium [31]. The acid strength of B is influenced by a function of the angel of the T–O–T bond. The acid strength of B sites is increased with an increase of the T–O–T bond angle. T–O–T bond angel in HFAU, HMFI and HMOR zeolite ranges from 138° to 147°, 133 to 177° and 143° to 180°, respectively, and accordingly HMOR possesses relatively strong acid sites and is active in n-butane and n-hexane isomerisations at 200–250 °C [32]. In addition to the acidity contributed by the hydroxyl groups in zeolite framework, EFALs also contribute to the overall enhance acidity of zeolites. In other circumstances where the zeolite is not protonated, trigonal coordinated Al-atoms (i.e., EFALs) possessing the vacant orbital is produced which can accept an electron pair and acts as a Lewis acid sites [33].

In comparison with the active sites within the zeolite framework, active sites locate on the external surface of zeolite crystals are insignificant, i.e., about <1% for crystallites of 1 μm. Therefore, the accessibility of the internal active sites plays a significant role in catalytic applications of zeolites. For

instance, the active sites located in the supercages of zeolite Y with maximum opening of 0.74 nm are relatively accessible to some organic molecules with relevant kinetic diameters, whereas those located in the hexagonal prims, are comparatively inaccessible to the molecules. Furthermore, it has been concluded that, in most cases, catalytic reactions over zeolites occur within their intracrystalline cages and channels [27]. Hence, the presence of active sites in the zeolite cages, channels in the apertures, gives rise to shape selectivity, which is one of the major characteristics of zeolite catalysis. Generally, the shape selectivity originates from the limitation of certain molecules in a reactant mixture entering the microporous framework of zeolites, or of certain product molecules existing from the framework. Shape selectivity also considerably influences the diffusion rate of both reactants and products, particularly in the case of the presence of distinct difference in the diffusivity reactant/product molecules in zeolite catalysis. Figure 2.6(a) presents that, when the dimension of molecules approaches those of zeolite pores, a new regime of intracrystalline diffusion arises. In this regime, also known as configurational diffusion, even subtle differences in pore dimensions (from 0.3 to 0.9 nm) can result in large changes (from 10^{-20} to 10^{-8} m^2 s^{-1}) in diffusivities [34]. Additionally, the formation of certain transition states is limited by the space available near the active sites, which depends on the size and geometry of the inner cavities as well. Meticulous illustration of three types of shape selectivity is shown in Figure 2.6 (b-d).

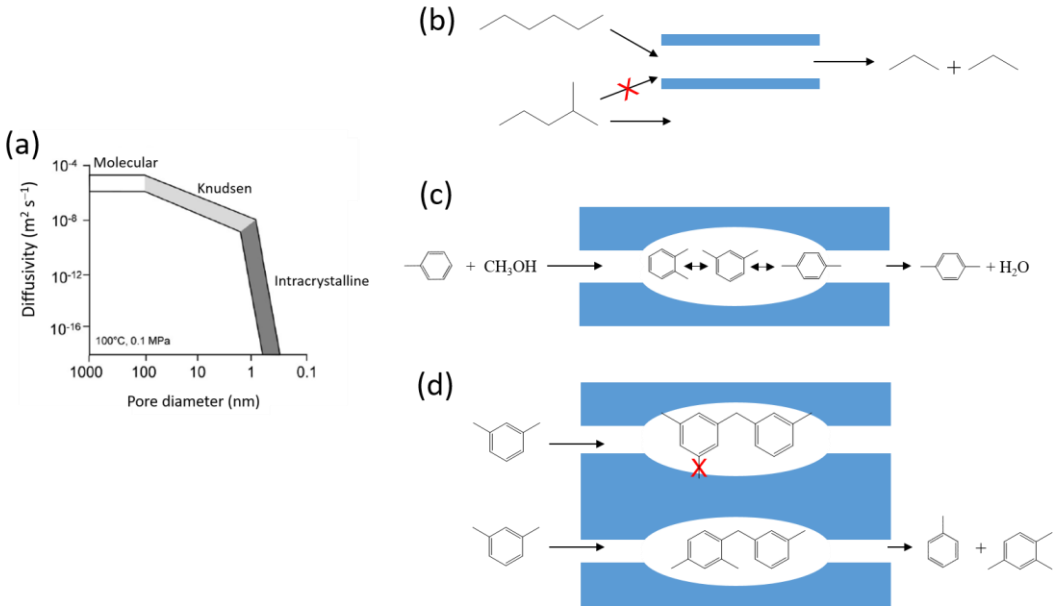

Figure 2.6 (a) Effect of pore diameter on diffusivity [35]. (b-d) Types of shape selectivity occurring during zeolite catalysis, where (a) product selectivity occurs (e.g. cracking of an *n*-iso C_6 mixture) when part of reactant mixture is small enough to diffuse into the pores; (b) reactant selectivity occurs (e.g. disproportionation of *m*-xylene) when some of the product molecules formed inside the pores are too large to transport out the pore systems; and (c) transition state selectivity arises (e.g. during the formation of 1,3,5-trimethylbenzene) when reactions are prevented because the corresponding transition state requires more space than that is available in the cavities.

2.2 Hierarchical zeolites

In response to improve the utilisation of zeolites as the catalyst, significant research efforts have been made to solve the accessibility and diffusion issues. Essentially, two different yet complementary strategies, i.e., reducing zeolite crystal sizes and increasing their pore sizes, can be followed. Firstly, by reducing the zeolite crystal size, and in some cases the shape, the effects due to diffusion can be mitigated along pore systems. For instance, nanosized zeolites with dimensions in a range 5–500 nm or zeolite materials with dimensions between 500 and 1,000 nm can introduce substantially higher external surface area and simultaneously preserve their properties similar to that of micronsized crystals [36]. Nanosized FAU-type zeolites with 10 nm and 70 nm crystal size were successfully synthesised, and nitrogen (N_2) analysis elucidated that the external surface area of nanosized FAU-type zeolites can be significantly improved by reducing the crystal size [37]. Further catalytic evaluation of dealkylation of 1,3,5-triisopropylbenzene (TiPBz) confirmed that the nanosized zeolites have the improved activity (i.e., conversion of TiPBz at 70–76%, and selectivity to 1,3-diisopropylbenzol (DiPBz) and 1,4-DiPBz at

around 85%) as compared to the commercial micronsized zeolite (i.e., conversion of TiPBz at ~34% and selectivity to 1,3-DiPBz and 1,4-DiPBz at about 78%). Additionally, the reduction of zeolite crystal sizes can also be achieved by developing two-dimensional (2D) zeolites [38-41]. Nanosheet MFI-type zeolites have shown their potentials in traditional catalysis such as benzyl alcohol alkylation with mesitylene [42], acylation (acylation of indole and benzoylation of resorcinol), esterification (hexanoic acid with benzyl alcohol), condensation (synthesis of vitamin E by the reaction of isophytol and 2,3,6-trimethylhydroquinone), and hydroamination (aniline with methyl acrylate) [43]. Although nanosized zeolites are much more stable than layered-like zeolites, the relevant strict/tedious synthesis conditions and low yields make them, at present, not suitable for large-scale production and application. Accordingly, more efforts are needed to improve the development of nanosized zeolites toward industrial adoption and application.

The second strategy, i.e., the introduction of secondary pore systems inside the zeolite framework, has received the attention over the past 20 years. The comparatively superior performance of zeolites with secondary pore systems in many traditional and emerging catalytic applications strongly supports the interest of zeolite community in developing such materials [44]. Zeolites with the secondary pore systems are also termed as mesoporous or hierarchical zeolites, in which zeolite structural elements (compartments) are characterised by more than one length scales, and each of these structural elements (microporosity and mesoporosity) has to have distinct but complementary functions such as minimising the mass transport resistance. The characteristic of hierarchical zeolites is that the inherent microporosity determined by the framework structure of the zeolite hierarchically connects with the secondary pore system which can be either intercrystalline or intracrystalline or even a combination thereof [45]. In general, to introduce secondary porous systems into the zeolite framework, it is vital to apply post-synthetic preparation on pre-synthesised zeolites or combine it with direct synthesis methods. Post-synthetic preparation is mostly performed either using bottom-up methods or top-down approaches. Additional porosity can be accomplished using bottom-up methods during the crystallisation of zeolites with either hard or soft templates or through dedicated assemblage of individual zeolite crystals [46]. Regarding top-down strategies, the formation of mesoporosity are commonly achieved by selective

extraction of specific framework elements from pristine microporous zeolites with or without additional pore-directing agents. Although bottom-up methods can tailor highly ordered mesopores disadvantages associated with templates, such as the availability, relatively high cost, time-consuming synthesis and safety concerns, still limit their potential in practical utilisation. Conversely, top-down methods (such as dealumination, desilication and/or followed by recrystallisation) are comparatively practical. An overview of the classification of hierarchical pure zeolites are shown in Figure 2.7, and only pure zeolites are considered (composites with other materials are not included). In principal, all preparation principles and materials can be combined to produce diverse (new) hierarchical zeolitic materials. For example, the combination of reducing crystal size and widening pore size to procedure such materials at a pilot scale was successfully accomplished by crystallisation and extraction, specifically, MFI-type hierarchical nanosized zeolite (hollow architecture with single crystal size less than 150 nm) has been investigated [47, 48].

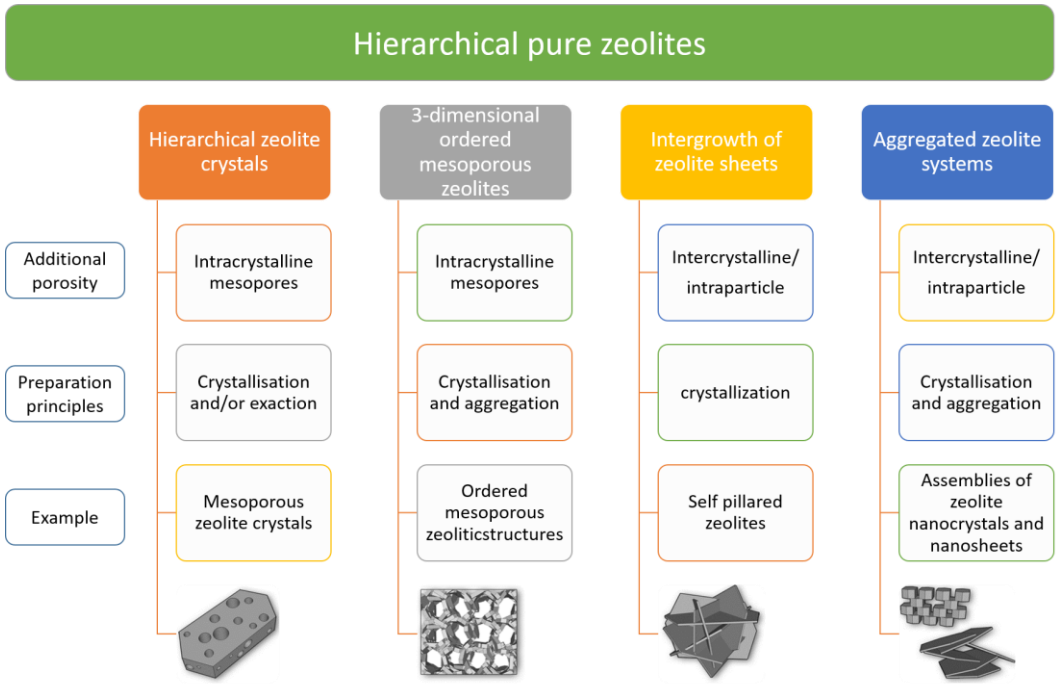

Figure 2.7 Classification of hierarchical pure zeolites (composites are not included) according to the origin of additional porosity and the preparation principles [45, 49].

2.2.1 Synthesis of hierarchical zeolites

2.2.1.1 Hard-templating

In order to form secondary pore systems during direct synthesis, porous or nonporous solid materials are used as the mesoporogen. The solid materials consist of carbonaceous materials, biological materials, polymeric microspheres as well as inorganic solid materials [50]. In a typical synthesis procedure, the reagents and zeolite precursors are prepared and mixed with the hard template. Thereafter, zeolite crystallisation with the hard template is treated in single or multiple steps under hydrothermal conditions, and, simultaneously, the microporous zeolite is formed around the hard template. Finally, the template is removed by calcination (for organic templates or carbon materials) or dissolution treatments (for inorganic templates) to render the secondary mesopores. Due to the simple removal by calcination, carbonaceous materials such as carbon nanoparticles [51], carbon fibres [52], carbon nanotubes [53], and carbon aerogels [54] are often used for introducing secondary mesopores in zeolites. However, the nanosized zeolite crystallites obtained from crystallisation with carbon nanoparticles were not aggregated, which implies that costly separation processes may be necessary to recover the zeolite after catalysis [55]. Chen *et al.* [56] used 3D mesoporous carbon as hard template successfully synthesised BEA-, FAU,- LTA- and LTL-type zeolite with highly ordered mesoporosity. The synthesis protocol involves costly, as well as being time-consuming. In addition to the carbonaceous materials, natural polymeric materials have also been explored as templates to scaffold secondary pore systems in zeolites. In comparison to the carbonaceous materials, they are relatively inexpensive, non-toxic and hydrophilic. Template removal of hard templates is always necessary in the method discussed above, which may require harsh conditions such as high temperatures and long duration of calcination, and hence can potentially jeopardise the crystallinity the resulting zeolites [45]. Generally, routine zeolite calcination after synthesis is achieved at 400–550 °C maximum 5 h, whereas, for instance, at least 550 °C and 12 h is necessary to remove carbon black [56] and carbon particles [57]. Alternatively, mesoporous silica particles [58] can also be applied as hard templates which do not necessitate the step for template removal, because they act as both mesoporogens and silica source during steam-assisted zeolite crystallisation. Other solid templates such as polyethylene [59] and wood [60] can also be the candidates

to substitute the conventional hard templates discussed above. Nevertheless, the hard templating strategies still face some intrinsic limitations such as multistep procedures, relatively high prices and possibly unavoidable health and environmental issues related to some of the hard templates.

2.2.1.2 Soft-templating

The idea of soft-templating is more generalised as compared to hard-templating route. In comparison with the hard-templating methods, the soft-templating methods generally have better control over mesopore size distribution and pore connectivity by treating bulky organic molecules as mesoporogens or structure-directing agent (SDA). Soft-templating methods are originated from the synthesis of ordered mesoporous silica material MCM-41 by employing the self-assembly ability of surfactant in 1992 [61]. However, their pore walls are completely amorphous. Since these surfactant molecules are used to direct the formation of the mesophase only, a microporogen must be added additionally [49]. Soft templates typically include commercial organosilanes [62], cationic polymers [63], commercial cation surfactants such as cetyltrimethylammonium bromide (CTAB) micelles [64, 65], and bespoke dual functional templates [66]. In ordered to create hierarchical zeolites with high crystallinity, dual-functional templates have been applied. The strategy of dual-functional templating is referred as the combination of a SDA for facilitating zeolite synthesis and a surfactant template for introducing mesoscopic phase, both are added to the reaction medium at the beginning of the synthesis [67, 68]. In such synthesis, silane-functionalised templates [69], bifunctional surfactants [70] and bifunctional cationic polymers [71] can not only enhance the interaction between dual-functional templates and zeolite frameworks but also minimise the interaction between templates themselves, being able to avoid phase separation. Choi et al. [72] gives an example of synthesis MFI-type zeolite nanosheets using a designed bi-functional ammonium-type surfactant ($C_{22}H_{45}$-$N^+(CH_3)_2$-C_6H_{12}-$N^+(CH_3)_2$-$C_6H_{13}(Br^-)_2$ ($C_{22\text{-}6\text{-}6}$)). Surfactant molecules are aligned along the straight channel of MFI framework and form mono MFI layers. These synthesised monolayers then regularly stack along one orientation to form multilamellar nanosheets or stack randomly in unilamellar nanosheets, and result in numerous intercrystalline pores. The protocol is relatively simple with a two-step procedure, which includes (i)

the aging of zeolite synthesis gel without surfactant and (ii) the mixture of the aged gel with the commercial surfactant of CTAB, to enable the formation of the hierarchical structure.

Although the use of these soft templates is a good strategy to prepare hierarchical zeolites with a high degree of interconnected mesopores and can be applied to different zeolitic structures, most of them are not commercially available and must be designed and synthesised prior to zeolite synthesis. The preparation of such templates can be very labour intensive and expensive. Even though CTAB has been applied for mesoporous zeolite preparation in industrial scale, the soft template removal still causes serious pollution (*e.g.* bromide from CTAB incomplete combustion) and limits the sustainable development, especially based on strict environmental protection policy.

2.2.2 Post-synthetic treatments of zeolites

2.2.2.1 Demetalation

Top-down approaches, also known as post-synthetic modifications, are initially developed to stabilise the zeolite framework (via dealumination for FAU zeolites) or tune the zeolite acidity [73]. Afterwards it was found that the post-synthetic methods are highly capable to introduce mesopores and/or macropores into the parent zeolite crystals by demetalation. Demetalation is based on the selective removal or extraction of framework atoms (T atoms) from crystalline zeolitic materials through acid leaching, steaming, alkaline treatment, recrystallisation or combinations of them.

Dealumination is a conventional method that involves the leaching of the tetrahedrally coordinated aluminium from the zeolite framework, such as FAU zeolites with low SAR values. It was primarily applied to improve the hydrothermal stability of FAU Y zeolites, and further investigation realised the associated generation of secondary mesoporosity in zeolites as the consequence of dealumination. Dealumination is generally achieved by acid leaching, calcination, steaming and chemical treatment. Both acid leaching and chemical treatment are performed in solution (solid-liquid interactions), whereas steaming is carried out in vapour phase (vapour-solid interactions). Dealumination was first reported with acid leaching, by Barrer and Makki in 1964 [74], in which clinoptilolite was treated by hydrochloric acid (HCl) solutions with various concentrations at ~100 °C for 4 hours. It was found that,

with an increase of the HCl concentration, the aluminium was progressively removed from the framework which leads to the improved benzene and isopentane sorption capacity of the dealuminated zeolites. However, mesoporosity formation by acid leaching is limited by the SAR of the parent zeolites [75]. For instance, Meng et al. [76] used HCl to modified sodium form ZSM-5 with SAR = 25, the external surface area and mesopore volume only improved ~6 m^2 g^{-1} and ~0.02 cm^3 g^{-1}, respectively, resulting in insignificant catalytic improvement in non-hydrocracking of diesel (both yield and selectivity to gasoline). As expected, acid leaching along is not effective in creating hierarchical BEA (SAR = 17.6) [77] and MOR (SAR = 14) [78] zeolites, and additional treatment steps (e.g. desilication) may be necessary. Dealumination by steaming is a common practice which has been applied at industrial scale for years. Steaming is mainly used to produce ultra-stable Y zeolite for fluid catalytic cracking [79]. It is generally performed at temperatures between 600–800 °C in the presence of steam. By contacting with steam, hydrolysis of Al–O–Si bonds on ammonium form Y frameworks occurs and Al atoms are expelled to form framework cavities with EFAL species. As mentioned above, EFAL offers Lewis acidity, which can be advantageous in some catalytic reactions. However, since amorphous debris may result in a partial blockage of both meso- and micropores due to the deposition of amorphous phases with the framework and/or on the external surface, a further mild acid (such as ethylenediaminetetraacetic acid, H_4EDTA) chemical treatment [80] might be necessary to ameliorate the accessibility of the multiscale pore system. Hierarchical zeolites can also be prepared *via* chemical treatment with H_4EDTA [81], gaseous silicon tetrachloride ($SiCl_4$) [82] and ammonium hexafluorosilicate (AHFS) [83, 84]. Since Kerr [73] used EDTA to partially remove Al atoms from sodium form Y zeolite about 40 years ago, this approach has been developed to tune the Al concentration in zeolite frameworks [81, 85-88], or selectively remove EFAL species in order to tune the accessibility and catalytic activity [89, 90]. Although the literature did not provide detailed information on porosity, the morphology obtained from TEM characterisation confirms the introduction of meso- and even macropores after contacting NaX zeolite with 0.1 M Na_2H_2EDTA solution for 4 h at 100 °C [85]. Verboekend et al. [91] modified NH_4Y (SAR = 2.6) with 0.11 M H_4EDTA solution under reflux for 72 h at 100 °C, which significantly improve external surface area and mesopore volume, in

comparison with the parent, from 28 to 388 $m^2 g^{-1}$ and 0.03 to 0.27 $cm^3 g^{-1}$, respectively, and meanwhile remained 78% relative crystallinity. Apparently, as simple yet low-cost (due to the availability of most of economic dealumination chemicals) modification procedures, dealumination treatments serve as practical solutions for creating hierarchical zeolites from the parent zeolites with relatively high framework aluminium concentration (i.e., low SAR).

To fabricate hierarchical zeolites, desilication by alkaline leaching of framework silicon species has become a very attractive method as well. The use of alkaline treatment was recorded as a patent by Dean Arthur Young [92] in 1960s, which claimed that alkaline treatment (treating mordenite with sodium hydroxide, NaOH solution, pH = 10.5) was found to increase the adsorptive capacity of the mordenite zeolites, as well as their catalytic activity. Apparently, by corroding the framework structure of zeolites by leaching Si species partially, the internal pore structure of the resulting zeolites was more accessible compared to the parent zeolite. After 25 years of silence, desilication gains the attention of the community again to be applied to ZSM-5. Regarding ZSM-5, the presence of aluminium in the framework dramatically influences the kinetics of crystal dissolution under basic conditions [93, 94]. Ogura et al. [95] firstly emphasised the formation of intercrystalline mesopores in ZSM-5 zeolites after leached by NaOH solution. Later on, Groen et al. [96-98] systematically investigated the mechanism of mesoporosity formation during disilication procedure over MFI-type zeolites, and concluded that the controlled desilication of ZSM-5 zeolites is possible with an optimal SAR of 25, being able to introduce intracrystalline mesoporosity, as well as preserving the intrinsic micropores to a large extent [99-101].

Al content significantly influences the degree of desilication in ZSM-5 zeolites. For ZSM-5 zeolites with an optimal window of SAR in a range of 20–50, controlled alkaline treatments lead to an impressive increase in mesopore surface area up to 235 $m^2 g^{-1}$, and a broad pore size distribution centred at around 10 nm can be obtained. Simultaneously, the original crystalline and acidic properties can be preserved to a large extent, which effectively contributes to the efficient utilisation of the functionality of the hierarchical porous architecture. For the parent ZSM-5 with higher SAR values (>50), unselective dissolution takes place leading to excessive leaching of framework species and severe loss of crystallinity. When it comes to the parent ZSM-5 with SAR below 25, the degree of dissolution of Si

species is restricted by the Al shielding effect. The repulsion between negatively charged AlO_4^- units on zeolite framework and OH^- decelerates the hydrolysis of Si−O−Al bonds, resulting in shielding of the Al^- bearing entities in partial skeletons at the initial stage of desilication. After the hydrolysis of Si−O−Al bonds, the dislodged Al species are hydrolysed to the hydroxides (e.g., $Al(OH)_4^-$), which reversely deposit on the etched zeolite surface and passivates the ongoing dissolutions of the affected zones [46]. Based on this knowledge, the framework Al can be served as pore-directing agents for further designing of hierarchical zeolites. For instance, efforts have been made to develop ZSM-5 zeolites with hollow structures recently. Some work demonstrated that high framework Al concentration suppresses Si extraction, conversely, low framework Al concentration leads to the excessive Si extraction [102]. The difference in the extraction rate of Si species in the Si-rich core and Al-rich shell of H-ZSM-5 (denoted Al-zoned) upon NaOH etching promotes the formation of hollow architectures. Such unique structure can greatly reduce the diffusion length of reactants/products, as well as the residence time of intermediates in the framework of zeolites, and thus suppressing the undesirable side reaction such as over-hydrocracking of hydrocarbons.

The other inorganic agents (such as $Al(NO)_3$, LiOH, Ga^{3+}, B^{3+} and so on) or organic additives (such as tetrapropylammonium TPA^+, tetrabutylammonium TBA^+, benzyltriethylammonium BTA^+ and cetyltrimethylammonium CTA^+) also have the shielding effect, which can act as external PDA to regulate the intracrystalline mesoporosity during base leaching [103]. Those special quaternary ammonium cations, present in basic solution, can shield the matrix by the interfacial affinity between alkyl chains and silicate zones. By treating MFI-type zeolite with tetrapropylammonium hydroxide (TPAOH), hierarchical ZSM-5 with the maximum external surface area of 287 $m^2\ g^{-1}$ and mesopore volume of 10.2 $cm^3\ g^{-1}$ can be fabricated [104]. Nevertheless, treating MFI-type zeolites with various concentrations NaOH solutions mixed with a constant amount of CTAB surfactant can enhance the mesoporosity and improve the catalytic performance in etherification 2,5-bis(hydroxymethyl)furan with ethanol to biofuels [105]. Consequently, desilication has been successfully applied to aluminosilicateous zeolites with different framework topologies, such as MOR [106, 107] AEI (SAPO-18) [108], BEA [109, 110] and FAU [111, 112].

2.2.2.2 Sequential modifications

Direct desilication of Al-rich zeolites (with SAR < 15) is challenging, specifically on zeolite Y with SAR of 2−3, as the high Al concentration retards the extraction of Si from the zeolite framework. In order to create mesoporosity in Al-rich zeolites, combinations of post-synthetic treatments were developed. Mordenite (SAR = 15) was sequentially leached with 2 M nitric acid at 100 °C for 4 h and 0.2 M NaOH for at 65 °C 0.5 h [113]. It was found that the SAR of the zeolite was firstly tuned to ~25 after dealumination without detectable mesoporosity. The subsequent desilication washed out the Si species, after which significant mesopores were rendered in the framework. The approach was later successfully applied to Al-rich mordenites with different SAR values (i.e., SAR = ~8 and ~10) [114]. Since the sequential approaches sustained the microporosity and acidity of the parent mordenite as well, the resulting mesoporous mordenite showed the improved performance in the liquid-phase alkylation of benzene with propylene to cumene (e.g. conversion of propylene at ~100% for mesoporous zeolites vs. ~15% for the parent zeolite). In addition to the acid-alkaline leaching (i.e., the dealumination-desilication protocol), the steaming-desilication protocol is also capable to introduce uniform intracrystalline mesopores (4–6 nm) into the microporous Al-rich ZSM-5 (SAR = 13.9) [115]. Shahid et al. [116] also found that steaming followed by sequential acid-base treatment for ZSM-5 leads to significant mesoporosity formation in comparison with the materials obtained by the conventional acid-base leaching treatment.

Sodium form Al-rich clinoptilolite with SAR = 5.2 can also be modified by sequential acid-alkaline treatment. Using HCl solution rises the SAR to ~10.4 and subsequent desilication by NaOH solution yields both external surface area and mesopore volume up to 4-fold increase relative to the parent Na-clinoptilolite [117]. In order to introduce more hierarchical mesoporosity into Al-rich zeolites, it is also an effective way to treat dealuminated zeolites with PDA under alkaline conditions. For instance, García-Martínez et al. [118] developed a post-synthetic method to prepare mesoporous zeolite Y with relatively uniform intracrystalline mesopores (~4 nm). The method involves dealumination of the parent

Y by citric acid and alkaline treatment with NH_4OH solution and CTAB. The well-controlled mesopores (determined by the chain length of PDA) are rendered after the removal of PDA by calcination. The sequential dealumination-(desilication+PDA) was also expanded to other zeolite frameworks. Góra-Marek et al. [119] uses a combined procedure of dealumination with nitric acid and desilication with NaOH and additional TPAOH to produce MOR zeolite with hierarchical porous structures which are beneficial to the conversion and the selectivity to primary products in TIPB and vacuum gasoil (VGO) cracking. They confirmed that desilication performed in the presence of PDA contributes significantly to the development of mesoporosity in comparison with the conventional alkaline treatment with NaOH solutions. Other combined methods were also developed, such as chemical treatment combined with desilication, which is exemplified by the modification of Al-rich ZSM-5 zeolites using the sequential fluorination-desilication. The resulting materials show broad distribution of significant mesopores , as well as maintained high Al concentration simultaneously [120].

For typical Al-rich zeolites such as faujasite zeolites X and Y, hierarchical structures commonly cannot be directly synthesised. Delamunination is necessary for introduce mesopores as the SAR value of FAU-type zeolites is far from the optimal range identified for the post-synthetic desilication protocol. Verboekend et al. [91, 121] performed the chemical treatment (using H_4EDTA) of zeolite Y. By reducing the treatment duration from 72 h to only 6 h, it did not strongly influence the formation of mesopores in Y zeolites. After the desilication treatment of the dealuminated Y with the optimal NaOH solution (i.e., 0.2 M NAOH at 65 °C for 30 min), both external surface area and mesopore volume of the materials were remarkably increased, however, significant amorphous phase was formed as well. They also found that the removal of amorphous Al-rich debris from the sequentially dealuminated and desilicated zeolites by a following moderate acid treatment (e.g. using Na_2H_2EDTA) could enhance micro- and mesoporosity, increase crystallinity, restore acidity and composition, and, ultimately, enhance catalytic activity. The conversion of benzene alcohol of three-step modified Y zeolite reaches 84% after 40 min, where pristine and dealunimated-desilicated Y zeolites can only achieved 47% and 53%, respectively. They then normalised the conversion to the Al content and found that the activity of the three-step modified Y is four-fold and twice of that of pristine Y and dealunimated-desilicated Y

zeolites, respectively, confirming the effectiveness of the three-step modification. Accordingly, a general strategy of preparing hierarchical FAU zeolites using the bottom-up and top-down methods was proposed as presented in Figure 2.8 [122]. A three-step post-synthetic method was then developed successfully for treating Al-rich MOR-type (SAR = 4.8) by Huang et al. [123]. Using steaming-acid leaching (with 3 M HNO_3)-alkaline treatment (0.1 M NaOH), hierarchical mordenite zeolites with intracrystalline mesopores centred around 20 nm were obtained, which were fully characterised by TEM and N_2 physisorption analysis. The crystallinity was preserved while the acidity dropped with an increase in SAR. Again, it was shown that the three-step treatment was more effective than the one-step or two-step methods.

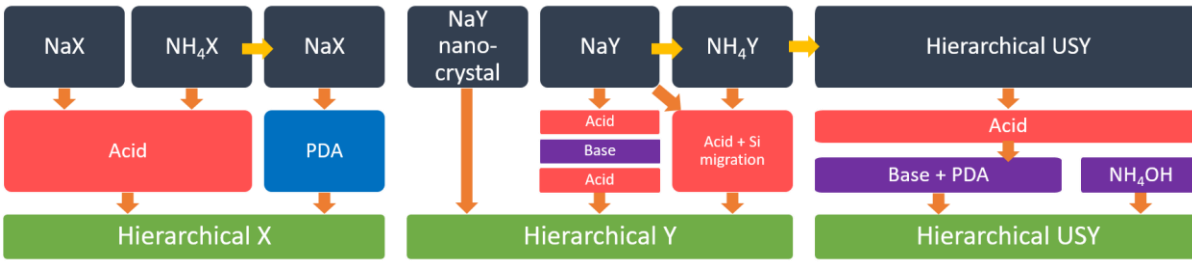

Figure 2.8 A flow chart of conclusion for hierarchical FAU-type zeolites synthesis using bottom-up and top-down strategies. Top-down methods consist of steam, acid (red), and base (purple) treatments [122].

2.3 Process intensification for post-synthetic mesoporous zeolites

Since the preparation of porous materials contributes significantly to the environmental impact and sustainability of the molecule which produced via catalytic synthesis, the sustainable aspects of porous materials, concerning aspects of raw materials, synthesis, and/or modification should be considered for the sustainability of their catalytic applications thereafter [124]. Based on the concept of green and sustainable chemistry, as mentioned in previous section, the bottom-up strategy still suffers from limitations such as non-recyclable and high-cost templates. By contrast, top-down method is more efficient and practical for sustainable industrial application. However, it is obvious that almost all top-down methods still experience relative long treatment duration at relative high temperature (nearly 80–200 °C) contributing to a high energy cost process and low efficiency. Thereafter, new developments to intensify post-synthetic methods are continuously reported in recent years. It has been

shown that alternative energy such as microwave (MW) and ultrasound (US) can remarkably reduce the synthesis time of zeolites thus making the synthesis and/or modification of zeolites more efficient regarding the energy and time usages [125-127].

2.3.1 Microwave energy and ultrasound energy

Microwaves are a form of electromagnetic radiation with wavelengths in a frequency range from 300 MHz to 300 GHz (wavelength between 1 m and 1 mm), where typical operation frequency of MW is 915 ± 15 MHz and 2.45 ± 0.15 GHz. The use of 2.45 GHz (12.2 cm wavelength) is more prevalent due to the fact that energy absorption is maximum for water at this frequency. Additionally, magnetrons at this frequency are widely available in laboratory (and household) microwave instrument [128, 129]. In the case of energy transfer under microwave irradiation, the alternating electric field is primarily responsible for heat generation, interacting with dielectric molecules via two modes of action: dipolar orientation and ionic conduction. In dipolar orientation, the dipole molecules in the electric field tend to align them with the magnetic field, and hence they oscillate according to the oscillation of the magnetic field. Dielectric heating occurs due to the friction between rotating molecules which results in heating the bulk phase. In ionic conduction, a free ion or ionic species moves translationally through space, attempting to align with the changing electric field. The friction between these moving species results in heat generation which is similar to dipolar orientation (as exhibited in Figure 2.9 (a)). In both cases, the more polar and/or ionic of species, the more efficient they promote heat generation. Microwave irradiation is fundamentally different from conventional heating (Figure 2.9 (b)), and thus having the potential to be explored for developing efficient and effective methods for the synthesis and post-modification of zeolites.

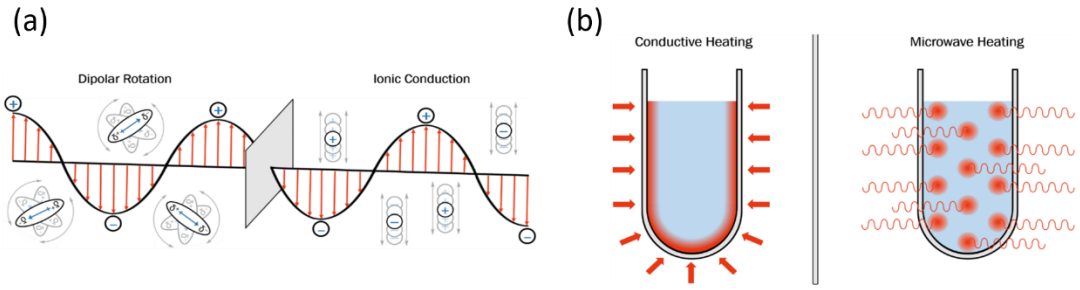

Figure 2.9 (a) Mechanisms of microwave heating: dipolar rotation (or orientation) and ionic (or electrical) conduction; and (b) comparison between conventionally conductive heating and microwave-assisted heating [130].

Ultrasonic irradiation has the frequency larger than 20 kHz, which can provide intensified localised conditions regarding temperatures and pressures in liquids[131]. In the field of zeolite synthesis and modification, sonication is the act of applying sound energy to agitate particles in a heterogeneous sample by using an ultrasonic bath or an ultrasonic probe, colloquially known as a sonicator. Since sound waves propagating through a liquid at ultrasonic frequencies with wavelengths much longer than molecular dimensions or the bond length between atoms in the molecule, the sound wave cannot directly affect the vibrational energy of the bond, therefore, cannot directly increase the internal energy of a molecule, i.e., no direct interaction between ultrasound and the chemical species at the molecular level [132]. Instead, ultrasound causes cavitation events that refer to the formation, growth and violent collapse of micro-bubbles in a liquid medium.

Ultrasonication generates alternating, expanding and compressing sound waves, leading to the formation and oscillation of small vacuum bubbles. During the expansion in ultrasonic field, gas in the liquid diffuses into the vacuum bubbles, and conversely, the gas within the bubble diffuses back into the liquid bulk during compression. However, due to the relatively small surface area of bubbles not all gas molecules within the bubble can diffuse out. After multiple expansion and compression, micro-bubbles holding ultrasonic energy grow continuously to reach a critical size, causing the bubble collapse during one compression cycle [23]. The collapse of the bubbles is an almost adiabatic process, resulting in high speed impinging liquid jets and strong hydrodynamic shear-forces. Bubble collapse in liquids produces enormous amounts of energy via the conversion of kinetic energy of the liquid motion to heat

of the content in the bubble. A very short-lived localised hot-spot is generated as the compression of the bubbles during cavitation is more rapid than thermal transport. These hot spots can reach a temperature of around 5,000 °C, pressures of roughly 1,000 bar, and heating and cooling rates above 1,010 °C s^{-1} [129]. For liquids containing solids, similar phenomena may occur when exposed to ultrasound. Once cavitation occurs near the extended solid surface (fin), the cavity collapse is nonspherical and causes high-speed ejection of liquid. These jets and associated shockwaves can damage the now highly heated solid surface. The liquid-solid suspension thereafter generates high-speed particle collisions, which alter the surface morphology, composition and reactivity of the solid particles [133].

Applications of ultrasound in chemistry often use frequencies of 20–100 kHz. When the intensity is higher than 10 watts per square centimetre, cavitation can be inducted in liquid media. In general, ultrasound baths in laboratory operate near to 40 kHz, where physical effects of ultrasound (e.g. emulsification and surface damage) are more dominant at lower frequencies, and cavitation occurs over the full frequency range [131]. Thus, sonication gives the benefits for accelerating the nucleation and crystallisation of various zeolites (e.g. SSZ-13 CHA-type [134], erionite ERI-type [135] and NaX FAU-type [136]).

2.3.2 Microwave-assisted post-synthetic treatments

Considering the thermal requirement in zeolite synthesis, microwave irradiation can instantly heat up the system via dipolar orientation and/or electrical conduction, therefore, in comparison with the conventional heating, resulting in a more efficient, more precise, and safer mode of heating, and hence has been acknowledged with its benefits for zeolite synthesis since 1980s [22, 137-139]. Moreover, it is found that under comparable conditions, the microwave heating is faster than the hydrothermal method and has no destructive effect on the molecular sieve skeleton structure [140].

MW-assisted post-synthetic modification was firstly applied on titanosilicate ETS-10 possessing a three-dimensional system of interconnected micropores with dimensions of about 0.8 × 0.5 nm [141, 142]. ETS-10 zeolites in hydrogen peroxide solutions with various weight percent were heated up to

150 °C under MW irradiation and held for 15 min. As compared to the conventional treatment (ETS-10 was treated three times with fresh 10 wt % H_2O_2 solution for 20 min each time at room temperature), MW-assisted method can introduce starkly mesopores in EST-10 zeolite frameworks, indicating the effective volume heating by MW accounted for the rapid fabrication of mesopores in ETS-10 [143]. Consequently, MW-assisted post-synthetic modification resulted in abundant intracrystalline mesopores and improved catalytic performance in the Beckmann rearrangement of cyclohexanone oxime.

Zhang et al. [144] also used H_2O_2 solution with MW-assisted method to generate mesoporosity in microporous Beta zeolite frameworks. Different from above mechanism which literally applied MW to intensify the extraction of Ti metals by H_2O_2, in this work secondary porosity was created via the local explosion by MW-assisted rapid decomposition of H_2O_2. Specifically, H_2O_2 was decomposed to generate gases under microwave irradiation (4–30 wt% of H_2O_2, MW is set at 180 °C holding for only 9 min), which rushed out from the framework and created secondary mesopores in line with the direction of the pristine crystal channels. In the microexplosion, both dealumination and desilication occured and the acidity and microporosity were well preserved. The hierarchical structure and preserved acidity in the modified Beta zeolites benefited to the catalysis, which was reflected by the increase in the conversion of 2-methoxynaphthalene acylation and the selectivity to the target molecule of 2-acetyl-6-methoxynapthalene.

Sònia Abelló and Javier Pérez-Ramírez [145] firstly applied MW-assisted desilication on NH_4-form ZSM-5 (SAR = 37 and 40) and successfully prepared hierarchically structured zeolites combining micro-/meso-porosity. In this work, the effect of the heating time of the alkaline treatment (with 0.2 M NaOH at 65 °C) under both microwave and conventional conditions was investigated. The optimal treatment time was measured as 30 and 3 min, respectively, for the conventional and MW treatment. Under the MW condition, substantial mesoporosity with $S_{external}$ of 230 m^2g^{-1} and V_{meso} of 0.39 cm^3g^{-1} was created in the resulting ZSM-5 after 3 min, which was comparable with that of the modified ZSM-5 from the 30 min conventional alkaline treatment. Other studies of employing MW irradiation to intensify the desilication treatment of zeolites for introducing hierarchical porosity into zeolite

frameworks, i.e., by reducing the treatment time, were also reported such as mild basic solution (e.g. treated ZSM-5 with NH_4OH or ethylenediamine) [146] or additional PDA (e.g. modified ZSM-5 with CTAB and modified BEA with TPAOH) [147, 148].

Paixão et al. [149] performed the MW-assisted desilication of NH_4-form MOR zeolites. Due to the relatively low SAR of the selected MOR (SAR = 20), under the conventional hydrothermal alkaline condition (0.2M at 85 °C) and extended treatment time of >2 h was necessary to generate mesopores in MOR. In comparison with ZSM-5 [145], MW-assisted desilication showed similar promoting effect on MOR zeolites regarding the mesoporosity development. However, MW irradiation benefited the conversion of the fraction of MOR framework (with intrinsic micropore size <0.7 nm) to large micropores with pore size between 0.7 and 2 nm. The authors claimed that, in the conventional hydrothermal desilication, inward corrosion (from the outer surface of zeolite crystals toward the interior) prevails which leads to the heterogeneous mesoporous features. On the other hand, in desilication under microwave conditions, the zeolite framework absorbs MW radiation directly to enable the quick and uniform heating, and hence the uniform extraction of Si species and the resulting homogeneous perforated crystals (confirmed by TEM analysis). Similar phenomena, i.e., the formation of well-dispersed mesopores in the modified MOR zeolite due to MW irradiation (0.4 M NaOH alkaline modification), were reported as well [150].

As previous work suggested that MW-assisted desilication may be a generic approach for efficient and effective creation of mesoporous zeolites, the method was employed to fabricate mesoporous ZSM-12 (MTW, which is a one-dimensional zeolite with framework of 12-membered ring channel systems) [151]. In this study, NaOH concentration was varied from 0.1 to 0.3 M and the treatment time was fixed at 10 min under MW irradiation. Again the method was effective to create intracrystalline mesoporous structures in ZSM-12 zeolite, e.g. V_{meso} = 0.34 and 0.53 $cm^3\,g^{-1}$, respectively, for the resulting zeolites treated with 0.2 M and 0.3 M NaOH solutions after 10 min as presented in Table 2.1. However, the silica-rich extra framework deposits were also formed and blocked the micropores. *n*-heptane cracking was performed to evaluate the catalytic activity of the modified ZSM-12. The sample modified with 0.3 M NaOH (by the MW method) presented a high conversion at ~ 75.4% and propylene-to-ethylene ratio

of 0.7. However, the improvement of catalytic activity was insignificant as compared with that by the parent ZSM-12, which could be contributed to the reduced acidity caused by the framework collapse.

Table 2.1 Porous properties of the parent and modified ZSM-12 zeolites [151].

Sample	$S_{external}$ ($m^2\ g^{-1}$)	S_{BET} ($m^2\ g^{-1}$)	V_{micro} ($cm^3\ g^{-1}$)	V_{meso} ($cm^3\ g^{-1}$)
Parent ZSM-12	40	306	0.175	0.09
0.2 M 10 min	205	134	0	0.34
0.3 M 10 min	380	180	0	0.53

MW-assisted dealumination of zeolites was also investigated uisng several Al-rich zeolites. González et al. modified Na-form MOR (SAR = 6.5) [152], Na-form ZSM-5 (SAR = 20) and Na-form Beta (SAR = 10) [153] with 6 M HCl using the MW-assisted and hydrothermal reflux or autoclaving methods. Comparatively, the treated samples by the MW method showed the relatively large reduction in the crystallinity and unit cell volume compared with those by the conventional treatments, reflecting the relatively high degree extraction of Al species from the framework under MW irradiation. However, compared with the parent MOR zeolite, the MW-assisted dealumination did not promote the creation of mesoporous structures, being comparable with the conventional hydrothermal methods. In order to evaluate the catalytic activity of the MOR zeolites under investigation, the isomerisation of styrene oxide to yiled β-phenylacetaldehyde (PA) and 2-ethoxy-2-phenylethanol (EPE) was carried out. The dealuminated zeolites by the MW method (15 min treatment time) showed high conversions of 73−100%, whereas the dealuminated zeolites by the conventional methods showed relatively low conversions of 32−49%. The difference of the modified MOR zeolites in catalysis was attributed to their acidic properties which were different (according to the NH_3-TPD analysis) depending on the heating methods employed by the dealumination method. Later, the same post-synthetic treatments were applied on Beta and ZSM-5 zeolites [153], which showed the effectiveness of the MW-assisted dealumination for Al extraction from Al-rich Beta and ZSM-5 zeolites.

Shekara et al. [154] systematically studied the influence of *p*-toluenesulfonic acid (*p*-TSA) concentration, dealumination temperature and time on BEA zeolites under both MW and hydrothermal conditions. It was found that 2 min was sufficient to dealuminate BEA zeolite under MW irradiation,

conversely, the conventional hydrothermal method required at least 2 h to achieve the same level of dealumination. Additionally, the extent of dealumination depended on the concentration of *p*-TSA at a fixed temperature. Although dealumination of BEA zeolite was achieved with high efficiency regarding the treatment time under the MW condition, mesoporosity development was not significant in the relevant treated zeolites. Comparative catalysis of esterification of *p*-cresol with phenylacetic acid (PAA) for *p*-cresyl phenyl acetate (PCPA)) showed that the MW modified Beta zeolite presented the high conversions of PAA and yield of PCPA, respectively, which could be contributed to the varied acid sites in the modified zeolites. This work demonstrated that the use of MW irradiation in the post-synthetic dealumination of zeolite Beta was more efficient and controllable than the conventional method. Recently, Wang et al. [140] modified H-form Beta (SAR = 16) using acetic acid (0.3–1.5 M) at 80 °C for 30 min under MW irradiation. As expected, MW-assisted dealumination did not contribute to the formation of mesoporosity in Beta zeolite, but adjusted the surface acidity of the resulting zeolites (e.g. reduction in strong acid).

2.3.3 Ultrasound-assisted post-synthetic treatments

The first post-synthetic treatment of zeolites under ultrasound irradiation was performed by Shu et al. [155], in whcih4A zeolite (LTA type, SAR = 1) was dispersed in the solution of toluene and thionyl chloride and kept in a sonication bath for 12, 24 or 48 h at 40 °C. The control experiments under the conventional hydrothermal conditions (i.e., in a water bath under stirring) were also performed. Ultrasound irradiation was highly efficient to dealuminate 4A zeolite under ambient conditions at around 40 °C, creating octahedral-coordinated Al species in the modified zeolites. The SAR value increased with an increase of the treatment time extends, and Al species were almost fully removed after 48 h treatment under sonication. The sonication treatment also caused the decrease of S_{BET}, i.e., 421.3 $m^2\ g^{-1}$ for the parent 4A zeolite and 293.8 $m^2\ g^{-1}$ for the modified sample after 48 h sonication treatment. Although the authors claimed the formation of mesopores in 4A zeolite due to Al extraction, no corresponding mesoporous data (e.g. S_{meso}, V_{meso} and mesopore PSD) were provided. Conversely, the treated 4A samples by the conventional method did not show the development of mesoporosity, showing the effect of ultrasound irradiation on dealumination of 4A zeolite under the condition

investigated. The work attributed the effective dealumination to the local heating phenomenon caused by ultrasound cavitation. The pioneering work showed the potential of employing sonication for intensifying dealumination of zeolites. Ultrasound-assisted dealumination was then performed on Al-rich zeolite Y after 8 years [156]. The work used acetylacetone solution to extract Al from zeolite framework, and the treatment was conducted under both sonication (for 30 min) and conventional (for 2 h under stirring) at room temperature. Similarly, ultrasound showed the capability of efficient dealumination of Y zeolite, giving the modified samples with high SAR values, reduced surface areas and relative crystallinity.

Ultrasound also showed the potential to shorten the desilication treatment and enabled the modification under milder conditions. Khoshbin and Karimzadeh [157] performed desilication of the as-synthesised microporous ZSM-5 (SAR = ~20) using 0.05 M NaOH at ambient temperature. The treatment was performed under the conventional stirring condition for 60 min and ultrasound condition (for 10, 20 and 30 min, respectively). It was found that, in comparison with the sample modified by the conventional method, the modified samples from the sonication treatment possesses lower crystallinity, higher external surface area and mesopore volume. Specifically, the sample from the sonication treatment (for 20 min) presented the well-developed hysteresis loop, indicating the introduction of mesoporosity (with external surface area of about 90 $m^2\ g^{-1}$ and mesopore volume of around 0.1 $cm^3\ g^{-1}$). The acidity and accessibility of the resulting zeolite increased with an increase in the treatment time under sonication which resulted in the improved performance in catalytic cracking of naphtha. Recent study also showed the positive effect of ultrasound irradiation on the post-synthetic desilication treatment of Y in presence of PDA for preparing hierarchical Y zeolites [158]. The authors mixed NaOH/TPAOH solution with Si-rich zeolite Y (SAR = 30) and kept the mixture at room temperature for 30 min under ultrasound irradiation (for comparison, conventional desilication method using the same alkaline solution at 80 °C for 30 min was also performed). The relevant SAR and porous properties of the parent and treated Y zeolites are shown in Table 2.2. Comparative catalysis of furfural decarbonylation was used to assess the activity of the zeolitic materials under investigation, and the mesoporous Y zeolites obtained by the

ultrasound-assisted method showed the improved activity due to the well-developed mesoporosity (Table 2.2).

Table 2.2 SAR values (by ICP) and porous properties (by N_2 physisorption) of the modified Y zeolites from the conventional and ultrasound-assisted desilication methods [158].

Sample	V_{micro} ($cm^3 g^{-1}$)	V_{meso} ($cm^3 g^{-1}$)	SAR
Parent Y	0.260	0.290	31
Conventional method with 10% TPAOH	0.190	0.947	20
Ultrasound-assisted method with 10% TPAOH	0.150	1.071	21
Conventional method with 40% TPAOH	0.232	0.936	24
Ultrasound-assisted method with 40% TPAOH	0.085	0.916	24
Conventional method with 70% TPAOH	0.208	0.717	26
Ultrasound-assisted method with 70% TPAOH	0.209	0.740	26

2.4 Characterisation of zeolites

2.4.1 Powder X-ray diffraction

Powder X-ray diffraction is widely used for crystallographic structure identification, chemical composition and unit cell dimensions of crystalline materials. X-rays considered as electromagnetic radiation with wavelength between 10^{-10} to 10^{-8} m are generated by accelerated electrons colliding with materials. In a vacuum cathode ray tube, electrons are produced by heating tungsten and then accelerated under high voltage to collide anode metal target. Orbital electrons are bombarded out of inner electron shell of the metal target (such as Cu, Fe, Mo and Cr) by those incident electrons with high energy. After that, electrons in higher energy levels (i.e., 2p and 3p) fill the vacancies in low energy level (1s), and characteristic X-ray spectra are emitted. The electronic transition from 2p to 1s is called Kα, whereas from 3p to 1s is called Kβ. In order to have monochromatic X-rays for further diffraction, foils (i.e., Ni, Mn, Zr or V) are applied to barricade Kβ which has weaker intensity than Kα. For zeolite characterisation, copper is commonly used as the anode target since copper gives the best cost and wavelengths above 1 Å (Kα = 1.5418 Å). The monochromatic X-rays then strike atoms of the sample and elastic scattering takes place. Due to the periodic arrangement of regular arrays of atoms or ions in crystals, constructive interference of scattered monochromatic waves occurs in specific directions when conditions satisfy with Bragg's law:

$$n\lambda = 2d\ \sin(\theta) \qquad \text{(Eq. 2.1)}$$

where n is an integer ($n \leq \frac{2d}{\lambda}$), λ it the wave length of the incident X-ray, d is the interplanar spacing in the atomic lattice and θ is the angle between incident X-ray and crystal reflecting planes.

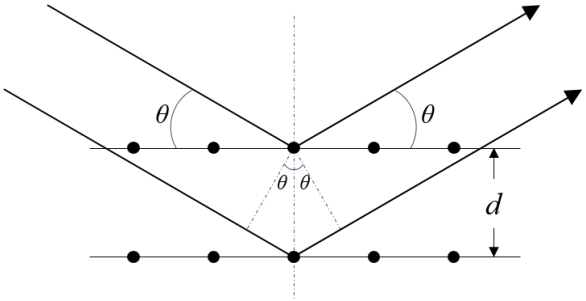

Figure 2.10 Two parallel lattice planes reflect two X-ray beams.

As the sample and detector rotated at an angle of 2θ, reflected signal of X-ray beams are recorded, processed, counted and converted to diffraction patterns. The intensity of the diffractions are determined by the distribution of the elections in the unit cell. Lattice planes going through areas with high electron density reflect strongly, and conversely low electron density gives weak diffracted intensities. Each type of crystallite has its specific diffraction pattern typically treated as 'fingerprint' for classification and identification. Moreover, the size of crystallite can also be obtained from X-ray diffraction pattern. The size is related to the full width of peak at half maximum according to Scherrer equation:

$$L = \frac{K\lambda}{\beta\cos(\theta)} \qquad \text{(Eq. 2.2)}$$

where L is the mean crystal size, K is a shape factor, λ is the X-ray wavelength, β is the half width subtracting the instrumental line broadening at 2θ in radians.

The crystallinity of the sample can be identified by comparison of d-spacings (or known as characteristic diffraction peaks) with standard patterns, and the framework SAR can theoretically be determined by diffraction patterns and empirical formula [159].

2.4.2 Gas sorption analysis

Gas physisorption is widely used to determining the pore architecture of porous materials, including zeolites. It occurs when gas or vapour phase (adsorbate) contacts with the solid surface (adsorbent). The interaction between gas molecules and the surface of the adsorbent is mainly governed by the Van der Waals forces and without any forms of chemical bonding. The interplay between the fluid-wall and fluid-fluid interactions as well as the effect of the confined pore space on the state of fluids confined to narrow pores always influence the behaviour of molecular physisorption in zeolites which lead to various types of isotherms. The International Union of Pure and Applied Chemistry (IUPAC) has classified six types of isotherms and three types of pores (according to their internal pore width, i.e., the diameter in case of cylindrical pores and the distance between opposite walls in case of slit pores) [160]. Pores with the pore width of smaller than 2 nm are called micropores, between 2−50 nm are called mesopores, and greater than 50 nm are called macropores. Regarding the definition of nanopores, they commonly refer to pores with the pore width not exceeding 100 nm. The isotherms illustrate the amount of adsorbate adsorbed as a function of the equilibrium pressure (as the relative pressure, p/p_0, where p is the actual pressure and p_0 is the saturation pressure at a given temperature) of the gas at constant temperature. Over the past 30 years, IUPAC refined the classification of physisorption isotherms as shown in Figure 2.11.

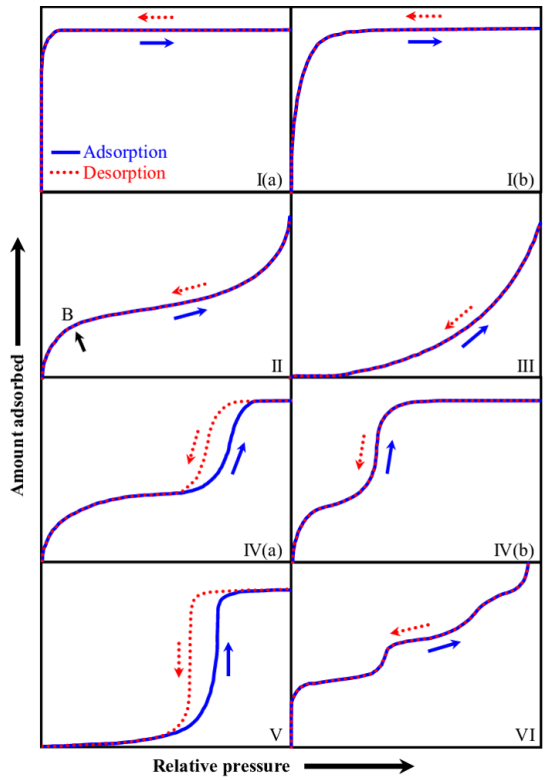

Figure 2.11 IUPAC classification of physisorption isotherms [161, 162]. B symphonises the formation of monolayer.

Common isotherms measured for porous solids include type I, II, and IV. Type I isotherms represent the monolayer adsorption on microporous solids (e.g. zeolites) which have small external surface areas, and hence the adsorption on them is limited by the accessible microporous volume. Type I(a) suggests microporous materials with narrow micropores smaller than 1 nm, and Type I(b) isotherms indicates wider micropores and narrow mesopores less than about 2.5 nm.

Type II isotherms are given by macroporous or non-porous solids, indicating monolayer-multilayer adsorption. Especially point B implies where adsorption multilayer is about to begin, and monolayer adsorption is finished. The amount of adsorbed gas molecules appears to increase without limit when $p/p_0 = 1$.

Type IV isotherms show similar sorption path to that of Type II initially, and then are followed by pore condensation. In the case of Type IV(a), the special feature of hysteresis loops is associated with the capillary condensation which occurs during the desorption of adsorbed gas molecules from mesopores

whose sizes are larger than 4 nm. At the initial stage of adsorption, monolayer adsorption of adsorbate molecules on the wall occurs. As the more vapour molecules enter the pore, vapour molecules interact with each other for multilayer adsorption which leads to the formation of condensed state. This process continues until meniscus is formed, which can keep gas-liquid phase equilibrium even below the saturated vapour pressure. Therefore, it is difficult to break this gas-liquid phase balance for desorption processes, in which case hysteresis loops occur. Reversible Type IV(b) isotherms are signatures of materials with relatively small mesopores (less than 4 nm) and/or conical and cylindrical mesopores that are closed at the tapered end.

2.4.2.1 Type of hysteresis loops

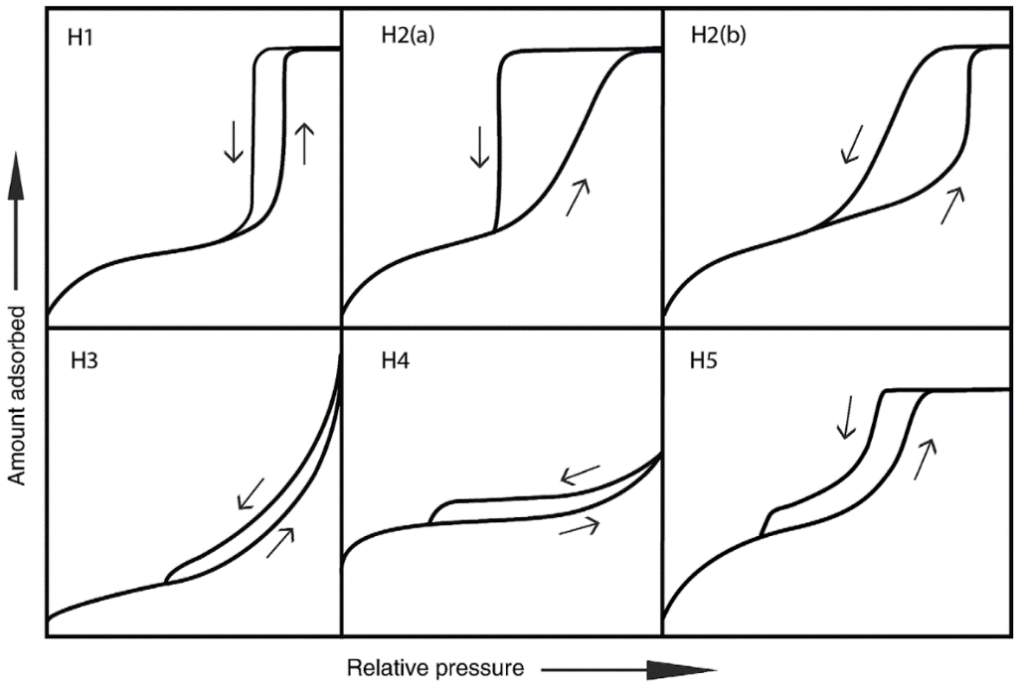

Figure 2.12 IUPAC classification of hysteresis loops [161].

Type H1 loop is associated with a narrow range of uniform mesopores. A common characteristic of many hysteresis loops is the steep region of the desorption branch which leads to the occurrence of the lower closure point. Particularly for ink-bottle-shape pores associated with type H2(a) and H2(b), the wide body of the pore remains filled until the neck part evaporates at a lower vapour pressure. Type H2(a) hysteresis loops have very steep desorption branch, which can be contributed to narrow range of

pore necks or cavitation-induced evaporation. At a given temperature, the neck size controls whether pore blocking or cavitation occurs. Above a certain critical neck size (For N_2 and argon, Ar, adsorption at −196.15 °C and −186.15 °C, respectively, ≈ 6 nm) pore blocking occurs, and below this cavitation controlled evaporation takes place. The Type H2(b) loop is related to pore blocking, where the size distribution of necks is much wider than the size distribution of pores.

Type H3 loop with adsorption branch resembles Type II isotherm, is found with slit-shape pores, arrogated plate-like materials or macroporous materials which are not completely filled by adsorbate condensate. Type H4 loop contains a composite of Type I and Type II adsorption branch. This loop is often found with arrogated zeolites or some mesoporous zeolites. Type H5 is caused by a material consisting of both open and partially blocked mesoporosity [163].

2.4.2.2 Choice of gas adsorbate

N_2 at −196.15 °C has been generally considered as the standard adsorbate for porosity analysis of porous materials. However, N_2 physisorption is not suitable for the quantitative assessment of ultramicropores (pore width < 0.7 nm). Because of the presence N_2 molecular quadrupole moment, they can generate specific interaction (e.g. fluid-wall attraction) with polar surfaces (i.e., surface functional groups and exposed ions) of zeolites or other microporous materials during adsorption leading to unsatisfied microporosity evaluation, especially for ultramicropore assessment. Argon (Ar) at −186.15 °C can overcome this limitation because Ar molecule does not have specific interaction with polar surfaces. However, kinetic restriction at cryogenic temperatures still prevents both Ar and N_2 at −186.15 °C and −196.15 °C, respectively, from diffusing into the small micropores with pore widths of <0.45 nm. Consequently, CO_2 adsorption at 0 °C is frequently used for the ultramicropore analysis. CO_2 molecule has the relatively small kinetic diameter of 0.33 nm (for comparison: 0.36 nm for N_2 and 0.34 nm for Ar) which facilitate the diffusion of CO_2 into ultramicropores. However, it is still challenging to perform the porosity analysis of porous materials with polar surfaces, mainly because of the existence of CO_2 molecular quadrupole moments, which is similar to N_2 molecules. Although a range of probe molecules has been explored and applied to probe porosity of porous materials, they all have different limitations.

Accordingly, combination of different gas physisorption analyses is necessary to obtain the comprehensive information on porosity [164].

2.4.2.3 Brunauer-Emmett-Teller (BET) surface area

The Langmuir adsorption model assumes that (i) the surface is homogeneous, (ii) adsorption is monolayer adsorption, (iii) no (or ideally) interactions between adsorptive and adsorbent, and (iv) all adsorbing sites are energetically equivalent. Accordingly, the Langmuir equation is applicable to describe Type I isotherms for microporous materials. The BET method extended the monolayer Langmuir theory to multilayer adsorption, being widely used as the standard method to analyse gas sorption data to obtain the specific surface area of porous materials [165]. To ensure the valid use of the BET method, the following assumptions are made: (i) gas molecules physically adsorb on a solid surface in layers infinitely, (ii) all the adsorption sites for multilayer adsorption are energetically identical, and (iii) multilayer adsorption is govern by the Van der Waals forces.

$$\frac{p/p_0}{n\left(1-p/p_0\right)} = \frac{1}{n_m C} + \frac{C-1}{n_m C}\left(p/p_0\right) \qquad \text{(Eq. 2.3)}$$

which is derived in:

$$1/\left[n\left(\left(p/p_0\right)-1\right)\right] = \left(1/n_m C\right) + \left[\left(C-1\right)/n_m C\right]\left(p/p_0\right) \qquad \text{(Eq. 2.4)}$$

where n is the specific adsorbed gas quantity in mol g^{-1} at the relative pressure p/p_0; n_m is the specific monolayer adsorbed gas quantity in mol g^{-1}; and C is the BET constant related to the enthalpy of adsorption.

The specific surface area, i.e., the BET surface area (S_{BET}), can be derived from monolayer capacity n_m in the range of linearity of the BET plot, which is always restricted within the p/p_0 range of ~ 0.05–0.30, as shown in (Eq. 2.5):

$$S_{BET} = n_m N_A \sigma \quad \text{(Eq. 2.5)}$$

where N_A is the Avogadro constant (6.022×10^{-23} mol^{-1}), and σ is the average cross-sectional area of the adsorptive molecule ($\sigma(N_2) = 0.162$ nm^2). The S_{BET} can also be derived from the volume of the adsorbed gas in the monolayer V_m (cm^3 g^{-1}) and molar volume M (22,414 cm^3 mol^{-1}):

$$S_{BET} = \frac{V_m N_A \sigma}{M} \quad \text{(Eq. 2.6)}$$

In practice, the following three principles are recommended when applying the BET method to the sorption data: (i) the C constant is positive (positive intercept of the linear fit); (ii) the value of the slope of the linear fit is positive (where the term $n(1-p/p_0)$ continuously increases with p/p_0); (iii) the BET monolayer capacity n_m falls within the pressure region selected for the calculation.

2.4.2.4 t-plot method

t-plot method [166] is generally used for assessing the micropore volume and external surface area in micro- and meso-porous zeolites. As the researchers found, the multi-molecular layer of adsorbed N_2 could be formed freely on all parts of the surface, its statistical thickness, t (nm), is practically independent of the nature of the sample. The relation of the volume of N_2 adsorbed (V_a, cm^3 [STP] g^{-1} of adsorbent) and the thickness of the adsorbed N_2 layer t are presented in following equation:

$$t = \frac{15.47 V_a}{S_{BET}} \quad \text{Eq. 2.7}$$

where the constant 15.47 represents the conversion of the gas to liquid volume. The data are expressed in terms of an average thickness of the adsorbed layer t and redrawn as a *t*-curve, a plot of the amount of adsorbed N_2 (cm^3 g^{-1}) at corresponding relative pressure (p/p_0) as an empirical function of t under −196.15 °C. The Harkins and Jura empirical equation is applied for calculating t [167]:

$$t = \left[\frac{13.99}{0.034 - \log(p/p_0)} \right]^{1/2} \quad \text{(Eq. 2.8)}$$

By plotting the V_a, for an unknown zeolite sample as a function of the experimental t, a straight line as long as the multilayer is formed unhindered. This straight line goes through the origin and its slope is a measure of surface area, S_t (m^2 g^{-1}):

$$S_t = \frac{15.47 V_a}{t} \qquad \text{Eq. 2.9}$$

The intercept and slope of the straight line are interpreted as the micropore volume and the external surface area, respectively, according to the following relations:

$$V_a = i \times 0.001547(\text{cm}^3) \qquad \text{Eq. 2.10}$$

$$S_t(\text{m}^2\text{g}^{-1}) = 15.47 \times s \qquad \text{Eq. 2.11}$$

where i and s are the intercept and slope of the straight line, respectively. In the presence of microporosity, it is necessary to define the external surface of the porous materials, that is, the non-microporous surface. For example, the external surface area refers to the mesopore surface area of the mesopore zeolites. Four shapes of t-plot are presented in Figure 2.13. For micro- and meso-porous zeolites, the intercept V_a (cm^3 g^{-1}) of the first linear segment on the y-axis is proportional to the micropore volume, V_{micro} (cm^3 g^{-1}) according to the Gurvich rule [168], whereas the slope s is proportional to the external surface area, S_{meso} (m^2 g^{-1}).

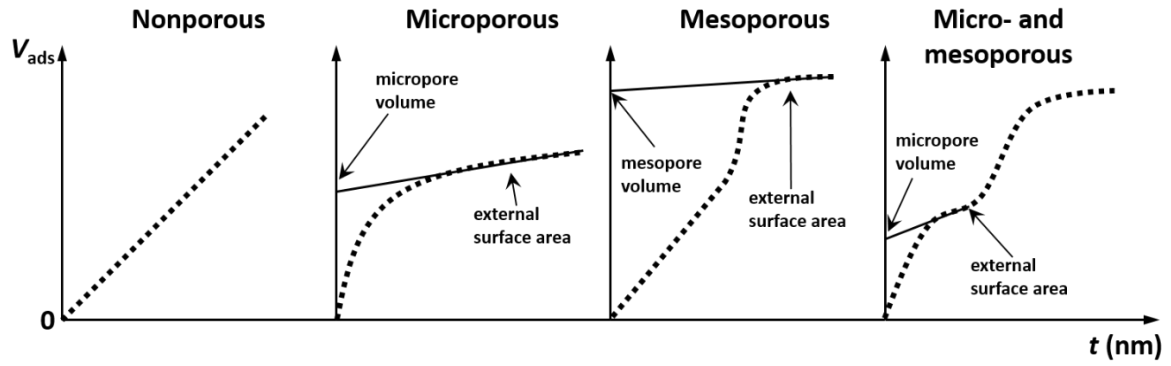

Figure 2.13 t-plot shapes derived from N_2 adsorption isotherms [168, 169].

2.4.2.5 Pore size distribution

A wide range of methods to determine characterisation of micropores are based on the standard gas adsorption analysis. The method for the determination of micropore volume is based on the work by Horvath and Kawzoe (HK), i.e., the H-K method. The H-K method can be used to calculate micropore volume distribution of pores with specific geometries such as slit, cylindrical and spherical pores. Recently, density functional theory (DFT) and non-local-density functional theory (NLDFT) methods are developed, which enable the pore size analysis of different size micropores with the improved accuracy.

BJH method developed by Harrett, Joyner and Halenda is based on modified Kelvin equation. The Kelvin equation provides a relationship between the pore diameter and the pore condensation pressure, and predicts that pore condensation shifts to a high relative pressure with an increase of pore diameter and temperature. The BJH method based on the adsorption and desorption branch of adsorption isotherms yields different results since adsorption corresponds to a progressive filling of mesopores, whereas desorption generally associates with the sudden evaporation of condensed adsorbate from the pores. Accordingly, when calculating pore size distribution, the selection of adsorption or desorption may give different results. The BJH pore size distribution (PSD) based on desorption branch always gives an artificial distribution at around 4 nm, caused by the spontaneous evaporation of metastable pore liquid (cavitation, i.e., the tensile strength effect). In contrast, the BJH method based PSD using the adsorption branch does not give this artificial peak. Therefore, in order to present the appropriate mesopore size distribution, it is a prudential choice to compare desorption and adsorption branches.

2.4.3 Mercury porosimetry

Mercury porosimetry is principally aimed at porous materials with pore between 500 μm and 3.5 nm. Since mercury is a non-wetting liquid (*i.e.* liquid-solid contact angle greater than 90°) and cannot spontaneously penetrate pores by capillary action, it must be forced into the pores by the application of a pressure (*i.e.* Δp, equilibrated pressure) exceeding the saturated vapour pressure [170]. Mercury porosimetry is most often conducted as a quasi-equilibrium experiment. The equilibrated pressure is

inversely proportional to the size of the pores, only slight pressure being required to intrude mercury into large macropores, whereas much greater pressures are required to force mercury into small pores. This is because forcing mercury into small pores greatly increases the mercury surface area in contact with the material, and the surface tension force (γ) opposes this unfavourable expansion in contact [171]. The Δ*p* needed to intrude mercury is calculated from the Young–Laplace equation [172]:

$$\Delta p = \gamma(\frac{1}{r_1} + \frac{1}{r_2}) \quad \text{(Eq. 2.12)}$$

where r_1 and r_2 are the radius of curvature of the mercury–gas meniscus. Essentially, the pore shape is assumed as a cylindrical pore geometry in mercury porosimetry such that:

$$r_1 = r_2 = r_{pore} \cos\theta \quad \text{(Eq. 2.13)}$$

where r_{pore} is the corresponding pore size, and θ is the mercury–gas–solid contact angle (> 90° for non-wetting liquid). After that, the Washburn equation can be derived:

$$\Delta p = \frac{2\gamma \cos\theta}{r_{pore}} \quad \text{(Eq. 2.14)}$$

The value of surface tension and contact angle are typically taken as 0.48 N m^{-1} and 130–140°, respectively. This provides a simple relationship to convert the mercury pressure into a pore size. By measuring the volume of mercury that intrudes into the sample material with each pressure change, the volume of pores in the corresponding size class is known. In addition, several techniques are available to determine a more accurate contact angle for mercury porosimetry, which was thoroughly discussed in elsewhere [170, 171].

2.4.4 Nuclear magnetic resonance (NMR)

2.4.4.1 The nuclear magnetic resonance phenomenon

In addition to mass (mass number, *A*) and charge (atomic number, *Z*), nuclei have angular momentum when experience spinning action. Practically, nuclei can be analysed by nuclear magnetic resonance (NMR) technique when their spin quantum number *I* is not zero. Based on quantum mechanics, the nucleus possesses magnetic moment when *I* is not zero, and it has 2*I*+1 possible spin orientations or

states. In the absence of a magnetic field, all the states have same energy level. When the nucleus is placed in a magnetic field B_0, these states present different potential energy (or called a split of spin energy levels) and transitions show up between adjacent states with the adsorption or emission of photons in radio frequency range. The nuclear moment can be aligned with (+) and against (–) the field B_0 direction. Nuclei experience different magnetic fields when they are in different environments since surrounding electrons can shield these magnetic fields in different degrees and thus slightly influence the frequencies of photons absorbed or emitted. The energy level transitions is reflected by NMR phenomena. The radio frequency of a nucleus is presented as chemical shift and measured relative to an external reference chemical. Literally, the spinning nuclei move on a cone around B_0 field performing like a gyroscope in the gravitational field, instead of flipping over and aligning with the B_0 field direction. This precessional motion of their spin axes is so called Larmor precession.

In NMR method, magnetic quantum number refers to *m* as the direction of the angular momentum vector, given by the series:

$$m = I, (I-1), (I-2), \ldots -I \qquad \text{(Eq. 2.15)}$$

For example, *I* of ^{1}H is 1/2, m may be +1/2 (lower energy level, align with the magnetic field) and −1/2 (higher energy level, against the magnetic field). If $I = 1$, the values of *m* are 1, 0 and −1. Particularly, *m* obtained by *I* based on empirical model relating to *A* and *Z*: (i) if both *A* and *Z* are even, *I* and *m* is 0 and nucleus has no magnetic moment (e.g. ^{12}C and ^{16}O), (ii) if *A* and *Z* are even and odd, respectively, *I* is integer and the nucleus is difficult for NMR analysis; and (iii) when *A* is odd *I* will be half-integer (e.g. ^{1}H, ^{17}O, ^{27}Al, ^{29}Si in aluminosilicate framework) which is suitable for NMR analysis. As mentioned above, only transitions between adjacent energy levels are allowed, so if $I = 3/2$, transitions between $m = +3/2$ and $m = +1/2$, between $m = +1/2$ and $m = -1/2$ and between $m = -1/2$ and $m = -3/2$ are possible.

Since the magnetisation vector is not permanent around the magnetic field, it will return to the thermodynamic equilibrium orientation, which is parallel to the B_0 field direction. This dynamic process is named as T_1 (longitudinal relaxation). There is another relaxation process, called T_2 (transverse relaxation) which determines the time for the transverse magnetisation decay. Figure 2.14 illustrates the

T_2 relaxation. In NMR spectroscopy, any process causing T_1 relaxation also results in T_2 relaxation as the energy exchange affects one of the spins contributing to the xy-plane, and T_2 is always less than or equal to T_1. Both processes occur simultaneously.

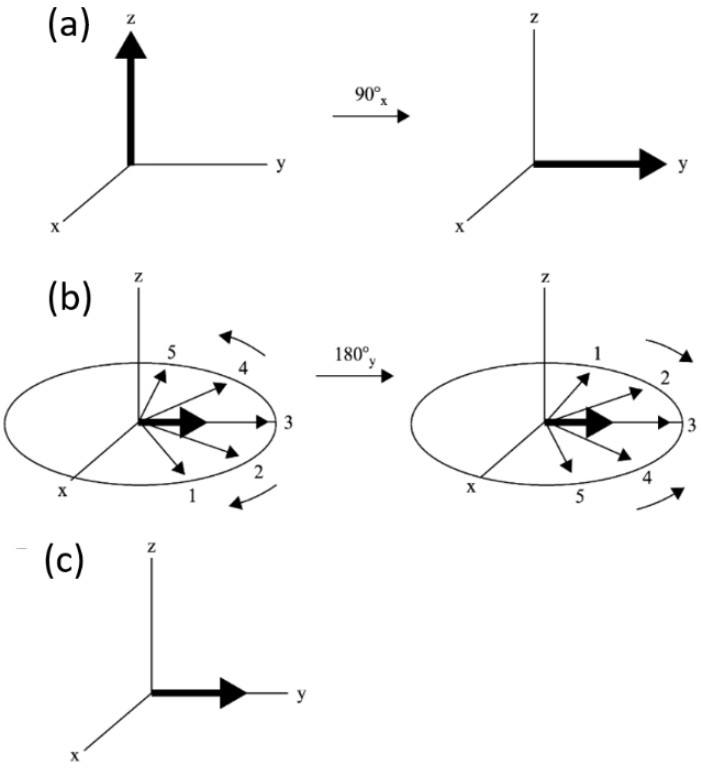

Figure 2.14 (a) A resonant 90° pulse rotates the spin magnetisation to the transverse plane; (b) spins in the z-direction are preserved and xy-plane transforms into phase coherence. After that, the 180° pulse flips the spins in the xy-plane; and (c) finally spins refocus align the y-axis [173].

2.4.4.2 Magic angle spinning (MAS)

In solid samples, more significant dipolar interaction arises due to the shorter space between a certain nucleus and neighbouring nuclear magnetic moments as compared to liquids. When the molecules have different orientations to the external magnetic field, nuclei will present different magnetic shielding and resonance frequencies, resulting in chemical shift anisotropy. Moreover, for solid samples nuclei with $I > 1/2$, the non-spherical electron distribution generates an electrical quadrupolar moment which interacts with the nucleus, and this interaction is called the quadrupolar interaction. As compared with liquid samples, solids always present broadened and overlapped NMR spectral lines due to the

disruption of dipolar interaction, chemical shift anisotropy, quadrupolar and relatively short spin-spin relaxation time.

Magic angle spinning (MAS) technique has been employed to diminish the dipolar interaction and chemical shift anisotropy to enhance the spectral resolution for solid-state NMR experiment. The sample rotor is rapidly spun at a fixed magic angle (β = 54.74° = 55°44′8″) respect to the magnetic field B_0 [174]. When the rotor spins at β = 54.74°, the chemical shift anisotropy will be entirely eliminated and the dipolar interaction will be partially disappeared. Hence, a narrow spectra with high resolution can be obtained for extracting the information.

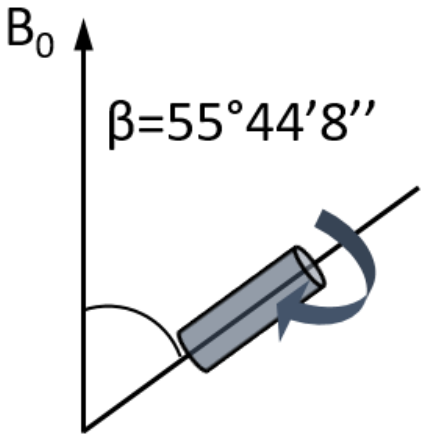

Figure 2.15 The sample (grey cylinder) is spinning at a high speed and inclined to the magnetic field.

2.4.4.3 NMR analysis in zeolites

NMR spectroscopy has been widely used in analysis of zeolite structure, diffusion, and catalysis. ^{27}Al MAS NMR can be applied to determine the chemical environment of zeolite frameworks, being suitable to allow the qualitative and quantitative analysis of Al species including both the framework and extra-framework Al. For zeolite in sodium form, the position of Na^+ can be detected by ^{23}Na MAS NMR. Commonly, ^{31}P and ^{47}Ti/^{49}Ti NMR are applied on zeolites with phosphorous (i.e., SAPO zeolites) and titanium (i.e., TS-1), respectively. When it comes to acid sites characterisation, ^{1}H MAS NMR has been developed to determine zeolite surface OH groups in diverse chemical environments. Table 2.3 lists the properties of the NMR isotopes at 9.4 T magnetic field.

Table 2.3 NMR isotopes and frequencies in zeolite chemistry.

Nucleus	*Z*	Spin	Natural abundance (%)	Frequency at 9.4 T (MHz)	Relative sensitivity
^{1}H	1	1/2	99.98	400.19	5,870.00
^{11}B	5	3/2	80.10	128.39	776.47
^{10}B	5	3	19.90	42.99	23.23
^{13}C	6	1/2	1.07	100.63	1.00
^{15}N	7	1/2	0.37	40.56	0.022
^{17}O	8	5/2	0.038	54.25	0.065
^{19}F	9	1/2	100.00	376.56	4,900.00
^{23}Na	11	3/2	100.00	105.86	545.29
^{25}Mg	12	5/2	10.00	24.49	1.58
^{27}Al	13	5/2	100.00	104.27	1,217.65
^{29}Si	14	1/2	4.68	79.50	2.16
^{31}P	15	1/2	100.00	162.00	391.00
^{47}Ti	22	5/2	7.44	22.56	0.92
^{49}Ti	22	7/2	5.41	22.57	1.21
^{129}Xe	54	1/2	26.44	111.29	33.60

^{29}Si chemical shifts

^{29}Si MAS NMR spectra are generally used for Si distribution. In aluminosilicate zeolite structure, silicon atoms are coordinated in tetrahedral form consisting of five different silicon chemical environments denoted as Si(*n*Al) units, where *n* = 0,1,2,3,4 corresponds to the number of neighbouring aluminium atoms. Each unit has one specific chemical shift range, which is summarised in Table 2.4 and Figure 2.16. As the amount n of neighbouring Al increased, the signals are systematically shifted to high field. In addition to the number of Al in the second coordination sphere of the central Si atom with a given number of Si–O–T bridges (degree of tetrahedral Al substitution), the presence of crystallographically inequivalent Si(*n*Al) sites may affect the ^{29}Si chemical shift (i.e., the length of Si–O and bond angles) as well. Accordingly, differences in ^{29}Si chemical shifts may be common in zeolites with different crystallography, though these zeolites have analogous chemical components [175]. In addition, the existence of OH groups bound with silicon atoms and located at the outer surface of zeolites structure or defect sites can also result in the shift of signals to low field from the corresponding Si(*n*Al) units and overlap with the Si(*n*+1(Al)) signal. In order to acquire the information for SiOH, ^{1}H/^{29}Si cross polarisation technique can be applied for qualitative analysis.

Table 2.4 ^{29}Si chemical shifts.

Si(*n*Al)	Chemical shift refers to TMS (ppm)
Si(0Al)	–102 ~ –120
Si(1Al)	–97 ~ –107
Si(2Al)	–92 ~ –100
Si(3Al)	–85 ~ –94
Si(4Al)	–82 ~ –92

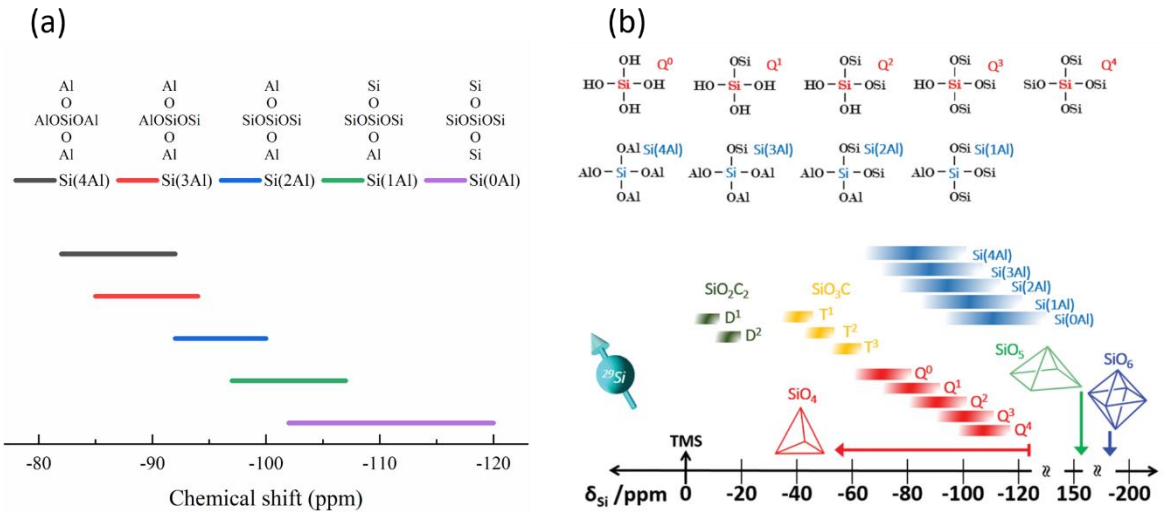

Figure 2.16 Range of ^{29}Si chemical shifts in zeolites [175, 176].

Loewenstein's rule suggests that each zeolite framework Al atom bonds with four O–Si–O and Al–O–Al linkages are not allowed. Accordingly, the zeolite framework silicon-to-aluminium ratio (SAR_F) can be directly calculated based on the peak intensity of the five ^{29}Si peaks using (Eq. 2.16):

$$SAR_F = \sum_{n=0}^{4} I_{Si(nAl)} \Big/ \sum_{n=0}^{4} 0.25 n I_{Si(nAl)} \qquad \text{(Eq. 2.16)}$$

where $I_{Si(nAl)}$ is the peak intensity of the Si(*n*Al) unit.

(Eq. 2.16) has been widely applied to zeolites X and Y. However, for zeolites containing crystallographically inequivalent Si sites such as mordenite, offretite and erionite, several inequivalent Si sites may simultaneously contribute to a certain Si(*n*Al) unit peak, which is likely to cause resonance peaks overlapping. For instance, as shown in Figure 2.17, comparison between zeolites with different

SAR values shows the existence of inequivalent Si sites in Si(0Al), and part of the Si sites may be the non-framework Si species, which can potentially lead to a higher SAR_F value when (Eq. 2.16) is used.

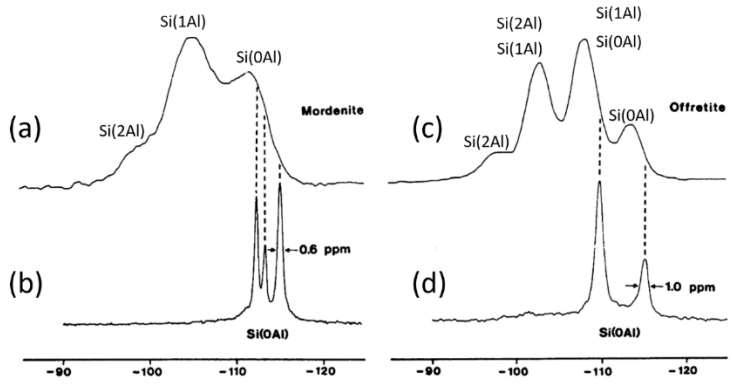

Figure 2.17 ^{29}Si NMR spectra of (a) mordenite (SAR < 10), (b) siliceous mordenite (SAR > 100); (c) offretite (SAR < 10) and (d) siliceous offretite (SAR > 100) [177].

^{27}Al chemical shifts

Since the spin quantum number of ^{27}Al is 5/2, the ^{27}Al resonance spectra are wider due to quadrupolar moment. In order to minimise the influence of broaden signals, several efforts such as applying significantly strong B_0 field, high spinning rates, and rehydration of zeolite samples, have been made to develop reliable and 'visible' aluminium spectra. MAS technique successfully narrows the ^{27}Al resonances by decreasing quadrupolar interaction. Generally, framework Al four-coordinated with four O–Si–O has a single resonance peak around 50 to 65 ppm, whereas non-framework six-coordinated Al presents one peak around 0 ppm (both use $Al(H_2O)_6^{3+}$ as the reference). Although one-dimensional ^{27}Al MAS NMR is a popular technique to determine framework and non-framework Al, it still cannot eliminate quadrupolar interaction. Thus 'invisible' aluminium gives rise to asymmetric tetrahedrally coordinated Al peak. Further detection of 'invisible' ^{27}Al can be achieved by double rotation, dynamic angle spinning, and multiple quantum two-dimensional NMR spectroscopy.

2.4.5 Fourier-transform infrared spectroscopy

Infrared spectroscopy has been developed to elucidate chemical bonds and then molecular structure of both organic and inorganic compounds. By measuring the absorption or transmission of infrared

radiation over a range of wavelengths, the functional groups in a chemical compound can be identified. When infrared radiation excites molecular vibrations, and if the radiation frequency matches with the vibration one of molecule, the infrared irradiation will be absorbed by molecule. This absorption causes transitions between two vibrational energy levels and transitions between quantised rotational energy levels occur at the same time [178]. The stretching frequency, ν (s^{-1}), of two linked atoms depends on the force constant (k) and the reduced mass (μ) [179], as shown in (Eq. 2.17) and (Eq. 2.18):

$$\nu = \frac{1}{2\pi}\sqrt{\frac{k}{\mu}} \quad \text{(Eq. 2.17)}$$

$$\mu = \frac{M_1 M_2}{M_1 + M_2} \quad \text{(Eq. 2.18)}$$

where M_1 and M_2 are masses of two atoms, respectively.

The absorbed IR frequency increases as the mass of attached atoms decreases. Once one of the atoms in the molecule is replaced by an isotope, the stretching frequency will be changed. In (Eq. 2.17), ν can be denoted as $\nu = v\tilde{\nu}$, where v is the light speed (3×10^8 m s^{-1}) and $\tilde{\nu}$ is the wavenumber (cm^{-1}).

Table 2.5 Electromagnetic spectrum [180].

Region	Wave number range (cm^{-1})	Molecular spectra
Visible & ultraviolet (UV)	> 14,000	Electronic transitions
Near IR	14,000–4,000	Molecular vibrations
Mid IR	4,000–400	Molecular vibrations
Far IR	400–4	Molecular vibrations
Microwave	< 4	Molecular rotations

Table 2.5 lists the electromagnetic spectrum. As moving from top to down, the energy, frequency and wavenumber all perform a decreased trending. FT-IR measurements for zeolites are generally used in the mid IR region, i.e., 4,000 to 400 cm^{-1} (as shown in Table 2.5) at a resolution of 4 cm^{-1}. The spectral resolution in cm^{-1} is equal to the reciprocal of the maximal retardation in cm. Thus, a resolution of 4 cm^{-1} is obtained from the maximal retardation in 0.25 cm. In order to calculate the absorbance of the functional group, the infrared spectrum of the amount of absorbed light versus wavenumber is plotted. The absorbance spectrum is calculated by:

$$A = \log(I_0 / I) \quad \text{(Eq. 2.19)}$$

where A is absorbance, I_0 is the intensity in the background spectrum, I is the intensity in the sample spectrum. A can also be presented trough Beer-Lambert Law, which is related to molecular concentration:

$$A = \varepsilon l c \quad \text{(Eq. 2.20)}$$

where ε is the molar attenuation coefficient of the material (L mol^{-1} cm^{-1}), l is the pathlength (cm) and c is the molar concentration (mol L^{-1}). Therefore, the height of a characteristic peak is proportional to concentration providing a possibility for quantitative analysis.

The infrared spectrum can also be plotted into percent transmittance T (%) versus wavenumber:

$$T(\%) = \frac{I}{I_0} \times 100\% \quad \text{(Eq. 2.21)}$$

Percent transmittance can be transformed to absorbance through $A = \log(1/T)$. Normally, percent transmittance and absorbance are used for identification and quantitative analysis, respectively.

Nowadays, a Fourier Transform Infrared (FTIR) Spectrometer commonly consists of a beam source and Michelson interferometer. Figure 2.18 elucidates the working principle of Michelson interferometer. In a Michelson interferometer adapted for FTIR, a beam from the polychromatic infrared source is collimated and directed to a beam splitter. The beam splitter reflects half of the beam toward a fixed mirror and transmits the rest toward a moving mirror. Two beams are reflected from two mirrors back to the beam splitter, and transmitted and reflected, respectively again. The latter beams interfere with each other, pass into the sample compartment and refocus on to the detector. As the relative path length is affected by the moving mirror, an interferogram can be obtained by translating the moving mirror to vary the optical path difference. After collecting signals, the spectrum is gained by carrying out an inverse Fourier transformation.

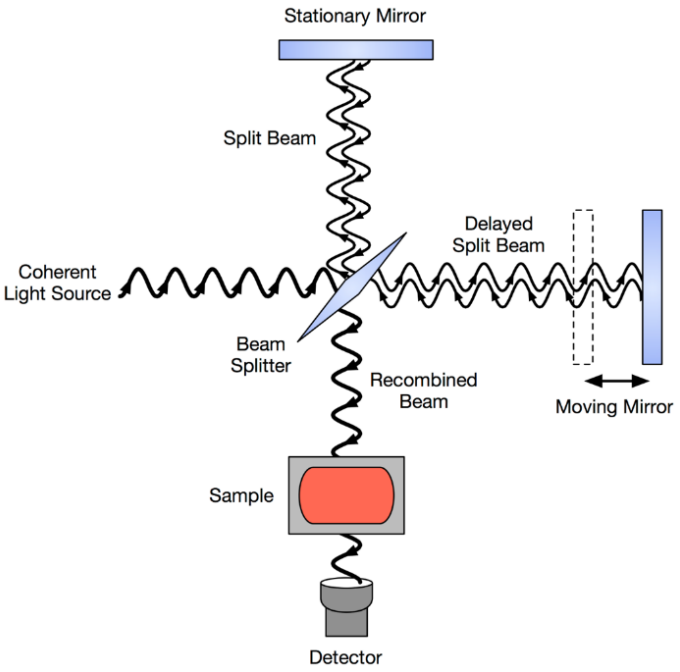

Figure 2.18 Schematic diagram of a Michelson interferometer.

FTIR provides the stretching information of zeolite frameworks and the nature of zeolite surface hydroxyl groups. Table 2.6 concludes various structural unit vibrational bands in zeolites. Although certain chemical groups or bonds only vibrate at the characteristic frequency range, more than one infrared frequency can be absorbed by certain bonds and groups. For instance, tetrahedral bonds (T–O–T, where T represents Si or Al atom) have three different vibrational modes at three different frequency ranges between 1,400 cm^{-1} and 400 cm^{-1}. IR spectroscopy also gives information about secondary building units such as single rings and double rings. The greater the member ring is, the lower vibrational frequency it will be.

Table 2.6 zeolite structural unit vibrational bands [181].

Internal tetrahedra		External linkages	
Vibrational mode	Frequency (cm^{-1})	Vibrational mode	Frequency (cm^{-1})
Asymmetric stretch	1,250–950	Asymmetric stretch	1,150–1,050
Symmetric stretch	720–650	Symmetric stretch	820–750
T-O bend	500–420	Double rings	650–500
		Pore openings	420–300

IR spectroscopy is not suitable to distinguish Al–O stretching and Si–O stretching, however, it is sensitive to the amount of aluminium in aluminosilicate zeolites. IR technique has been used for tracking changes in SAR_F Variation of Al amount changes the T–O–T bond angles because the Al atoms have smaller size and different charge density compared to Si atoms, which lead to a shift in frequency for symmetric and asymmetric stretching in zeolite. With a decrease in the Al content in zeolite frameworks, the symmetric and asymmetric stretching, as well as secondary building unit vibrations such as double rings, show a shift to higher frequency (or known as higher wavenumber).

Acidity of hydroxyl groups in dehydrated zeolites can also be studied by IR spectroscopy measuring O–H stretching. Normally three types O–H groups are mainly present on protonic form zeolite: bridging hydroxyl groups (Si–OH–Al, Brønsted acid site), silanol groups on the zeolite outer surfaces (Si–OH, external silanols) and O–H on lattice defects (e.g. Si–OH, internal silanols and Si–OH–HO–Si silanol nests). Nevertheless, hydrogen-bonded hydroxyl groups located in silanol nests also contribute to zeolite O–H stretching. The stretching frequency of bridging hydroxyl groups depends on the size and shape of the rings or cages where the hydroxyl group is located and on chemical composition such as SAR_F and the cations. Generally, the bridging hydroxyl group stretching is identified by IR in two ranges: (i) the high frequency signals between 3,650 and 3,550 cm^{-1} correspond to the O–H located in large rings (larger than eight-membered ring, i.e., supercage of FAU type zeolites); and (ii) low frequency signals 3,580–3,530 cm^{-1} correspond to the O–H vibration in six- or eight-membered rings (i.e., sodalite cages in FAU type zeolites) [182]. The frequency of external silanols is in a range of 3,750–3,745 cm^{-1}, whereas internal silanols and silanol nests have a frequency range between 3,735 and 3,700 cm^{-1}. Due to hydrogen bonding, hydrogen-bonded hydroxyl groups result in a prominently broad absorption band at 3,650–3,200 cm^{-1} centred around 3,500 cm^{-1}.

In order to gain detailed information on acidity, IR measurement of probe molecules absorbed on zeolite frameworks is very useful. Both Brønsted and Lewis acid sites can be identified and quantified by the technique. Pyridine is one of the most widely used probe molecules, especially in FAU type zeolites. Commonly, the pyridine absorption bands at ~1,540 cm^{-1} belongs to the protonated pyridine on

Brønsted acid sites, whilst the band at ~1,450 cm^{-1} is related to non-protonated pyridine on Lewis acid sites. The physisorbed pyridine bands are present at around 1,490 cm^{-1} and absorption bands of pyridinium ion adsorbed on cations (e.g. Na^+, K^+ and so on) are centred at around 1,440 cm^{-1}. Based on Beer-Lambert Law (Eq. 2.20), the concentration of acid sites can be derived through molar extinction coefficient (*p*, cm $mmol^{-1}$) and the amount of adsorbed probe molecule [159]:

$$c_{(Brønsted)} = \frac{p_{(Brønsted)} \times \int I_B \times r^2}{w} \quad \text{(Eq. 2.22)}$$

$$c_{(Lewis)} = \frac{p_{(Lewis)} \times \int I_L \times r^2}{w} \quad \text{(Eq. 2.23)}$$

where *c* (mmol g^{-1}) is concentrations of acid sites, $\int I_B$ and $\int I_L$ are the integral intensity of bands corresponding to Brønsted and Lewis acidity, respectively. *r* (cm) and *w* (g) are the diameter and weight of zeolite wafer, respectively. It is worth noting that the molar coefficient should be determined for a particular probe on a given zeolite.

Chapter 3 On the effect of mesoporosity of FAU Y zeolites in the liquid-phase catalysis

This chapter was based on the published work on the porosity, acidity and activity in liquid-phase catalysis of three commercial Y zeolites possessing different SAR. R. Zhang, S. Xu, D. Raja, N.B. Khusni, J. Liu, J. Zhang, S. Abdulridha, H. Xiang, S. Jiang, Y. Guan, Y. Jiao, X. Fan, Microporous and Mesoporous Mater., 278 (2019) 297–306. https://doi.org/10.1016/j.micromeso.2018.12.003

3.1 Introduction

Considering zeolite catalysis, both porous and acidic properties of zeolites are important. However, the microporous nature of zeolites (pore width <1 nm) generally limits the accessibility of acidic sites to bulky molecules, resulting in diffusion-limited reactions and/or deactivation due to coking [122, 183-187]. This is, in general, the driving force for developing zeolites with mesoporosity and/or mesoporous materials such as MCM-41 and SBA-15 [188]. Comparing zeolites with the hierarchical (or open) mesoporosity to mesoporous materials, the former shows much better performance in catalysis (regarding activity and stability), due to the presence of strong acidity along with the hierarchical inter-connected mesoporosity [184]. For example, the amphiphilic organosilane surfactant promoted mesoporous MFI zeolite (BET surface area = 590 m^2 g^{-1}, SAR = 20, average pore size = 7.4 nm) demonstrated a drastically high activity in the ethanol to olefin/gasoline reaction in comparison to the mesoporous Al-MCM-41 (BET = 948 m^2 g^{-1}, SAR (silicon-to-aluminium ratio) = 20), i.e., 86% *versus* < 1% in conversion [189].

Among various developed strategies of making zeolites with mesoporosity, post-synthetic modifications of zeolites, such as dealumination by steaming, acid leaching and/or chemical treatment and desilication by alkaline treatment, are practical methods to obtain zeolite with mesoporosity robustly and economically [122, 185, 190-192], exemplified by the commercial success of ultra-stable Y zeolites (USY) [91, 121, 193]. Post-synthetic modifications are well-known 'top-down' method [122, 183, 185, 186], creating mesoporous structures *via* the destructive approaches by removing framework Al and/or Si species. Undoubtedly, the modification of the acidity of the resulting zeolites also occurs

along with the development of intercrystalline mesoporosity, and hence contributing to the improved catalytic performance. Therefore, systematic and comparative studies into the role of both acidity and porosity in catalysis are necessary to facilitate the rational design of zeolites with mesoporosity. Remy et al. performed the combined MAS NMR and XPS spectroscopic study of a series of commercial dealuminated Y zeolites (hydrogen form or H form), suggesting that the presence of tetra-/penta-coordinated aluminium sites were responsible for the activity in hydroisomerisation of heptane and decane [193]. However, the detailed analysis of porous properties was missing from the study [193], which might contribute to the measured activity as well. Insight into the effect of pore size and shape selectivity of various zeolites (ranging from ZK-5 to Y) on the catalytic conversion of glucose was obtained by Jae et al. without the consideration of the acidic property of these zeolites [194]. Very recent work by Osatiashtiani et al. on Y catalysed acetic acid esterification reactions showed the specific effect of surface hydrophobicity (due to dealumination) on esterification, as well as the importance of active site accessibility (due to mesoporosity) [195].

In addition to the traditional petrochemical reactions such as cracking and alkylation [187], zeolites have also found increasing applications as catalysts for liquid-phase reactions [186], especially the condensation-type reactions for fine chemical synthesis [196, 197] and biochemical conversion [195]. In the liquid-phase system, zeolites with mesoporosity show the significantly improved catalytic performance than the parent microporous zeolites [189, 195, 198, 199], because the improved mass transport of molecules is particularly more important in the liquid-phase than the gas-phase reactions [200]. As the influence of the acidity of zeolites on the observed catalytic behaviours is also important, more work on the liquid-phase catalysis on zeolites and zeolites with mesoporosity is required to deepen the understanding of the influence of mesoporosity and acidity on the catalytic activity of zeolites in the liquid phase.

This chapter presents a comprehensive analysis of porosity and acidity of three commercial FAU Y zeolites followed by their catalytic evaluation in condensation reactions, aiming at understanding the influence of porous and acidic properties on the catalytic activity of the commercial Y zeolites. Specifically, the porosity of Y zeolites was analysed using the combined N_2 physisorption and mercury

(Hg) porosimetry to obtain the comprehensive description and characterisation of the hierarchical feature of mesopores in the samples. Acidic properties of the catalysts were characterised using the ammonia temperature-programmed desorption (NH_3-TPD), and pyridine Fourier transform infrared (pyridine-IR) analyses. Aldol condensation of benzaldehyde with 1-heptanal and Fischer esterification of methanol with carboxylic acids were used as model reactions to determine catalytic activity.

3.2 Experimental

3.2.1 Zeolite Y catalysts and chemicals

Commercial Y zeolites (CBV300, CVB720 and CVB760) were obtained from Zeolyst International. CBV300 (NH_4 form) has a SAR of 2.6. Before use, CBV300 was and calcined at 450 °C (heating rate = 5 °C min^{-1}, holding time = 5 h) to convert to its H^+ form (denoted as HY-2.6). CVB720 and CVB760 have the SAR of 15 and 30, respectively, and are in their H forms, denoted as HY-15 and HY-30, respectively. According to the literature [193], HY-15 and HY-30 were prepared by the steam and acid treatment of CBV300.

Chemical for catalytic condensation reactions were all used as received, including benzaldehyde (ReagentPlus®, ⩾ 99%, Sigma-Aldrich), 1-heptanal (97%, Alfa Saesar), dodecane (ReagentPlus®, ⩾ 99%, Sigma-Aldrich), α-Amylcinnamaldehyde (jasminaldehyde, 97%, Sigma-Aldrich), propionic acid (ACS Reagent, ≥ 99.5%, Sigma-Aldrich), hexanoic acid (≥ 99%, Aldrich), lauric acid (Fluorochem), methanol (anhydrous, 99.8%, Aldrich), methyl propionate (99%, Aldrich), methyl hexanoate (99%, Alfa Aesar), methyl laurate (≥ 98%, FG ,Aldrich), dihexyl ether (97%, Sigma-Aldrich) and ethanol (99.7−100%, absolute, VWR International).

3.2.2 Characterisation of materials

N_2 physisorption analysis of catalysts at −196.5 °C was performed using a Micromeritics 3Flex Surface Characterisation Analyser. Prior to N_2 sorption measurements, zeolite samples (150 mg) were degassed at 200 °C under vacuum overnight. Specific surface area of materials was determined based on the BET method. Pore size distribution was obtained by the BJH method (using the adsorption branch of

isotherms) and the non-local density functional theory (NLDFT) [201]. The meso-macro-pore sizes of the catalysts were also analysed using Hg intrusion porosimetry performed on AutoPore IV 9510 analyser (Micromeritics, pressure range: 0.10 to 60000 psi(a)).

NH_3-TPD was performed using a Micromeritics AutoChem II 2920 chemisorption analyser (~100 mg sample, 10 °C min^{-1}, He flow rate = 30 cm^3 STP min^{-1}). Details of the NH_3-TPD analysis is described elsewhere [202]. Pyridine Fourier transform infrared (py-FTIR) tests were performed using a nexus Model Infrared Spectrophotometer (Termo Nicolet Co, USA) operating at 2 cm^{-1} full width at half maximum (FWHM) equipped with an *in situ* cell containing CaF_2 windows. Adsorption of pyridine was performed at room temperature and then evacuated at 200 °C measuring pyridine adsorbed at all acid sites. After that, the sample was evacuated *in situ* at 350 °C corresponding to the pyridine adsorption at the strong acid sites.

The morphology of Y zeolites was examined by scanning electron microscopy (SEM, Fei Inspect S50 operating at 5 kV accelerating voltage) and transmission electron microscopy (TEM, Fei Tecnai F20 with the operating voltage of 200 kV). Powder X-ray diffraction (PXRD) patterns of the zeolite catalysts were obtained using a Philips X'Pert X-ray diffractometer with the condition of Cu$K\alpha_1$ radiation, λ = 1.5406 Å, 40 kV, 40 mA, 5° < 2θ < 65°, 0.0167° step size. Fourier transform infrared transmission spectroscopy (FTIR) was performed in a Bruker VERTEX 70 spectrometer with the red light emission from a Helium-Neon laser and the wide range MIR-FIR beamsplitter and detector. The spectra were obtained at ambient temperature by 56 scans at 4 cm^{-1} resolution in the wavelength range of 400–4,000 cm^{-1}.

3.2.3 Catalytic reactions

Catalytic condensation reactions were carried out using Schlaker reaction tubes (Aldrich®) under N_2. Before the catalytic tests, all catalysts were dried in an oven at 150 °C overnight to remove the moisture. In aldol condensation, the catalyst (200 mg) was firstly loaded into 25 ml Schlaker tube followed by the addition of benzaldehyde (5 ml, 48.7 mmol), heptanal (1.2 ml, 8.7 mmol) and dodecane (0.2 ml, 0.87 mmol, as the internal standard). Then the resulting suspension was stirred at 300 rpm and 130 °C

(in an oil bath) under the inert atmosphere (N_2). The reaction mixture (about 0.2 ml) was sampled periodically (diluted with ethanol and filtered) for gas chromatography (GC) analysis.

The reaction condition of Fischer esterification was adapted from the literature [16, 20]. Typically, 30 mg of the catalyst was first introduced into the Schlaker reaction tube reactor (10 ml), followed by methanol (6.11 ml, 150 mmol), carboxylic acid (propionic acid: 0.375 ml, hexanoic acid 0.633 ml, lauric acid 1.129 ml, all 5 mmol) and dihexyl ether (0.12 ml, 0.5 mmol, as the internal standard). Liquid phase esterification was carried out in an oil bath at an isothermal temperature of 60 °C under stirring (500 rpm) and an inert atmosphere of N_2. Aliquots of the mixture (0.2 ml) were withdrawn during the reaction then diluted with ethanol and filtered into a 2 ml GC vial before being analysed by GC.

Sample analysis was performed using Agilent 7820A GC System with an Agilent J&W HP-5 capillary column, stationary phase = (5%-Phenyl)-methylpolysiloxane, dimension = 30 m × 0.32 μm × 0.25 μm). Details of GC methods are described in Table 3.1 and Table 3.2. .Products identification was performed in an Agilent 6890N GC with 5973N Inert MSD (mass selective detectors) system using the same capillary column.

Table 3.1 GC method for benzaldehyde, heptanal and dodecane (internal standard) using ethanol as a solvent.

Injection	10 μl Agilent syringe 1 μl injection volume with ×2 pre-injection and ×2 post-injection washes
Inlets	heater temperature = 280 °C split ratio = 50:1 (split flow = 65 ml min^{-1})
Column	temperature limits = −60 °C to 325 °C stationary phase = (5%-Phenyl)-methylpolysiloxane dimension = 30 m (length)×0.32 mm (ID)×0.25 μm (film) carrier hydrogen flow = 1 ml min^{-1} (20 cm sec^{-1})
Oven	initial temperature = 130 °C initial hold time at 130 °C = 2.5 min ramp = 15 °C min^{-1}. final temperature = 240 °C final hold time at 240°C = 5 min
Detector	Flame ionization detector (FID) heater temperature = 320 °C air flow = 400 mL min^{-1} H_2 fuel flow = 30 ml min^{-1} N_2 make-up flow = 20 ml min^{-1}
Signals	data rate = 100 Hz minimum peak width = 0.002 min zero at the start of the run

Table 3.2 GC methods for Fischer esterification of methanol with carboxylic acids, dodecane (internal standard) using dihexyl ether as an internal standard.

	Propionic acid	Hexanoic acid	Lauric acid
Injection volume (µl)	0.3	0.3	0.3
Inlet heater temperature (°C)	280	280	325
Split ratio (-)	220:1	220:1	220:1
Column flow (ml min^{-1})	1.3	1.3	1.3
FID heater temperature (°C)	280	320	325
Oven temperature programme (-)	initial T = 75 °C initial hold time at 75 °C = 5 min ramp = 25 °C min^{-1}. final T = 195 °C final hold time at 195 °C = 2 min	initial T = 120 °C initial hold time at 120 °C = 5 min ramp = 25 °C min^{-1}. final T = 195 °C final hold time at 195 °C = 2 min	initial T = 120 °C initial hold time at 120 °C = 5 min ramp = 25 °C min^{-1}. final T = 195 °C final hold time at 195 °C = 7 min
Total run time (min)	11.4	10	15.8

3.3 Results and discussion

3.3.1 Characterisation of Y zeolites

Both XRD patterns and IR spectra of the three catalysts (Figure 3.1) show the characteristic features of FAU type zeolite. XRD analysis of the catalysts (Figure 3.1 (a)) display the identical characteristic diffraction peaks of FAU zeolite in the wide angle range of 15.5 to 34.8° 2θ. By using the Integrated Peak Area Method [201, 203][204], HY samples show the crystallinity of 100% (HY-2.6), 67% (HY-15) and 49% (HY-30), respectively. The characteristic vibration bands of Y zeolite were measured by FT-IR (Figure 3.1 (b)). The band at around 451 cm^{-1} is the structure-insensitive Si–O and/or Al–O bending vibration of the internal tetrahedral alumosilicate framework [187]. The band at 573 cm^{-1} corresponds to the double six membered ring external linkage peak of FAU zeolites [187, 205]. The bands between 660 cm^{-1} to 820 cm^{-1} are assigned to zeolite Y symmetric stretching vibrations [206]. The other two distinct peaks at 1,005 cm^{-1} and 1,143 cm^{-1} are attributed to internal tetrahedral asymmetrical stretching and external linkage asymmetrical stretching, respectively [207]. The band shifts of HY-15 and HY-30 (to higher wavenumber) were due to the lower Al content in the sample compared to that of HY-2.6. Since the Si–O bond length of 1.61 Å [208] is shorter than the bond length of Al–O (1.75 Å [209]), the strong Si electronegativity leads to higher vibration frequency, causing the band shifts to greater wavenumber in HY-15 and 30.

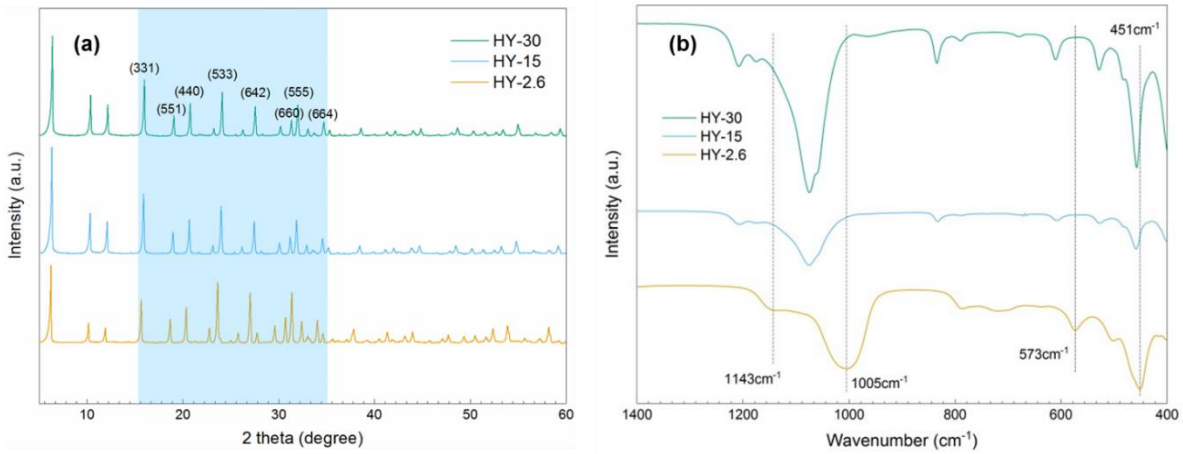

Figure 3.1 (a) PXRD patterns and (b) FT-IR spectra of zeolite Y catalysts.

Figure 3.3 shows the SEM and TEM micrographs of Y zeolites. As shown in Figure 3.3a, c and e, all materials present the similar morphology of crystallite aggregates with comparable sizes of 400–600 nm, which is typical for FAU type zeolite. Surface EDS analysis (insets Figure 3.2, Figure 3.3 (a), (c) and (e), and Table 3.3) gave the SAR of three samples as 2.5, 14.2 and 29.4, respectively, for HY-2.6, HY-15 and HY-30, similar to their corresponding theoretical SAR values. TEM analysis presents the close observation of the morphology of Y zeolites. TEM micrograph of HY-2.6 is shown in Figure 3.3 (b), in which a dense and uniform crystalline region was identified, suggesting the absence of mesoporosity in HY-2.6. Conversely, for HY-15 and HY-30 (Figure 3.3 (d) and (f)), the bright areas in the micrographs represent intracrystalline mesopores within the two Y zeolites materials. TEM images of Figure 3.3 (d) and (f) also reveal that the mesopores in HY-15 and HY-30 are not well shaped with estimated pore sizes of < 20 nm, possibly open at the crystal surface.

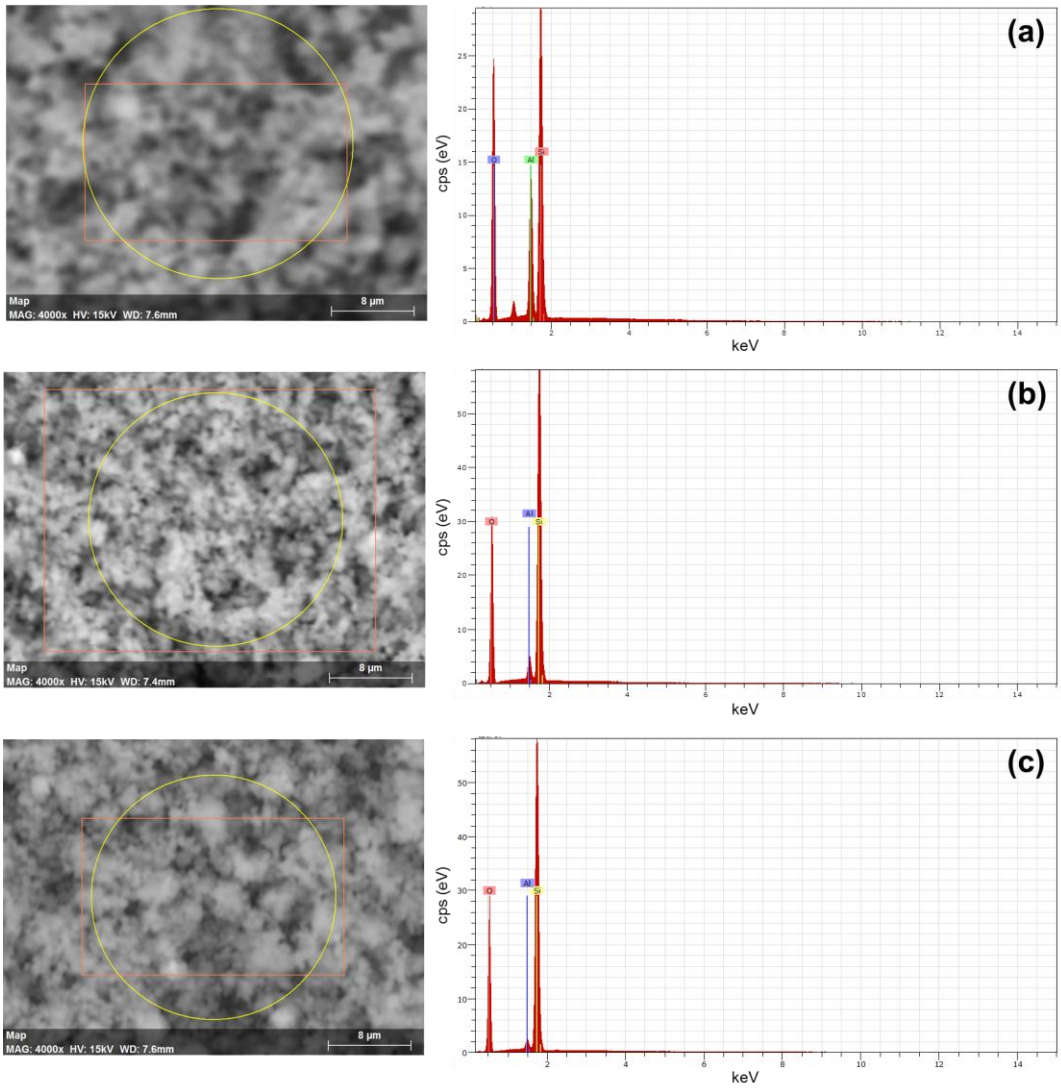

Figure 3.2 EDS surface elemental analysis of Y zeolites: (a) for HY-2.6, (b) for HY-15 and (c) for HY-30.

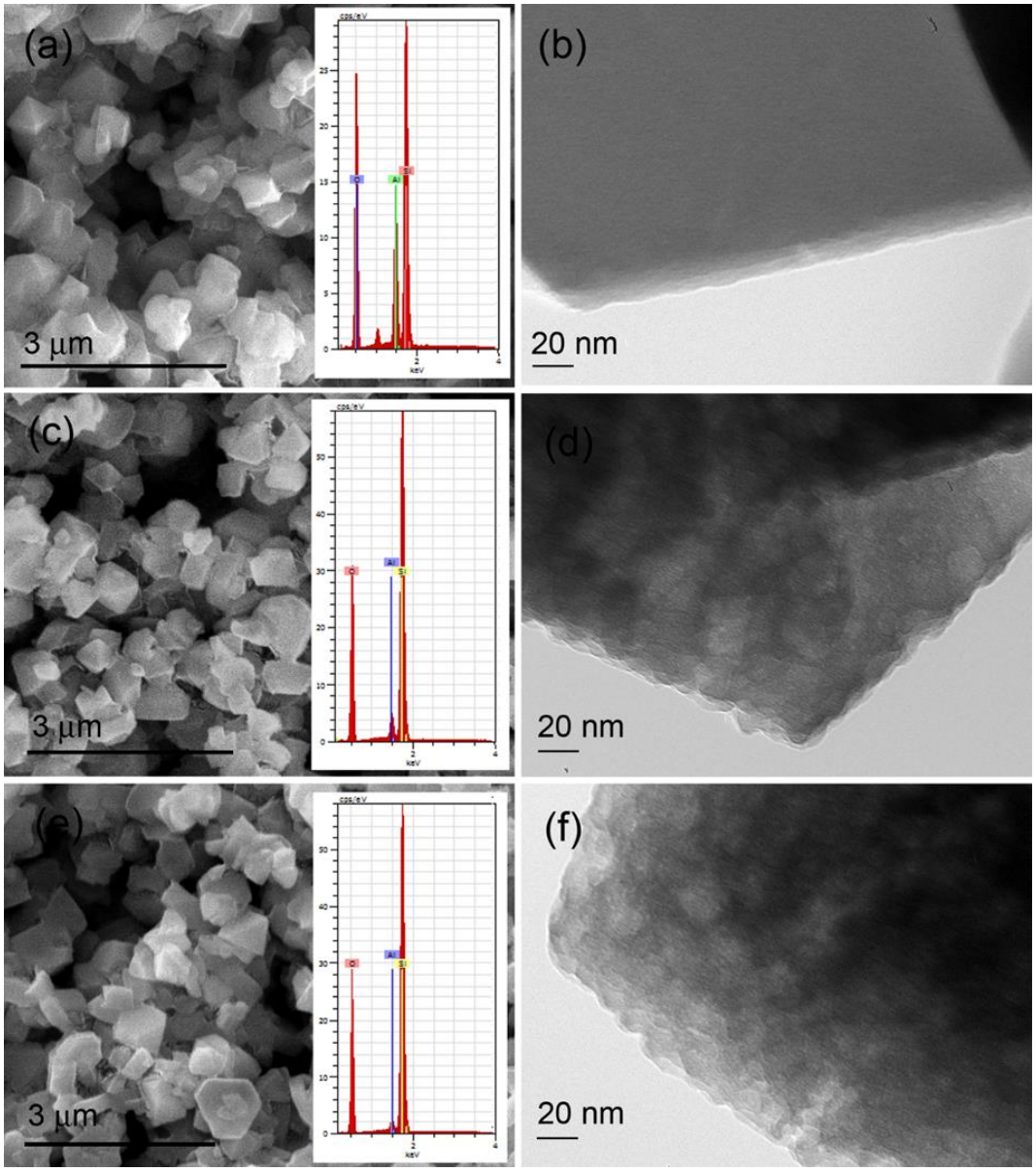

Figure 3.3 SEM and TEM micrograms of commercial zeolite Y catalysts: (a) and (b) for HY-2.6; (c) and (d) for HY-15; (e) and (f) for HY-30. Insets: the relevant EDS spectra of catalysts.

Table 3.3 EDS surface elemental analysis of Y zeolites.

Sample	HY-2.6		HY-15		HY-30	
Element	Atomic percentage [at.%]	Error [%]	Atomic percentage [at.%]	Error [%]	Atomic percentage [at.%]	Error [%]
Oxygen	71.95	6.6	70.01	6.8	67.81	6.2
Silicon (Si)	19.99	1.3	28.02	1.9	31.13	2.0
Aluminium (Al)	8.06	0.6	1.98	0.2	1.06	0.1
SAR[a]	2.5		14.2		29.4	

[a]Silicon-to-aluminium ratio

3.3.2 Pore structure analysis of Y zeolites

N_2 adsorption-desorption isotherms of Y zeolites are shown in Figure 3.4 (a), from which the comprehensive information of their porous characteristics was extracted, especially the specific surface areas and pore volumes, as summarised in Table 3.4. N_2 sorption isotherm of HY-2.6 is a typical Langmuir type isotherm (type I in the Brunauer-Deming-Deming-Teller (BDDT) classification [210]) which is the signature for the microporous crystalline materials. On the other hand, N_2 sorption isotherms of HY-15 and HY-30 show the hysteresis loops after the micropore adsorption, indicating the presence of mesoporous structures in their crystalline domain. According to the literature [193], HY-15 and 30 were obtained using the post-synthetic treatment of HY-2.6 (i.e., the parent material) by steaming (twice under severe conditions) and subsequently by mineral acid leaching. In the former step, the parent zeolite Y was dealuminated due to the high-temperature steam treatment [193], after which the aluminium agglomerates are present in the crystalline framework, blocking the porous networks. The subsequent acid leaching could dissolve the aluminium agglomerates, rendering mesopores in the resulting zeolitic materials. Since the HY-15 and HY-30 went through the comparable post-synthetic treatment, similarities in their N_2 adsorption-desorption curves and porous features could be explained. Through the destructive post-synthetic treatments, mesoporosity was created in the zeolitic framework by sacrificing zeolites' intrinsic microporosity, leading to the decrease in the micropore area (as the values of S_{micro} in Table 3.4, reduced by 16.6% and 23.8%, respectively, for HY-15 and 30 comparing to HY-2.6). However, the total specific surface areas (i.e., S_{BET}) of HY-15 and HY-30 were compensated by the created external surface area, resulting in the improved S_{BET} than that of HY-2.6.

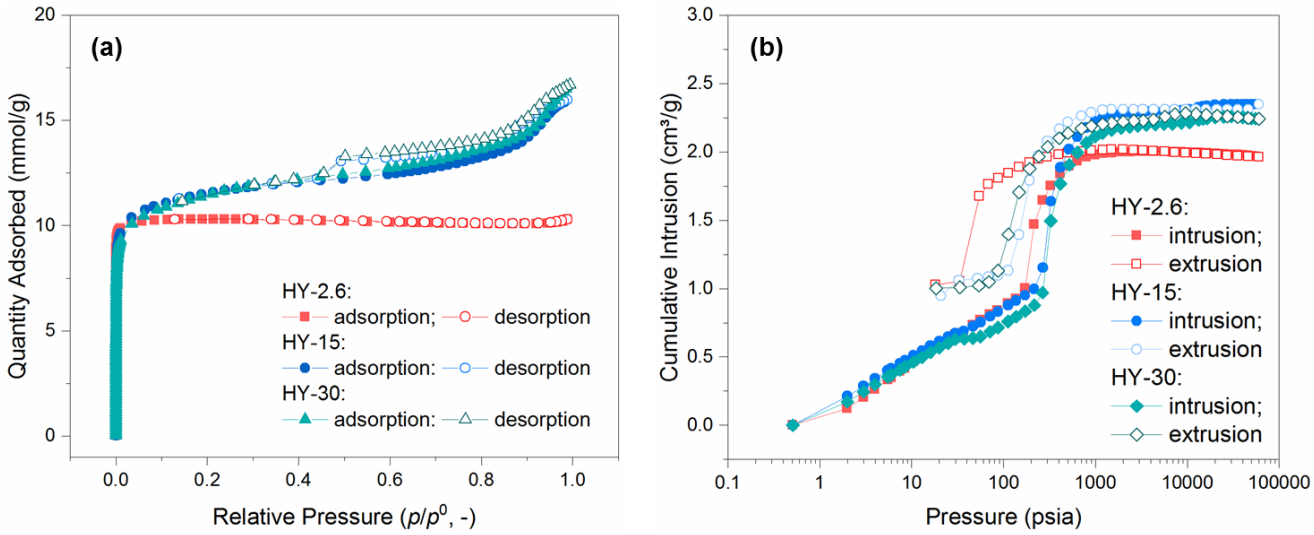

Figure 3.4 (a) N_2 sorption isotherms at −196.5 °C and (b) mercury intrusion/extrusion curves of commercial Y zeolites with different SAR.

Table 3.4 Comprehensive analysis of pore structures (regarding specific surface areas and pore volumes) of commercial Y zeolites.

Catalysts	N_2 sorption							Mercury porosimetry	
	Specific surface areas [$m^2\ g^{-1}$]			Specific pore volumes [$cm^3\ g^{-1}$]					
	S_{micro}[a]	$S_{external}$[a]	BET	V_{micro}[a]	$V_{meso,\ s}$[b]	$V_{meso,\ l}$[c]	V_{total}[d]	S_{Hg}[e] [$m^2\ g^{-1}$]	V_{Hg}[f] [$cm^3\ g^{-1}$]
HY-2.6	858	9	867	0.36	0	0	0.36	0	0
HY-15	716	231	947	0.30	7.4×10^{-2}	0.11	0.55	14.6	5.0×10^{-2}
HY-30	654	291	946	0.27	4.6×10^{-2}	0.13	0.58	14.1	5.8×10^{-2}

[a] *t*-plot method; [b] pore size range = 2–5 nm, calculations were based on the cumulative pore volume from the BJH method; [c] pore size range >5 nm, calculations were based on the cumulative pore volume from the BJH method; [d]single point adsorption total pore volume at $p/p^0 = 0.99$; [e]pore size range >5 nm, calculations were based on the cumulative pore by Hg intrusion; [f]pore size range >5 nm, calculations were based on the cumulative Hg intrusion.

The differential pore size distribution (DPSD) and cumulative pore volume (CPV) curves with reference to the pore sizes of the materials are shown in Figure 3.5 and Figure 3.6. According to DPSD (Figure 3.5), three Y zeolites show the comparable distribution of pore sizes in the micropore region (centred at about 0.74 nm). Mesopores with average pore diameters of around 4 and 18 nm were identified in H-15 and H-30 by the BJH method (red open circles in Figure 3.5 (b), (c) and Figure 3.6, the comparison of PSD by the BJH and NLDFT method is presented in Figure 3.7). CPV of Y zeolites by N_2 sorption analysis (Figure 3.5 (a)) shows the pure microporous nature of HY-2.6, i.e., an insignificant increase of CPV in the mesopore region in comparison to that of HY-15 and HY-30. Conversely, step changes in

CPV were measured for HY-15 and HY-30 after 2 nm pore size, suggesting the contribution of mesopores to the cumulative pore volume.

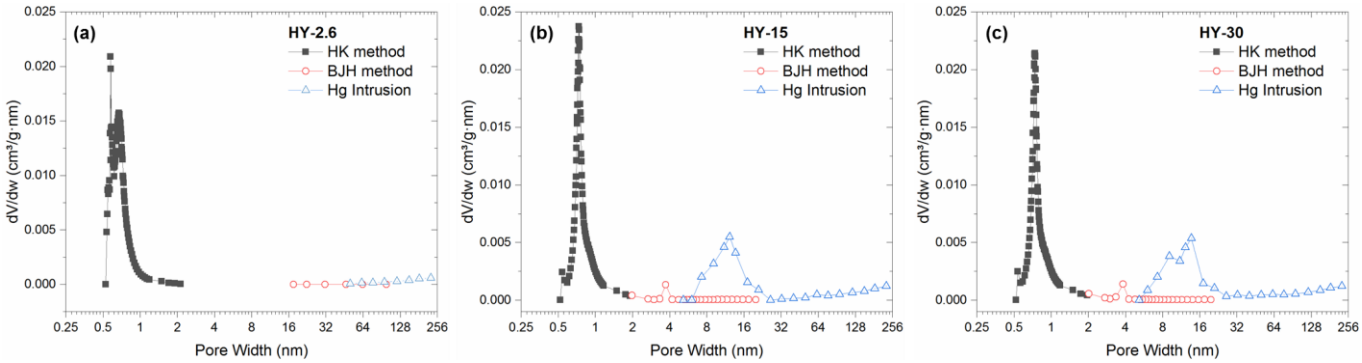

Figure 3.5 Full range DPSD of commercial Y zeolites by N_2 sorption and Hg porosimetry analysis: (a) HY-2.6, (b) HY-15 and (c) HY-30.

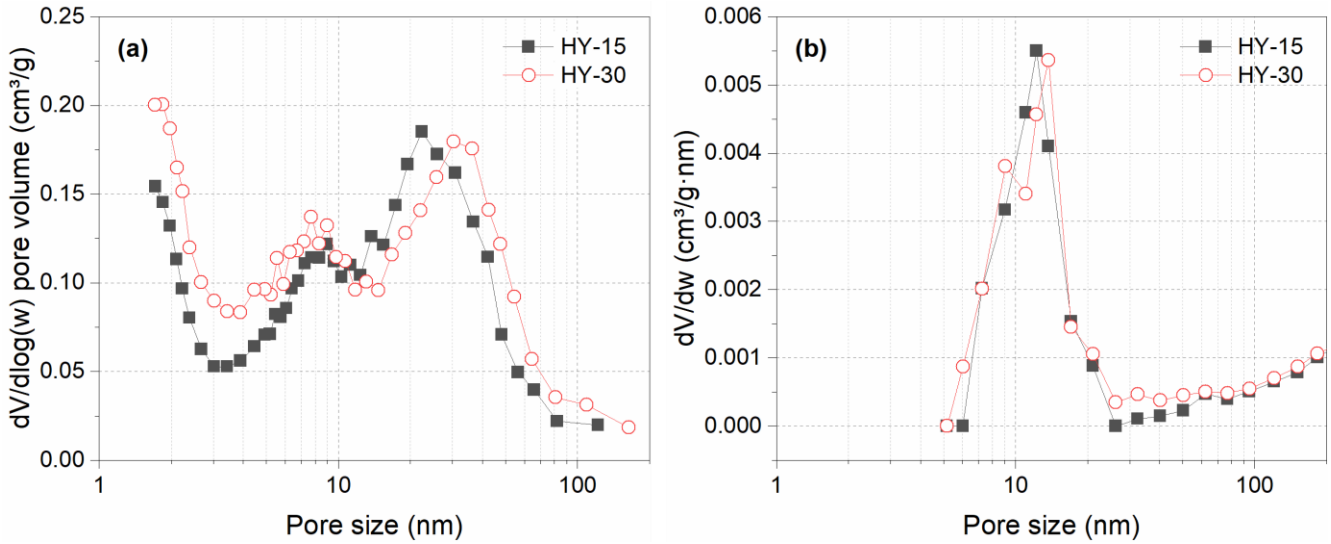

Figure 3.6 Comparison of the DPSD of mesopores (a) using the BJH method based on the adsorption branch of N_2 physisorption isotherms and (b) using the differential intrusion by Hg porosimetry analysis for HY-15 and HY-30.

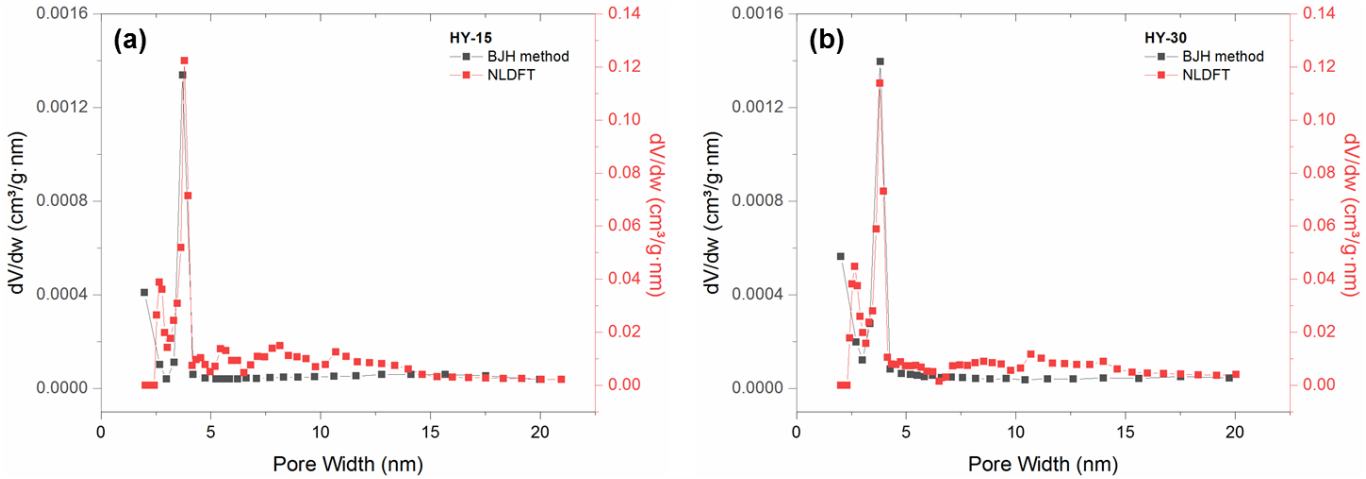

Figure 3.7 Comparison of the PSD of mesopores obtained by the BJH method and the non-local density functional theory (NLDFT) method: (a) HY-15 and (b) HY-30.

Considering the reaction in the liquid phase, the diffusivity of species is generally five orders of magnitude lower than that in the gas phase [211]. Therefore, the open mesoporosity (or hierarchical mesoporosity) is preferred to be created out from the microporous zeolitic phases to facilitate the molecular diffusion and increase the accessibility of acid sites (located on the external surface) from the outside [29, 122]. However, N_2 sorption only provides the total mesoporosity including both open and close mesoporosity (i.e., the closed mesoporoes in crystals that cannot be accessed from the outside, but can be probed by gas molecules under the gas sorption conditions), as the mesopore volumes by N_2 sorption (V_{meso}) shown in Table 3.4. Although mercury porosimetry is recognised the standard method for macropore analysis, recent studies also showed its potential for pore size analysis over a certain range of meso-macro-pore widths [163, 212-214]. On the other hand, the mercury porosimetric measurement has the lower theoretical boundary of about 3.5 nm [170], overlooking the hierarchical mesopores with the pore sizes < 5 nm (which is the practical lower boundary). Therefore, the effectiveness of a method for creating open mesopores in zeolites needs to be analysed carefully using the mesopore information from both techniques [163, 215] to avoid any misleading conclusions.

In order to complement the evaluation of mesoporosity in Y zeolites by N_2 sorption, mercury porosimetric measurements were performed (Hg intrusion/extrusion curves are shown in Figure 3.4 (b)), in which the mercury was intruded into accessible gaps/pores in the bulk zeolite samples from the outside. DPSD of materials by mercury porosimetry is illustrated in Figure 3.5 as the blue hollow

triangles. In DPSD analysis of Hg porosimetry data for the open mesoporosity, only the pore size range of 5–100 nm was presented since crystal sizes of Y zeolites were about 400–600 nm (Figure 3.3).

In comparison to DPSD by the BJH method (by N_2 physisorption), the presence of large mesopores with pore sizes of 5–30 nm in HY-15 and HY-30 is obvious, corresponding to the rise in their cumulative intrusion curves (Figure 3.8 (b)). The detailed comparison of PSDs by the corresponding logarithmic differential and differential intrusion curves is shown in Figure 3.6. The two methods show PSDs with a similar trend in region of 10–30 nm, confirming that these larger mesopores are open at the surface of Y zeolites (i.e., HY-15 and HY-30). However, it is worth noting that, in comparison to N_2 sorption, Hg porosimetry tends to underestimate the pore sizes in this range (Figure 3.6 (b)), showing the inefficiency of using Hg intrusion to probe small mesopores.

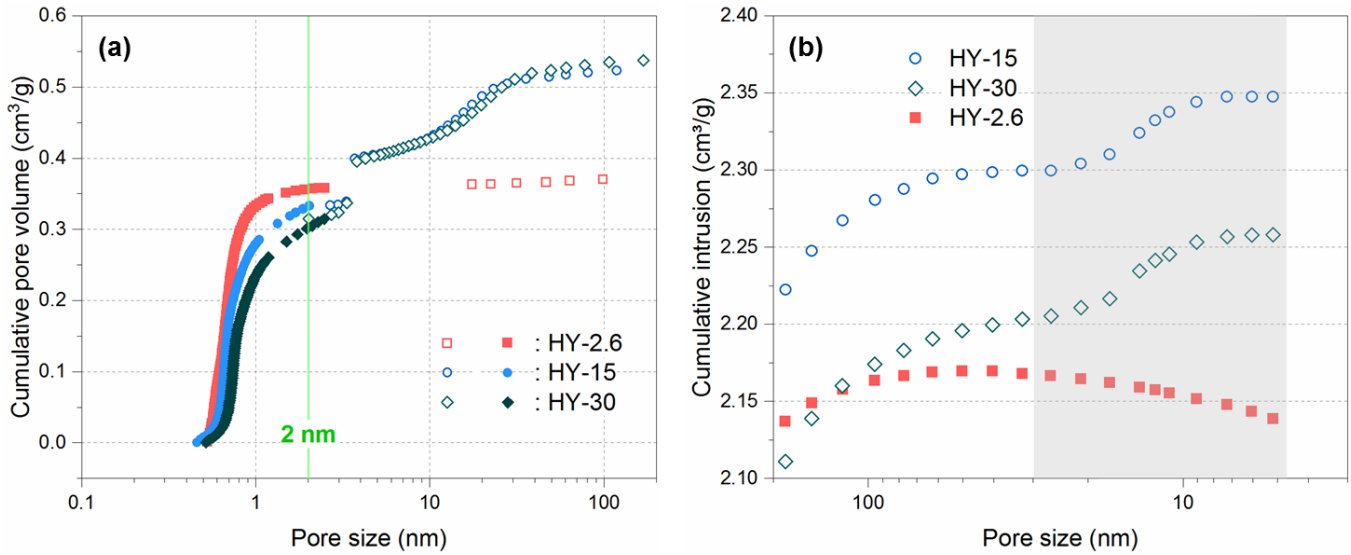

Figure 3.8 Cumulative pore volume (CPV) curves of commercial Y zeolites by (a) N_2 sorption (solid scatters: H-K cumulative micropore volume; open scatters: BJH desorption cumulative mesopore volume) and (b) Hg porosimetric measurements.

By comparing the specific mesopore volume data by N_2 sorption and mercury porosimetry in Table 3.4, we found that, in the large mesopores region (>5 nm), mercury porosimetry discounted the specific mesopore volume comparably, by about >50% (i.e., 52.4% for HY-15 and 55.2% for HY-30, respectively). This confirms that at least 50% of large mesopores in HY-15 and HY-30 is hierarchical, and hence open (to the outside) at the crystal surface. In the small mesopores region (2–5 nm), N_2 sorption reveals that HY-15 possesses a larger proportion of small mesopores (*ca.* 70.1% out of the total

specific mesopores volume) than that of HY (*ca.* 35.4%). However, the hierarchical connection between the small and large mesopores is not clear due to the limitation of the current characterisation techniques. In summary, N_2 physisorption and Hg porosimetry analysis reveals that HY-30 possesses an improved hierarchical mesoporosity than HY-15 with higher values in $S_{external}$, $V_{meso,\ 1}$ and V_{Hg}, as presented in Table 3.4.

3.3.3 Acidic properties of Y zeolites by NH_3-TPD and pyridine-IR

The evaluation of the acid strength of zeolite catalysts along with the relevant concentration was conducted using NH_3-TPD (Figure 3.9 (a) and Table 3.5). NH_3-TPD spectra (Figure 3.9 (a)) show two desorption steps (relevant peak desorption temperatures of NH_3-TPD spectra are shown in Table 3.5) for all FAU zeolites by ramping the temperature linearly from 100 to 600 °C, suggesting the presence of acid sites with two strengths in the catalysts. The acid site concentration (Table 3.5) was calculated using the amount of ammonia desorbed from the catalysts above the two temperatures, showing that HY-2.6 possesses much more acid sites, especially strong ones, than that of HY-15 and HY-30. The relative values of total acidity of catalysts correlate well with the amount of aluminium in the catalysts since Brønsted acid sites are described as a hydroxyl group bridged between Al and Si (Al-OH-Si are primarily responsible in zeolites for their strong acidity).

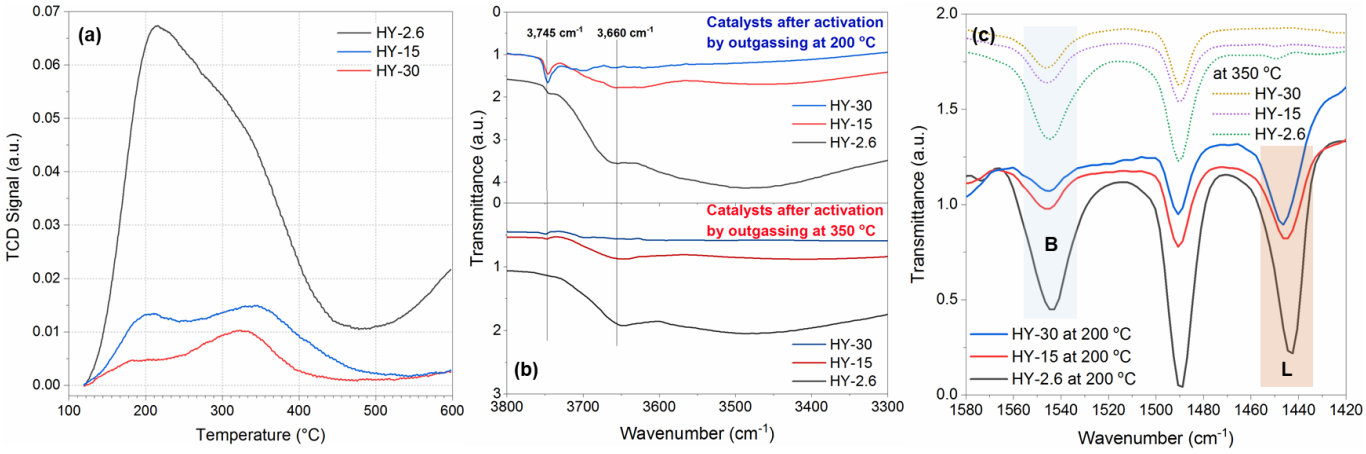

Figure 3.9 (a) NH_3-TPD profiles of zeolite Y catalysts; (b) ν(OH) vibrations of the catalysts after pyridine sorption and subsequent evacuation at 200 °C (top) and 350 °C (bottom); (c) IR spectra, in the region characteristic of adsorbed pyridine vibrations, of the catalysts after pyridine sorption and evacuation at 200 °C and 350 °C.

The comprehensive characterisation of acid sites of the catalysts was examined by infrared (IR) spectroscopic study of pyridine adsorption on the catalysts at the peak desorption temperatures according to the NH_3-TPD. Background IR spectra of the catalysts, in *v*(OH) region (Figure 3.9 (b)), show two identifiable bands at around 3,745±3 and 3,660±5 cm^{-1}, respectively. Vibration bands associated with surface isolated silanol groups (Si–OH, or terminal silanols) at about 3,745 cm^{-1} are obvious after the activation (by outgassing) at 200 °C, suggesting the presence of Si(0Al) building units in the catalysts [182, 216-218]. Compared to HY-2.6, the presence of terminal silanols in the dealuminated catalysts of HY-15 and HY-30 is more obvious, reflecting the removal of framework Al from the two zeolites. The band at around 3,660 cm^{-1} can be assigned to the bridging OH groups structuring the supercages of Y zeolites [182, 219], which is more observable in HY-2.6 and HY-15 than in HY-30, suggesting the effect due to the sever dealumination. The broad band at lower frequencies of 3,500–3,200 cm^{-1} was assigned to acidic OH groups in sodalitecages of Y zeolites, which is common for Al-rich zeolites such as HY-2.6 [218, 219].

Table 3.5 Analysis of NH_3-TPD and Py-FTIR data for zeolite Y catalysts.

Sample	Temperature at maximum [°C]		Weak acidity[a] [mmol g^{-1}]		Strong acidity[b] [mmol g^{-1}]		Total acidity [mmol g^{-1}]	
	First peak	Second peak	Brønsted[c]	Lewis[c]	Brønsted[c]	Lewis[c]	Brønsted[c]	Lewis[c]
HY-2.6	209.1	320.4	0.102	0.951	0.796	0.023	0.898	0.974
HY-15	199.4	338.0	0.011	0.316	0.148	0.002	0.160	0.318
HY-30	190.2	325.9	0	0.050	0.013	0	0.013	0.050

[a]acidity of the first peak in the NH_3-TPD spectra; [b]acidity of the second peak in the NH_3-TPD spectra; [c]determined by the pyridine-IR.

Pyridine-IR spectra of the catalysts (Figure 3.9 (c)) allow us to identify the acidity of surface OH groups, as well as determining the relevant concentration of Brønsted and Lewis acid sites on zeolite catalysts. It is well understood that the pyridine adsorption on Brønsted acid sites forms the pyridinium ions (*via* the protonation of pyridine by the OH groups of Brønsted acid sites), giving the characteristic band at 1,545 cm^{-1} [217-222], which was measured for all three catalysts (Figure 3.9 (c)) after activation at 200 and 350 °C, respectively. After outgassing at 200 °C, bands at 1,455–1,435 cm^{-1} were also measured which could be attributed to the band of pyridine bonded to Lewis acid sites (surface OH groups of oxides [217, 223] and/or Lewis acidic low-coordination Al^{3+} species [218]). Typically, pyridine

adsorption on strong Lewis acid gives the characteristic vibration band at about 1,455 cm^{-1} [218]. It is worth noting that H-bonded pyridine, i.e., physically adsorbed pyridine, typically vibrating at 1,445 cm^{-1}, was unlikely to be in the catalyst after activation at 200 °C. Therefore, in this chapter, we assigned bands in the range of 1,455–1,435 cm^{-1} to Lewis acidity. Acidic features of the catalysts after the evacuation at 350 °C were shown as the dash lines in Figure 3.9(c), showing the insignificant presence of Lewis acidity. By integrating the IR bands according to the characteristic peaks of Brønsted and Lewis acidity, concentrations of Brønsted and Lewis acidity were quantified for the three zeolite catalysts [221], which was summarised in Table 3.5. HY-2.6 shows a strong presence of Brønsted and Lewis acid sites of 0.898 and 0.974 mmol g^{-1}, respectively. In general, HY-15 still possesses silica-alumina domains (i.e., Si(*n*Al), n = 1–4) as evidenced by a 0.148 mmol g^{-1} Brønsted acid sites within its strong acidity, whereas, in HY-30, the existance of Brønsted acid sites appears to be less significant. NH_3-TPD and pyridine-IR analyses of the catalysts show that the total acidity and the Brønsted-to-Lewis acidity ratio corresponds well to the SAR, in an exponential decay manner, as shown in Figure 3.10. The analysis of the acidic property of Y zeolites suggests that the type of acid sites may vary significantly, though the similar porous structures are obtained for dealuminated Y zeolites of HY-15 and HY-30.

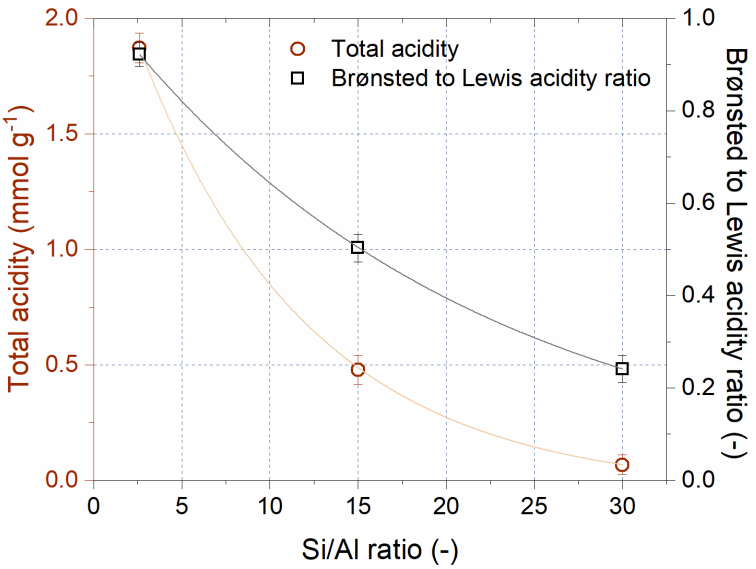

Figure 3.10 Total acidity and Brønsted to Lewis acidity ratio as a function of the SAR of zeolite Y catalysts.

3.3.4 Catalytic performance of Y zeolites in condensation reactions

Acid catalysed condensation reactions, such as esterification [195, 198, 199], acetalisation [198] and aldol-type reactions [8], have been used as the effective tool to assess the effectiveness of zeolites with mesoporosity in liquid-phase catalysis. In condensation reactions, reactants or products with the large molecular size compared to the dimensions of zeolite pores are involved, making the hierarchical mesoporosity ideal to allow the reactions. In this chapter, the catalytic activity of Y zeolites was probed by the Fischer esterification of carboxylic acids of different molecular sizes with methanol and aldol condensation of benzaldehyde with 1-heptanal for the synthesis of jasminaldehyde (Scheme 3.1). Repeated reactions were performed with the catalyst used in this chapter, showing that the conversion and selectivity values were reproducible to better than ±5% (Figure 3.11).

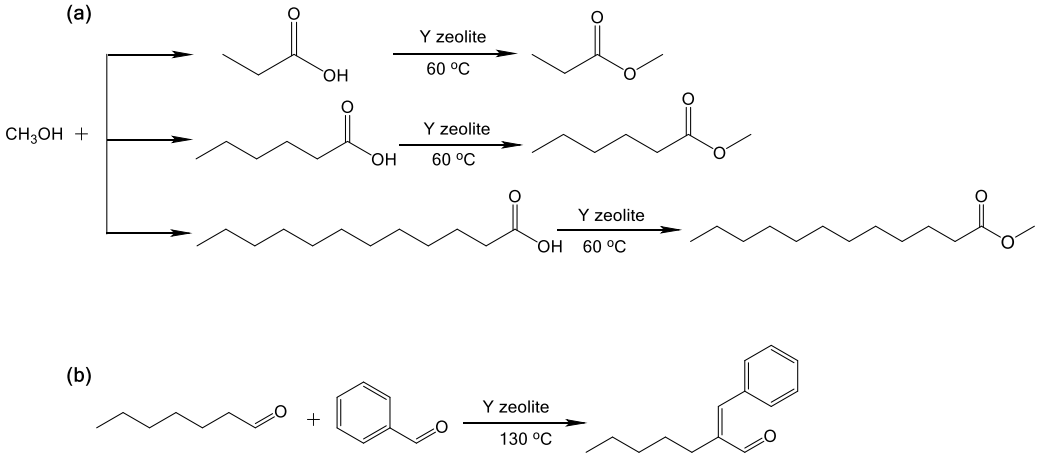

Scheme 3.1 (a) Fischer esterification of methanol with carboxylic acids and (b) aldol condensation of benzaldehyde with 1-heptanal.

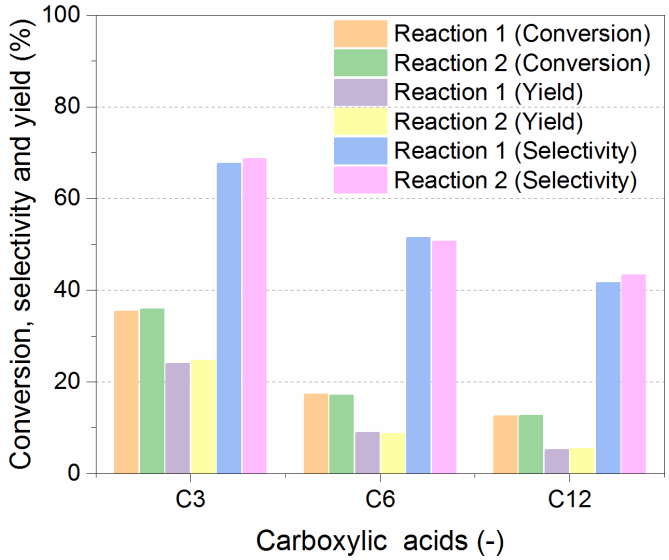

Figure 3.11 Repeatability test of Y zeolites catalysed reactions (HY-15 as the catalyst for Fischer esterification reactions, in which C3 = propionic acid, C6 = hexanoic acid, C12 = lauric acid).

Esterification over solid acid catalysts is recently demonstrated by Wilson's group for upgrading fast pyrolysis bio-oil [195, 199]. Three carboxylic acids of propionic, hexanoic and lauric acid have the kinetic diameter of about 0.52, 0.60 and 0.72 nm, respectively, therefore, indicating different levels of diffusion limitations in the catalytic esterification over zeolite Y having the intrinsic 0.74 nm micropore size. Kinetic diameters were estimated using the empirical correlation developed by Wang and Frenklach [224], which has been proved to be adequate to approximate the kinetic diameter of organic acids [194]. Conversion is intuitive to understand the effect of pore sizes on zeolite catalysed esterification since the accessibility of acid sites (especially Brønsted acidic sites on the external surface) to the organic acid is the prerequisite for the reaction to occur (esterification is initiated by the protonation of the carbonyl oxygen by acid sites of zeolites, making the carbonyl carbon electrophilic). Conversely, selectivity is a function of both porosity and acidity in esterification on zeolites.

Figure 3.12 (a) shows that HY-2.6 is not effective to promote the esterification of the three carboxylic acids with methanol, which is evidenced by <10% conversions in all reactions, suggesting that the reactions may only take place on the surface of zeolite crystals. Conversely, HY-15 and HY-30 with hierarchical mesopores (by Hg porosimetry) show significantly improved activities in all esterification reactions, for example, 4.0% of lauric acid was converted by HY-2.6, while 7.9% and 24.5% was

converted by HY-15 and HY-30, respectively. Additionally, for the conversion of three carboxylic acids over one specific catalyst, although the sizes of probing molecules (<1 nm) are much smaller than the mesopores sizes of HY-15 and HY-30, the steric hindrance imposed by the porous structure of catalysts is still significant. In Figure 3.12 (a), it was found that the trend conversion of different carboxylic acids over the catalyst correlates well with the kinetic diameter of carboxylic acids, manifesting the steric hindrance of molecules in the porous zeolites,

Although HY-15 possesses a higher percentage of small mesopores of 2–5 nm, i.e., $V_{meso,\ s}$ is 70% out of the total specific mesopore volume with HY-30 having only 31%, they seem not contributing to the conversion of carboxylic acids. As shown in Figure 3.12 (a), HY-30 promote the highest conversion in esterification reactions, surpassing that of HY-15 by *ca.* 20% in all cases. This agrees with their specific external surface areas ($S_{external}$), as well as the mesopore volume data (>50 nm, $V_{meso,\ h}$ and V_{Hg} in Table 3.4), i.e., both N_2 sorption and Hg porosimetry measured about 20% more $S_{external}$ and mesopore volume in HY-30 than HY-15. Figure 3.12 (b) shows that the selectivity to the corresponding esters depends on both molecule size (of carboxylic acids) and zeolites (detailed and quantitative analysis of side reactions/by-products is out of the scope of present chapter). It is found that, for microporous HY-2.6, the selectivity was affected notably by the size of carboxylic acids. For propionic acids, 55.5% selectivity to ethyl propionate was obtained, while only 6.3 % selectivity to methyl laurate was achieved using lauric acid. Comparatively, this effect was less significant for HY-15 and HY-30 with mesoporosity. For the esterification of a specific carboxylic acid over different zeolites, HY-30 with the best hierarchical meso-micro-pore structure demonstrated the highest selectivity to the corresponding ester. The findings from this study agree well with that by the previous work using ion-exchange resin catalysts (average pore sizes > 23 nm, average porosity > 0.35 $cm^3\ g^{-1}$) [225]. In esterification over mesoporous resin catalysts, side reactions such as alcohol dehydration and transesterification between the reactants occurred alongside the main reaction, primarily on the active sites inside the pores of catalysts because the diffusion resistance within the pores is insignificant for these slow reactions. Conversely, the target reaction of carboxylic acid esterification with alcohol (i.e., the relative fast reaction) was promoted mainly on the external surface of catalyst particles due to the significant

diffusion effect on it [225]. Therefore, we expect a similar scenario happened in the system under study. The presence of open mesoporosity in zeolites is particularly important to the selectivity to esters in the liquid phase esterification of carboxylic acids with different molecular sizes.

Previously, the hierarchy factor (HF, which is a function of BET and external surface areas and total and mesopore volumes) was defined to quantify the hierarchy and connectivity of pores in hybrid micro-meso-porous zeolite materials [226], and hence suggesting the catalyst's catalytic performance (i.e., the higher of the HF value, the better of the catalytic activity, although other factors such as acid site strength also play a role in catalysis). In this chapter, HF values for HY-2.6, HY-15 and HY-30 are calculated as 0.01, 0.13 and 0.14, respectively, not reflecting their activity data regarding conversion. HY-15 and HY-30 have comparable values of HF, however, HY-30 gave higher conversions, yields and selectivities as compared to HY-15. Therefore, the findings of this chapter suggest that the accessible mesoporosity is still the dominating factor for zeolite catalysis in the liquid phase, especially for esterification. However, the activity and selectivity data of esterification reaction over Y zeolites do not correlate well with their acidic properties, suggesting that the porous characteristics have a more significant impact on esterification than acidity.

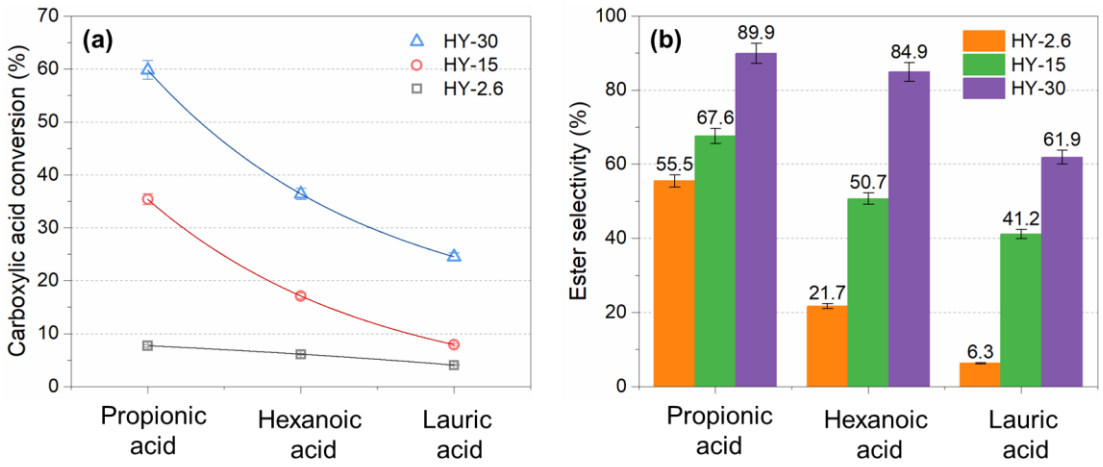

Figure 3.12 (a) Conversion of carboxylic acids in esterification and (b) ester selectivity over zeolite catalysts (30 mg) at 60 °C (molar ratio of carboxylic acid to methanol = 1:30, reaction time = 6 h).

Figure 3.13 shows the results of aldol condensation of 1-heptanal and benzaldehyde over Y zeolites. Mechanistic studies of the synthesis of jasminaldehyde over aluminosilicates have been previously reported by Corma et al. [196, 197], which is beyond the scope of this chapter. Among the three catalysts, HY-2.6 displays the lowest global reaction rates regarding conversions of 1-heptanal, suggesting that reactions over HY-2.6 are limited significantly by diffusion. HY-2.6 has the lowest conversion of 1-heptanal over the course of the reaction (i.e., about 63% at the end of the reaction at 46 h), while HY-15 and HY-30 exhibits comparable performance of *ca.* 80% for HY-15 and 78% for HY-30). By considering the porous structures, the *ca.* 25% increase in the conversion of 1-heptanal from HY-2.6 to the HY-15 and HY-30 can be attributed to the presence of a mesoporosity in the latter two cases, enhancing the accessibility of the reactants into the acid sites within their zeolitic frameworks. For the selectivity to jasminaldehyde at the end of the reaction (based on the conversion of 1-heptanal), HY-15 exhibited the best performance (*ca.* 31%), followed by HY-30 (*ca.* 22%) and HY-2.6 (*ca.* 12%). Since both HY-15 and HY-30 have mesoporosities, the promoted formation of jasminaldehyde (kinetic diameter = 0.74 nm) due to aldol condensation can be expected.

Solid acids catalysed aldol condensation is different from esterification because both reactants, i.e., 1-heptanal and benzaldehyde, can be protonated and react with the enolic form of 1-heptanal, giving the major by-product of (*E*) 2-*n*-pentyl-2-nonenal and the target product of jasminaldehyde [196, 197]. Again, the link of selectivity to jasminaldehyde in aldol condensation to the acidic property of Y zeolites is not evident. HY-15 possesses considerably higher amount of acidity (Table 3.5 and Figure 3.9) than HY-30 (i.e., by 123% for the Brønsted acidity and by 576% for the total acidity), not reflecting the improved selectivity by only *ca.* 41%. Accordingly, the substantial deficiency of acidity in HY-30 compared to HY-15 does affect the production of jasminaldehyde, as well as not being detrimental regarding the conversions of 1-heptanal and benzaldehyde.

Regarding the experimental procedure used for the reaction, i.e., catalysts were saturated first by benzaldehyde (kinetic diameter = 0.58 nm), the larger proportion of mesopores open at the crystal surface as well as the larger external surface area of HY-30 are prone to be occupied by benzaldehyde. Hence, the possibility towards other side reactions involving benzaldehyde such as benzoin

condensation to form benzoin [227] is more likely in HY-30 than HY-15. It is the plausible explanation for the higher benzaldehyde conversion associated with a lower jasminaldehyde selectivity given by HY-30 compared to HY-15 (Figure 3.13), despite having more favourable porous properties.

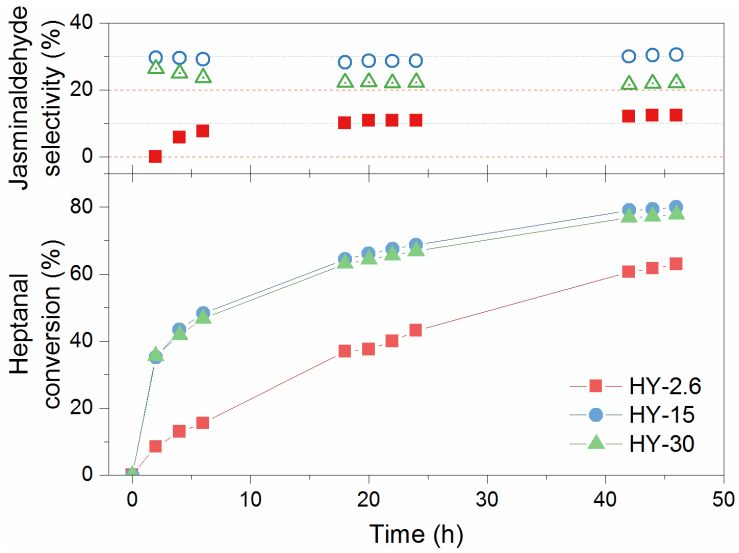

Figure 3.13 Conversion of 1-heptanal and selectivity to jasminaldehyde as a function of reaction time in the aldol condensation on Y zeolites (200 mg) at 130 °C (molar ratio of benzaldehyde to 1-heptanal = 5.6).

3.4 Conclusion

The development of zeolitic framework materials sees more their applications in the liquid-phase catalysis, where mesoporosity is beneficial to mitigate the serious diffusion limitation commonly experienced by the intrinsic micropores of zeolites. In this chapter, three commercial FAU Y zeolites were analysed comprehensively for their porous and acidic properties, aiming at elucidating their catalytic performance in two types of liquid-phase reactions of Fischer esterification and aldol condensation. The integrated results by N_2 physisorption and Hg porosimetry showed the importance of the combined method for obtaining the hierarchical feature of mesoporosity in zeolites. For example, although HY-15 and HY-30 possess comparable BET surface area and total pore volume, the proportion of > 5 nm large mesopores in HY-30 was confirmed by the combined method as about 17% higher than that in HY-15, explaining its better catalytic performance in Fischer esterification reactions.

In comparison to the microporous FAU Y (HY-2.6), the hierarchical mesoporosity in HY-15 and HY-30 showed significantly improved catalytic performance in both reactions, especially for ones involving

bulky reactants and products. Detailed acidic characters of Y zeolites showed that the introduction of meso-micro-pore hierarchy into Y zeolite (*via* the post-synthetic methods) compromises the acidities of mesoporous Y significantly. However, the substantial absence of acid sites in HY-15 and HY-30 compared to that of the parent HY-2.6 did not affect the conversion of substrates, suggesting the determinate role of mesoporosity in the Y zeolite catalysed liquid-phase reactions.

Chapter 4 Using ultrasound to improve the sequential post-synthetic modification method for making mesoporous Y zeolites

This chapter was based on the published work on creating hierarchical Y zeolites by sequential treatments based on ultrasound-assisted desilication methods. R. Zhang, P. Zhong, H. Arandiyan, Y. Guan, J. Liu, N. Wang, Y. Jiao, X. Fan, Front. Chem. Sci. Eng., 14 (2020) 275–287. https://doi.org/10.1007/s11705-019-1905-1

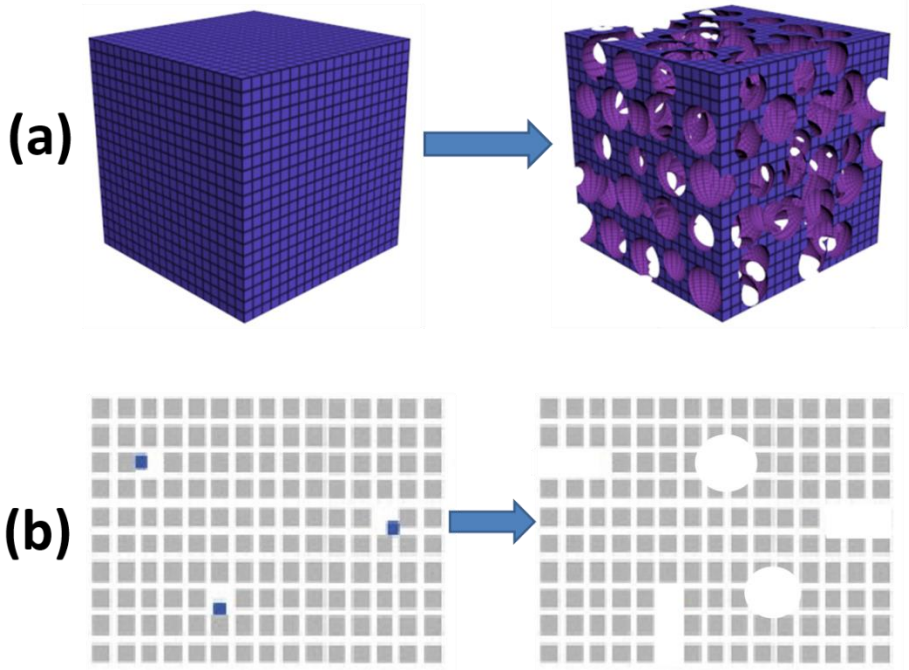

Scheme 4.1 Graphical abstract of mesopore formation from (a) 3-dimentional view and (b) plane view.

4.1 Introduction

Zeolites as a class of crystalline porous materials with intrinsic micropores (i.e., < 1 nm) are being used considerably by industry as adsorbents and catalysts due to their high specific surface areas, excellent hydrothermal stability, inclusion of acidity and ion exchange ability. For catalytic application, zeolite Y, with the intrinsic low SAR of ~2.6 and 12-member ring windows of a 3D channel system (with the pore width of ~0.74 nm), has been widely used in FCC after its successful synthesis by Breck in 1964 [74], representing the most important technical breakthrough in petrochemical conversions. The microporous structure of zeolite Y imposes the accessibility and diffusion limitation on their

applications, which is one of the primary contributing factors to the catalyst deactivation [183], due to the coke deposition covering acidic sites and/or clogging the micropores [228, 229]. Therefore, to improve the catalytic performance of zeolites, especially FAU zeolite Y for FCC, it is necessary to make zeolites with hierarchical meso-micro-pores (or mesoporous zeolites) to mitigate the accessibility and diffusion limitation. Common strategies for making hierarchical zeolites can be categorised into the destructive (top-down) and constructive (bottom-up) methods [230]. Although the bottom-up method can remarkably enhance pore accessibility by soft [231, 232] or hard templating [54], the associated cost and environmental issues (of using templates) can be problematic for largescale applications in industry [185]. The top-down method, which creates the intracrystalline mesopores by the post-synthetic dealumination and/or desilication (*via* steaming, chemical treatment, acid and base washing) [185, 233-236], is simple and effective, as well as being practical for industrial adoption.

Dealumination involves the extraction of framework Al species, and it is commonly achieved by steaming, acid and chemical treatment using mineral (e.g. hydrochloric acid [237]) and organic chelating agents (or chelators such as ethylenediaminetetraacetic acid, H_4EDTA [73] and citric acid [238]). Chelators not only provide the hydronium ions (for the hydrolysis of framework Al species) but also complex non-framework Al species to water-soluble complexes which can be easily removed from the zeolite framework [73, 239]. Particularly for the pristine FAU Y zeolite with low SAR of 2.4–2.6, dealumination is also necessary to reduce the framework Al concentration, and thus improving its thermal stability for harsh FCC reaction (500 °C–550 °C) and regeneration (650 °C–760 °C) steps [3, 183]. Desilication via the alkaline treatment is generally effective for zeolites with high SAR (> 20), such as ZSM-5 (Mobile FIve, MFI type) [240], beta (BEA type) [109], mordenite (MOR type) [241], to create hierarchical mesopores. Direct desilication of pristine Y zeolite is not effective since the high concentration of framework Al species protects the framework Si against the attack by OH^-. Accordingly, the sequential dealumination and alkaline treatments of zeolite Y were proposed, creating mesoporous Y zeolites effectively, in which the first step of dealumination helps to remove the framework Al partially from the pristine Y zeolite, and the second step of alkaline treatment has multiple functions, including (i) removing the debris remaining in the zeolite framework by dealumination

treatment, (ii) enabling the desilication for improving the intracrystalline mesoporosity, and (iii) facilitating the recrystallisation to recover the crystallinity partially. Verboekend et al. performed the chemical treatment of a parent Y with SAR = 2.4 for dealumination (using H_4EDTA and ethylenediaminetetraacetic acid disodium salt, Na_2H_2EDTA, at 100°C for 6 h), and then alkaline treatment (using aqueous NaOH solution at 65 °C for 30 min), and created hierarchical Y zeolites with high specific mesopore areas ($S_{external}$, up to 388 $m^2\ g^{-1}$) and mesopore volumes (V_{meso} > 0.1 $cm^3\ g^{-1}$) [121]. Accordingly, for the pristine Y zeolite, the preliminary dealumination to increase the bulk SAR is the prerequisite for the subsequent alkaline treatment to be effective for desilication, and thus the creation of hierarchical mesoporosity [75, 122].

Although the post-synthetic treatment is robust, effective and practical, the associated drawbacks, such as being energy intensive (e.g. the steam generation for steaming and lengthy operation at elevated temperatures for acid leaching and chemical treatment), still need to be addressed for improving the sustainability of such protocols and the resulting mesoporous zeolites. Over the past years, process intensification of zeolite synthesis using alternative energy such as microwave and ultrasound has been proposed and researched and found to be greener and safer than the conventional hydrothermal synthesis at high temperatures (80–200 °C) and autogenous pressures of the aqueous synthesis solution [36]. Such process intensification strategies are also extended to post-synthetic modification of zeolites such as microwave-assisted dealumination [154, 242] and desilication [145].

Ultrasound irradiation (with frequencies > 20 kHz) has proven to be very useful in organic synthesis and synthesis of nanomaterials (known as sonochemistry) [243]. Ultrasound can be transmitted through solids, gases and liquids. In liquids, longitudinal vibrations of molecules cause cavitation (i.e., the rapid formation and collapse of cavities or bubbles in a liquid medium), being responsible for most of the ultrasonic physical and chemical effects [243]. For post-synthetic treatment systems for zeolite modification, i.e., liquid-solid systems of zeolite slurry, cavitation due to ultrasound irradiation may make the additional microscopic stirring effect, intensifying the treatments by improving the local mass transfer [244]. Ultrasound-assisted desilication of zeolite Y (SAR = 2.6) has been attempted by Oruji et al. for preparing Y zeolites with mesoporous features [245]. The alkaline treatments were performed

with 0.5 mol L^{-1} NaOH at 30 °C for various treatment durations (i.e., 20, 40 and 60 min) under ultrasound irradiation (at 20 kHz with a probe sonicator). However, the use of ultrasound seemed not to intensify the post-synthetic alkaline treatment, and the ultrasonic treatment produced the resulting Y zeolites with $S_{external} < 10$ m^2 g^{-1} and $V_{meso} < 0.05$ cm^3 g^{-1}, which can hardly be classified into mesoporous zeolites. Such results can be expected, as discussed above, because it is very difficult to achieve effective desilication due to the high concentration of framework Al species in the pristine Y zeolite. Even under severe alkaline conditions (e.g. $\geqslant$ 3 mol L^{-1} NaOH and $\geqslant$65 °C), mesoporosity cannot be introduced in zeolite Y effectively [122]. Therefore, to utilise ultrasound irradiation for intensifying desilication, either using the parent zeolites with high SAR (i.e., > 20, for the one-step direct alkaline treatment) or developing relevant sequential dealumination-alkaline treatment strategies for the parent zeolites with low SAR, especially the pristine zeolite Y, is necessary to realise the desired effect, i.e., making mesoporous zeolites.

In this chapter, the possibility of using ultrasound irradiation to intensify the alkaline treatment step in the sequential post-synthetic treatment of pristine zeolite Y was explored, aiming at preparing hierarchical Y zeolites more efficiently than the conventional sequential method under hydrothermal conditions. The first-step chemical treatment of the pristine Y zeolite for dealumination was performed under hydrothermal conditions using different chelating agents, concentrations and treatment time. Then the second step of alkaline treatment (of the dealuminated Y zeolites) was performed comparatively using the conventional hydrothermal treatment and ultrasound-assisted treatment in the NaOH solution at 65 °C. The resulting Y zeolites are comprehensively characterised regarding their physical and chemical properties such as crystallinity, porosity, SAR and acidity, as well as being assessed using the model cracking reactions, demonstrating the effectiveness of the developed ultrasonic treatment to improve the sequential post-synthetic treatment for making mesoporous Y zeolites.

4.2 Materials and methods

4.2.1 Sequential post-synthetic treatments under hydrothermal conditions

For all experiments in this study, the parent ammonium zeolite Y was purchased from Zeolyst International (i.e., CBV 300, molar SAR = 2.6), and was used as received. H_4EDTA (titration, ⩾ 99%, Aldrich), citric acid (ACS reagent, ⩾ 99.5%, Aldrich) and NaOH (reagent grade, 97%, Aldrich) were all used as received.

For chemical treatment of the parent zeolite Y using different chelators, zeolite Y (4 g for each experiment) was dispersed in 50 mL of aqueous solution of citric acid and H_4EDTA with different concentrations (in a three-neck flask) and mixed well, then treated hydrothermally at 100 °C (temperature was maintained by immersing the flask in an oil bath) under stirring and reflux for different durations from 30 min to 6 h. After the chemical treatment, the system was cooled down to room temperature, and the dealuminated sample was separated from the solution by centrifugation (at 4400 r min^{-1}). Then, it was washed thoroughly with deionised (DI) water for 5 times and dried at 100 °C in an oven overnight to obtain the dry dealuminated sample.

For alkaline treatment under the hydrothermal condition, a dry dealuminated sample was treated in 0.2 mol L^{-1} NaOH solution at 65 °C under stirring for 30 min. The desilicated sample was then separated by centrifugation, washed with DI water for 5 times and dried at 100 °C before characterisation. The yield after the treatment was determined by comparing the dry mass of the resulting material against the weight of the starting material.

4.2.2 Sequential post-synthetic treatments involving the ultrasound-assisted alkaline treatment

The same procedure was used to obtain the dry dealuminated sample. For ultrasound-assisted alkaline treatment, the dry dealuminated sample was dispersed in 0.2 mol L^{-1} NaOH solution and sonicated at 65 °C for 5 min by immersing the flask in an ultrasonic bath (U500H, 50–60 Hz). The resulting sample was subject to the same work-up procedure before characterisation.

Loss of materials was inevitable during the sequential post-synthetic treatments and the work-up procedure. Therefore, blank experiments (i.e., treating the parent zeolite using the same procedures with the DI water) were performed to estimate the sample weight loss due to the protocol. The relevant weigh losses for chemical and alkaline treatments are about 5% and 6%, respectively. The samples were named accordingly as *a*Y-*b*-*c*-*d*, where *a* is the acronym of chelators used (i.e., EA for H_4EDTA and CA for citric acid) in chemical treatments, *b* is the concentration of chelator, *c* is the time of the chemical treatment, and *d* is the condition used for alkaline treatment ofdesilication (i.e., HT for the hydrothermal treatment and S for the ultrasonic treatment), respectively.

4.2.3 Characterisation of materials

PXRD patterns of materials were obtained using a Philips X'Pert X-ray diffractometer with monochromatised CuKα_1 radiation (40 kV, 30 mA, λ = 1.5406 Å). XRD data were recorded in the 2θ range of 5–40° with an angular step size of 0.0168° and a counting time of 1.167° min^{-1}. The relative crystallinity (RC, using the XRD pattern of the parent zeolite Y as the reference with 100% RC) of the modified zeolites was calculated using the Integrated Peak Area Method [246]. The total integrated peak area of the eight peaks corresponding to the 15.7°, 18.7°, 20.4°, 23.6°, 27.0°, 30.7°, 31.4°, and 34.1° was calculated for determining the RC values of the modified zeolites ((Eq. 4.1).

$$\mathrm{RC} = \frac{\sum \text{Intergrated peak area of the modified zeolite}}{\sum \text{Intergrated peak area of the parentzeolite}} \times 100\% \qquad \text{(Eq. 4.1)}$$

N_2 adsorption-desorption analysis was performed at –196.5 °C on a Micromeritics 3Flex Surface Characterisation Analyser to characterise the porous property of materials. Prior to the measurements, 120 mg samples was degassed at 350 °C under vacuum overnight. Specific surface areas of samples were calculated by the BET method. The pore size distribution was obtained by the BJH method using the adsorption branch of isotherms. The micropore surface area, micropore volume and external surface area were obtained by the *t*-plot method. The morphology of samples was obtained by field SEM (FEI Inspect F50 operating at 5 kV accelerating voltage) and field emission TEM (FEI Tecnai F20 with the operating voltage of 200 kV). An energy-dispersive XRF (EDXRF) spectrometer (PANalytical MiniPal 4 EDXRF) was used to determine the elemental composition of materials, and hence the calculation of

bulk SAR of zeolites. NH_3-TPD analysis of the acidity of zeolites was carried out on a Micrometrics AutoChem II 2920 chemisorption analyser (100 mg sample), and the relevant technical details of NH_3-TPD analysis are described elsewhere [201].

4.2.4 Catalysis

Selected zeolites were ion-exchanged using 1 mol L^{-1} aqueous ammonium nitrate (NH_4NO_3, $\geqslant$ 98%, Aldrich) solution at 80 °C for 24 h and calcined at 500 °C (heating rate = 5 °C min^{-1}, 3 h) to be evaluated using cracking reactions with n-octane as the model compound. The catalysis was performed at 350 °C using a fixed bed reactor (I.D. = 10 mm) with 1 g pelletised zeolite diluted with glass beads. Before the catalytic reaction, the catalyst bed was preheated at 350 °C for 2 h, then n-octane (0.1 mL min^{-1} with N_2 as the inert carrier gas at 240 mL min^{-1}) was introduced to initiate the cracking. The cracking products were analysed using an in-line GC (Agilent 7890B) equipped with a flame ionisation detector (FID) and Agilent PoraPLOT Q column.

4.3 Results and discussion

For the pristine Y zeolite with a low SAR of ~2.6, dealumination before the alkaline treatment is necessary to improve mesoporous structures. Therefore, to compare the effectiveness of hydrothermal (at 65 °C for 30 min) and ultrasonic (at 65 °C for 5 min) alkaline treatment in modifying the dealuminated Y zeolites, the treatment time (30–360 min) of the first-step chemical dealumination (with 0.1 mol L^{-1} H_4EDTA solution) was varied. The yield of materials after the chemical treatment for dealumination (DA) and the overall sequential treatment are showed in Figure 4.1. All yield values were corrected according to the blank experiments. By varying the time of DA treatment from 30 min to 6 h, the relevant yields are measured at 80%±5%, suggesting the extraction of Al species from the pristine zeolite Y. After the second step of alkaline treatment, regardless of the ultrasonic or hydrothermal method, comparable overall yields were obtained at 70%±5%, indicating the removal of Si species under the alkaline conditions.

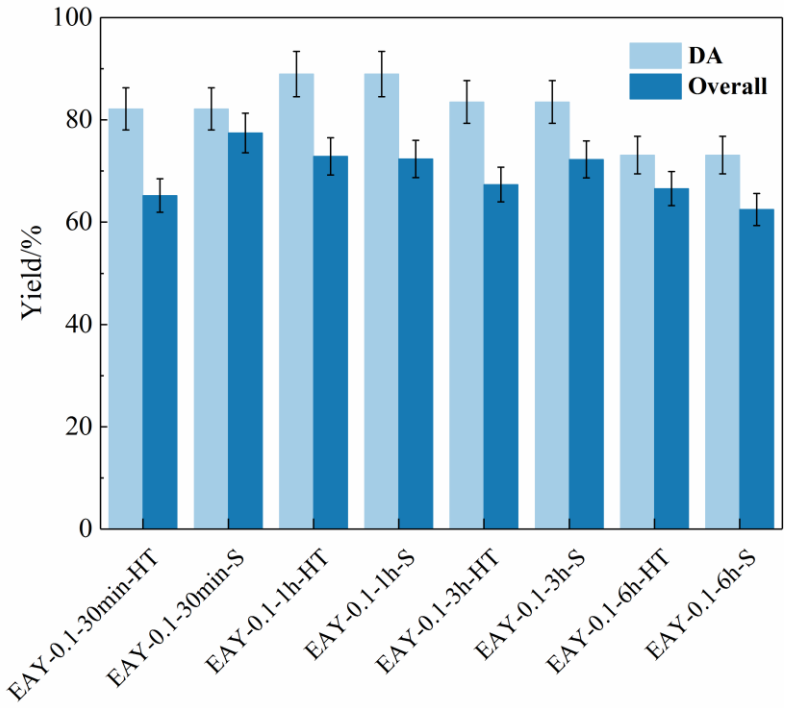

Figure 4.1 Yields of EAY zeolites after the sequential chemical (using H_4EDTA) and hydrothermal/ultrasonic alkaline treatments of the pristine zeolite Y.

XRD patterns of EAY zeolites in reference to that of the parent zeolite Yare shown in Figure 4.2, and the calculated RC values of the zeolites are summarised in Table 4.1. In general, EAY zeolites obtained by different post-synthetic treatments, regardless of the duration of the chemical dealumination treatment or the method used by desilication, show the analogous crystalline properties such as the characteristic diffraction peaks. However, it is noticeable that, in comparison with the parent zeolite Y, the relevant XRD characteristic peaks shifted towards high 2θ, suggesting the decrease of unit cell parameter [247]. Since the content of framework Al in the zeolite is proportional to unit cell parameter, the findings confirm the extraction of framework Al species during the sequential treatments. Especially for EAY-*0.1-6h-HT* and EAY-*0.1-6h-S*, the shift is comparably significant, suggesting the effective dealumination by treating the parent Y for 6 h. The extraction of Al species from the parent Y zeolite is also confirmed by XRF analysis, as shown in Table 4.1, showing that all EAY zeolites have larger SARs than that of the parent Y (SAR of ~2.6). Specifically, based on the SARs of the materials, the chemical treatment seems to require at least 3 h to be effective for dealumination, i.e., the SAR of EAY zeolites treated for $\leqslant$ 3h is comparable at 3.92±0.07, while that treated for 6 h has the ratio of 4.32±0.1.

Based on the calculated RC values, EAY zeolites became less crystalline with the extension of the treatment time used by the chemical dealumination treatment. By extending the time of dealumination from 30 min to 6 h, RC values of the resulting materials by the ultrasonic and hydrothermal alkaline treatment are about 89% and 71%, respectively. Comparing the alkaline treatments after the same dealumination treatment, EAY zeolites obtained by the ultrasonic treatment shows the relatively low crystallinity than that by the hydrothermal treatment, e.g. $RC_{EAY\text{-}0.1\text{-}6h\text{-}S}$ = 64% vs. $RC_{EAY\text{-}0.1\text{-}6h\text{-}HT}$ = 71%.

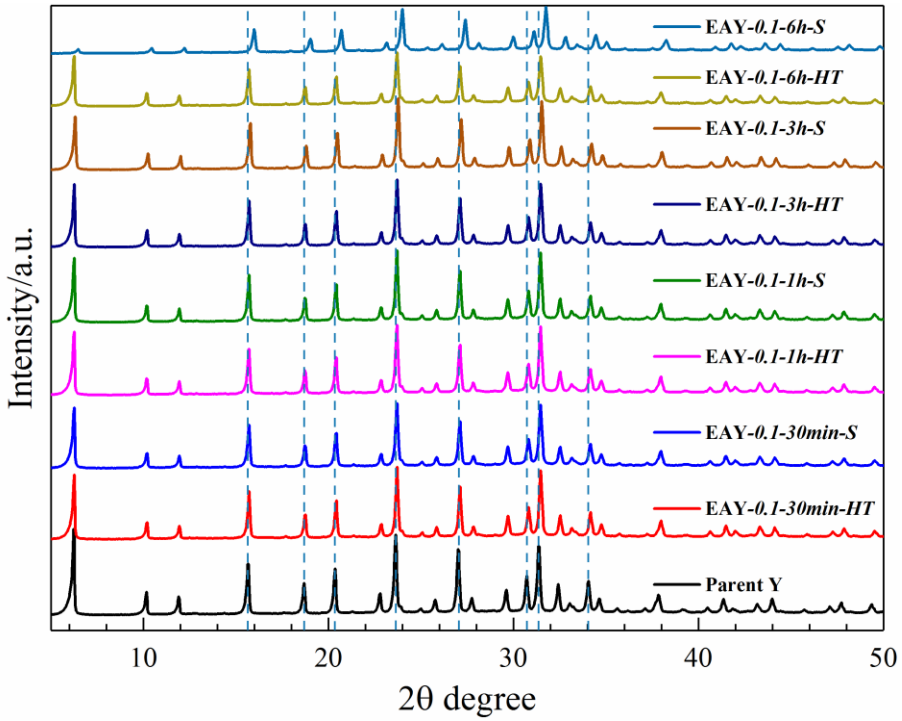

Figure 4.2 XRD patterns of EAY zeolites obtained by the sequential post-synthetic treatments under different conditions.

Table 4.1 SARs and values of RC of the parent Y and EAY zeolites.

Sample	SAR by XRF	RC by XRD	Sample	SAR by XRF	RC by XRD
Parent Y	2.60	100%			
EAY-*0.1-30min-HT*	3.88	89%	EAY-*0.1-30min-S*	3.98	84%
EAY-*0.1-1h-HT*	3.88	87%	EAY-*0.1-1h-S*	3.86	83%
EAY-*0.1-3h-HT*	4.05	85%	EAY-*0.1-3h-S*	3.86	81%
EAY-*0.1-6h-HT*	4.39	71%	EAY-*0.1-6h-S*	4.25	64%

The textural property of the resulting materials was analysed by N_2 physisorption, and the corresponding adsorption-desorption isotherms and the BJH PSD (obtained from the adsorption branches of isotherms) are shown in Figure 4.3. The parent Y exhibits a typical Type-I isotherm for microporous materials,

whereas all EAYs show the hysteresis loop which is the evidence of the presence of mesoporous features in the materials. Concerning the mesoporosity in EAYs, the chemical treatment with the treatment time of <3 h was less effective in comparison with the 6 h treatment. This is evidenced by the corresponding specific mesopore volumes (V_{meso}) and external surface areas ($S_{external}$) presented in Table 4.2, in which the EAYs dealuminated for <3 h show V_{meso} = 0.1±0.01 $cm^3\ g^{-1}$ and $S_{external}$ = 64±9$m^2\ g^{-1}$. Comparatively, for EAY-*0.1-6h-S* and EAY-*0.1-6h-HT*, the values for V_{meso} and $S_{external}$ are higher than 0.19 $cm^3\ g^{-1}$ and 120 $m^2\ g^{-1}$, respectively. According to the previous work by Kerr [73, 248], the chemical dealumination treatment of zeolite Y using H_4EDTA relies on the hydrolysis of framework Al species, which needs hours to be effective to produce non-framework Al species. Conversely, the complexation of non-framework Al species using H_4EDTA is relatively fast to extract Al species and create defective framework to make mesoporosity. Based on the same chemical dealumination treatment, the consecutive ultrasonic alkaline treatment was relatively more effective than the hydrothermal alkaline treatment and delivered better results regarding the mesoporous features of the relevant EAY zeolites. For example, V_{meso} values for EAY-*0.1-6h-S* and EAY-*0.1-6h-HT* are 0.19 $cm^3\ g^{-1}$ and 0.22 $cm^3\ g^{-1}$, respectively. According to SEM and TEM analyses, exemplified by EAY-*0.1-6h-S* and EAY-*0.1-6h-HT*, surface defects and mesoporous structures were observed for EAY zeolites, suggesting the effectiveness of the sequential post-synthetic treatments under study for creating hierarchical mesoporous structures in the pristine zeolite Y. Also, as shown in Figure 4.3 (b), (d) and (f), PSDs of the obtained EAY zeolites all have the monomodal distribution centred on ~8.5 nm.

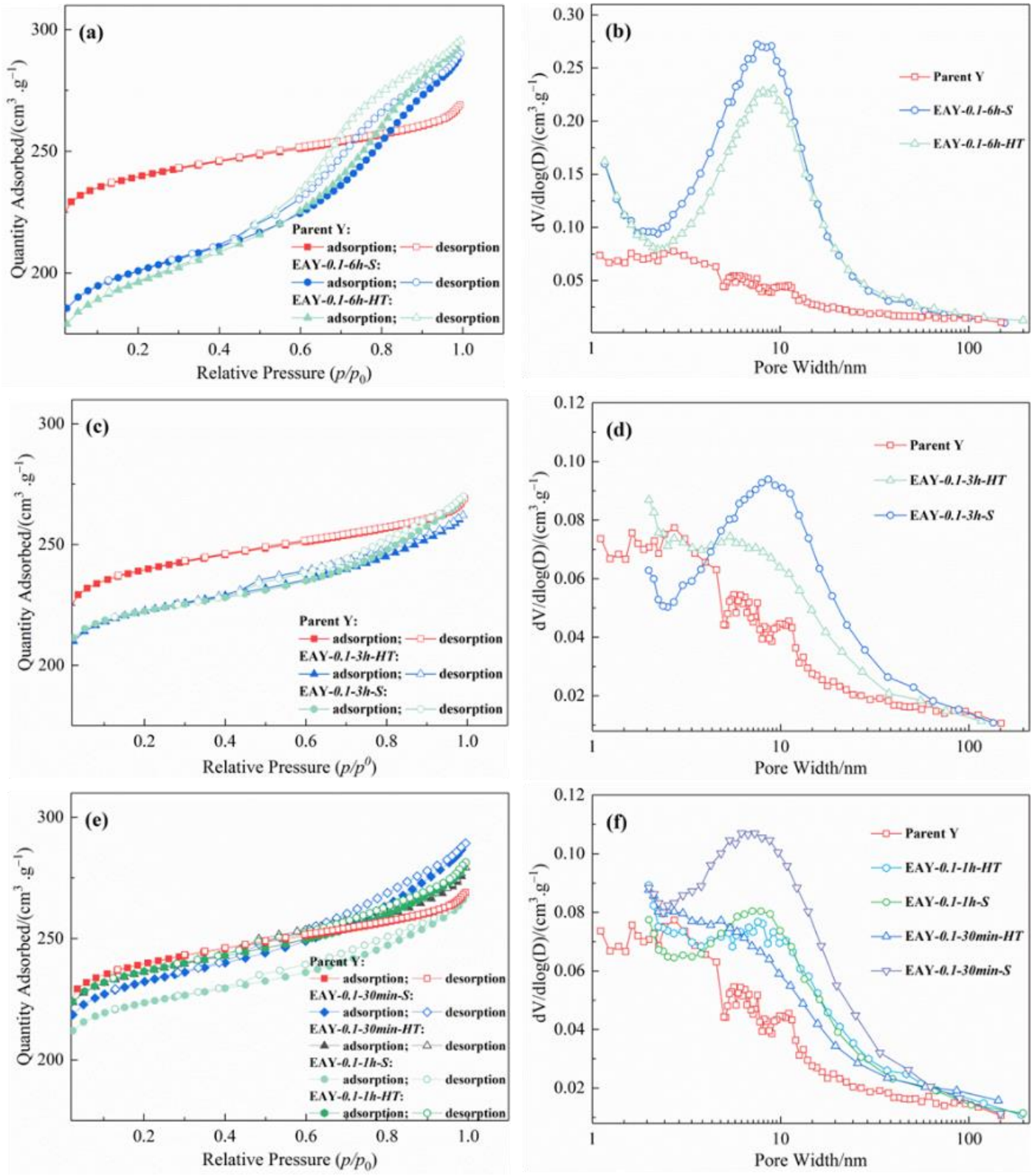

Figure 4.3 N_2 adsorption-desorption isotherms and PSDs for (a–b) EAY-*0.1-6h-HT* and EAY-*0.1-6h-S*; (c–d) EAY-*0.1-3h-HT* and EAY-*0.1-3h-S*; (e–f) for EAY-*0.1-1h-HT*, EAY-*0.1-1h-S*, EAY-*0.1-30min-HT*, EAY-*0.1-30min-S*.

Table 4.2 Porous properties of the parent Y zeolite and EAY zeolites.

Samples	Specific surface areas [$m^2\ g^{-1}$]			Specific pore volumes [$cm^3\ g^{-1}$]		
	S_{micro}[a]	$S_{external}$[a]	BET	V_{micro}[a]	V_{meso}[b]	V_{total}[c]
Parent Y	858	9	867	0.35	0.01	0.36
EAY-*0.1-30min-S*	722	82	804	0.33	0.12	0.45
EAY-*0.1-30min-HT*	757	61	818	0.34	0.09	0.43
EAY-*0.1-1h-S*	713	60	773	0.33	0.10	0.41
EAY-*0.1-1h-HT*	759	59	818	0.34	0.09	0.43
EAY-*0.1-3h-S*	706	63	769	0.32	0.10	0.42
EAY-*0.1-3h-HT*	711	59	770	0.32	0.09	0.41
EAY-*0.1-6h-S*	568	128	696	0.25	0.19	0.45
EAY-*0.1-6h-HT*	521	160	681	0.23	0.22	0.46

[a] by the t-plot method; [b] pore size range = 2–50 nm, calculations were based on the cumulative pore volume using the BJH method; [c] single point adsorption total pore volume at p/p0 = 0.99.

As discussed above, the ultrasound-assisted alkaline treatment of dealuminated zeolite Y is comparatively effective and efficient to make mesoporous Y zeolites, especially compared with the conventional alkaline treatment under the hydrothermal condition. The ultrasound irradiation enables the rapid extraction of Si species from the dealuminated zeolite framework [249], leading to the structural defects in the resulting EAY zeolites, and thus the relatively low crystallinity (Table 4.1, compared to the EAY zeolites obtained by the hydrothermal alkaline treatment). Previously, the direct ultrasound-assisted alkaline treatment of the pristine Y zeolite (SAR = 2.6) was reported, stating that the mesoporous Y zeolites were obtained [245]. However, the obtained zeolites only have insignificant mesoporous features, especially $V_{meso} < 0.1\ cm^3\ g^{-1}$. Accordingly, it is difficult to classify such zeolites as mesoporous zeolites. By using the sequential chemical and ultrasound-assisted alkaline treatment, the EAY zeolites represent a 5-fold increase of the mesopore volume and a 14-fold increase of the mesopore area in comparison to the Y zeolites reported by Oruji et al. [245]. The findings of this study suggest that dealumination of the parent zeolite is necessary before the ultrasound-assisted alkaline treatment for preparing mesoporous zeolites via the post-synthetic modification of zeolites with low SARs, exemplified by the Y zeolite.

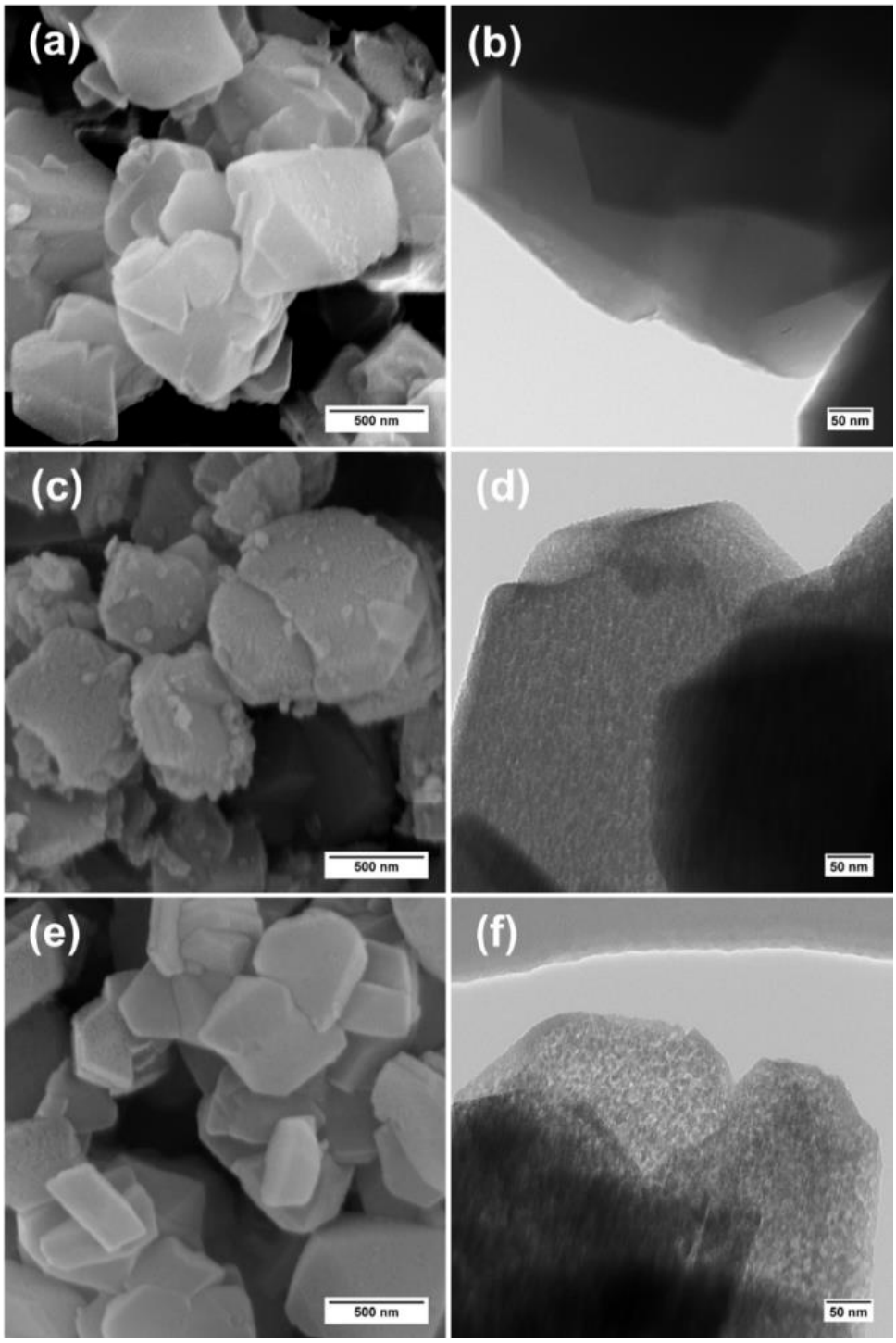

Figure 4.4 SEM and TEM micrographs of (a–b**)** the parent zeolite Y, (c–d) EAY-*0.1-6h-HT* and (e–f) EAY-*0.1-6h-S*.

The developed protocol facilitated by ultrasonication is generic, which was proved by using citric acid (CA) as the chelator in the chemical dealumination step. Citric acid has been used commonly in the post-synthetic dealumination of various zeolites such as ZSM-5 [250-252], zeolite beta [253-255] and zeolite Y [228, 231, 234, 256, 257] with few studies using CA in the sequential treatment [121, 234,

256]. For example, Xing et al. [256] performed the sequential hydrothermal treatment of zeolite Y using 0.17 mol L^{-1} citric acid for dealumination (4 h) and 0.1 mol L^{-1} for desilication (6 h), and introduced a large amount of NaOH mesopores in the resulting zeolite (V_{meso} = 0.29 cm^3 g^{-1}). Li et al. prepared the hierarchical Y zeolite with high mesoporosity with V_{meso} = 0.34 cm^3 g^{-1} chemical (with 0.15 mol L^{-1} alkaline treatment (0.8 mol L^{-1} using a sequential citric acid for 1 h) and NaOH for 0.5 h) [228]. However, the PDA (e.g. tetrabutylphosphonium hydroxide, TBPH) was employed during the alkaline treatment to enable the mesopore formation. Although the reported methods are effective in creating mesopore in Y zeolite, they require lengthy treatment time and PDAs, which may be improved using the developed ultrasonic method in the sequential treatment. Therefore, the sequential chemical treatment of the parent Y zeolite using citric acid for dealumination and followed by the hydrothermal and ultrasonic alkaline treatment were performed to demonstrate the effectiveness of using ultrasound irradiation to improve the alkaline treatment.

During the chemical dealumination treatment using citric acid, two treatment durations of 1 h and 3 h and three citric acid concentrations (i.e., 0.1, 0.14 and 0.16 mol L^{-1}) were used, and the relevant yields and XRD patterns of the resulting CAY zeolites are presented in Figure 4.5. Overall, the findings regarding the yield and XRD analysis of CAY are in line with that of EAY zeolites. An increase of the treatment time of chemical dealumination from 1 h to 3 h with citric acid caused the slight decrease of DA and overall yields (Figure 4.5 (a)), revealing the insignificant effect of treatment time (< 3 h) on the extent of dealumination. The RC value and SAR of CAY zeolites are shown in Table 4.3, showing that the two features do not have the strong correlation with the chemical treatment time under study (i.e., < 3 h). By comparing the two methods used for the alkaline treatment, they showed the comparable performance regarding the yield. Again, the ultrasonic desilication treatment was found more intensive than the hydrothermal one, as shown in Table 4.3, producing the CAY zeolites with lower RC values, e.g. 86% for CAY0.1-1h-HT *versus* 83% for CAY-0.1-1h-S. Figure 4.5 (b) presents the XRD patterns of the materials, showing that the characterised peaks of CAY zeolites from the ultrasonic treatment shift more to high 2θ compared to that by the conventional hydrothermal desilication. All findings

confirm the effectiveness of the ultrasound irradiation in the alkaline desilication treatment, being able to extract Si species from the dealuminated Y zeolites efficiently.

Compared to the method using H_4EDTA as the chelator, the one employing citric acid delivered the mesoporous Y zeolites with similar yields and RC values after the sequential treatments. Since the ability of citric acid for removing framework Al species is comparable with that of EDTA, the effective dealumination with the concentrated citric acid and short treatment time may be possible. This hypothesis was confirmed by the relevant yield and XRD data of CAY-*0.14-1h-S* and CAY-*0.16-1h-S*, as shown in Figure 4.5 (a) and Table 4.3. Moreover, for the comparatively severely dealuminated Y zeolites, i.e., the CAY zeolites produced using concentrated citric acid solutions (i.e., 0.14 and 0.16 M), the ultrasound-assisted alkaline treatment was also very effective.

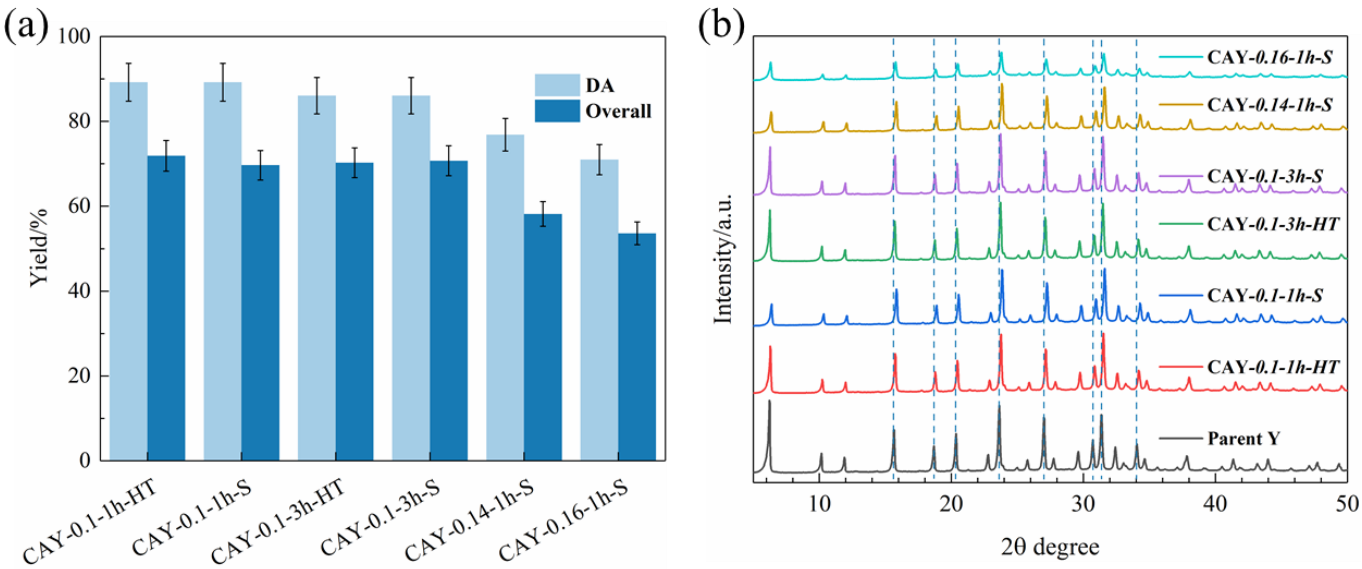

Figure 4.5 (a) Yields of CAY zeolites after the sequential chemical (using citric acid) and hydrothermal/ultrasonic alkaline treatments of the pristine zeolite Y; (b) XRD patterns of CAY zeolites the sequential post-synthetic treatments under different conditions.

Table 4.3 SARs and values of relative crystallinity (RC) of the parent Y and CAY zeolites.

Sample	SAR by XRF	RC by XRD	Sample	SAR by XRF	RC by XRD
			CAY-*0.1-1h-S*	3.94	83%
Parent Y	2.60	100%	CAY-*0.1-3h-S*	3.95	81%
CAY-*0.1-1h-HT*	3.95	86%	CAY-*0.14-1h-S*	4.40	73%
CAY-*0.1-3h-HT*	4.02	82%	CAY-*0.16-1h-S*	4.92	69%

All CAY zeolites were analysed by N_2 physisorption analysis, as shown in Figure 4.6. It is clear that after the sequential treatment (using citric acid for dealumination), all samples present hysteresis loops at middle to high relative pressure, which are typical features for mesoporous zeolite with the Type IV isotherm. These hysteresis loops and high crystallinity (without amorphous phase), as well as the TEM analysis of the selected CAY zeolites (as shown in Figure 4.7), prove that intracrystalline mesopores were successfully introduced into the parent Y zeolite. N_2 isotherms of the hydrothermally desilicated CAYs show similar uptake values at low relative pressure, but being slightly smaller than that of the ultrasonically desilicated CAYs and the parent Y. When 0.1 M citric acid was used for dealumination, the subsequent ultrasonic alkaline treatment showed relatively better effectiveness than the hydrothermal treatment, as shown by the comparison of mesoporous features of the resulting CAY zeolites in Table 4.4 (e.g. values of $S_{external}$). Additionally, by comparing the CAY zeolites with the relevant EAY zeolites (both treated using 0.1 M chelating agents for 1 h and 3 h), it was found that citric acid is more effective than H_4EDTA to perform the first step chemical dealumination treatment, which led to the comparatively improved mesoporous features in the resulting zeolites (Table 4.2 and Table 4.4). PSDs of CAY-*0.1-1h* and CAY-*0.1-3h* zeolites are shown in Figure 4.6 (b), showing that the mesopores in these samples are centred around 9 nm.

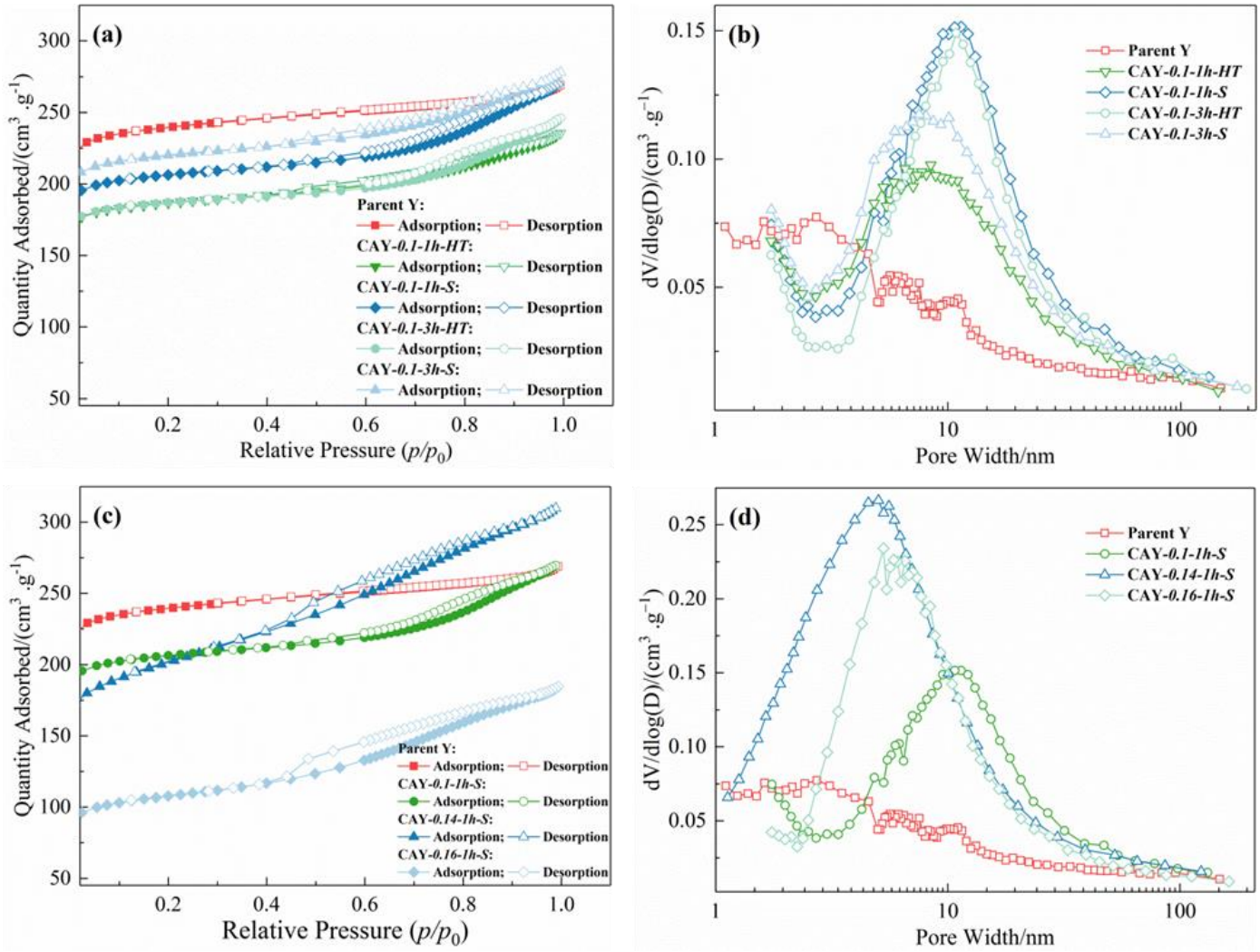

Figure 4.6 (a) and (c) N_2 adsorption-desorption isotherms; and (b) and (d) PSDs for CAY zeolites produced using different sequential post-synthetic treatments.

Table 4.4 Porous properties of the parent Y zeolite and CAY zeolites.

Samples	Specific surface areas [m^2 g^{-1}]			Specific pore volumes [cm^3 g^{-1}]		
	S_{micro}[a]	$S_{external}$[a]	BET	V_{micro}[a]	V_{meso}[b]	V_{total}[c]
Parent Y	858	9	867	0.35	0.01	0.36
CAY-*0.1-1h-S*	545	82	627	0.28	0.14	0.42
CAY-*0.1-1h-HT*	491	76	567	0.26	0.10	0.36
CAY-*0.1-3h-S*	581	87	668	0.30	0.12	0.42
CAY-*0.1-3h-HT*	499	68	567	0.26	0.12	0.38
CAY-*0.14-1h-S*	531	206	737	0.23	0.25	0.48
CAY-*0.16-1h-S*	236	101	337	0.12	0.16	0.28

[a] *t*-plot method; [b] pore size range = 2–50 nm, calculations were based on $V_{total} - V_{micro}$.

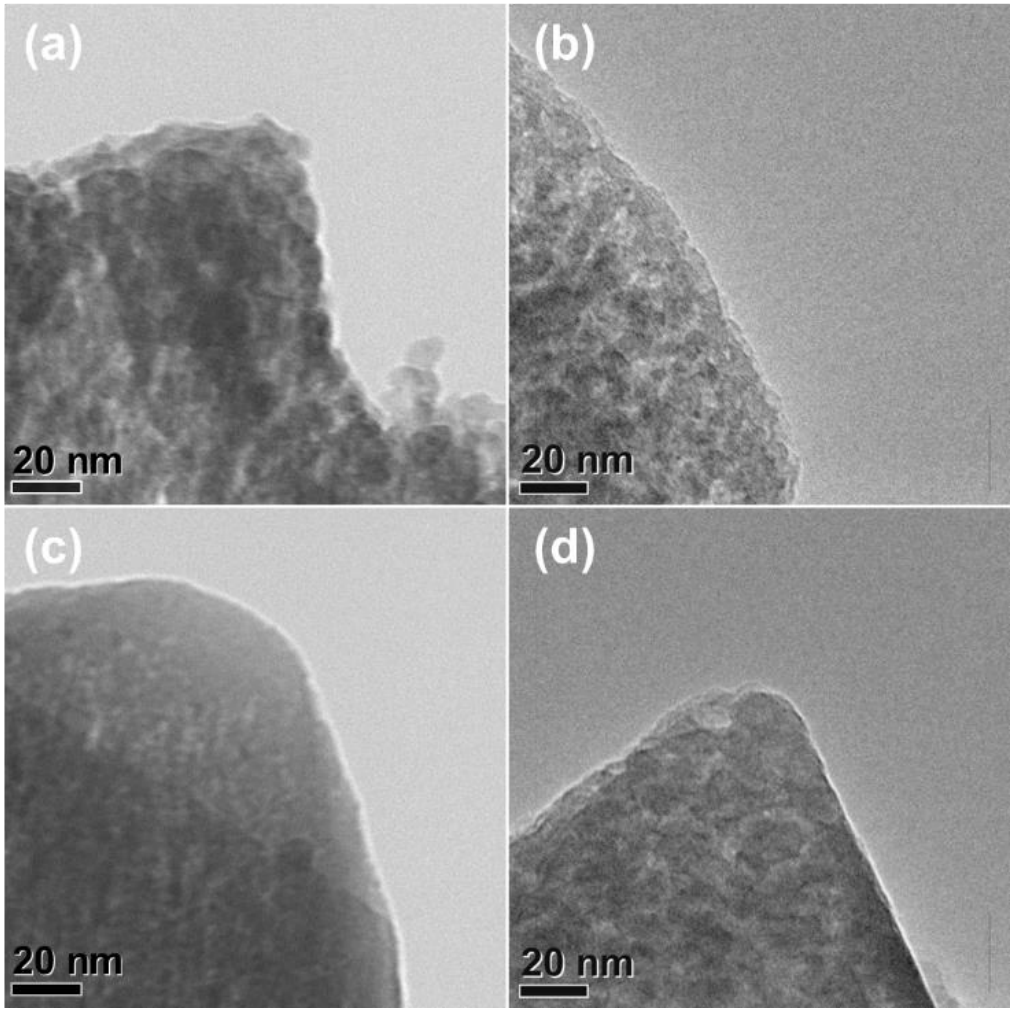

Figure 4.7 TEM micrographs for (a) CAY-*0.1-1h-HT*, (b) CAY-*0.1-1h-S*, (c) CAY-*0.14-1h-S* and (d) CAY-*0.16-1h-S*

Based on the ultrasonic desilication treatment, the effect of citric acid concentration (i.e., 0.1, 0.14 and 0.16 mol L^{-1}) used in the chemical dealumination treatment on the mesoporosity of the resulting CAY zeolites was studied. As expected, an increase in the concentration of citric acid in the dealumination step caused the decrease of the yield (Figure 4.5 (a)) and relative crystallinity (Table 4.3), as well as the increase of the SAR of the final CAYs, suggesting the important role of the chelator concentration in removing the framework Al (based on the same treatment time), and hence the effectiveness of mesopore formation at the end of the sequential treatment. By comparing the relevant N_2 isotherms, CAY-*0.16-1h-S* shows the lowest uptake at the low relative pressure compared to CAY-*0.1-1h-S* and CAY-*0.14-1h-S*, suggesting severe dealumination, and hence the damage of the microporous crystalline

domain. Table 4.4 shows that the micropore surface area of CAY-*0.16-1h-S* is appreciably low at only 236 $m^2 g^{-1}$, while that of CAY-*0.1-1h-S* and CAY-*0.14-1h-S* is above 530 $m^2 g^{-1}$. Comparatively, CAY-*0.14-1h-S* possesses the best combination of the mesoporous and microporous features with high external and micropore surface area of 206 and 531 $m^2 g^{-1}$, respectively, as well as the specific pore volumes (Table 4.4). Considering the mesoporous property of the resulting zeolites, the developed sequential method employing ultrasound is as effective as the previously reported ones such as the sequential chemical treatment (using H_4EDTA [121] or citric acid [91])-alkaline treatment, sequential steaming-chemical treatment (using H_4EDTA) [90, 258], sequential chemical treatment (using citric acid)-surfactant-templating method [238, 259] and sequential acid leaching (using HCl)-alkaline treatment [121]. For CAY-*0.16-1h-S*, the sequential treatment using the highly concentrated citric acid caused the excessive Al extraction, and hence the destruction of the zeolite framework, leading to the collapse of the framework. This is also reflected by comparing the RC values of the relevant samples, and CAY-*0.16-1h-S* shows the lowest one at 69%.

Selected samples were ion-exchanged and analysed by NH_3-TPD to compare the effect of different sequential treatments on the acidic property of the resulting materials in reference to the parent Y, and the obtained results are presented in Figure 4.8 (a) and Table 4.5. All zeolites exhibited the typical NH_3 desorption behaviour corresponding to the Y zeolite, being in line with Chapter 3 findings. The desorption peaks can be deconvoluted into two which are related to the weak (< 200 °C) and strong acidic sites (> 300°C), respectively (Table 4.5). Compared to the acidic property of the parent Y, the sequential post-synthetic treatments, regardless of the chelator and the desilication method used, caused the decrease of strong acidity, i.e., 0.818 mmol g^{-1} for the parent Y *versus* < 0.618 mmol g^{-1} for the mesoporous Y. Based on the same first-step chemical treatment, the conventional hydrothermal and the proposed ultrasound-assisted alkaline treatments are equivalently effective, producing mesoporous zeolites with the comparable acidic property, as shown in Table 4.5. The selected mesoporous zeolites along with the parent Y were assessed by the comparative catalytic cracking of *n*-octane at 350 °C. Figure 4.8 (b) shows the absolute conversion of *n*-octane over different zeolites as a function of time-on-stream. All catalysts show the comparable initial activity close to ~97%. The parent Y deactivated significantly (deactivation rate = –3.4%·h^{-1}), and the conversion of *n*-octane was about 65% after 10 h test. Conversely, the mesoporous Y

zeolites demonstrated the improved catalytic performance, especially the EAY zeolites, which almost sustained their activity during the test. By comparing the EAY and CAY zeolites used in the catalytic tests, the former possesses the better mesoporosity (~0.21 $cm^3\ g^{-1}$) than the latter (about 0.12 $cm^3\ g^{-1}$). Therefore, although the strong acidity is relatively low in EAY zeolites (compared to the CAY zeolites, Table 4.5), the well-developed mesopores facilitate the accessibility and diffusion of molecules in their frameworks, leading to the improved performance in the cracking reaction. CAY zeolites deactivated gradually over time at the rate of about $-1\%\cdot h^{-1}$. More importantly, the catalytic tests show that during the sequential post-synthetic treatments, the developed ultrasound-assisted method (in the alkaline treatment) is as effective as the conventional hydrothermal method, however, the efficiency of the ultrasonic method is better than the hydrothermal one, i.e., the reduction in the treatment time by 6-fold.

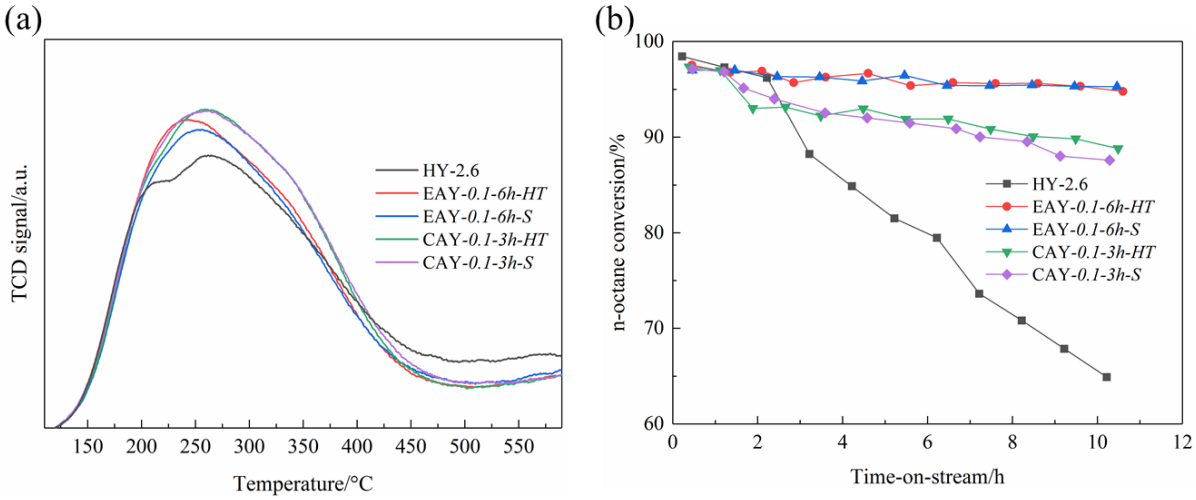

Figure 4.8 (a) NH_3-TPD spectra and (b) catalytic cracking activity (regarding the absolute conversion of *n*-octane) of the parent Y and selected mesoporous Y zeolites (including EAY-*0.1-6h-HT*, EAY-*0.1-3h-S*, CAY-*0.1-3h-HT* and CAY-*0.1-3h-S*).

Table 4.5 Analysis of NH_3-TPD data for the parent Y and selected mesoporous Y zeolites.

Catalyst	*T* of desorption peaks [°C]		Weak acidity [mmol g^{-1}]	Strong acidity [mmol g^{-1}]	Total acidity [mmol g^{-1}]
	First peak	Second peak			
HY-2.6	202.1	296.5	0.396	0.818	1.214
EAY-*0.1-6h-HT*	227.0	331.5	0.895	0.458	1.353
EAY-*0.1-6h-S*	225.0	315.9	0.743	0.544	1.287
CAY-*0.1-3h-HT*	227.5	325.5	0.815	0.618	1.433
CAY-*0.1-3h-S*	227.5	328.6	0.840	0.606	1.446

4.4 Conclusions

Mesopore zeolites are practical solutions to solve the accessibility issues experienced by the pristine microporous zeolites in the important chemical conversions, especially petrochemicals. Therefore, the continuous development and innovation of preparing various types of mesoporous zeolites are necessary to improve the sustainability of zeolites and the processes (not limited to the catalytic petrochemical conversions) using zeolites, contributing to the sustainable development of the industry and society. In this chapter, sequential post-synthetic chemical dealumination and desilication of the pristine Y zeolite (with SAR of ~2.6, the most important catalyst for FCC to produce gasoline range organics) was performed to prepare mesoporous Y zeolites. H_4EDTA was first used as the chelating agent in the study, and the effect of the dealumination treatment time (30 min to 6 h) and the method for desilication, i.e., hydrothermal and ultrasonic desilication, on the creation of mesoporosity was investigated. It was found that, for the pristine Y zeolite, the condition used by the dealumination step in the sequential treatment is critical for creating mesopores. When 0.1 mol·L^{-1} H_4EDTAwas used, if the dealumination treatment was performed for < 3 h, the sequential method was not very effective for making zeolites with mesoporous features, e.g. $S_{external}$ < 100 m^2 g^{-1}. More importantly, the ultrasound-assisted desilication treatment of the dealuminated zeolites was found effective in the sequential treatment method to facilitate the creation of mesopores, being more efficient than the conventional hydrothermal dealumination treatment with the reduced treatment time, i.e., 5 min vs. 30 min. The effect of the ultrasound irradiation on the desilication is generic, which was confirmed by the comparative work using the citric acid dealuminated Y zeolites. In addition, based on the same first-step chemical treatment, the developed ultrasonic alkaline treatment method was as effective as the hydrothermal alkaline treatment, which was evidenced by the analysis of the porous, acidic and catalytic properties of the selected mesoporous zeolite analogues. The findings from this chapter emphasised that the ultrasound irradiation is a promising alternative to the conventional hydrothermal heating, being more energy and time-efficient, in the sequential post-synthetic dealumination-desilication method for making hierarchical mesoporous zeolites.

Chapter 5 Sequential microwave-assisted dealumination and hydrothermal alkaline treatments of Y zeolite for preparing hierarchical mesoporous zeolite catalysts

This chapter was based on the published work on introducing secondary mesopores into Y zeolite framework by a novel post-synthetic method combining the microwave-assisted chemical dealumination and hydrothermal alkaline treatment. R. Zhang, D. Raja, Y. Zhang, Y. Yan, A.A. Garforth, Y. Jiao, X. Fan, Sequential Microwave-Assisted Dealumination and Hydrothermal Alkaline Treatments of Y Zeolite for Preparing Hierarchical Mesoporous Zeolite Catalysts, Top. Catal., 63 (2020) 340−350. https://doi.org/10.1007/s11244-020-01285-0

5.1 Introduction

Synthetic zeolites represent one of the most important industrial catalysts since 1954, which have been being used widely in various heterogeneous catalysis such as fluid catalytic cracking (FCC, over zeolite Y) and cumene production (over mordenites [260]), as well as the emerging bio-refinery such as catalytic transformation of various platform biomolecules including organic acids, alcohols and sugars [261, 262] due to their strong acidity, high surface area, good hydrothermal stability and relatively low cost [185, 232]. Although the pristine microporosity of zeolites (<1 nm) offers the important functionality of shape/size selectivity in applications such as xylene isomerisation and toluene disproportionation over ZSM-5 zeolites, it often imposes the accessibility and intracrystalline diffusion limitations for processes involving bulky molecules such as FCC and liquid-phase fine chemicals synthesis [46, 98, 183, 257, 263, 264]. Accordingly, to mitigate the molecular transport limitation within the microporous framework of zeolites, substantial effort has been devoted to prepare alternative zeolitic materials such as nano-sized zeolites with different geometries, zeolite hollow structures and mesoporous zeolites [265, 266]. Creation of hierarchical mesopores within the microporous domain of zeolites via the post-synthetic methods is relatively practical and convenient in comparison with the direct synthesis routes, such as the templating methods [29]. Common post-synthetic modification methods include steaming, calcination, acid leaching, chemical treatment and alkaline treatment [267].

However, the specific treatment and procedure of a post-synthetic method depends on the nature of zeolites, especially their chemical composition represented by the SAR [46, 185, 268].

For the pristine zeolite Y with the intrinsically low SAR of 2.4–2.6, direct post-synthetic modification by alkaline treatment is ineffective to create mesoporous features, since the highly concentrated framework Al species protect the framework Si species from the alkaline attack [228, 235, 236, 266]. Conversely, steaming and acid treatments are commonly used to dealuminating Y zeolites, and hence creating mesoporosity, as well as improving the thermal stability of the resulting zeolite [121, 237, 269, 270]. By combining the alkaline treatment after the dealumination of zeolite Y, i.e., the sequential post-synthetic dealumination and desilication treatments, mesoporous Y zeolites with the improved hierarchical features and crystallinity can be obtained due to the removal of amorphous Al-rich debris resulted from the dealumination [121]. Verboekend et al. demonstrated that the sequential chemical treatment-alkaline treatment for the post-synthetic treatment of commercial Y zeolites such as CBV 300 (SAR = 2.6, by Zeolyst International) is highly effective to create well-developed mesoporosity in the resulting zeolites (i.e., $S_{external}$ = 330 m^2 g^{-1}) [91, 121]. The first-step dealumination was achieved by chemical treatment using H_4EDTA or Na_2H_2EDTA as the chelating agents, being milder than the conventional steaming method. However, the dealumination with H_4EDTA and Na_2H_2EDTA aqueous solutions requires at least 6 h to be effective under the hydrothermal conditions at 100 °C, still being relatively energy intensive. The sequential ammonium hexafluorosilicate (AHFS) and alkaline treatment (i.e., using NaOH solutions) of a NaY (SAR = ~2.4) was also effective, producing the resulting mesoporous zeolite Y with the mesopore volume at ~0.45 cm^3 g^{-1} [264]. Although the relative milder temperature at 65 °C was used for the sequential treatment, the use of toxic AHFS is not desired for practical applications at large scale.

Since both synthesis and modification (especially the post-synthetic treatments) of zeolites are relatively energy-intensive and time-consuming, as well as involving environmental issues for some cases such as the removal of organic template via calcination, strategies to improve the sustainability of these processes were explored over the recent years. MW and ultrasonic irradiation has been proved to be comparatively effective (in comparison with the conventional hydrothermal, HT, methods) to promote

the green synthesis and modification of porous framework materials such as zeolites [203, 271, 272] and metal-organic frameworks (MOFs) [273] due to the advantages such as the absence of thermal gradient and rapid volumetric heating.

There are few reports, as reviewed by ref. [262], on the use of MW for the single-step liquid-phase modification of zeolites for tuning the acidity (*via* dealumination) and porosity (*via* desilication or detitanation), claiming that the MW only serves the purpose of improving the heat transfer of the systems via the effective and rapid volumetric heating. However, the resulting zeolites with mesoporous characteristics only comparable to the analogues produced under the conventional HT conditions in spite of the reduced treatment time from hours to minutes. In our recent development, the combination of MW irradiation with the chelating agent (i.e., the MWAC method), especially H_4EDTA, was found highly efficient and effective to produce hierarchical Y zeolites [274]. Compared with the HT treatment, at the laboratory scale, the MWAC method showed about 12.5-fold decrease in energy consumption, as well as being able to prepare mesoporous Y zeolite with exceptional mesopore volume of >0.48 cm^3 g^{-1}.

In this chapter, sequential post-synthetic treatments combining the MW-assisted dealumination and HT alkaline treatments of the pristine Y zeolite using different acids (e.g. the mineral acid such as hydrochloric acid (HCl) and carboxylic acids such as oxalic and citric acid) were developed, and the effect of the type of acids on the mesoporous feature of the post-treated zeolites from the sequential treatments was investigated. The physiochemical properties of the resulting materials were characterised by N_2 physisorption, PXRD, FT-IR, inductively coupled plasma optical emission spectrometer (ICP-OES), TEM and NH_3-TPD analysis. The correlation between the number of carboxyl groups in carboxylic acids and the mesoporous features was investigated preliminarily. Additionally, the mesoporosity in the modified Y zeolite by the sequential method was assessed by the aldol condensation (of 1-heptanal with benzaldehyde), in which the selective formation of the bulky product of jasminaldehyde, as well as its diffusion into the liquid bulk, was promoted by hierarchical porous structures.

5.2 Experimental

5.2.1 Sequential microwave-assisted dealumination and hydrothermal alkaline treatments of Y zeolite

The pristine zeolite used in this work is the commercial NH_4Y zeolite (CBV 300, SAR = 2.6) purchased from Zeolyst International, and used as received (i.e., the Parent Y). Post-synthetic dealumination treatments under the MW conditions were carried out in a monomode CEM Discover microwave reactor using the following chemicals: hydrochloric acid (HCl, ACS reagent, 37%, Aldrich), citric acid (CA, ACS reagent, ≥99.5%, Aldrich), oxalic acid (OA, 98%, anhydrous, Acros Organics), tartaric acid (TA, L-(+)-Tartaric acid, ACS reagent, ≥99.5%, Aldrich) and diethylenetriaminepentaacetic acid (DA, ⩾ 99%, Aldrich). In a typical MW-assisted dealumination post-synthetic treatment, 2 g pristine zeolite was dispersed in 20 ml acidic solution (with different acids at 0.16 M) in a 35 ml Pyrex pressure vessel under stirring at room temperature. The vessel was then introduced into the MW reactor and heated to 100 °C and held for 1 min at 150 W. The resulting mixture was then cooled in an ice-water bath and centrifuged to separate the solid from the solution. The solid was washed with DI water repeatedly for 5 times and dried in an oven at 100 °C overnight.

All dried samples after dealumination were subject to the alkaline treatment under the hydrothermal condition (i.e., with 0.2 M sodium hydroxide, NaOH, at 65 °C for 30 min under stirring) to remove the amorphous Al-rich debris from the framework. NaOH (reagent grade, 97%) was purchased from Sigma Aldrich and used as received. After the HT alkaline treatment, samples were washed using DI water and dried at 100 °C overnight for characterisation or ion exchange. The resulting Y zeolites were named as *a*-Y, where *a* is the acronym of the acid used in the MW-assisted dealumination treatment (such as HCl for hydrochloric acid and CA for citric acid, as defined above). A control experiment of performing the single-step HT alkaline treatment of the Parent Y (under the HT condition at 65 °C with 0.2 M NaOH for 30 min) was also carried out, the resulting material was worked up using the same procedure described above and denoted as AK-Y. The loss of materials in the process of the sequential treatments

and work-up was estimated using blank experiments (with DI water), and relevant solid yields were about 95%.

5.2.2 Characterisation of materials

N_2 physisorption analysis was performed at the liquid nitrogen temperature of about −196.15 °C using a Micromeritics 3Flex Surface Characterisation Analyser. Prior to the N_2 sorption measurements, samples (~150 mg) were degassed at 350 °C under vacuum overnight. Specific surface area of materials was determined using the BET method. The micropore and external surface areas, as well as the micropore volume, were determined by the *t*-plot method. Pore size distributions were obtained using the HK (for micropores) and the BJH method (for mesopores). XRD analysis was performed using a Philips X'Pert X-ray diffractometer with monochromatised Cu$K\alpha_1$ radiation (40 kV, 30 mA, λ = 1.5406 Å). XRD patterns of materials were collected for 2θ diffraction angles ranging from 5° to 40°, and the scanning rate was 1.167° min^{-1} with a step size of 0.0168°. The RC was estimated by comparing the integrated peak areas of the modified samples with that of the Parent Y (which was considered to have 100% RC) according to the ASTM Standard [275]. The total integrated areas of the eight peaks assigned to the (331), (511), (440), (533), (642), (822), (555), and (664) facets were calculated for comparison. FT-IR analysis was performed on a Bruker VERTEX 70 spectrometer with the red light emission from a Helium-Neon laser and the wide range MIR-FIR beamsplitter and detector. The IR spectra were obtained at ambient temperature by 56 scans at 4 cm^{-1} resolution in the wavelength range of 400–4,000 cm^{-1}. The bulk elemental Si and Al concentrations in zeolites were measured by ICP-OES (Analytik Jena PlasmaQuant PQ 9000). NH_3-TPD analysis was performed using a Micromeritics AutoChem II 2920 chemisorption analyser (~100 mg sample, 10 K min^{-1}, He flow rate = 30 cm^3 STP min^{-1}) to determine the strength and amount of the acidic sites on the zeolites. TEM analysis of samples was performed on a JEOL JEM-2100 electron microscope operated at 200 kV.

5.2.3 Ion exchange

The modified Y and Parent Y zeolites were ion exchanged to be converted into their H forms for catalysis. To perform the ion exchange, 1 g zeolite was added into 20 ml of 1 M ammonium nitrate

(NH_4NO_3, ⩾98%, Aldrich) solution. The mixture was stirred at 500 rpm at 80 °C for 24 hours. Then the zeolite was centrifuged (at 4,400 rpm for 5 min) and washed 3 times with DI water and dried in an oven at approximately 100 °C overnight. All ion exchanged zeolites were calcined at 450 °C (temperature programme: ramp from the room temperature to 450 °C at 5 °C min^{-1}; at 450 °C for 5 h; cooling naturally to room temperature).

5.2.4 Catalysis

In order to probe the hierarchy of the mesoporosity in the modified Y zeolites, the liquid-phase aldol condensation of benzaldehyde with 1-heptanal was used as the model reaction. Before reaction, the calcined zeolites were dried overnight at 120 °C to remove the moisture in the framework. The reaction was performed using Schlaker reaction tubes (Aldrich®) under N_2 for 24 h. Detailed experimental procedure and sample analysis using GC is described in Section 3.2.3. The fractional conversion of 1-heptanal (C_h) and selectivity to jasminaldehyde (S_{jas}) were calculated according to (Eq. 5.1–2), and the normalised selectivity ($S_{jas.norm.}$) is defined as (Eq. 5.3).

$$C_h\ (\%) = \frac{n_{i,h} - n_{f,h}}{n_{i,h}} \times 100\% \qquad \text{(Eq. 5.1)}$$

$$S_{jas}\ (\%) = \frac{n_{jas}}{n_{i,bz} - n_{f,bz}} \times 100\% \qquad \text{(Eq. 5.2)}$$

$$S_{jas.norm.}\ (\%\ \text{mmol}^{-1}\ \text{g}) = \frac{S_{jas}}{\text{Concentration of strong acidity [mmol g}^{-1}\text{]}} \qquad \text{(Eq. 5.3)}$$

where $n_{i,h}$ and $n_{f,h}$ are the moles of 1-heptanal in the initial and final system, respectively; n_{jas} is the mole of jasminaldehyde produced.

5.3 Results and discussion

5.3.1 Properties of the modified Y zeolites

Alkaline treatments of Al-rich zeolites such as Y and mordenite zeolites are generally not effective concerning altering the SAR of the zeolites via the treatment [185, 235], which was confirmed by this work as well. As shown in Table 5.1, AK-Y resulted from the direct alkaline treatment of the Parent Y

shows the insignificant change in solid yield (sample weight loss of ~5%) compared to other samples obtained by the sequential treatments (hence AK-Y was not further characterised for the comparative study afterwards). Therefore, to produce mesoporous zeolites from the Al-rich pristine zeolite, i.e., Parent Y in this study, preparatory dealumination is necessary. In the sequential MW-assisted dealumination-HT alkaline treatments of Parent Y, it was found that the use of mineral acid of HCl in the MW-assisted dealumination was not ineffective, regarding the solid yield (92±5%) and the variation in SAR (at ~3.1, determined by ICP-OES, being slightly higher than that of Parent Y at ~2.7) after the treatment.

When carboxylic acids were used, the solid yield decreased noticeably (i.e., <76±5%), and the SAR increased by varying the acid from dicarboxylic acids (at ~3.8) to polycarboxylic acids (> ~3.9) with the increased numbers of carboxyl groups (as shown in). This phenomenon may be correlated to (i) the concentration of hydrogen ions (H^+) in the solution and (ii) availability of coordination centres (i.e., the COO^- group and nitrogen (N) centre). As the concentration of acids used in the MW-assisted dealumination was the same, the H^+ concentration of the system is expected to increase when polycarboxylic acids are used instead of the dicarboxylic acids. In an acidic environment, H^+ attacks the framework Al species to initiate hydrolysis, leading to the formation of non-framework Al species [276], which can be removed to achieve dealumination. In the presence of chelating agents such as polycarboxylic acids, the extraction of Al species is accomplished via complexation reactions [73]. Oxalic acid and tartaric acid have the same number of coordination centres (i.e., ×2 COO^- groups), and hence produced the OA-Y and TA-Y zeolites with the comparable solid yields and SAR values. Tartaric acid has two additional hydroxyl groups which did not affect the dealumination step significantly under the MW condition, being in line with the previous findings (for zeolite beta under hydrothermal conditions) [77]. Although citric acid possesses three carboxyl groups, it is relatively weak acid (the acid dissociation constant for the first proton, pK_{a1} = 3.13) compared to oxalic acid (pK_{a1} = 1.27). Under the condition used, the solid yield of the resulting CA-Y was lower than that of OA-Y and TA-Y, while the SAR values were comparable. Diethylenetriaminepentaacetic acid with a diethylenetriamine backbone (×3 N centres) with five carboxyl groups showed the comparably best ability to dealuminate

Parent Y under the MW condition due to the combination of the relatively strong acidity (pK_{a1} = 1.80) and high affinity for metal cations. DA-Y has a SAR of ~6.3, being much higher than that of other post-treated Y zeolites, which reflects the effectiveness of using diethylenetriaminepentaacetic acid for dealumination of Al-rich zeolite Y (as effective as H_4EDTA, under the MW condition [31]).

Table 5.1 The solid yield (for the modified Y zeolites from the post-synthetic treatments), SAR (by ICP-OES), RC values and unit cell sizes of the Parent Y and modified Y zeolites.

Sample	Solid yield[a] [%]	SAR[b] [-]	RC[c] [%]	Unit cell size [Å]
Parent Y	-	2.7	100	24.70
AK-Y	94	-	-	-
HCl-Y	92	3.1	72	24.55
OA-Y	76	3.8	82	24.64
TA-Y	69	3.9	75	24.64
CA-Y	59	3.9	38	24.60
DA-Y	61	6.3	20	24.58

[a] isolated mass of solid after the single-step alkaline or the sequential post-synthetic treatments divided by the mass of the starting pristine zeolite (±5% margin of errors); [b] determined by ICP-OES; [c] determined by XRD.

Comparative XRD analysis of the zeolites was shown in Figure 5.1 (a). The characteristic diffraction peaks in a range of 15° to 35° 2θ, which are the crystallographic features of FAU crystalline phase, are clearly identified for all the samples, confirming the preserved Y lattice structure in the modified zeolites. However, the peak intensity of the samples varies differently, suggesting the change of the RC after the post-synthetic treatments. Using the peak intensity of the Parent Y as the reference, RC values of the modified zeolites were listed in Table 5.1. Using HCl in the MW-assisted treatment, the resulting HCl-Y has a RC value of ~72% which was due to acid-induced hydrolysis of the Parent Y, causing the damage on the crystalline structure. When carboxylic acids were used, RC values seem to be correlated well with the number of coordination centres in them. Carboxylic acids with two COO^- groups, i.e., oxalic and tartaric acid, can preserve the crystallinity relatively well after the sequential treatment at about 82% and 75%, respectively, being higher than that of HCl-Y. Conversely, the crystallinity of the modified zeolites was reduced notably when polycarboxylic acids were used in the MW-assisted dealumination, as shown in Table 5.1. Considering the concentration of carboxylic acids used in the treatment was the same, then the phenomena can be explained by the complexation mechanism. For Al^{3+}, which normally adopt octahedral geometries to form six-coordinate complexes [277], three oxalates or tartrates will be bound with Al^{3+} to form an anionic complex, whilst two citrates or one

pentetate will be sufficient to complex one Al^{3+}. Accordingly, the extraction of Al species from the zeolite framework using citric and diethylenetriaminepentaacetic acid can be much more effective, leading to relatively severe damage on the microporous crystalline phase for creating mesopores (which will be discussed later). This was also confirmed by the relevant changes of XRD patterns and unit cell sizes of the modified zeolites, i.e., after the sequential post-synthetic treatment (excluding the HCl-Y), compared with the Parent Y, (i) the characteristic peaks of the modified Y zeolites shift slightly to the higher two theta values, and (ii) their unit cell dimensions decrease continuously from 24.70 Å to 24.58 Å with an increase in the number of coordination centres of the acids used. The unit cell parameter of Y zeolites (including USY) are normally in the range of 24.2–25.0 Å with cubic symmetry [32], Parent Y used in this work has a unit cell size of 24.70 Å, being in the range above. The decrease in the unit cell size after the post-synthetic treatments can be attributed to Al extraction from the Al-rich Parent Y since the Al-O-Al bond length (of ~1.75 Å) is relatively longer than that of Si-O-Si bond (about 1.62 Å) [278]. The comparison of HCl-Y with the modified Y zeolites using carboxylic acids (concerning the solid yield, SAR and RC values) suggests that the mineral acid might be only effective for hydrolyse the pristine zeolite (causing the compromised crystallinity), whereas carboxylic acids were much more effective for Al extraction under the condition used for the sequential post-synthetic treatment.

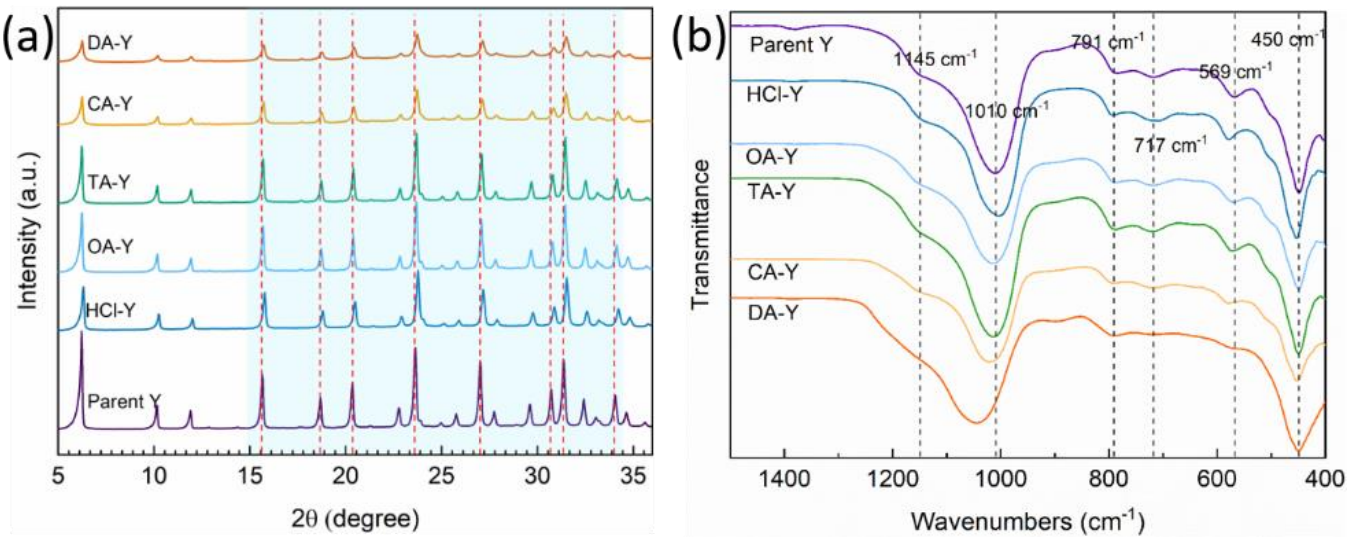

Figure 5.1 (a) XRD and (b) FT-IR patterns of the modified Y zeolites after the sequential post-synthetic treatments.

FT-IR spectra for the Parent and modified Y zeolites are shown in Figure 5.1 (b). The positions of IR band at 450 cm^{-1} are generally comparable corresponding to the structural insensitive internal Si-O_4 and Al-O_4 tetrahedral bending vibration. The band at 569 cm^{-1}, 717 cm^{-1} and 1,145 cm^{-1} corresponds to spectral feature of the double six-member rings, the external linkage symmetrical stretching and asymmetrical stretching in FAU zeolites [279], respectively, confirming the FAU framework of the modified zeolites after the post-synthetic treatments. However, DA-Y does not show strong signal at these wavenumbers, which might be attributed to the severely damaged FAU framework, as evidenced by XRD analysis. The other two bands at 791 cm^{-1} and 1,010 cm^{-1} are attributed to internal tetrahedral symmetrical stretching and asymmetrical stretching vibrations, respectively [280]. The latter was found shifted to higher wavenumber after the post-synthetic treatments, especially DA-Y, due to the sever dealumination (i.e., the relatively strong electronegativity of Si than that of Al, leading to high vibration frequency).

N_2 adsorption-desorption analysis was performed to show the effect of acid types on the porous feature of the modified zeolites from the sequential post-synthetic treatments in reference with that of Parent Y, and the relevant results are presented in Figure 5.2 and Table 5.2. Parent Y shows the type I N_2 physisorption isotherm which is the characteristic of microporous adsorbents. After the treatment using HCl, the resulting HCl-Y shows the similar isotherm to that of Parent Y, but with reduced amount of micropores which is evidenced by its relatively low quantity adsorbed at low relative pressure ($p/p^0 <$ 0.01, Figure 5.2 (a)) and the reduced specific surface areas (i.e., the BET surface area, S_{BET}, micropore surface area, S_{micro}) and pore volume (i.e., the micropore volume, V_{micro}), as shown in Table 5.2. The post-synthetic treatment using HCl did not develop significant mesoporous features in HCl-Y (only with $S_{external}$ of 77 $m^2\ g^{-1}$). The findings are in line with the discussion above, i.e., under the condition used for the sequential post-synthetic treatment, the mineral acid of HCl was only effective for hydrolysis rather than the extraction of Al species for mesopores formation.

Using dicarboxylic acids in the sequential post-synthetic treatment, although their acidities are weaker than that of HCl, they were comparatively more effective than HCl to create mesopores in zeolite Y. As shown in Figure 5.2 (a), the isotherms of OA-Y and TA-Y show hysteresis loops with the relevant

mesoporous information extracted as $S_{external}$ = ~144 m^2 g^{-1} and V_{meso} = ~0.15 cm^3 g^{-1}, being much more significant than the relevant features of HCl-Y and Parent Y. When polycarboxylic acids of citric and diethylenetriaminepentaacetic acid were used in the post-synthetic treatment, the resulting CA-Y and DA-Y present the type IV N_2 adsorption-desorption isotherms (Figure 5.2 (a)) with the H4 type hysteresis loop, suggesting the significant presence of mesopores in the two modified zeolites. Accordingly, $S_{external}$ values of CA-Y and DA-Y were measured at 270 and 214 m^2 g^{-1}, respectively. However, it is worth noting that the post-synthetic treatment methods are 'top-down' approaches to create mesopores in the parent zeolites, and hence compromising the pristine microporous crystalline framework. Therefore, although diethylenetriaminepentaacetic acid (0.16 M, as the example of multidentate chelating agents) was highly effective regarding the creation of mesopores, the loss of crystallinity and micropores were comparatively significant, which may not be very ideal for applications requires the shape/size selectivity and/or stability under harsh conditions.

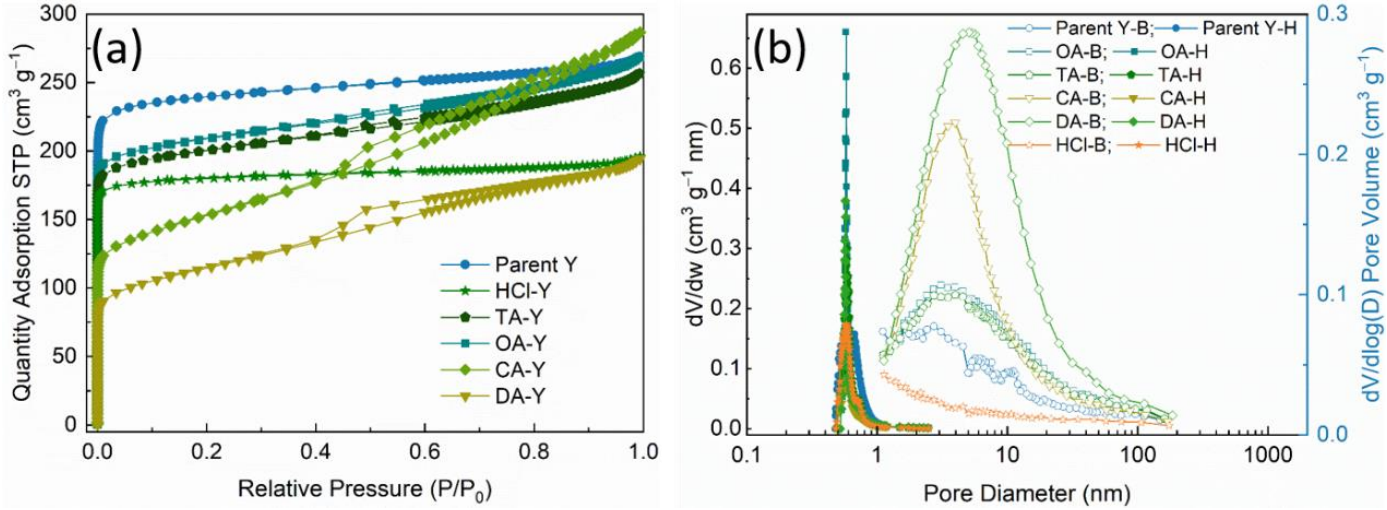

Figure 5.2 (a) N_2 adsorption-desorption isotherms at −196.15 °C and (b) micro (H)-/meso (B)-pore size distributions of the modified Y zeolites after the sequential post-synthetic treatments.

Table 5.2 Porous properties of the Parent and modified Y zeolites (from the sequential post-synthetic treatments).

Samples	Specific surface area [m^2 g^{-1}]			Specific pore volume [cm^3 g^{-1}]		
	S_{BET}[a]	$S_{external}$[b]	S_{micro}[b]	V_{total}[c]	V_{micro}[b]	V_{meso}[d]
Parent Y	867	9	858	0.36	0.35	0.01
HCl-Y	600	77	523	0.34	0.24	0.10
OA-Y	774	148	626	0.42	0.26	0.16
TA-Y	742	140	602	0.40	0.25	0.15
CA-Y	531	270	261	0.44	0.12	0.32
DA-Y	414	214	200	0.30	0.08	0.22

[a] determined by the BET method; [b] determined by the *t*-plot method; [c] the specific single point adsorption total pore volume of materials at adsorbed at p/p^0 = 0.99; [d] $V_{meso} = V_{total} - V_{micro}$.

PSDs of the materials were analysed using the H-K and BJH (on adsorption isotherms) method for micropores and mesopores, respectively, as shown in Figure 5.2 (b). All zeolites show the narrow PSD centring at about 0.7 nm corresponding to the pristine micropore width of zeolite Y, and the amount of micropores was reduced after the sequential treatments. HCl-Y does not show obvious mesopore PSD, while the mesopore PSD of the modified zeolites using carboxylic acids in the post-synthetic treatments correlates well with the number of coordination centres in the acids, for example the average mesopore sizes of CA-Y, TA-Y, CA-Y and DA-Y are about 2, 3 and 5 nm, respectively. The results of textural properties by N_2 physisorption agree well with the previous discussion regarding the solid yield and relative crystallinity. Accordingly, in the sequential post-synthetic treatments of zeolite Y: (i) the mineral acid (exemplified by HCl) was not effective regarding the Al extraction and mesopores formation; (ii) the carboxylic acids were capable of dealuminating the zeolite, possibly due to the synergistic effect of MW irradiation and chelation; and (iii) when carboxylic acids were used, the degree of dealumination and formation of mesopores are a function of the number of coordination centres in the acids (or chelating agent). TEM analysis of the materials is shown in Figure 5.3, and the relevant micrographs illustrate the distinct features of the Parent Y and modified Y zeolite crystals, i.e., (i) the dense and uniform crystalline region in the crystal of the Parent Y (Figure 5.3 (a)) and (ii) the dense and light features of the modified zeolites, suggesting the presence of intracrystalline mesoporosity (Figure 5.3 (a–f)). Specifically for CA-Y and DA-Y (Figure 5.3 (e) and (f)), the formation of relatively large mesopores is evident after the sequential post-synthetic treatments.

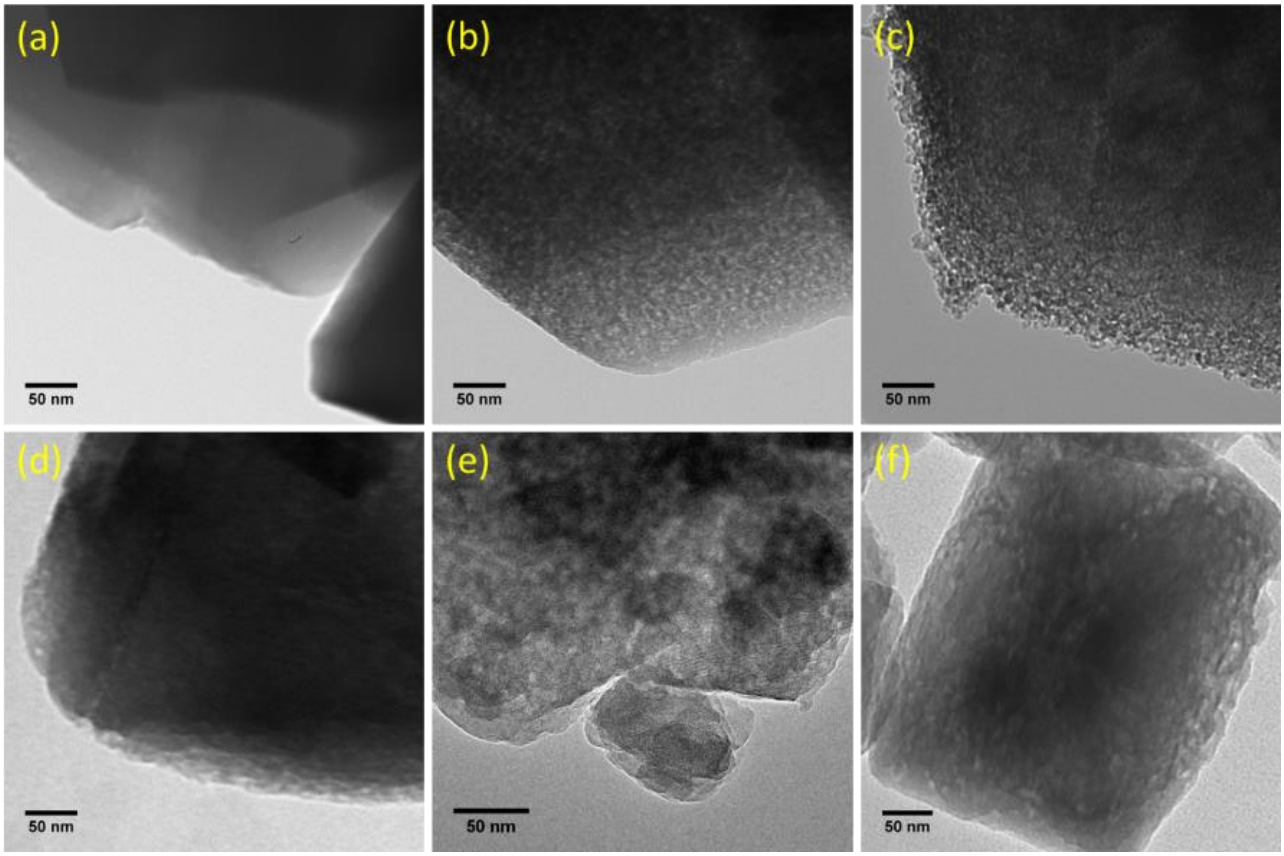

Figure 5.3 TEM micrographs of (a) Parent Y, (b) HCl-Y, (c) OA-Y, (d) TA-Y, (e) CA-Y and (f) DA-Y.

The acidic property of the zeolites was analysed by NH_3-TPD, as shown in Figure 5.4, and the corresponding amount of ammonia desorbed are reported in Table 5.3. Figure 5.4 shows the typical NH_3-TPD profiles of Y zeolites, which can be arbitrarily deconvoluted into two desorption peaks at around 200 and 300 °C, respectively, corresponding to the weak and strong acidic sites on the Parent and modified Y zeolites. Again, the post-synthetic treatment using HCl did not alter the mass specific acidity of the zeolite significantly, being comparable to that of the Parent Y. Conversely, compared with the Parent Y, the total mass specific acidity of the carboxylic acids modified Y zeolites dropped considerably (by *ca.* 45%), due to the effective dealumination of Parent Y under the post-synthetic treatment conditions used, especially DA-Y, which only has a total acidity of 0.79 mmol g^{-1}. OA-Y, TA-Y and CA-Y show the similar total mass specific acidity at about 1 mmol g^{-1}, and the results from NH_3-TPD analysis are in line with that by ICP-OES for SAR values of the zeolites (Table 5.1). Interestingly, in comparison with Parent Y, the BET specific weak acidity of the zeolites after the post-synthetic treatments (using organic acids) dropped by 45.0±17.6%. Conversely, the variation of their

BET specific strong acidity depended on the type of organic acid used. This aspect deserves further investigation, i.e., the concentration distribution of acidity as functions of mass and relevant specific surface areas.

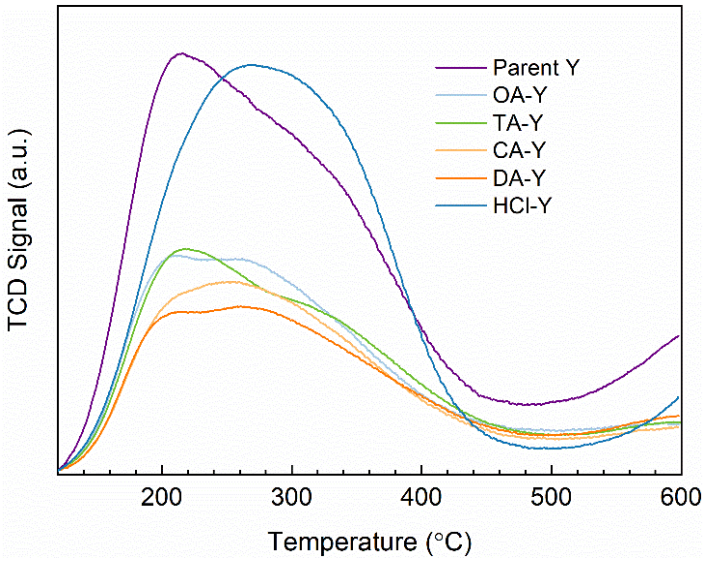

Figure 5.4 NH_3-TPD profiles of the Parent Y and modified zeolites.

Table 5.3 Acidic properties of the Parent and modified Y zeolites.

Catalyst	*T* of desorption peaks		Weak acidity[a]		Strong acidity[b]		Total acidity	
	First peak	Second peak						
	[°C]		[mmol g^{-1}]	[mmol m^{-2}]	[mmol g^{-1}]	[mmol m^{-2}]	[mmol g^{-1}]	[mmol m^{-2}]
Parent Y	209.1	320.4	1.05	1.21×10^{-3}	0.82	9.46×10^{-4}	1.87	2.16×10^{-3}
HCl-Y	235.2	331.1	1.11	1.85×10^{-3}	0.85	1.42×10^{-3}	1.96	3.27×10^{-3}
OA-Y	195.8	283.1	0.29	3.75×10^{-4}	0.71	9.17×10^{-4}	1.00	1.29×10^{-3}
TA-Y	211.2	325.6	0.54	7.28×10^{-4}	0.45	6.06×10^{-4}	0.99	1.33×10^{-3}
CA-Y	210.6	301.6	0.47	8.85×10^{-4}	0.55	1.04×10^{-3}	1.02	1.92×10^{-3}
DA-Y	199.1	296.7	0.28	6.76×10^{-4}	0.51	1.23×10^{-3}	0.79	1.91×10^{-3}

[a]mass and BET specific acidity of the first peak, [b]weight and BET specific acidity of the second peak. The acidity was determined from the amount of ammonia adsorbed using a density of 0.769 kg m^{-3} and molecular mass of 17.03 g mol^{-1}.

5.3.2 Probing hierarchical mesopores in the modified Y zeolites

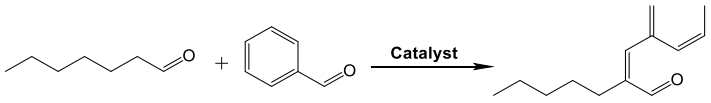

Scheme 5.1 Synthesis of α-n-amylcinnamaldehyde (jasminaldehyde) via the condensation of 1-heptanal with benzaldehyde.

Hierarchical mesoporous zeolites are highly beneficial to catalysis, mitigating the accessibility and diffusion issues experienced by the pristine microporous zeolites. To probe the hierarchy of the modified Y zeolites in this work, the condensation reaction of 1-heptanal with benzaldehyde in the liquid phase was employed (Scheme 5.1). This aldol condensation is carried out primarily over base catalysts (such as NaOH) for the synthesis of *α-n*-amylcinnamaldehyde (i.e., jasminaldehyde, an important perfumery chemical) [197]. However, the catalytic reactions can also proceed over solid acid catalysts (such as zeolites and MCM-41) with relatively slow rates in comparison with the catalysis over base catalysts [196], but being effective as a model system to probe the mesoporous features of the porous solid acid catalysts. The target molecule of jasminaldehyde has a kinetic diameter of about 0.74 nm. Accordingly, the selective formation of jasminaldehyde, as well as and transportation of jasminaldehyde from the porous solid acid catalyst to the bulk liquid, can be significantly enhanced by the presence of hierarchical mesopores in zeolites, being the indicator of the hierarchy in mesoporous zeolites . Therefore, in this work, the aldol condensation was used as the model reaction to assess the porous features of the modified Y zeolites only. Reaction mechanisms and kinetics of the model reaction over aluminosilicates have been previously reported by Corma et al. [196, 197], which are not the aim of this work. Therefore, during the catalysis, only the conversion of 1-heptanal and formation of jasminaldehyde were monitored by GC analysis.

Figure 5.5 (a) shows the results of aldol condensation over different zeolites. The margin of errors of the presented data is smaller than 3%, and the errors were due to sampling and instrumental errors. Among all catalysts investigated, CA-Y with highest mesopore volume (~0.32 $cm^3\ g^{-1}$) promoted the best performance regarding the absolute 1-heptanal conversion (C_h = ~63%) and selectivity to jasminaldehyde (S_{jas} = ~37%), whereas the microporous Parent Y only achieved the S_{jas} at ~14%. Previous research [196, 197, 281] has confirmed that the selectivity to jasminaldehyde was strongly dependent on the topology of the porous acid catalysts. It was found that (as shown in Figure 5.5 (a)), generally, the values of S_{jas} correlate well with the mesopore volume of the zeolites (Table 5.2), suggesting that the mesopores in the modified zeolites (by the sequential post-synthetic treatments) are hierarchical. For acid catalysed aldol condensation, the reaction is initiated by the acid site, as a proton

donor, to activate the carbonyl oxygen into a protonated form. Therefore, if one assumes that only the strong acidity (likely the Brønsted sites) of the zeolites is responsible for the catalysis, then the normalised selectivity (i.e., $S_{jas.norm.}$, (Eq. 5.3), with respect to the relevant strong acidity, Table 5.3) can be correlated with the V_{meso} values of the zeolites, as shown in Figure 5.5 (a). Figure 5.5 (b) shows that $S_{jas.norm.}$ is proportionally related to the specific mesopores volume of the zeolites in a near positive linear fashion, suggesting the effect of hierarchical mesopores in the zeolites on their catalytic performance.

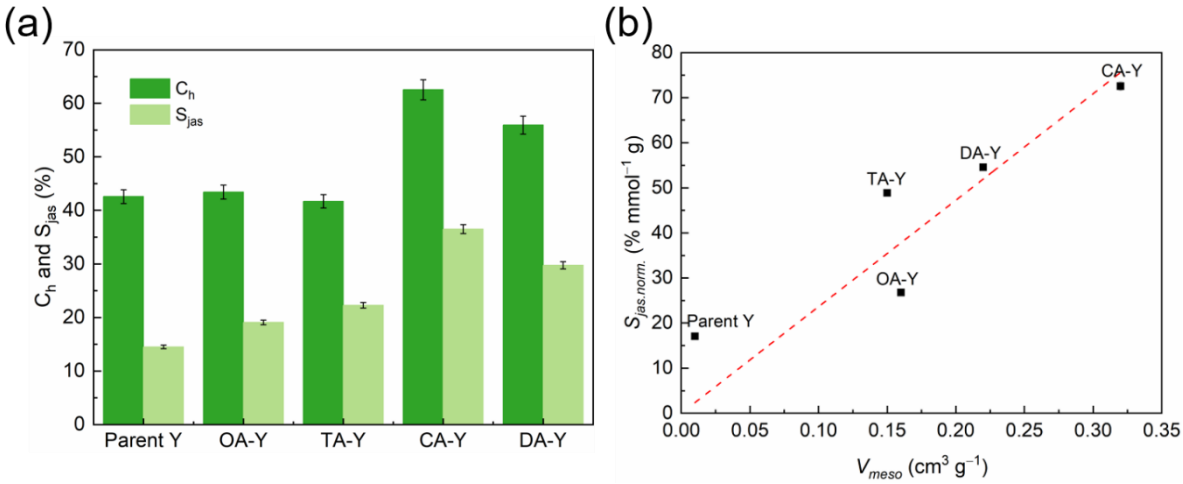

Figure 5.5 (a) 1-heptanal conversion (C_h) and selectivity to jasminaldehyde (S_{jas}) of the aldol condensation over the zeolites under study; (b) normalised selectivity ($S_{jas.norm.}$) as a function of V_{meso} for the Parent and modified Y zeolites.

5.4 Conclusion

This chapter demonstrates that the developed sequential post-synthetic treatment, involving the MW-assisted dealumination and HT alkaline treatment, for making mesoporous zeolite Y catalysts is generic, being effective with various carboxylic acids (as the chelating agents). The degree of effectiveness of dealumination and mesopores formation of the method depends primarily on the coordination centres in the acidic chelating agent. For example, by comparing oxalic acid (with two COO^- groups) and diethylenetriaminepentaacetic acid (with three nitrogen centres and five carboxyl groups), the latter showed the relatively significant ability to dealuminated the pristine zeolite Y, and hence creating mesopores. SAR values of the resulting OA-Y and DA-Y zeolites were about 3.8 and 6.3, respectively, and the relevant specific surface areas are 148 and 214 m^2 g^{-1}, respectively. Conversely, the used of

mineral acid such as HCl in the developed sequential post-synthetic treatment method was not effective, resulting in the material with the reduced crystallinity and insignificant mesoporous features. The findings suggest that the use of acidic chelating agents is the key factor to ensure the effectiveness of the developed sequential post-synthetic treatment regarding the formation of mesopores in zeolites, especially for Al-rich zeolite Y.

The mesopores in the resulting zeolites are hierarchical, facilitating the formation of the bulky product and the efficient diffusion of the product into the bulk stream, which was evidenced by the catalytic results from the model aldol condensation over the zeolite catalysts. The findings makes the developed method promising for expanding its application to other zeolites, as well as being worthy for developing a fundamental understanding of the dealumination mechanism in the system combining the microwave irradiation and chelating agents.

Chapter 6 Mechanism of mesopore formation in zeolites in post-synthetic microwave-assisted chelation treatment

6.1 Introduction

Zeolites, as crystalline aluminosilicates with homogeneous microporous frameworks, high specific surface areas and good thermal stability, are widely used in heterogeneous catalysis such as petrochemical refining processes [282]. Specifically, zeolite Y (with the FAU topology), Beta (with the BEA topology) and ZSM-5 (with the MFI topology) have significant industrial values [283-285]. During catalysis, the intrinsic microporosity (pore size <1 nm) of zeolites leads to accessibility and diffusion issues which deactivate the zeolite catalysts [286]. Accordingly, efforts have been made develop relevant strategies of designing and/or modifying zeolites to improve the accessibility of the active sites in the framework, which exemplified by nano-sized, 2-dimensional and mesoporous zeolites [16, 287, 288]. Among these strategies, post-synthetic treatments, such as calcination, steaming and acid/base leaching, are a class of methods for making zeolites with mesoporosity [80, 289, 290], being relatively robust and practical, as well as suitable for possible scaling up toward applications in practical settings [232, 291].

Appropriate selection of the post-synthetic treatments depends on the property of the parent zeolites. For the most important parent zeolite for catalysis, i.e., zeolite Y with low SAR (~2.6), post-synthetic dealumination by steaming or acid/chemical leaching is the prerequisite for creating secondary mesopores and improving hydrothermal stability of the resulting zeolites [80, 289, 290]. Therefore, mechanistic understanding of dealumination and mesopore formation processes is necessary to enable the optimisation of the process, as well as the rational design of mesoporous zeolites. Both theoretical (such as density functional theory, DFT) and experimental (such as solid-state nuclear magnetic resonance, NMR, spectroscopy [98, 239, 292]) studies of the dealumination mechanism were performed for steaming and acid leaching treatments, and relevant results showed the important role of water and hydrolysis of framework Al–O bond for producing EFAl species (which could be removed from the framework to render mesopores) [293-297].

Recently, a microwave (MW)-assisted chelation, i.e., MWAC, method was developed which showed the high efficiency in reducing the treatment time and energy consumption, as well as being highly effective to create hierarchical mesopores [298]. The MWAC method was developed based on the post-synthetic chemical treatment using chelating agents such as ethylenediaminetetraacetic acid (H_4EDTA) [73]. In comparison with the recent relevant methods under conventional hydrothermal conditions [91, 121], the MWAC method significantly reduced the treatment time from at least 6 hours to minutes (for dealumination), and hence reduced the energy consumption of the process. Although preliminary results have suggested the direct chelation of framework Al during the MWAC treatment, mechanistic understanding of chemical dealumination under MW irradiation is not yet fully understood.

Herein, we present a comparative investigation of the mechanism of dealumination and mesopore formation in zeolite Y via the sequential post-synthetic treatments using chelating agent (i.e., H_4EDTA) and mineral acid (i.e., hydrochloric acid) under MW conditions, and alkaline treatment. The physiochemical properties of the relevant zeolitic materials at different stages of the treatment were comprehensively characterised by N_2 physisorption, XRD, ICP-OES, SEM and TEM and solid-state magic-angle spinning (MAS) and liquid NMR analysis, contributing to the interpretation of the dealumination mechanism of the MWAC method. Specifically, *in situ* IR studies of the MWAC treated zeolites (using deuterium water, D_2O, and water as media without a chelating agent) was performed to gain the additional information on the role of water molecule in the MWAC process.

6.2 Experimental

6.2.1 Materials and methods

The parent Y zeolite was purchased from Zeolyst International (CBV 300 with molar SAR = 2.6). Hydrochloric acid (HCl, reagent, 37%, Aldrich), ethylenediaminetriacetic acid (H_4EDTA, bioultra, $\geqslant$ 99%, Aldrich), ethylenediaminetriacetic acid tetrasodium salt dihydrate ($Na_4EDTA \cdot 2H_2O$, bioreagent, 99.0–102.0%, Aldrich) and sodium hydroxide (NaOH, reagent grade, 97%, Aldrich) were all used as received.

The liquid media for the MWAC treatment include 0.1 M H_4EDTA, 0.4 M HCl, 0.1 M Na_4EDTA and 0.1 M Na_4EDTA/0.4 M HCl. In a typical MWAC treatment, 2 g parent zeolite was dispersed into a 20 mL solution in a 35 ml Pyrex pressure vessel and stirred for 5 min at room temperature. The mixture was subsequently transferred in a CEM Discover SP microwave synthesiser and heated up to 100 °C in 2 min followed by isothermal treatment for 1 min. After the treatment, the resulting slurry was quenched to 30 °C in ice bath, and then the solid was separated by centrifugation. The remaining liquid phase from the separation was kept for further ICP-OES analysis. The solid was washed with deionised water (DI) till the pH value reached ~7 and dried in an oven at 100 °C overnight. The resulting modified Y zeolites were denoted as MW*a*, where *a* referred to the chemicals in the solution, i.e., EA for H_4EDTA, HCl for hydrochloric acid, EN for Na_4EDTA and ENH for the mixture of EN and HCl).

After the MW treatment, sequential alkaline treatment was performed on the modified Y zeolites at 65 °C using 0.2 M NaOH aqueous solution for 30 min (1 g zeolite per 30 mL NaOH solution), followed by washing with DI water. Then, the sample was separated by centrifugation and dried at 100 °C. The resulting materials were named as MW*a*+HT.

6.2.2 Characterisation of materials

PXRD patterns of materials were obtained on Philips X'Pert X-ray diffractometer with monochromatised CuKα_1 radiation (40 kV, 30 mA, λ = 1.5406 Å). XRD data were recorded in a 2θ range of 5°–40° with an angular step size of 0.0199°. The RC was determined by using the parent Y zeolite as the reference, and the total intensity of the eight strongest reflections in the region of 2θ from 15° to 36° [299]. Nitrogen (N_2) physisorption measurements were performed at –196.15 °C using Micromeritics 3Flex Surface Characterisation Analyser. Before measurement, the sample (~100 mg) was degassed at 350 °C under vacuum for 12 h. Pore size distributions (PSD) were determined using the H-K method for micropores and the BJH method for mesopores. Elemental Si and Al concentrations in liquid phase were measured by ICP-OES (Quant PQ 900). Bulk SAR of zeolites was determined by an EDXRF spectroscopy (PANalytical MiniPal 4 EDXRF, operated at 30kV). Morphology of materials was investigated using TESCAN Mira 3 field emission SEM (FE-SEM) at an accelerating voltage of

10 kV. The high-resolution transmission electron TEM (HR-TEM) was performed on an FEI Tecnai G20 transmission electron microscope operating at 200 kV. Before TEM analysis, the samples were dispersed in acetone by sonication for 1 h and dropped on carbon-coated copper grids.

Solid-state ^{29}Si and ^{27}Al MAS NMR analysis was performed on a Bruker Bruker Avance III 400 instrument (MHz) using 4 mm ZrO_2 rotors at 21 °C. ^{29}Si MAS NMR spectra were acquired at 80 MHz with 4,096 number of scans, pulse width (PW) = 2.5 µs, recycle delay (D1) = 10 s, acquisition time (AQ) = 0.05 s, free induction decay (FID) = 3964 points, scanning = 4,096 times, dwell time (DW) = 12.6 µs, and receiver gain = 1150. ^{27}Al MAS NMR spectra were obtained at 104 MHz with 1,024 number of scans, PW = 2.5 µs, D1 = 5 s, and DW = 6 µs. The data AQ and FID were set to 0.024 s and 3964 points, respectively. All MAS NMR spectra were recorded at a spinning rate of 11 kHz. Chemical shifts were referenced to 1 M $Al(NO_3)_3$ for Al and tetramethylsilane (TMS) for Si with a secondary reference sample of Al-ZSM-5. All liquid NMR spectra were recorded on a Bruker AVIII HD 400 with PW = 11.75 µs, pulse angle = 15°, D1 = 1 s, AQ = 0.1966 s at 104.261 MHz. The number of scans was 32 with a DW = 12 µs and FID = 1,6384 points. 5 cm long capillary with deuterium water (D_2O) was applied to avoid the contamination for the field-frequency locking [300]. 1 M $Al(NO_3)_3$ and TMS were used as the external chemical-shift reference for ^{29}Si and ^{27}Al, respectively.

6.2.3 IR study with isotopic labelling

To understand the role of water in the MWAC treatment, isotopic labelling using D_2O (to substitute DI as solvent) in the MWAC modification of Y zeolite using EA was performed, and the sample was denoted as MWEA-D. The resulting samples were investigated in situ by IR microspectroscopy based in the B22 beamline (i.e. Multimode InfraRed Imaging and Microspectroscopy, MIRIAM, beamline) at the Diamond Light Source, Harwell Science Campus (UK). The IR system is comprised of a Bruker Hyperion 3000 microscope with a 15× objective and liquid nitrogen cooled Mercury-Cadmium-Telluride (MCT) detector, coupled to a Bruker Vertex 80V Fourier Transform IR interferometer using radiation generated from a bending magnet source. During the measurement in transmission, spectra were collected (512 scans) in a range 500–4,000 cm^{-1} with 4 cm^{-1} resolution, and infrared spot size on

the sample was approximately 20 × 20 μm. Samples were diluted with potassium bromide (KBr) placed onto a zinc selenide (ZnSe) disk then placed in a Linkam FTIR 600 gas-tight sample cell equipped with ZnSe windows, a heating stage and gas inlet and outlets. During the *in situ* IR characterisation at atmospheric pressure, dry N_2 (using a zeolite filtre) were dosed volumetrically to the sample cell via mass flow controllers (at 100 cm^3 min^{-1}). The specific sampling position of a sample was visually selected using the microscope, then infrared spectra were measured under the conditions of drying under N_2 at room temperature (RT, ~25 °C) for 1 h, and heating from RT to 300 °C.

6.3 Results and discussion

6.3.1 MW-assisted dealumination

In situ IR study of isotopic labelled Y zeolite samples from the MWAC treatment was performed to understand the participation of water molecules in dealumination of zeolite Y via MWAC. In both MWEA and MWEA-D samples, IR bands related to hydroxyl groups at 1,635 cm^{-1} and 3,700–3,000 cm^{-1} (corresponding to the adsorbed water molecules and surface hydroxyl groups in Y zeolites) were identified. With an increase of temperature (from RT to 300 °C), the intensity of the IR bands diminished, as shown in Figure 6.1 (a) and (b). Bands at 785 and 1,006 cm^{-1} corresponds to internal tetrahedral symmetrical stretching and asymmetrical stretching vibrations, respectively. As compared to that of the parent Y, both shifted to higher wavenumber due to the reduced Al species in MWEA and MWEA-D (since Si presents relatively higher vibration frequency than Al) [280]. The band at 903 cm^{-1} corresponding to Si–OH vibration was measured in MWEA and MWEA-D at RT, suggesting the formation of silanol nests after MWAC dealumination of the parent Y. The other remarkable band at 1,402 cm^{-1} was showed up of the MWAC dealuminated Y samples, which indicated the considerable formation of silanol nests on the dealuminated zeolite framework. The Si–OH band disappeared gradually as the temperature increased to 300 °C, indicating the re-insertion of the Si species into the framework vacancies (cause by dealumination) to stabilise the structure [301]. Interestingly, the IR spectrum of MWEA-D did not the characteristic bands of DH group, which normally locates at ~ 2500 and 1200 cm^{-1}.

Cruz *et al.* [296] studied the post-treatment of clinoptilolite (HEU type, by aqueous HCl solution at RT) using hybrid density functional theory (DFT), and proposed the dealumination mechanism via the following four steps: (i) breakage of Al–O bonds by proton attack, (ii) adsorptive coordination of two water molecules with Al, (iii) formation of 5-coordinated Al with a double Si–OH–Al bridges and with three water molecules, and (iv) formation of octahedral Al atoms (EFAl) due to the rearrangement between Al and the neighbouring O atoms. The findings of the DFT study suggested the important role of water molecules in dealuminating framework Al under the conventional hydrothermal via acid leaching, which contributes to the formation of EFAl. However, the findings of the comparative IR study of the MWEA and MWEA-D samples showed the insignificant contribution of water molecules to the dealumination of Y zeolite under the MWAC condition, that is, IR bands related to DH group was not measured for the MWEA-D sample from the MWAC treatment with isotopic labelling (using deuterium water as the solvent).

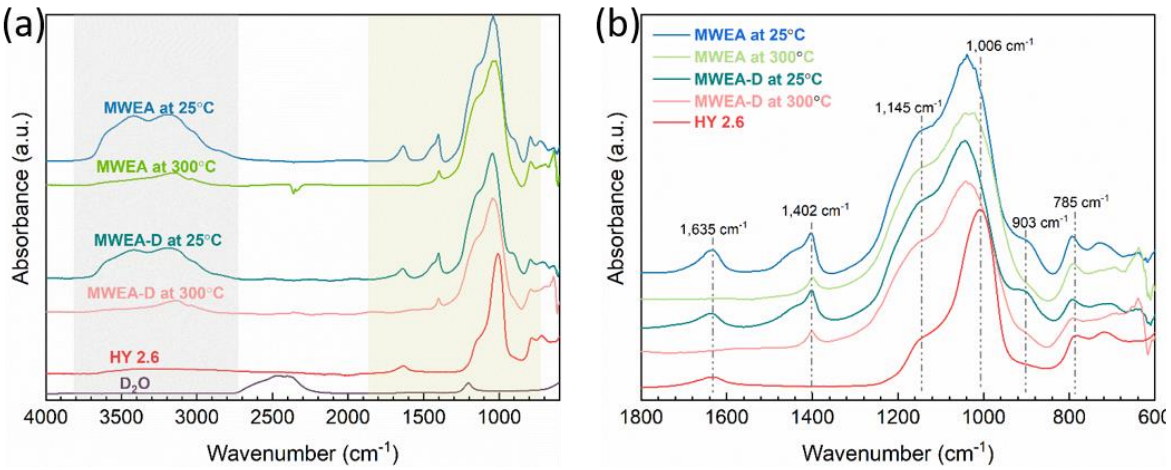

Figure 6.1 (a) FT-IR spectra of MWEA and MWEA-D Y zeolites at RT and 300 °C, H-form parent Y zeolite at RT and liquid D_2O; and (b) IR spectra in the region from 1800 to 600 cm^{-1} of (a).

Under the MW condition, $(EDTA)^{4-}$ was hypothesised to be important for Al extraction, i.e., via coordination with EFAl and stabilisation of the zeolite framework. As shown in Figure 6.2(a), liquid state ^{27}Al NMR of the MWEA filtrate showed only one broad peak at ~39 ppm, that is, $[Al(EDTA)]^-$, representing the complex of Al^{3+} with $(EDTA)^{4-}$, according to the previous research [302]. Conversely, chemical shifts associated with diprotonated complexes of $H_2[Al(EDTA)]^-$ and $[Al(H_2O)_6]^{3+}$ were not

detected. In the filtrate of MWHCl, ^{27}Al NMR spectra presented monosignal at ~0.0 ppm, which corresponds to the monomeric non-hydrolysed aquo-cation $Al(H_2O)_6^{3+}$, suggesting that, for the system with HCl under MW irradiation, formation of Al complexes is not possible [303]. The findings obtained so far show that the dealumination mechanism of the MWAC method is fundamentally different from that of the acid leaching (using mineral acid media) and calcination methods [296]. Specifically, in combination with the findings of IR studies, one can propose that $(EDTA)^-$, rather than water molecules and/or the OH group of water, complexed framework Al directly for effective Al extraction under the MWAC condition.

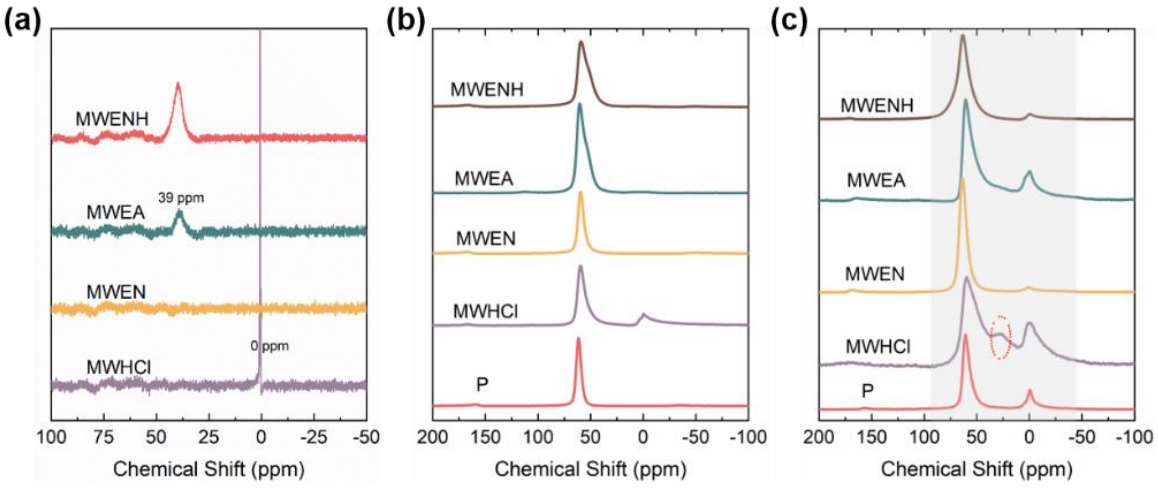

Figure 6.2 (a) liquid state ^{27}Al NMR of filtrates separated after the MW-assisted dealumination treatment of Y zeolite using different agents; ^{27}Al MAS SS-NMR spectra of (b) after MW-assisted dealumination modified Y zeolites before calcination and (c) after calcination.

Table 6.1 Yields of the zeolite samples from the MW-assisted dealumination treatment, Si and Al information on the resulting samples and the relevant filtrates from the treatment.

Samples	Yield (%)	SAR[a] (-)	SAR_F[b] (-)	Concentration of filtrate (g L^{-1})[c]	
				Al	Si
P	-	2.68	2.50	-	-
MWEA	88	4.25	4.40	4.14	0.52
MWEN	99	3.18	2.75	0.06	0.06
MWHCl	90	3.56	5.48	1.80	0.23
MWENH	86	3.43	3.63	3.82	0.47

[a]by XRF; [b]based on ^{29}Si MAS NMR; [c]by ICP-OES

After the MW-assisted dealumination treatment, SAR of the resulting samples increased as shown in Table 6.1, in comparison with SAR of the parent Y of 2.68. By analysing the filtrate from the process, it was found that the MW-assisted dealumination treatment with H_4EDTA and (Na_4EDTA + HCl) was very effective for extracting Al from the zeolite framework, that is, the Al concentration of the filtrate

from the process of obtaining MWEA and MWENH (i.e., 4.14 g L^{-1} and 3.82 g L^{-1}, respectively) was much higher than that from the process of obtaining MWEN and MWHCl. Comparatively, the Al concentration in the filtrate of MWEN was the lowest at 0.06 g L^{-1}. Also, by comparing the Si to framework Al ratios (SAR_F, based on Loewenstein rule [304]) of the parent Y (P) and MWEN, i.e., 2.50 vs. 2.75, $(EDTA)^{4-}$ alone (i.e., without excessive hydrogen ions) was not capable of complexing FAl under MW irradiation for dealumination (Na_4EDTA aqueous solution was measured with a pH value of about 11). As shown in Table 6.1, SAR and SAR_F values of MWHCl are 3.56 and 5.48, respectively, showing that, under the MW condition, HCl could destroy FAl, however, it was not effective for Al extraction. The latter was confirmed by measuring the Al concentration of the filtrate from the MW method of producing MWHCl, which is relatively low at 1.80 g L^{-1}. Accordingly, the findings above suggest that, in the MW-assisted dealumination treatment, both the chelating agent and acidic environment are crucial for the effective extraction of framework Al species, i.e., dealumination by the MWAC method.

After dealumination, as shown in Figure 6.2(b) and (c), ^{27}Al MAS NMR spectra of the MW-assisted dealumination samples show the tetrahedral Al (Al^{IV}) signal centred at around 60 ppm. Additionally, the octahedral Al (Al^{VI}) signal (at ~0 ppm) was measured as well for MWHCl, confirming the creation of EFAl in in the defective framework of MWHCl from the MW treatment with HCl solution, being in line with the findings above (i.e., the Al concentration of the filtrates, Figure 6.1(a) and Table 6.1).

By carefully examining the ^{27}Al MAS NMR signals at ~60 ppm of MWEA, MWHCl and MWENH, they are rather asymmetric as compared with that of the parent Y, as well as being broadened, suggesting the presence of distorted Al^{IV} species in their frameworks. Previous work on the modified FAU Y zeolites (which was produced by steaming [305, 306] and calcination [294, 307]) and USY zeolites [308-313] (which have EFAl species in their structures) attributed the resonance broadening to the presence of tetrahedral EFAl species (i.e. aluminium-oxide) in the zeolitic frameworks. In this work, as shown in Table 6.1, values of SAR_F and SAR of the three samples are rather comparable, indicating the possible absence of EFAl species in their frameworks. Accordingly, the asymmetrical resonance of Al^{IV} in MWEA, MWHCl and MWENH was attributed to the distorted Al species, being in line with the

previous findings [257, 314, 315]. As compared Figure 6.2b with Figure 6.2c, the ^{27}Al MAS NMR signals at ~60 ppm are presented in all calcined Y samples. Ravi *et al.* [316] concluded that these 6-coordinated aluminium species belong to framework-associated aluminium, which refers to species that are not entirely dislodged from the zeolite framework, and on being charge balanced Al chemical shift by cations such as sodium, potassium and ammonium, this aluminium species assumes converting into a tetrahedral coordination (around 60 ppm) in the hydrated form of the zeolite. However, 2-dimensional double/multi-quantum MAS NMR study is necessary to investigate this aspect further since one-dimensional single pulse ^{27}Al MAS NMR is unable to provide unambiguous Al coordination states.

Results of ^{29}Si MAS NMR analysis of the samples are presented in Figure 6.3 and Table 6.2. In the parent Y (P), all Si(*n*Al) structure units were identified without amorphous phases. After the MW-assisted dealumination treatment with H_4EDTA, the Si(4Al) and Si(3Al) units were reduced at 0 and 1.1%, respectively, in the resulting MWEA. The decrease of the Si(4Al) and Si(3Al) structure units, as well as the increase of amorphous phases in Y zeolite confirm the removal of framework aluminium due to the treatment. Comparatively, after the treatment with Na_4EDTA, the coordination environment in the resulting MWEN did not change significantly in comparison with that of the parent Y (P), confirming the relevant finding above based on the solid-/liquid-state NMR analysis, i.e., the important role played by the excessive hydrogen ions to attack the Al–O–Si bond in zeolite framework during the MW-assisted dealumination treatment. Interestingly, during the post-treatment under MW irradiation, when HCl was used together with Na_4EDTA (to provide the hydrogen ions), the obtained MWENH showed compositions of Si(*n*Al) structure units similar to that of MWEA except higher percentage of Si(3Al) unit (~7.3%), which again confirmed the finding above. Conversely, if the mineral acid (i.e., HCl) was used in the MW-assisted dealumination treatment, it could damage the coordination environment more severely than H_4EDTA. According to the comparative ^{29}Si MAS NMR analysis of P and MWHCl, as shown in Table 6.2, (i) Si(3Al) units were eliminated entirely, and Si(2Al) units decreased by ~50% and (ii) Si(0Al) units and amorphous Si phases increased noticeably. The findings suggest that, under the MW condition, HCl, as a mineral acid, has a strong ability to hydrolyse Al–O–Si bonds in zeolite framework. Additionally, based on the comparative study of the Si(*n*Al) structure units

of different samples from the MW-assisted treatment and the parent Y (P), the Al-rich environment of P was beneficial to Al removal.

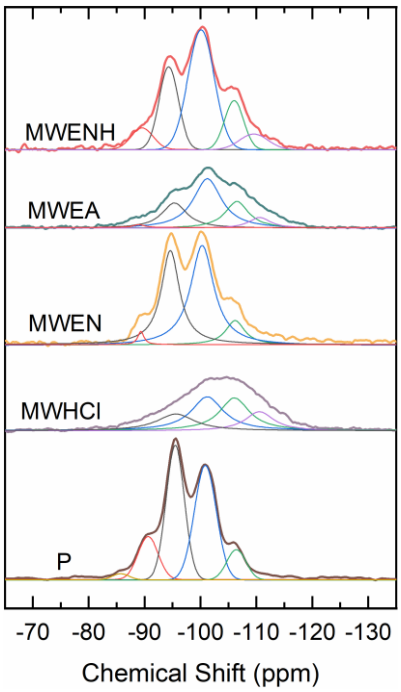

Figure 6.3 ^{29}Si MAS NMR spectra of the parent and modified Y zeolites under investigation.

Table 6.2 Information on Si(nAl) structure units of the zeolite samples determined by ^{29}Si MAS NMR.

Sample	Si(4Al) at –85 ppm	Si(3Al) at –90 ppm	Si(2Al) at –95 ppm	Si(1Al) at –101 ppm	Si(0Al) at –106 ppm	Amorphous phases at –111 ppm
Samples	Integrated Area Percentage [%]					
P	1.6	13.2	37.7	38.5	8.9	-
MWEA	-	1.1	21.5	48.0	21.5	7.9
MWEN	-	10.3	34.7	44.9	10.1	-
MWHCl	-	-	19.8	33.4	29.8	17.0
MWENH	-	7.3	24.1	47.7	14.1	7.1

After the MW-assisted post treatment with H_4EDTA and HCl as the agent, significant loss of crystallinity in the resulting MWEA and MWHCl was measured by XRD, as shown in Figure 6.4 and Table 6.3. Comparative XRD patterns (Figure 6.4) show that the intensity of the characteristic peaks of FAU Y zeolite in MWEA and MWHCl was significantly lower than that of the parent Y. For example, the RC value of MWHCl was calculated only at about 4%. Additionally, amorphisation of MWEA and MWHCl was also obvious by XRD after the treatment, confirming the damage of the crystalline

framework of Y by H_4EDTA and HCl under MW irradiation. Comparatively, Na_4EDTA was not very effective for dealumination of Y under the MW condition, and the crystallinity of MWEN was preserved rather well. By combining hydrogen ions with Na_4EDTA in the system (i.e., Na_4EDTA + HCl), dealumination process was improved, but being less effective than the system with H_4EDTA. XRD analysis show that MWENH has a higher RC value of *ca.* 69%. In general, findings by XRD analysis suggest various capacity of Al extraction of the MW system with different agents, being in line with the relevant results (of SAR, SAR_F and Al concentration of the filtrate) by the Al NMR analysis (Table 6.1).

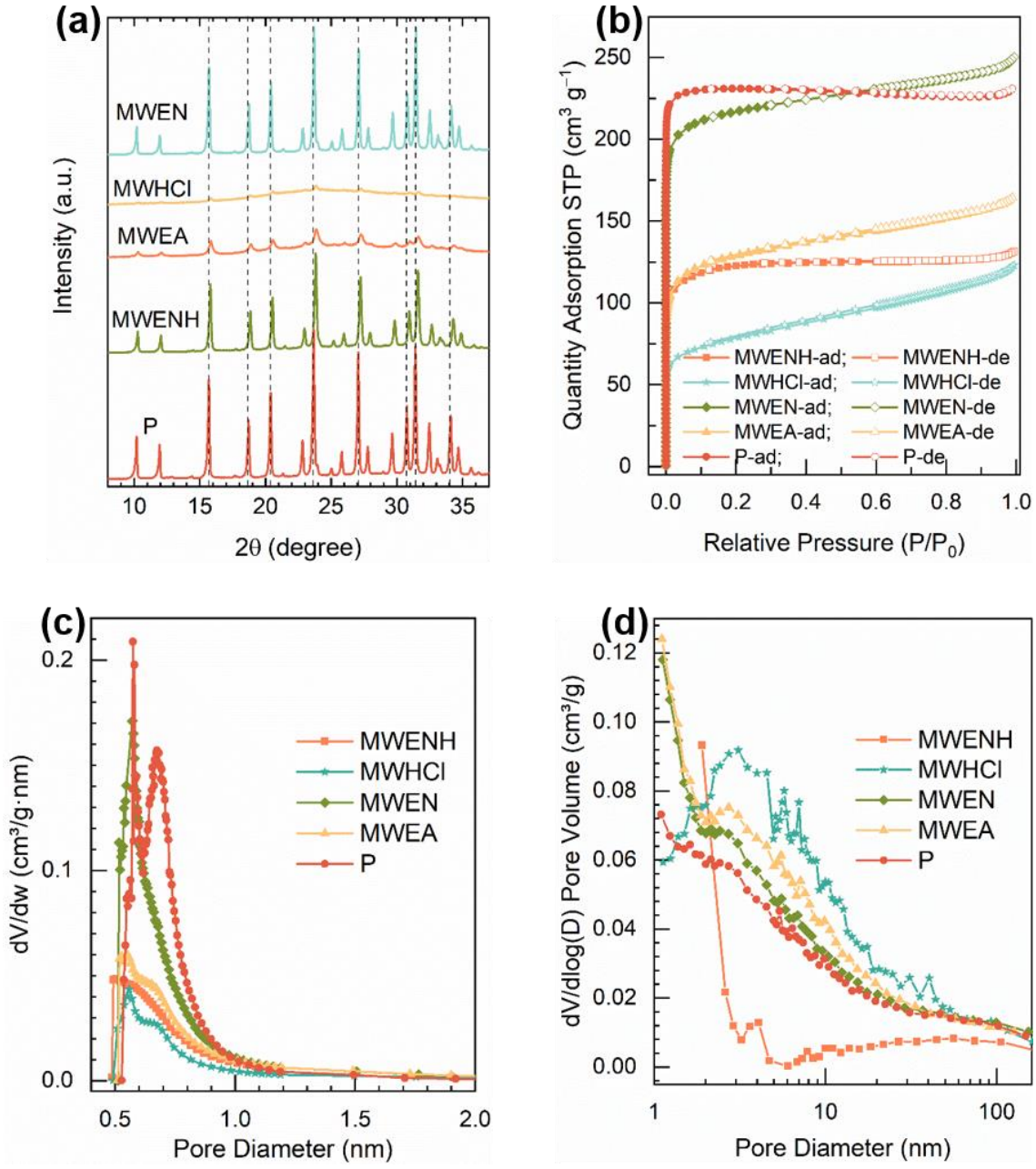

Figure 6.4 (a) XRD patterns; (b) N_2 adsorption and desorption isotherms; (c) H-K micropore PSDs; and (d) BJH mesopore PSDs of the MW-assisted dealuminated Y and parent Y zeolites.

Regarding mesoporosity formation, previous studies have shown that H_4EDTA was more capable than mineral acids under the hydrothermal conditions due to its ability to remove FAl selectively [121, 317]. Consequently, formation of mesoporosity in the framework can be attributed to the formation among silanol nests and associated vacancies in the zeolitic framework [74, 296, 318, 319]. N_2 physisorption isotherms of the materials under investigation are shown in Figure 6.4(b). In comparison with the parent Y (P), the resulting MWEA and MWENH present the type-I isotherm but with the relatively low N_2 quantity adsorbed at low relative pressure ($p/p^0 < 0.01$, i.e., the monolayer adsorption range), decreased

specific surface areas (i.e., BET surface areas, S_{BET}, and micropore surface areas, S_{micro}) and reduced micropore volumes (V_{micro}), as listed in Table 6.3. Figure 6.4(c) shows the micropore size distribution (PSD) of the zeolite samples under investigation, which also confirms that the presence of $(EDTA)^{4-}$ and hydrogen ions was beneficial to interact with the Y framework under the MW condition. Relevant mesoporous features of MWEA and MWENH of the mesopore volume (V_{meso}) and external surface areas ($S_{external}$) were improved, but not significant after the MW treatment, as shown in Table 6.3. Under the condition used, the sole use of Na_4EDTA without the likely presence of hydrogen ions, the post treatment was not effective for creating mesopores in Y zeolite, as evidenced by the results of N_2 physisorption analysis of MWEN, which are comparable to that of P. Comparatively, the use of HCl under the MW condition could damage the microporous framework significantly, as confirmed by the considerable reduction of S_{BET} and S_{micro} to 287 and 164 $m^2\ g^{-1}$, respectively. Although previous research claimed that FAl elimination *via* mineral acid dealumination can enlarge the defects in zeolite structure (as reviewed in Chapter 2), relevant findings by N_2 physisorption in Figure 6.4(b–d) show conflicting results. Therefore, it can be proposed that in MW-assisted dealumination treatment, HCl contributes hydrogen ions to hydrolyse FAl and form EFAl remained in the structure. Mesopore PSD of the samples is shown in Figure 6.4(d). All post-treated samples showed the development of mesopores, but being not significant. This was also confirmed by TEM analysis of the samples, as shown in Figure 6.5, showing no obvious presence of mesopores.

Table 6.3 Porous properties and RC values of the parent Y and MW-assisted dealuminated Y zeolites.

Samples	S_{BET} [$m^2\ g^{-1}$]	S_{micro} [$m^2\ g^{-1}$]	$S_{external}$ [$m^2\ g^{-1}$]	V_{total} [$cm^3\ g^{-1}$]	V_{micro} [$cm^3\ g^{-1}$]	V_{meso} [$cm^3\ g^{-1}$]	RC [%]
P	867	858	9	0.36	0.35	0.01	100
MWEA	484	383	101	0.25	0.16	0.09	20
MWEN	831	738	69	0.39	0.30	0.09	87
MWHCl	287	164	113	0.19	0.07	0.12	4
MWENH	472	403	93	0.20	0.16	0.04	69

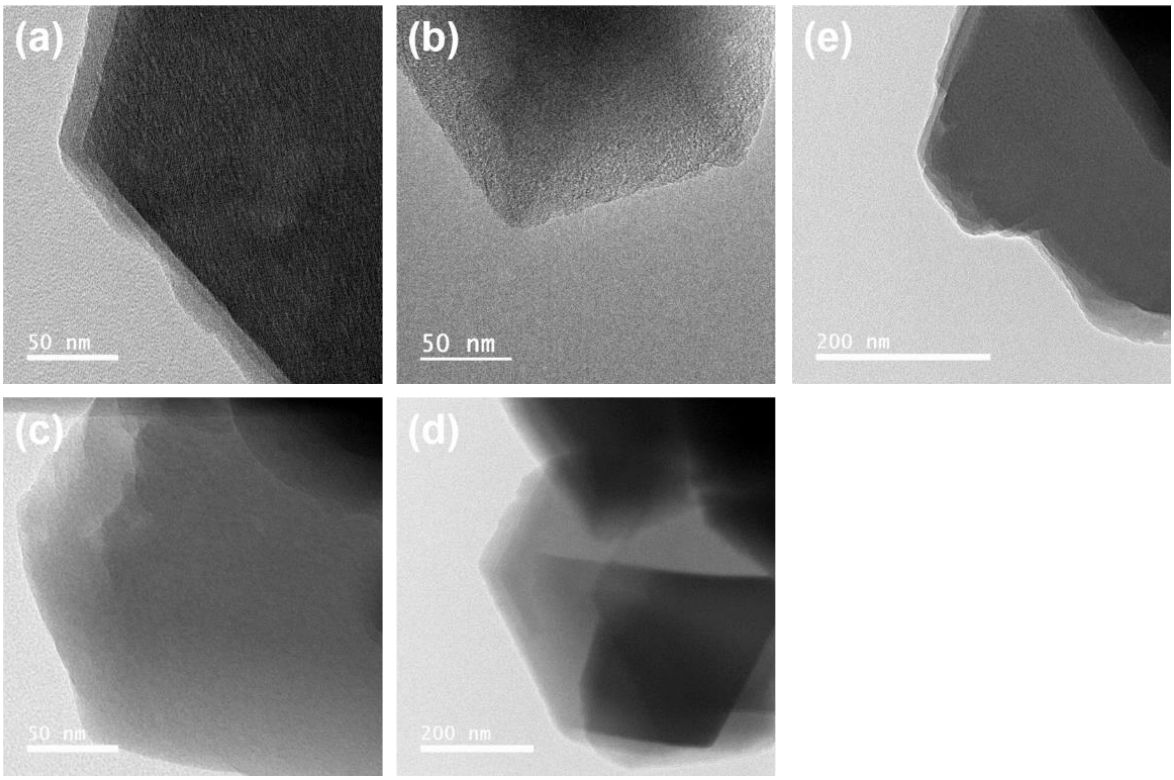

Figure 6.5 TEM micrographs of (a) MWENH, (b) MWEA, (c) MWHCl, (d) MWEN and (e) P.

Comparative study of the samples from the MW-assisted treatment of zeolite Y using different agents suggested the importance of co-existence of hydrogen ions and chelating agent (i.e., $(EDTA)^{4-}$) to enable MWAC dealumination via the fast hydrolysis of Al–O bonds by hydrogen ions and complexation of Al species by chelating agent to form soluble Al complex under MW irradiation. The findings so far suggest that the MWAC dealumination proceeded with distinct features: (i) the remained hydroxyl groups in MWEA and MWAE-D were not the result of water induced hydrolysis [73] but from H_4EDTA-zeolite interaction, (ii) the solution Al complex of $[Al(EDTA)]^-$ was the only Al product in the filtrate from the process of obtaining MWEA and MWENH, and (iii) after MWAC, EFAl species are not detected in the rustling framework, being different from the case with HCl.

6.3.2 Subsequent alkaline treatment

After the MW-assisted treatment, all resulting samples underwent the same alkaline treatment. In this work, ICP-OES analysis (Table 6.4) of the resulting filtrates from the sequential alkaline treatment showed noticeable dissolution of Si species from the system containing MWEA, MWHCl and MWENH. In detail, Al and Si species leaching from the sequential alkaline treatment of MWEA and MWENH are comparable (as shown in Table 6.4), and that from the treatment of MWHCl are relatively low at 0.03 g L^{-1} for Al and 2.38 g L^{-1} for Si, respectively. Regarding MWEN, Al and Si species in its filtrate after the sequential alkaline treatment were comparatively insignificant at 0.10 and 0.42 g L^{-1}, respectively. This finding again confirmed that the MW-assisted treatment with $(EDTA)^{4-}$ only was not effective to extract FAl from zeolite Y, and the resulting MWEN has a low SAR at 3.18, being resistant to alkaline desilication. Al species in the filtrate from the sequential alkaline treatment of MWEA, MWEN and MWENH zeolites are more concentrated (at about 0.14 g L^{-1}) than that in the filtrate from the treatment of MWHCl (~0.03 g L^{-1}), confirming that the MWAC treatment produce soluble Al species rather than EFAl, being in line with the results discussed above (Figure 6.2(a) and Table 6.1).

Table 6.4 ICP-OES analysis of Al and Si species in the filtrate from the sequential alkaline treatment of dealuminated Y zeolites under investigation.

Samples	Al (g L^{-1})	Si (g L^{-1})
MWEA+HT	0.18	4.25
MWEN+HT	0.10	0.42
MWHCl+HT	0.03	2.38
MWENH+HT	0.14	4.57

After the alkaline treatment, ^{27}Al MAS SS NMR analysis of MW*a*+HT samples was performed, showing the monosignal at ~60 ppm of tetrahedral Al chemical shift (Figure 6.6). Alkaline treatment of dealuminated Y was able to heal the defective framework (via EFAl realumination) and recover crystallinity partially, as reported previously [247, 320-322]. Based on ^{27}Al MAS SS-NMR analysis of MWHCl (Figure 6.2(b)) and MWHCl+HT (Figure 6.6(a)), and the quantitative analysis of Al and Si species in the filtrate from the alkaline treatment of MWHCl, one can propose the occurrence of EFAl realumination and Si removal during the alkaline treatment of MWHCl.

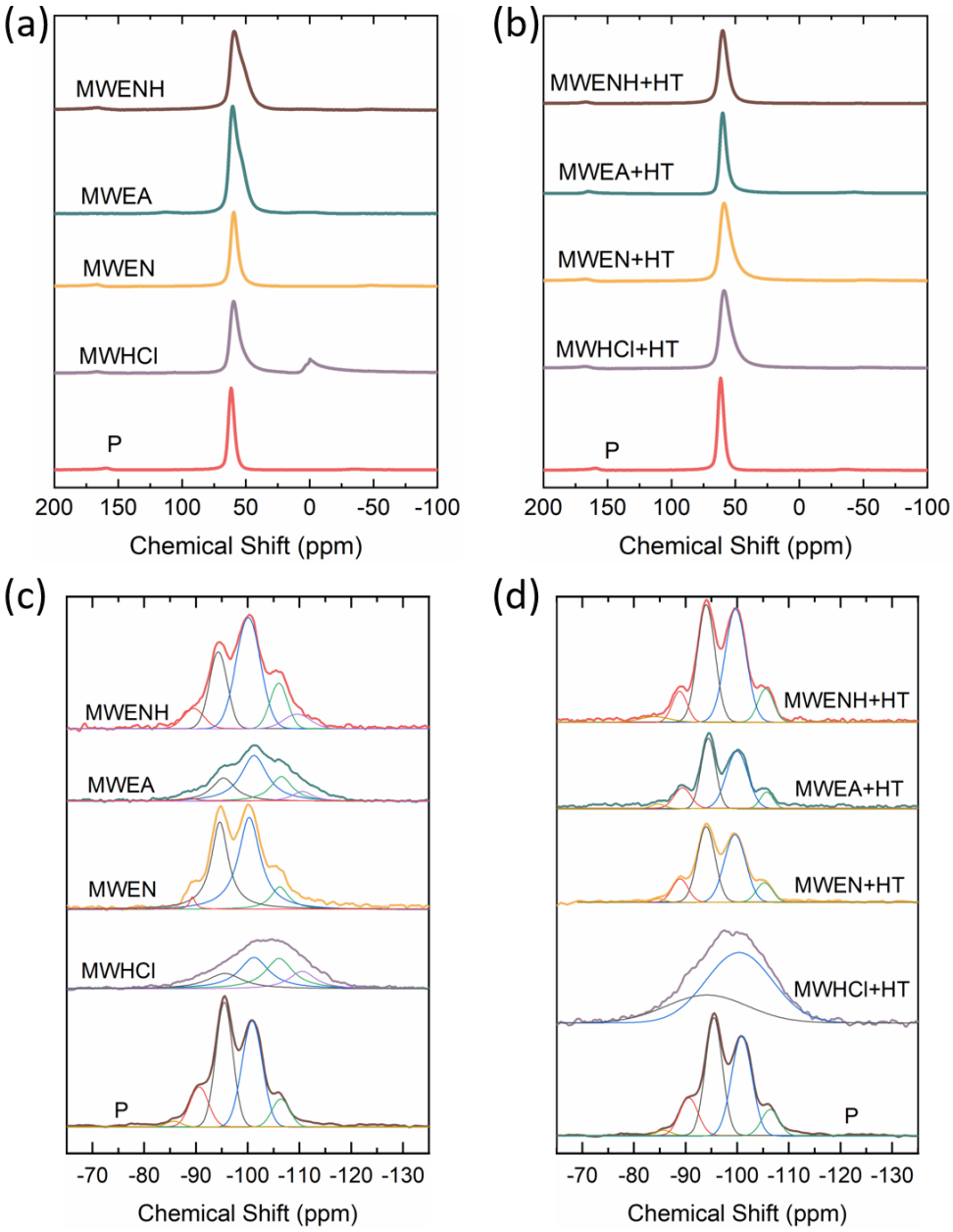

Figure 6.6 ^{27}Al MAS SS-NMR of (a) MW*a* samples and (b) MW*a*+HT samples from the alkaline treatment of MW*a* samples; ^{29}Si MAS SS-NMR spectra of (c) MW*a* samples and (d) MW*a*+HT samples from the alkaline treatment of MW*a* samples.

^{29}Si MAS NMR spectra of MW*a*+HT samples are shown in Figure 6.6(b). MWEA+HT, MWEN+HT and MWENH+HT zeolites show analogous Si(*n*Al) structure unit distributions to that of the parent Y zeolite. Specifically, after the sequential treatment using Na_4EDTA, coordination change of Si atoms in MWEN+HT and total intensity variation of its Si(*n*Al) signals were insignificant as compared to the parent zeolite, as shown in Table 6.5. In comparison with MWEA and MWENH, the proportion of

Si(*n*Al) sites, where n $\geqslant$ 2, was increased in MWEA+HT and MWENH+HT after the alkaline treatment, especially for the samples treated with H_4EDTA. Specifically, proportions of Si(4Al), Si(3Al) and Si(2Al) sites in MWEA are 0%, 1.1% and 21.5%, respectively, whereas in MWEA+HT, they are 2.9%, 12.0% and 35.7%, respectively. The findings suggest that the zeolite framework could be recovered to a large extent by alkaline treatment of the samples from the MWAC treatment. For MWHCl+HT, as shown in Figure 6.6(b), Si(4Al) and Si(3Al) signals could not be deconvoluted, suggesting the severe damage of the Al–O–Si bond by HCl under then MW condition, which could not be recovered by the sequential alkaline treatment. Additionally, by comparing the data related to the Si(0Al) sites and amorphous Si phase in all samples under study (as shown in Tables 6.2 and 6.5), the total disappearance of amorphous Si phase and the reduction in the Si(0Al) site proportion show the selectively desilication of Si species without the protection of FAl [323], which may benefit the preferential mesopore formation at silanol nests.

Table 6.5 Information on Si(*n*Al) structure units of the sequential desilicated zeolite samples determined by ^{29}Si MAS NMR.

	Si(4Al) −85 ppm	Si(3Al) −90 ppm	Si(2Al) −95 ppm	Si(1Al) −101 ppm	Si(0Al) −106 ppm	Amorphous −111 ppm
Samples	Integrated Area Percentage [%]					
P	1.6	13.2	37.7	38.5	8.9	-
MWEA+HT	2.9	12.0	35.7	43.0	7.3	-
MWEN+HT	1.3	10.6	37.8	41.4	8.9	-
MWHCl+HT	-	-	32.7	63.3	-	-
MWENH+HT	2.9	8.3	37.0	42.5	9.2	-

In addition to the comparative analysis of the chemical structures of MW*a* and MW*a*+HT samples, porous properties of MW*a*+HT samples were probed by N_2 physisorption to show the effect of the sequential treatment on mesopore formation in reference with the parent Y zeolite, as presented in Figure 6.7(b–d) and Table 6.6. MWEN+HT remained as microporous, which again conforms the ineffectiveness of using Na_4EDTA for dealumination under the MW condition and the subsequent hydrothermal alkaline treatment, being consistent with the discussion above, i.e., Na_4EDTA cannot remove FAl from Y zeolite framework without H^+ ions and desilication is not promoted with low SAR zeolites. After the sequential alkaline treatment, MWEA+HT and MWENH+HT displayed the increased slopes at middle-to-high relative pressure (i.e., 0.1 $<p/p^0<$ 1.0) and H4 hysteresis loops

(Figure 6.7(b)), indicating the presence of mesopores and multilayer adsorption. Extracted data of $S_{external}$ and V_{meso} for MWENH+HT and MWEA+HT (Table 6.6) confirm the presence of mesoporosity in the two materials, whereas their lower amount of quantity adsorbed at low relative pressure and smaller S_{micro} values, as compared to that of P, suggest the loss of microporosity after the sequential treatment. Mesopore PSD of the MW*a*+HT samples is exhibited in Figure 6.7(d), showing that MWENH+HT and MWEA+HT have the distribution centred at around 5 nm and 8 nm, respectively.

MWHCl+HT presented the H2 type hysteresis loop with S_{BET} = ~340 $m^2 g^{-1}$ and total pore volume (V_{total}) = ~0.19 $m^3 g^{-1}$, respectively, suggesting a significantly damaged framework. Additionally, the specific external surface area and mesopore volume of MWHCl+HT are significantly low at 37 $m^2 g^{-1}$ and 0.03 $m^3 g^{-1}$, respectively, suggesting that the sequential treatment of MW-assisted dealumination with HCl and alkaline treatment was not as effective as that with MWAC in creating mesoporosity in Y zeolite. Invisible mesoporosity of MWHCl+HT sample could be assigned to EFAl realumination inhibits the removal of silanol groups which is related to mesoporous formation [16].

Compared to the MW*a* samples (Table 6.3), the microporous crystalline phase in the MW*a*+HT samples was recovered from the corresponding MW*a* samples after the alkaline treatment. Taking MWEA as the example, after the alkaline treatment, S_{micro} of MWEA+HT was recovered to 675 $m^2 g^{-1}$ (for MWEA, S_{micro} =383 $m^2 g^{-1}$) and RC was ~88%, being much higher than that of MWEA (about 20%). XRD patterns and RC values of the MW*a*+HT samples are shown in Figure 6.7(a) and Table 6.6, respectively, showing that crystallinity of all samples was recovered to different degrees. In detail, MWEA+HT and MWENH+HT have RC values of about 88% and 96%, respectively, whereas MWHCl+HT still has the lowest RC value of ~42% which was resulted from the severe framework damage during the MW assisted treatment using HCl. The findings so far suggest that, regardless the non-framework Al species created during the MW-assisted treatment, realumination of dealuminated Y zeolites occurred during the sequential alkaline treatment [324, 325], which could partially recover the microporosity and crystallinity of the dealuminated samples, but the method using the combination of chelating agent and hydrogen ions is more advantageous than that using mineral acids regarding the two aspects.

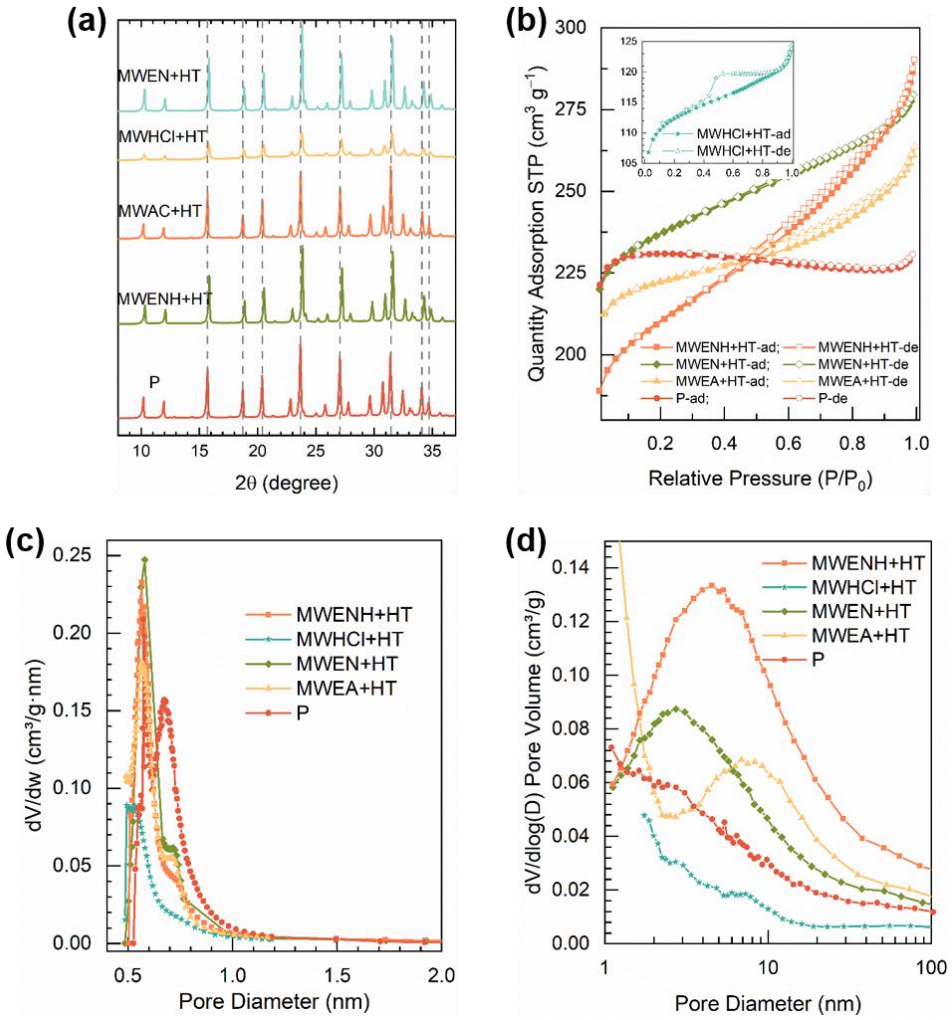

Figure 6.7 (a) XRD patterns; (b) N_2 adsorption and desorption isotherms; (c) H-K micropore PSDs; and (d) BJH mesopore PSDs of the of MW*a*+HT samples from the alkaline treatment of MW*a* samples and parent Y zeolite.

Table 6.6 Porous properies and RC values of the parent and MW*a*+HT Y zeolites after the sequential treatment.

Samples	S_{BET} [$m^2\ g^{-1}$]	S_{micro} [$m^2\ g^{-1}$]	$S_{external}$ [$m^2\ g^{-1}$]	V_{total} [$cm^3\ g^{-1}$]	V_{micro} [$cm^3\ g^{-1}$]	V_{meso} [$cm^3\ g^{-1}$]	RC [%]
P	867	858	9	0.36	0.35	0.01	100
MWEA+HT	747	675	72	0.41	0.31	0.10	88
MWEN+HT	936	822	114	0.43	0.32	0.11	99
MWHCl+HT	340	303	37	0.19	0.16	0.03	42
MWENH+HT	807	649	158	0.45	0.27	0.18	96

The morphology of the MW*a*+HT zeolites was characterised by HRTEM as displayed in Figure 6.8. Surface defects and well-developed mesoporous features were observed clearly for MWEA+HT and MWENH, as shown in Figure 6.8(a–d). As mesopore PSDs exhibited in Figure 6.7(d), MWENH+HT

had a more centred distribution around 5 nm and MWEA+HT consisted of a relatively larger mesopore diameter centred on ~8 nm, which were corresponding to their morphologies (Figure 6.8(a–d)). The micrograph of MWHCl+HT in Figure 6.8 (e) performed small defects on the surface, which was caused by sequential treatment corrosion. All the morphology analysis was in line with above porous properties investigations. As anticipated, MWEN+HT (Figure 6.8(f)) presented the typical crystal morphology, being similar to that of the microporous parent Y zeolite (Figure 6.5(e)).

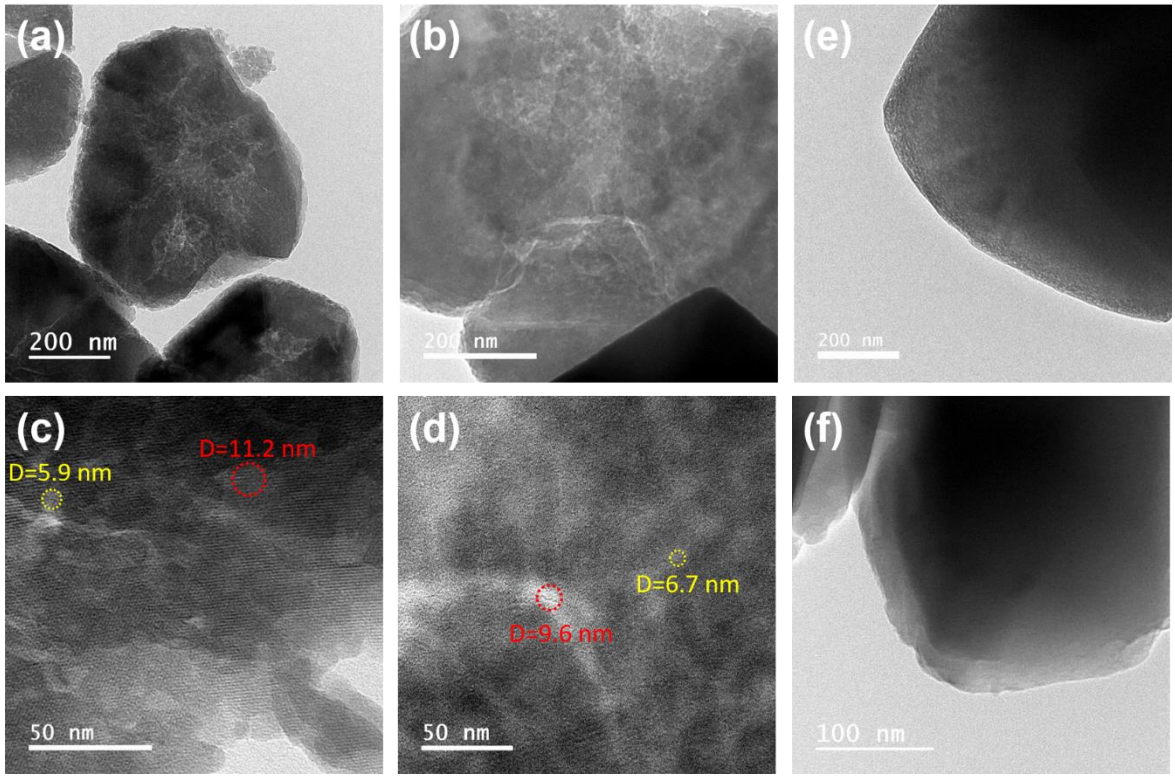

Figure 6.8 TEM micrographs of (a) and (c) MWEA+HT, (b) and (d) MWENH+HT, (e) MWHCl+HT and (f) MWEN+HT.

6.4 Conclusions

This chapter reports the systematic investigation of the microwave (MW)-assisted dealumination and the subsequent alkaline treatment on zeolite Y to develop an understanding of mechanisms of dealumination and mesopore formation under the MW condition with different agents. The degree of dealumination and mesopore formation depends on the participation of both chelating agents (in this case, $EDTA^{4-}$) and hydrogen ions (H^{+}). The findings showed that the mechanism of dealumination (of

zeolite Y) with H_4EDTA and HCl under the microwave condition is distinct. In detail, the process with H_4EDTA (i.e. the MWAC method) showed a strong ability in direct framework Al removal, which results in the creation of framework defects (i.e., less than 2nm) along with silanol nests. Conversely, HCl under MW irradiation can destroy the framework Al–O bond of Y zeolite significantly, leading to the formation of EFAl in the defective zeolite framework and structure collapse. Moreover, D_2O isotopic labelling proved that, in the MWAC system, H^+ contributed to hydrolysis of framework Al–O bonds and silanol group formation rather than water molecules.

Sequential alkaline desilication was essential after the dealumination treatments to recover the zeolitic framework (to some extent) and render mesopores of the treated zeolites. It was found that the removed amount of Si of MW-assisted dealuminated samples was in line with Al extraction in the dealumination step in order to remain a stable crystal structure. In general, this study shows that, under the MW condition, the use of chelating agent in presence of hydrogen ions was highly effective to achieve the mild dealumination of zeolite, and the subsequent alkaline treatment helped to recover the crystalline framework and create mesoporosity, being more advantageous than the system using the mineral acid.

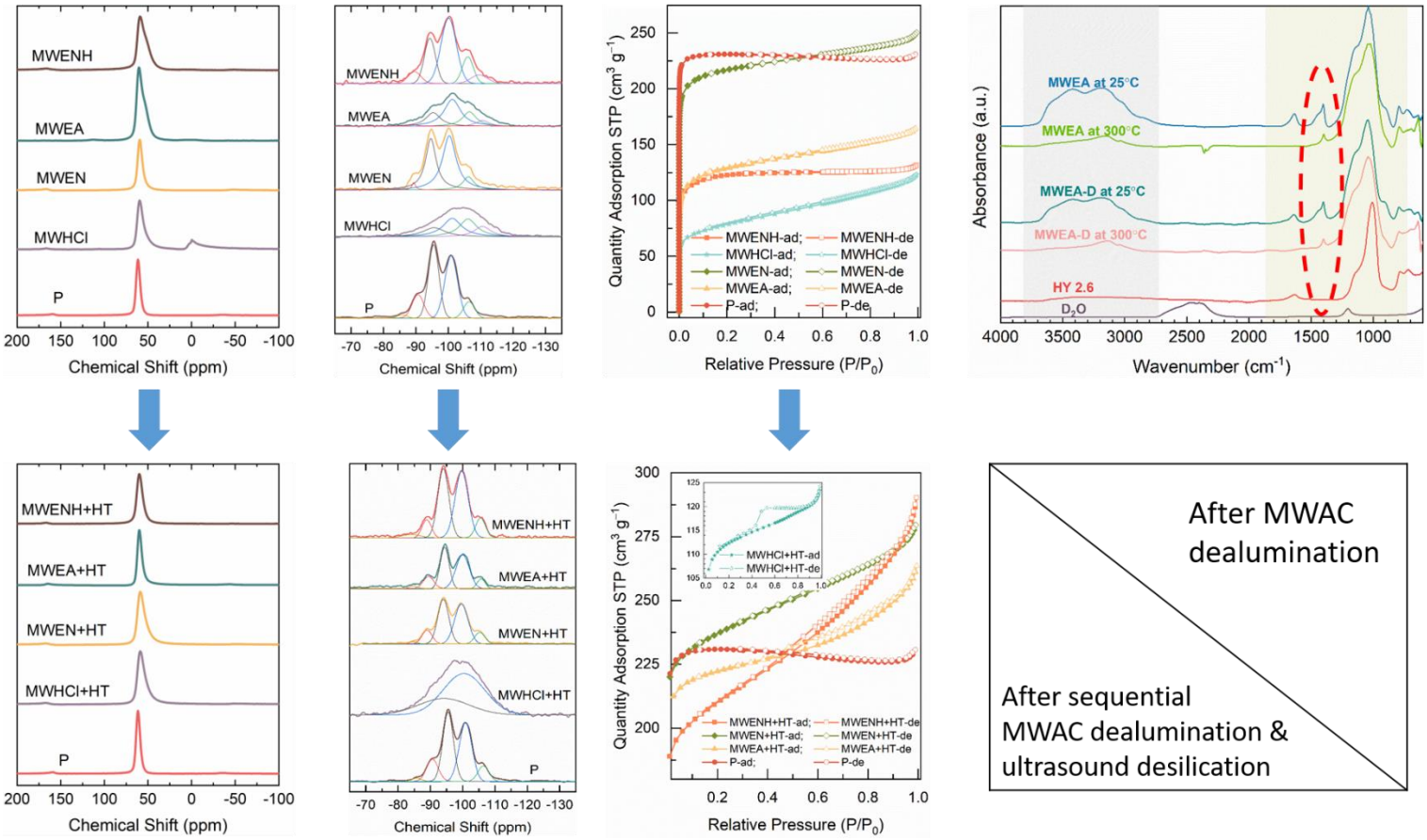

Scheme 6.1 Summary mechanism scheme of sequential MWAC dealumination and ultrasound desilication.

Chapter 7 Conclusions and future work

7.1 Conclusions

Zeolites with unique porous and acidity properties are important catalysts for both the conventional and emerging applications in sustainable chemistry. As compared with the hierarchical zeolitic framework, intrinsic micropores of pristine zeolites induce severe molecular diffusion limitations, and hence leading to the relevant accessibility and diffusional issues, such as coke formation and undesired benzene formation during disproportionation of toluene into xylenes in ZSM-5 zeolites. In order to overcome these limitations, post-synthetic modifications have been proposed and developed extensively over the last decades to introduce secondary porosity (i.e. mesoporosity) in zeolite framework to improve the mass transfer. Acid and alkaline treatments under hydrothermal conditions are relatively practical ways to prepare hierarchical zeolites, tuning acidity and stability among the researched post-synthetic modification treatments. However, due to the relatively long treatment time and the associated high energy consumption during the conventional post-synthetic treatment processes, further effort is required to improve the sustainability of such treatments. In this PhD project, the possibility of introducing hierarchical porous structures into zeolitic frameworks by post-synthetic treatments with novel energy sources was proposed and investigated. The work was carried out in order to (i) gain insight into the formation of secondary mesopores by intensified post-synthetic modifications under microwave and ultrasound irradiation, and (ii) emphasise the importance of hierarchical zeolite porous structures to improve the catalytic activity in heterogeneous reactions comprising bulky molecules.

Before fabricating hierarchical zeolites, it is vital to elucidate the importance of secondary mesoporosity in catalytic reactions with bulky molecular size. Therefore, three commercial H-form Y zeolites with different SARs, HY-2.6, HY-15 and HY-30, were comprehensively analysed in the assessment of zeolite catalyst performance for liquid-phase reactions of Fischer esterification and aldol condensation. Compared to microporous HY-2.6, N_2 physisorption and Hg porosimetry indicated that both HY-15 and HY-30 presented large mesopores with pore sizes of 5–30 nm and half of these mesopores are open to the outside at the crystal surface. The presence of mesoporosity in HY-15 and HY-30 enhanced the accessibility of the reactants (propionic, hexanoic and lauric acid, and benzaldehyde have the kinetic

diameter of about 0.52, 0.60 and 0.72 nm, and 0.58, respectively) to active sites, and facilitated the creation of bulky products (i.e., jasminaldehyde possessing kinetic diameter of about 0.74 nm), although these two zeolites only had around 26% and 4% out of the HY-2.6 total acidity. The results demonstrated mesoporosity in Y zeolites played a main role in catalytic reactions with bulky molecules.

Thereafter, sequential post-synthetic modification was carried out for introducing mesopores into the Al-rich Y zeolite. Both citric acid and H_4EDTA were selected as chelating agents in the first conventional dealumination step. Interestingly, when the dealumination duration was not long enough (i.e., 0.1 mol·L^{-1} H_4EDTA was used for < 3 h) or the concentration of chelating agents were not high enough (i.e., citric acid < 0.14 mol L^{-1}), sequential post-treatment was not very effective for fabricating mesoporosity. The first step of chemical dealumination treatment was crucial to enable the effective creation of mesopores in the parent Y zeolite (with a silicon-to-aluminium ratio, Si/Al = 2.6) regardless of the subsequent alkaline desilication treatment (i.e., ultrasonic or hydrothermal). Therefore, appropriate selection of the condition of the chemical dealumination treatment based on the property of parent zeolites, such as SAR and crystallinity, is important for making mesoporous zeolites effectively. More importantly, ultrasound irradiation was found more efficient for desilication of dealuminated Y zeolites as compared to conventional alkaline treatment (i.e., 5 min ultrasound irradiation vs. 30 min hydrothermal condition), and not only physical properties of modified Y zeolites were analogous, but performed similar improvement of catalytic activity and stability in *n*-octane cracking.

As concluded above, in the sequential post-synthetic treatment, dealumination not only governs the formation of hierarchical porous structure in Al-rich Y zeolites, but is time wasting and highly energy consuming, it is necessary to optimise the dealumination procedure with MW assistance to achieve the sustainability. The MW irradiation with chelating agents successfully reduced the dealumination time to in total 3 min and simultaneously introduced significant mesopores into Y zeolites (e.g. V_{meso} of 0.32 and 0.22 cm^3 g^{-1} for 0.16 M both of citric acid and DTPA modified Y zeolites in the developed sequential post-synthetic treatments), resulting in better catalytic activity performance. Moreover, mineral acid such as HCl was not effective in sequential post-modification only resulting in crystallinity loss. Conversely, organic acids performed superiorly in preparing hierarchical Y zeolites, and the degree

of dealumination is highly related to the number coordination centres in the acidic chelating agent. Chelating agent containing higher number of coordination centres performed higher effectiveness of the introduction of mesopores in zeolites regarding the sequential post-synthetic treatment.

Chapter 6 was carried out in order to understand the mechanism of mesopores development in Y zeolites by MW-assisted chelation/strong mineral acid dealumination (i.e., H_4EDTA and HCl) and subsequent conventional hydrothermal desilication. Under the MW condition with the chelating agents, direct complexation of Al species was enabled to the soluble Al complex rather than octahedral EFAl, being very different from the mechanism of the system with HCl. MW-assisted chelating dealumination showed an intensive ability in Al removal, whereas HCl had strong capability hydrolysis Y zeolite framework Al–O bond resulting in EFAl formation and zeolite structure collapse. After MW-assisted dealumination, structural defects with the characteristic dimension of < 2nm were generated along with silanol nests. However, these silanol species blocked most of microporosity and no obvious mesopore was formed. Therefore, sequential alkaline desilication was demanded to wash out the Si species for the development of mesopores. The sequential MW-assisted chelating dealumination leaded to mesopore formation in Y zeolite. Mesoporosity always occurred in Al-rich environment since Al distributed in Si(*n*Al) where n > 3 are sensitive and fragile under MW-assisted dealumination conditions. After the Al–O bonds were destroyed, the formed silanol species were effectively dissolved by the sequential alkaline treatment, and hence created relatively huger vacancies with around 4–8 nm diameters.

7.2 Future works

The work described in this thesis has led to achievements in the synthesis and application of hierarchical Y zeolites by intensified post-synthetic modifications with the improved process efficiency. Nevertheless, a number of subjects deserve more dedicated study. For example, calcination is a variable factor during EFAl analysis after dealumination. It is important for further studies to consider about whether the EFAl species generate in dealumination procedure, or Al–O bonds hydrolysis with water molecules at high temperatures. Furthermore, the interconnection between introduced mesopores and

intrinsic micropores hasn’t been elucidated. The study of interconnection can provide the potential in ion exchange, molecular diffusion and so on. In addition, the comprehensive description of acidity and combining porosity with changes in acid sites can be devised. It is also worth to study further catalytic applications of the developed hierarchical zeolites as catalysts and/or catalyst supports.

In this work, process intensification was investigated separately, hence, it is worth to integrate intensified procedures for further research. The emphasis of the thesis is on intensification of the top down approach to the introduction of hierarchical mesoporosity. The work done shows that it is possible to prepare similar materials to those prepared conventionally via the more efficient routes of microwave and ultrasound. The future work should delicately discuss that of how much more efficient the new routes are expected to be, for example when used in tandem (time, energy and cost). Moreover, this method has potential to apply on other Al- rich zeolites with different topology types. Since the developed sequential post-synthetic modification is aiming to meet the sustainable requests, it is necessary to analyse the energy consumption compared to conventional methods, and large-scale synthesis of hierarchical zeolites should be considered as well.

Chapter 8 References

[1] P. Bai, U.J. Etim, Z. Yan, S. Mintova, Z. Zhang, Z. Zhong, X. Gao, Fluid catalytic cracking technology: current status and recent discoveries on catalyst contamination, Catalysis Reviews, 61 (2019) 333-405.
[2] Refinery Catalysts Market Global Forecast to 2025, Markets and Markets, https://www.marketsandmarkets.com/Market-Reports/refinery-catalyst-advanced-technologies-and-global-market-84.html
[3] E. Vogt, B. Weckhuysen, Fluid catalytic cracking: recent developments on the grand old lady of zeolite catalysis, Chem. Soc. Rev., 44 (2015) 7342-7370.
[4] M.A. den Hollander, M. Wissink, M. Makkee, J.A. Moulijn, Gasoline conversion: reactivity towards cracking with equilibrated FCC and ZSM-5 catalysts, Appl. Catal., A, 223 (2002) 85-102.
[5] R. Newell, D. Raimi, S. Villanueva, B. Prest, Global Energy Outlook 2020: Energy Transition or Energy Addition? Resources for the Future, https://media.rff.org/documents/GEO_2020_Report.pdf
[6] International Energy Outlook 2019 with projections to 2050, U.S. Energy Information Administration, https://www.eia.gov/outlooks/ieo/pdf/ieo2019.pdf
[7] M. Pan, J. Zheng, Y. Liu, W. Ning, H. Tian, R. Li, Construction and practical application of a novel zeolite catalyst for hierarchically cracking of heavy oil, J. Catal., 369 (2019) 72-85.
[8] E.G. Fawaz, D.A. Salam, L. Pinard, T.J. Daou, Study on the catalytic performance of different crystal morphologies of HZSM-5 zeolites for the production of biodiesel: a strategy to increase catalyst effectiveness, Catal. Sci. Technol., 9 (2019) 5456-5471.
[9] A.F. Silva, P. Neves, S.M. Rocha, C.M. Silva, A.A. Valente, Optimization of continuous-flow heterogeneous catalytic oligomerization of 1-butene by design of experiments and response surface methodology, Fuel, 259 (2020) 116256.
[10] M.-L. Gou, J. Cai, W. Song, Y. Duan, Z. Liu, Q. Niu, Improved performance of mesoporous HZSM-5 designed with selective deactivation of external surface acidity in the isomerization of styrene oxide, Microporous Mesoporous Mater., 297 (2020) 110037.
[11] A. Talebian-Kiakalaieh, S. Tarighi, Synthesis of hierarchical Y and ZSM-5 zeolites using post-treatment approach to maximize catalytic cracking performance, Journal of Industrial and Engineering Chemistry, 88 (2020) 167-177.
[12] A. Krejčí, S. Al-Khattaf, M.A. Ali, M. Bejblová, J. Čejka, Transalkylation of toluene with trimethylbenzenes over large-pore zeolites, Appl. Catal., A, 377 (2010) 99-106.
[13] R. Mann, Catalyst deactivation by coke deposition: Approaches based on interactions of coke laydown with pore structure, Catal. Today, 37 (1997) 331-349.
[14] S. He, C. Sun, X. Yang, B. Wang, X. Dai, Z. Bai, Characterization of coke deposited on spent catalysts for long-chain-paraffin dehydrogenation, Chem. Eng. J., 163 (2010) 389-394.
[15] J. Kim, M. Choi, R. Ryoo, Effect of mesoporosity against the deactivation of MFI zeolite catalyst during the methanol-to-hydrocarbon conversion process, J. Catal., 269 (2010) 219-228.
[16] T. Weissenberger, B. Reiprich, A.G.F. Machoke, K. Klühspies, J. Bauer, R. Dotzel, J.L. Casci, W. Schwieger, Hierarchical MFI type zeolites with intracrystalline macropores: the effect of the macropore size on the deactivation behaviour in the MTO reaction, Catal. Sci. Technol., 9 (2019) 3259-3269.
[17] F.M. Alotaibi, S. González-Cortés, M.F. Alotibi, T. Xiao, H. Al-Megren, G. Yang, P.P. Edwards, Enhancing the production of light olefins from heavy crude oils: Turning challenges into opportunities, Catal. Today, 317 (2018) 86-98.
[18] V. Blay, E. Epelde, R. Miravalles, L.A. Perea, Converting olefins to propene: Ethene to propene and olefin cracking, Catalysis Reviews, 60 (2018) 278-335.
[19] M. Yang, B. Wang, F. Hu, X. Mi, H. Liu, H. Liu, X. Gao, C. Xu, Synergy between crystal seeds and amphiphilic organosilane surfactant: A facile approach for mesoporous ZSM–5 with high SiO2/Al2O3 ratio, Mater. Lett., 222 (2018) 153-155.
[20] H.X. Vu, M. Schneider, U. Bentrup, T.T. Dang, B.M.Q. Phan, D.A. Nguyen, U. Armbruster, A. Martin, Hierarchical ZSM-5 Materials for an Enhanced Formation of Gasoline-Range Hydrocarbons and Light Olefins in Catalytic Cracking of Triglyceride-Rich Biomass, Ind. Eng. Chem. Res., 54 (2015) 1773-1782.

[21] J. Shi, Y. Wang, W. Yang, Y. Tang, Z. Xie, Recent advances of pore system construction in zeolite-catalyzed chemical industry processes, Chem. Soc. Rev., 44 (2015) 8877-8903.
[22] C.S.J.C.o.C.c.c. Cundy, Microwave techniques in the synthesis and modification of zeolite catalysts. A review, 63 (1998) 1699-1723.
[23] M. Ashokkumar, F. Grieser, Ultrasound assisted chemical processes, Rev. Chem. Eng., 15 (1999) 41-83.
[24] J.-L. Guth, H. Kessler, Synthesis of Aluminosilicate Zeolites and Related Silica-Based Materials, in: J. Weitkamp, L. Puppe (Eds.) Catalysis and Zeolites: Fundamentals and Applications, Springer Berlin Heidelberg, Berlin, Heidelberg, 1999, pp. 1-52.
[25] C. Baerlocher, L.B. McCusker, D.H. Olson, Atlas of zeolite framework types, 6th ed., Elsevier, 2007.
[26] C. Baerlocher, L. B. McCusker, Database of Zeolite Structures, http://www.iza-structure.org/databases/(accessed Aug 10, 2019).
[27] M. Guisnet, J.-P. Gilson, Zeolites for Cleaner Technologies, Imperial College Press London, 2002.
[28] V. Komvokis, L.X.L. Tan, M. Clough, S.S. Pan, B. Yilmaz, Zeolites in Fluid Catalytic Cracking (FCC), in: F.-S. Xiao, X. Meng (Eds.) Zeolites in Sustainable Chemistry: Synthesis, Characterization and Catalytic Applications, Springer Berlin Heidelberg, Berlin, Heidelberg, 2016, pp. 271-297.
[29] J. Garcia-Martinez, K. Li, Mesoporous Zeolites: preparation, characterization and applications, Wiley-VCH, 2015.
[30] E.J.M. Hensen, J.A.R. van Veen, Encapsulation of transition metal sulfides in faujasite zeolite for hydroprocessing applications, Catal. Today, 86 (2003) 87-109.
[31] D.C. Sherrington, A.P. Kybett, Supported Catalysts and Their Applications, Royal Society of Chemistry, 2001.
[32] R.A. van Santen, B.W.H. van Beest, A.J.M. de Man, On Lattice Dynamics, Stability and Acidity of Zeolites, in: D. Barthomeuf, E.G. Derouane, W. Hölderich (Eds.) Guidelines for Mastering the Properties of Molecular Sieves: Relationship between the Physicochemical Properties of Zeolitic Systems and Their Low Dimensionality, Springer US, Boston, MA, 1990, pp. 201-224.
[33] B.Y.S. Al-Zaidi, The effect of modification techniques on the performance of zeolite-Y catalysts in hydrocarbon cracking reactions, in, The University of Manchester (United Kingdom), 2011.
[34] M.F.M. Post, Chapter 11 Diffusion in Zeolite Molecular Sieves, in: H. van Bekkum, E.M. Flanigen, J.C. Jansen (Eds.) Stud. Surf. Sci. Catal., Elsevier, 1991, pp. 391-443.
[35] A. Corma, Inorganic Solid Acids and Their Use in Acid-Catalyzed Hydrocarbon Reactions, Chem. Rev., 95 (1995) 559-614.
[36] X. Meng, F.-S. Xiao, Green Routes for Synthesis of Zeolites, Chem. Rev., 114 (2014) 1521-1543.
[37] H. Awala, J.-P. Gilson, R. Retoux, P. Boullay, J.-M. Goupil, V. Valtchev, S. Mintova, Template-free nanosized faujasite-type zeolites, Nature Materials, 14 (2015) 447-451.
[38] W.J. Roth, P. Nachtigall, R.E. Morris, J. Čejka, Two-Dimensional Zeolites: Current Status and Perspectives, Chem. Rev., 114 (2014) 4807-4837.
[39] J. Přech, P. Pizarro, D.P. Serrano, J. Čejka, From 3D to 2D zeolite catalytic materials, Chem. Soc. Rev., 47 (2018) 8263-8306.
[40] C.J. Heard, J. Čejka, M. Opanasenko, P. Nachtigall, G. Centi, S. Perathoner, 2D Oxide Nanomaterials to Address the Energy Transition and Catalysis, Adv. Mater., 31 (2019) 1801712.
[41] C. Li, M. Moliner, A. Corma, Building Zeolites from Precrystallized Units: Nanoscale Architecture, Angew. Chem. Int. Ed., 57 (2018) 15330-15353.
[42] Y. Guefrachi, G. Sharma, D.D. Xu, G. Kumar, K.P. Vinter, O.A. Abdelrahman, X.Y. Li, S. Alhassan, P.J. Dauenhauer, A. Navrotsky, W. Zhang, M. Tsapatsis, Steam-Induced Coarsening of Single-Unit-Cell MFI Zeolite Nanosheets and Its Effect on External Surface Bronsted Acid Catalysis, Angew. Chem.-Int. Edit., (2020) 8.
[43] R. Kore, R. Srivastava, B. Satpati, ZSM-5 Zeolite Nanosheets with Improved Catalytic Activity Synthesized Using a New Class of Structure-Directing Agents, Chemistry-a European Journal, 20 (2014) 11511-11521.
[44] J. Pérez-Ramírez, C.H. Christensen, K. Egeblad, C.H. Christensen, J.C. Groen, Hierarchical zeolites: enhanced utilisation of microporous crystals in catalysis by advances in materials design, Chem. Soc. Rev., 37 (2008) 2530-2542.

[45] W. Schwieger, A.G. Machoke, T. Weissenberger, A. Inayat, T. Selvam, M. Klumpp, A. Inayat, Hierarchy concepts: classification and preparation strategies for zeolite containing materials with hierarchical porosity, Chem. Soc. Rev., 45 (2016) 3353-3376.
[46] Y. Wei, T.E. Parmentier, K.P. de Jong, J. Zečević, Tailoring and visualizing the pore architecture of hierarchical zeolites, Chem. Soc. Rev., 44 (2015) 7234-7261.
[47] X. Niu, X. Li, G. Yuan, F. Feng, M. Wang, X. Zhang, Q. Wang, Hollow Hierarchical Silicalite-1 Zeolite Encapsulated PtNi Bimetals for Selective Hydroconversion of Methyl Stearate into Aviation Fuel Range Alkanes, Ind. Eng. Chem. Res., 59 (2020) 8601-8611.
[48] T. Fu, Y. Wang, Z. Li, Surface-Protection-Induced Controllable Restructuring of Pores and Acid Sites of the Nano-ZSM-5 Catalyst and Its Influence on the Catalytic Conversion of Methanol to Hydrocarbons, Langmuir, 36 (2020) 3737-3749.
[49] M. Hartmann, A.G. Machoke, W. Schwieger, Catalytic test reactions for the evaluation of hierarchical zeolites, Chem. Soc. Rev., 45 (2016) 3313-3330.
[50] S. Lopez-Orozco, A. Inayat, A. Schwab, T. Selvam, W. Schwieger, Zeolitic Materials with Hierarchical Porous Structures, Adv. Mater., 23 (2011) 2602-2615.
[51] S. Zhao, W.D. Wang, L. Wang, W. Schwieger, W. Wang, J. Huang, Tuning Hierarchical ZSM-5 Zeolite for Both Gas- and Liquid-Phase Biorefining, ACS Catal., 10 (2020) 1185-1194.
[52] A.H. Janssen, I. Schmidt, C.J.H. Jacobsen, A.J. Koster, K.P. de Jong, Exploratory study of mesopore templating with carbon during zeolite synthesis, Microporous Mesoporous Mater., 65 (2003) 59-75.
[53] L. Zhang, X. Sun, M. Pan, X. Yang, Y. Liu, J. Sun, Q. Wang, J. Zheng, Y. Wang, J. Ma, Interfacial effects between carbon nanotube templates and precursors on fabricating a wall-crystallized hierarchical pore system in zeolite crystals, Journal of Materials Science, (2020) 1-15.
[54] Y. Tao, H. Kanoh, K. Kaneko, Uniform mesopore-donated zeolite Y using carbon aerogel templating, The Journal of Physical Chemistry B, 107 (2003) 10974-10976.
[55] D.P. Serrano, J.M. Escola, P. Pizarro, Synthesis strategies in the search for hierarchical zeolites, Chem. Soc. Rev., 42 (2013) 4004-4035.
[56] H. Chen, J. Wydra, X. Zhang, P.-S. Lee, Z. Wang, W. Fan, M. Tsapatsis, Hydrothermal Synthesis of Zeolites with Three-Dimensionally Ordered Mesoporous-Imprinted Structure, J. Am. Chem. Soc., 133 (2011) 12390-12393.
[57] X. Wei, P.G. Smirniotis, Synthesis and characterization of mesoporous ZSM-12 by using carbon particles, Microporous Mesoporous Mater., 89 (2006) 170-178.
[58] Y. Du, Q. Kong, Z. Gao, Z. Wang, J. Zheng, B. Qin, M. Pan, W. Li, R. Li, Flowerlike Hierarchical Y with Dramatically Increased External Surface: A Potential Catalyst Contributing to Improving Precracking for Bulky Reactant Molecules, Ind. Eng. Chem. Res., 57 (2018) 7395-7403.
[59] S. Xu, M. Zhang, S. Guo, M. Li, Q. Huang, X. Chen, Synthesis of Hierarchically Porous Zeolite Ti-MWW with Different Hard Templates and Their Application in Allyl Alcohol Conversion, Catal. Lett., 150 (2020) 209-221.
[60] A. Dong, Y. Wang, Y. Tang, N. Ren, Y. Zhang, Y. Yue, Z. Gao, Zeolitic Tissue Through Wood Cell Templating, Adv. Mater., 14 (2002) 926-929.
[61] J.S. Beck, J.C. Vartuli, W.J. Roth, M.E. Leonowicz, C.T. Kresge, K.D. Schmitt, C.T.W. Chu, D.H. Olson, E.W. Sheppard, S.B. McCullen, J.B. Higgins, J.L. Schlenker, A new family of mesoporous molecular sieves prepared with liquid crystal templates, J. Am. Chem. Soc., 114 (1992) 10834-10843.
[62] M. Alonso-Doncel, A. Peral, M. Shamzhy, J. Čejka, R. Sanz, D.P. Serrano, Fine-tuning hierarchical ZSM-5 zeolite by controlled aggregation of protozeolitic units functionalized with tertiary amine-containing organosilane, Microporous Mesoporous Mater., 303 (2020) 110189.
[63] F.-S. Xiao, L. Wang, C. Yin, K. Lin, Y. Di, J. Li, R. Xu, D.S. Su, R. Schlögl, T. Yokoi, T. Tatsumi, Catalytic Properties of Hierarchical Mesoporous Zeolites Templated with a Mixture of Small Organic Ammonium Salts and Mesoscale Cationic Polymers, 45 (2006) 3090-3093.
[64] R. Barakov, N. Shcherban, P. Yaremov, I. Bezverkhyy, V. Tsyrina, M. Opanasenko, Hierarchical Beta zeolites obtained in concentrated reaction mixtures as catalysts in tetrahydropyranylation of alcohols, Appl. Catal., A, 594 (2020) 117380.
[65] F.N. Gu, F. Wei, J.Y. Yang, N. Lin, W.G. Lin, Y. Wang, J.H. Zhu, New Strategy to Synthesis of Hierarchical Mesoporous Zeolites, Chem. Mater., 22 (2010) 2442-2450.

[66] X. Dong, S. Shaikh, J.R. Vittenet, J. Wang, Z. Liu, K.D. Bhatte, O. Ali, W. Xu, I. Osorio, Y. Saih, J.-M. Basset, S.A. Ali, Y. Han, Fine Tuning the Diffusion Length in Hierarchical ZSM-5 To Maximize the Yield of Propylene in Catalytic Cracking of Hydrocarbons, ACS Sustainable Chemistry & Engineering, 6 (2018) 15832-15840.
[67] H. Zhu, Z. Liu, Y. Wang, D. Kong, X. Yuan, Z. Xie, Nanosized CaCO3 as Hard Template for Creation of Intracrystal Pores within Silicalite-1 Crystal, Chem. Mater., 20 (2008) 1134-1139.
[68] F. Liu, T. Willhammar, L. Wang, L. Zhu, Q. Sun, X. Meng, W. Carrillo-Cabrera, X. Zou, F.-S. Xiao, ZSM-5 Zeolite Single Crystals with b-Axis-Aligned Mesoporous Channels as an Efficient Catalyst for Conversion of Bulky Organic Molecules, J. Am. Chem. Soc., 134 (2012) 4557-4560.
[69] D. Guo, C. Shi, H. Zhao, R. Chen, S. Chen, P. Sun, T. Chen, Polyacrylic acid as mesoscale template for synthesis of MFI zeolite with plentiful intracrystalline mesopores, Microporous Mesoporous Mater., 293 (2020) 109821.
[70] Y. Shen, H. Li, X. Zhang, X. Wang, G. Lv, The diquaternary ammonium surfactant-directed synthesis of single-unit-cell nanowires of ZSM-5 zeolite, Nanoscale, 12 (2020) 5824-5828.
[71] A.A. Dabbawala, I. Ismail, B.V. Vaithilingam, K. Polychronopoulou, G. Singaravel, S. Morin, M. Berthod, Y. Al Wahedi, Synthesis of hierarchical porous Zeolite-Y for enhanced CO_2 capture, Microporous Mesoporous Mater., 303 (2020) 110261.
[72] M. Choi, K. Na, J. Kim, Y. Sakamoto, O. Terasaki, R. Ryoo, Stable single-unit-cell nanosheets of zeolite MFI as active and long-lived catalysts, Nature, 461 (2009) 246-249.
[73] G.T. Kerr, Chemistry of crystalline aluminosilicates. V. Preparation of aluminum-deficient faujasites, The Journal of Physical Chemistry, 72 (1968) 2594-2596.
[74] R. Barrer, M. Makki, Molecular sieve sorbents from clinoptilolite, Can. J. Chem., 42 (1964) 1481-1487.
[75] D. Verboekend, S. Mitchell, J. Pérez-Ramírez, Hierarchical zeolites overcome all obstacles: next stop industrial implementation, CHIMIA International Journal for Chemistry, 67 (2013) 327-332.
[76] X. Meng, Z. Lian, X. Wang, L. Shi, N. Liu, Effect of dealumination of HZSM-5 by acid treatment on catalytic properties in non-hydrocracking of diesel, Fuel, 270 (2020) 117426.
[77] R. Srivastava, N. Iwasa, S.-i. Fujita, M. Arai, Dealumination of Zeolite Beta Catalyst Under Controlled Conditions for Enhancing its Activity in Acylation and Esterification, Catal. Lett., 130 (2009) 655-663.
[78] P. Tamizhdurai, A. Ramesh, P.S. Krishnan, S. Narayanan, K. Shanthi, S. Sivasanker, Effect of acidity and porosity changes of dealuminated mordenite on n-pentane, n-hexane and light naphtha isomerization, Microporous Mesoporous Mater., 287 (2019) 192-202.
[79] M. Milina, Property-Function Interplay in the Design of Hierarchical Zeolite Catalysts, in, ETH-Zürich, 2014.
[80] A.A. Asadi, S.M. Alavi, S.J. Royaee, M. Bazmi, Dependency of acidic and surficial characteristics of steamed Y zeolite on potentially effective synthesis parameters: Screening, prioritizing and model development, Microporous Mesoporous Mater., 259 (2018) 142-154.
[81] A. Ristić, F. Fischer, A. Hauer, N. Zabukovec Logar, Improved performance of binder-free zeolite Y for low-temperature sorption heat storage, Journal of Materials Chemistry A, 6 (2018) 11521-11530.
[82] D. Yuan, C. Kang, W. Wang, H. Li, X. Zhu, Y. Wang, X. Gao, B. Wang, H. Zhao, C. Liu, B. Shen, Creation of mesostructured hollow Y zeolite by selective demetallation of an artificial heterogeneous Al distributed zeolite crystal, Catal. Sci. Technol., 6 (2016) 8364-8374.
[83] C. Li, L. Guo, P. Liu, K. Gong, W. Jin, L. Li, X. Zhu, X. Liu, B. Shen, Defects in AHFS-dealuminated Y zeolite: A crucial factor for mesopores formation in the following base treatment procedure, Microporous Mesoporous Mater., 255 (2017).
[84] D. Suttipat, T. Yutthalekha, W. Wannapakdee, P. Dugkhuntod, P. Wetchasat, P. Kidkhunthod, C. Wattanakit, Tunable Acid-Base Bifunction of Hierarchical Aluminum-Rich Zeolites for the One-Pot Tandem Deacetalization-Henry Reaction, ChemPlusChem, 84 (2019) 1503-1507.
[85] S. Lee, H. Kim, M. Choi, Controlled decationization of X zeolite: mesopore generation within zeolite crystallites for bulky molecular adsorption and transformation, Journal of Materials Chemistry A, 1 (2013) 12096-12102.
[86] D. Verboekend, M. Milina, J. Pérez-Ramírez, Hierarchical Silicoaluminophosphates by Postsynthetic Modification: Influence of Topology, Composition, and Silicon Distribution, Chem. Mater., 26 (2014) 4552-4562.

[87] B. Zhang, G. Tan, Z. Zhong, R. Ruan, Microwave-assisted catalytic fast pyrolysis of spent edible mushroom substrate for bio-oil production using surface modified zeolite catalyst, J. Anal. Appl. Pyrolysis, 123 (2017) 92-98.
[88] X. Zhao, Y. Hong, L. Wang, D. Fan, N. Yan, X. Liu, P. Tian, X. Guo, Z. Liu, External surface modification of as-made ZSM-5 and their catalytic performance in the methanol to propylene reaction, Chinese Journal of Catalysis, 39 (2018) 1418-1426.
[89] B. Zhang, Z. Zhong, Z. Song, K. Ding, P. Chen, R. Ruan, Optimizing anti-coking abilities of zeolites by ethylene diamine tetraacetie acid modification on catalytic fast pyrolysis of corn stalk, J. Power Sources, 300 (2015) 87-94.
[90] J.L. Agudelo, B. Mezari, E.J.M. Hensen, S.A. Giraldo, L.J. Hoyos, On the effect of EDTA treatment on the acidic properties of USY zeolite and its performance in vacuum gas oil hydrocracking, Appl. Catal., A, 488 (2014) 219-230.
[91] D. Verboekend, T.C. Keller, S. Mitchell, J. Pérez-Ramírez, Hierarchical FAU-and LTA-Type Zeolites by Post-Synthetic Design: A New Generation of Highly Efficient Base Catalysts, Adv. Funct. Mater., 23 (2013) 1923-1934.
[92] Y.D. Arthur, Hydrocarbon conversion process and catalyst comprising a crystalline alumino-silicate leached with sodium hydroxide, in, Google Patents, 1967.
[93] R.M. Dessau, E.W. Valyocsik, N.H. Goeke, Aluminum zoning in ZSM-5 as revealed by selective silica removal, Zeolites, 12 (1992) 776-779.
[94] A. Čimek, B. Subotić, I. Šmit, A. Tonejc, R. Aiello, F. Crea, A. Nastro, Dissolution of high-silica zeolites in alkaline solutions II. Dissolution of 'activated' silicalite-1 and ZSM-5 with different aluminum content, Microporous Mater., 8 (1997) 159-169.
[95] O. Masaru, S. Shin-ya, T. Junko, N. Yasuto, K. Eiichi, M. Masahiko, Formation of Uniform Mesopores in ZSM-5 Zeolite through Treatment in Alkaline Solution, 29 (2000) 882-883.
[96] G.J. C., P.-R. J., P.L.A. A., Formation of Uniform Mesopores in ZSM-5 Zeolite upon Alkaline Post-treatment?, Chem. Lett., 31 (2002) 94-95.
[97] J.C. Groen, J.C. Jansen, J.A. Moulijn, J. Pérez-Ramírez, Optimal Aluminum-Assisted Mesoporosity Development in MFI Zeolites by Desilication, The Journal of Physical Chemistry B, 108 (2004) 13062-13065.
[98] J.C. Groen, L.A. Peffer, J.A. Moulijn, J. Pérez-Ramírez, Mechanism of hierarchical porosity development in MFI zeolites by desilication: The role of aluminium as a pore‐directing agent, Chemistry-A European Journal, 11 (2005) 4983-4994.
[99] J.C. Groen, L.A.A. Peffer, J.A. Moulijn, J. Pérez-Ramírez, Mesoporosity development in ZSM-5 zeolite upon optimized desilication conditions in alkaline medium, Colloids and Surfaces A: Physicochemical and Engineering Aspects, 241 (2004) 53-58.
[100] J.C. Groen, J.A. Moulijn, J. Pérez-Ramírez, Alkaline Posttreatment of MFI Zeolites. From Accelerated Screening to Scale-up, Ind. Eng. Chem. Res., 46 (2007) 4193-4201.
[101] D. Zhang, C. Jin, M. Zou, S. Huang, Mesopore Engineering for Well-Defined Mesoporosity in Al-Rich Aluminosilicate Zeolites, Chem. Eur. J., 25 (2019) 2675-2683.
[102] Y. Wang, S. Kazumi, W. Gao, X. Gao, H. Li, X. Guo, Y. Yoneyama, G. Yang, N. Tsubaki, Direct conversion of CO2 to aromatics with high yield via a modified Fischer-Tropsch synthesis pathway, Appl. Catal., B, 269 (2020) 118792.
[103] I.I. Ivanova, E.E. Knyazeva, Micro–mesoporous materials obtained by zeolite recrystallization: synthesis, characterization and catalytic applications, Chem. Soc. Rev., 42 (2013) 3671-3688.
[104] J. Shao, T. Fu, Z. Ma, C. Zhang, H. Li, L. Cui, Z. Li, Facile creation of hierarchical nano-sized ZSM-5 with a large external surface area via desilication-recrystallization of silicalite-1 for conversion of methanol to hydrocarbons, Catal. Sci. Technol., 9 (2019) 6647-6658.
[105] D. Hu, H. Hu, H. Jin, P. Zhang, Y. Hu, S. Ying, X. Li, Y. Yang, J. Zhang, L. Wang, Building hierarchical zeolite structure by post-synthesis treatment to promote the conversion of furanic molecules into biofuels, Appl. Catal., A, 590 (2020) 117338.
[106] D. Ottaviani, V. Van-Dúnem, A.P. Carvalho, A. Martins, L.M.D.R.S. Martins, Eco-friendly cyclohexane oxidation by a V-scorpionate complex immobilized at hierarchical MOR zeolite, Catal. Today, 348 (2020) 37-44.

[107] H. Issa, N. Chaouati, J. Toufaily, T. Hamieh, A. Sachse, L. Pinard, Toolbox of Post-Synthetic Mordenite Modification Strategies: Impact on Textural, Acidic and Catalytic Properties, Chem. Eur. J., 11 (2019) 4581-4592.
[108] D. Fan, Y. Qiao, K. Cao, L. Sun, S. Xu, P. Tian, Z. Liu, Preparation of hierarchical SAPO-18 via alkaline/acid etching, Microporous Mesoporous Mater., 300 (2020) 110156.
[109] K. Tarach, K. Góra-Marek, J. Tekla, K. Brylewska, J. Datka, K. Mlekodaj, W. Makowski, M.C. Igualada López, J. Martínez Triguero, F. Rey, Catalytic cracking performance of alkaline-treated zeolite Beta in the terms of acid sites properties and their accessibility, J. Catal., 312 (2014) 46-57.
[110] H. Sun, A. Wang, K. Sun, J. Jiang, F. Wang, Z. Gu, Effect of acidity and porosity of hierarchical HBEA zeolite on catalytic stability of α-methylnaphthalene isomerization, J. Porous Mater., (2018).
[111] N. Linares, E.O. Jardim, A. Sachse, E. Serrano, J. García-Martínez, The Energetics of Surfactant-Templating of Zeolites, Angew. Chem. Int. Ed., 57 (2018) 8724-8728.
[112] C. Peng, Z. Liu, Y. Yonezawa, N. Linares, Y. Yanaba, C.A. Trujillo, T. Okubo, T. Matsumoto, J. García-Martínez, T. Wakihara, Testing the limits of zeolite structural flexibility: ultrafast introduction of mesoporosity in zeolites, Journal of Materials Chemistry A, 8 (2020) 735-742.
[113] X. Li, R. Prins, J.A. van Bokhoven, Synthesis and characterization of mesoporous mordenite, J. Catal., 262 (2009) 257-265.
[114] A.N.C. van Laak, S.L. Sagala, J. Zečević, H. Friedrich, P.E. de Jongh, K.P. de Jong, Mesoporous mordenites obtained by sequential acid and alkaline treatments–Catalysts for cumene production with enhanced accessibility, J. Catal., 276 (2010) 170-180.
[115] S. Yang, C. Yu, L. Yu, S. Miao, M. Zou, C. Jin, D. Zhang, L. Xu, S. Huang, Bridging Dealumination and Desilication for the Synthesis of Hierarchical MFI Zeolites, Angew. Chem. Int. Ed., 56 (2017) 12553-12556.
[116] A. Shahid, S. Lopez-Orozco, V.R. Marthala, M. Hartmann, W. Schwieger, Direct oxidation of benzene to phenol over hierarchical ZSM-5 zeolites prepared by sequential post synthesis modification, Microporous Mesoporous Mater., 237 (2017) 151-159.
[117] D. Verboekend, T.C. Keller, M. Milina, R. Hauert, J. Pérez-Ramírez, Hierarchy Brings Function: Mesoporous Clinoptilolite and L Zeolite Catalysts Synthesized by Tandem Acid–Base Treatments, Chem. Mater., 25 (2013) 1947-1959.
[118] J. García-Martínez, K. Li, G. Krishnaiah, A mesostructured Y zeolite as a superior FCC catalyst – from lab to refinery, Chem. Commun., 48 (2012) 11841-11843.
[119] K. Góra-Marek, K. Tarach, J. Tekla, Z. Olejniczak, P. Kuśtrowski, L. Liu, J. Martinez-Triguero, F. Rey, Hierarchical Mordenite Dedicated to the Fluid Catalytic Cracking Process: Catalytic Performance Regarding Textural and Acidic Properties, The Journal of Physical Chemistry C, 118 (2014) 28043-28054.
[120] L. Yu, S. Huang, S. Miao, F. Chen, S. Zhang, Z. Liu, S. Xie, L. Xu, A Facile Top-Down Protocol for Postsynthesis Modification of Hierarchical Aluminum-Rich MFI Zeolites, Chem. Eur. J., 21 (2015) 1048-1054.
[121] D. Verboekend, G. Vilé, J. Pérez-Ramírez, Hierarchical Y and USY zeolites designed by post-synthetic strategies, Adv. Funct. Mater., 22 (2012) 916-928.
[122] D. Verboekend, N. Nuttens, R. Locus, J. Van Aelst, P. Verolme, J.C. Groen, J. Perez-Ramirez, B.F. Sels, Synthesis, characterisation, and catalytic evaluation of hierarchical faujasite zeolites: milestones, challenges, and future directions, Chem. Soc. Rev., 45 (2016) 3331-3352.
[123] S. Huang, X. Liu, L. Yu, S. Miao, Z. Liu, S. Zhang, S. Xie, L. Xu, Preparation of hierarchical mordenite zeolites by sequential steaming-acid leaching-alkaline treatment, Microporous Mesoporous Mater., 191 (2014) 18-26.
[124] X. Fan, Y. Jiao, Chapter 5 - Porous Materials for Catalysis: Toward Sustainable Synthesis and Applications of Zeolites, in: G. Szekely, A. Livingston (Eds.) Sustainable Nanoscale Engineering, Elsevier, 2020, pp. 115-137.
[125] R. Sabouni, H. Kazemian, S. Rohani, A novel combined manufacturing technique for rapid production of IRMOF-1 using ultrasound and microwave energies, Chem. Eng. J., 165 (2010) 966-973.
[126] J. Gordon, H. Kazemian, S. Rohani, Rapid and efficient crystallization of MIL-53(Fe) by ultrasound and microwave irradiation, Microporous Mesoporous Mater., 162 (2012) 36-43.

[127] X. Fu, X. Sheng, Y. Zhou, Z. Fu, S. Zhao, Z. Zhang, Y. Zhang, Ultrasonic/microwave synergistic synthesis of well-dispersed hierarchical zeolite Y with improved alkylation catalytic activity, Korean J. Chem. Eng., 33 (2016) 1931-1937.
[128] S. Roberto, B. Giovanni, Introduction, in: C. Kai, S. Roberto, B. Giovanni (Eds.) Microwave and RF Engineering, John Wiley, 2010, pp. 1-8.
[129] S.S. Bukhari, J. Behin, H. Kazemian, S. Rohani, Conversion of coal fly ash to zeolite utilizing microwave and ultrasound energies: A review, Fuel, 140 (2015) 250-266.
[130] L. Brittany, D. Hayes, Microwave synthesis: Chemistry at the speed of light, CEM Publishing, (2002) 11-27.
[131] J.H. Bang, K.S. Suslick, Applications of Ultrasound to the Synthesis of Nanostructured Materials, Adv. Mater., 22 (2010) 1039-1059.
[132] K.S. Suslick, Sonochemistry, Science, 247 (1990) 1439-1445.
[133] T.G. Leighton, 5 - Effects and Mechanisms, in: T.G. Leighton (Ed.) The Acoustic Bubble, Academic Press, 1994, pp. 439-590.
[134] J. Han, Y. Ha, M. Guo, P. Zhao, Q. Liu, C. Liu, C. Song, N. Ji, X. Lu, D. Ma, Z. Li, Synthesis of zeolite SSZ-13 from coal gangue via ultrasonic pretreatment combined with hydrothermal growth method, Ultrason. Sonochem., 59 (2019) 104703.
[135] Y. Liu, H. Zhang, F. Zhang, M. Zhu, N. Hu, X. Chen, Facile synthesis of low-silica zeolite erionite by ultrasonic-assisted method, Mater. Lett., 260 (2020) 126934.
[136] H. Ramirez Mendoza, J. Jordens, M. Valdez Lancinha Pereira, C. Lutz, T. Van Gerven, Effects of ultrasonic irradiation on crystallization kinetics, morphological and structural properties of zeolite FAU, Ultrason. Sonochem., 64 (2020) 105010.
[137] S. Mintova, J.-P. Gilson, V. Valtchev, Advances in nanosized zeolites, Nanoscale, 5 (2013) 6693-6703.
[138] V. Valtchev, L. Tosheva, Porous Nanosized Particles: Preparation, Properties, and Applications, Chem. Rev., 113 (2013) 6734-6760.
[139] P. Lv, L. Yan, Y. Liu, M. Wang, W. Bao, F. Li, Catalytic Upgrading of Coal Pyrolysis Gaseous Tar over Hierarchical Y-Type Zeolites Synthesized Using a Microwave Hydrothermal Method, Ind. Eng. Chem. Res., 58 (2019) 21817-21826.
[140] T. Wang, H. Yu, B. Bian, Y. Liu, S. Liu, S. Yu, Z. Wang, One-Pot Synthesis of Anthraquinone Catalyzed by Microwave Acetic Acid Modified Hβ Zeolite, Catal. Lett., (2020).
[141] C.C. Pavel, W. Schmidt, Generation of hierarchical pore systems in the titanosilicate ETS-10 by hydrogen peroxide treatment under microwave irradiation, Chem. Commun., (2006) 882-884.
[142] C.C. Pavel, R. Palkovits, F. Schüth, W. Schmidt, The benefit of mesopores in ETS-10 on the vapor-phase Beckmann rearrangement of cyclohexanone oxime, J. Catal., 254 (2008) 84-90.
[143] C.C. Pavel, S.-H. Park, A. Dreier, B. Tesche, W. Schmidt, Structural Defects Induced in ETS-10 by Postsynthesis Treatment with H2O2 Solution, Chem. Mater., 18 (2006) 3813-3820.
[144] B. Zhang, Y. Zhang, Y. Hu, Z. Shi, A. Azhati, S. Xie, H. He, Y. Tang, Microexplosion under microwave irradiation: A facile approach to create mesopores in zeolites, Chem. Mater., 28 (2016) 2757-2767.
[145] S. Abelló, J. Pérez-Ramírez, Accelerated generation of intracrystalline mesoporosity in zeolites by microwave-mediated desilication, PCCP, 11 (2009) 2959-2963.
[146] Z. Hasan, J.W. Jun, C.-U. Kim, K.-E. Jeong, S.-Y. Jeong, S.H. Jhung, Desilication of ZSM-5 zeolites for mesoporosity development using microwave irradiation, Mater. Res. Bull., 61 (2015) 469-474.
[147] X.-L. Luo, F. Pei, W. Wang, H.-m. Qian, K.-K. Miao, Z. Pan, Y.-S. Chen, G.-D. Feng, Microwave synthesis of hierarchical porous materials with various structures by controllable desilication and recrystallization, Microporous Mesoporous Mater., 262 (2018) 148-153.
[148] M.A. Sanhoob, U. Khalil, E.N. Shafei, K.-H. Choi, T. Yokoi, O. Muraza, Steam cracking of green diesel (C12) to BTX and olefins over silane-treated hierarchical BEA, Fuel, 263 (2020) 116624.
[149] V. Paixão, R. Monteiro, M. Andrade, A. Fernandes, J. Rocha, A.P. Carvalho, A. Martins, Desilication of MOR zeolite: Conventional versus microwave assisted heating, Appl. Catal., A, 402 (2011) 59-68.

[150] Y. Liu, D. Zheng, B. Li, Y. Lyu, X. Wang, X. Liu, L. Li, S. Yu, X. Liu, Z. Yan, Isomerization of α-pinene with a hierarchical mordenite molecular sieve prepared by the microwave assisted alkaline treatment, Microporous Mesoporous Mater., 299 (2020) 110117.
[151] O. Muraza, M.A. Sanhoob, M.A.B. Siddiqui, Fabrication of desilicated MTW zeolite and its application in catalytic cracking of n-heptane, Adv. Powder Technol., 27 (2016) 372-378.
[152] M.D. González, Y. Cesteros, P. Salagre, F. Medina, J.E. Sueiras, Effect of microwaves in the dealumination of mordenite on its surface and acidic properties, Microporous Mesoporous Mater., 118 (2009) 341-347.
[153] M.D. González, Y. Cesteros, P. Salagre, Comparison of dealumination of zeolites beta, mordenite and ZSM-5 by treatment with acid under microwave irradiation, Microporous Mesoporous Mater., 144 (2011) 162-170.
[154] B.M. Chandra Shekara, B.S. Jai Prakash, Y.S. Bhat, Dealumination of Zeolite BEA under Microwave Irradiation, ACS Catal., 1 (2011) 193-199.
[155] Shu, S. Husain, W.J. Koros, Sonication-Assisted Dealumination of Zeolite A with Thionyl Chloride, Ind. Eng. Chem. Res., 46 (2007) 767-772.
[156] M. Hosseini, M.A. Zanjanchi, B. Ghalami-Choobar, H. Golmojdeh, Ultrasound-assisted dealumination of zeolite Y, Journal of Chemical Sciences, 127 (2015) 25-31.
[157] R. Khoshbin, R. Karimzadeh, Synthesis of mesoporous ZSM-5 from rice husk ash with ultrasound assisted alkali-treatment method used in catalytic cracking of light naphtha, Adv. Powder Technol., 28 (2017) 1888-1897.
[158] Ł. Kuterasiński, W. Rojek, M. Gackowski, M. Zimowska, P.J. Jodłowski, Sonically modified hierarchical FAU-type zeolites as active catalysts for the production of furan from furfural, Ultrason. Sonochem., 60 (2020) 104785.
[159] A. Jentys, J.A. Lercher, Chapter 8 Techniques of zeolite characterization, in: H. van Bekkum, E.M. Flanigen, P.A. Jacobs, J.C. Jansen (Eds.) Stud. Surf. Sci. Catal., Elsevier, 2001, pp. 345-386.
[160] K.S.W. Sing, D.H. Everett, R.A.W. Haul, L. Mouscou, R.A. Pierotti, J. Rouquerol, T. Siemieniewska, Reporting physisorption data for gas/solid systems with special reference to the determination of surface area and porosity (Recommendations 1984), Pure Appl. Chem., 57 (1985) 603.
[161] M. Thommes, K. Kaneko, A.V. Neimark, J.P. Olivier, F. Rodriguez-Reinoso, J. Rouquerol, K.S. Sing, Physisorption of gases, with special reference to the evaluation of surface area and pore size distribution (IUPAC Technical Report), Pure Appl. Chem., 87 (2015) 1051-1069.
[162] M. Rahman, M. Muttakin, A. Pal, A.Z. Shafiullah, B. Saha, A Statistical Approach to Determine Optimal Models for IUPAC-Classified Adsorption Isotherms, Energies, 12 (2019) 4565.
[163] K.A. Cychosz, R. Guillet-Nicolas, J. García-Martínez, M. Thommes, Recent advances in the textural characterization of hierarchically structured nanoporous materials, Chem. Soc. Rev., 46 (2017) 389-414.
[164] M. Thommes, Physical Adsorption Characterization of Nanoporous Materials, Chem. Ing. Tech., 82 (2010) 1059-1073.
[165] S. Lowell, J.E. Shields, M.A. Thomas, M. Thommes, Surface area analysis from the Langmuir and BET theories, in: Characterization of Porous Solids and Powders: Surface Area, Pore Size and Density, Springer Netherlands, Dordrecht, 2004, pp. 58-81.
[166] B.C. Lippens, J.H. de Boer, Studies on pore systems in catalysts: V. The t method, J. Catal., 4 (1965) 319-323.
[167] J. Cejka, A. Corma, S. Zones, Zeolites and catalysis: synthesis, reactions and applications, John Wiley & Sons, 2010.
[168] G. Leofanti, M. Padovan, G. Tozzola, B. Venturelli, Surface area and pore texture of catalysts, Catal. Today, 41 (1998) 207-219.
[169] S. Mintova, J. Čejka, Chapter 9 - Micro/Mesoporous Composites, in: J. Čejka, H. van Bekkum, A. Corma, F. Schüth (Eds.) Stud. Surf. Sci. Catal., Elsevier, 2007, pp. 301-VI.
[170] H. Giesche, Mercury Porosimetry: A General (Practical) Overview, 23 (2006) 9-19.
[171] S.P. Rigby, Mercury Porosimetry, in: Structural Characterisation of Natural and Industrial Porous Materials: A Manual, Springer International Publishing, Cham, 2020, pp. 49-68.
[172] R. Haul, S. J. Gregg, K. S. W. Sing: Adsorption, Surface Area and Porosity. 2. Auflage, Academic Press, London 1982. 303 Seiten, Preis: $ 49.50, 86 (1982) 957-957.

[173] L.v.d. Weerd, D.L. Thomas, J.S. Thornton, M.F. Lythgoe, MRI of Animal Models of Brain Disease, in: Methods Enzymol., Academic Press, 2004, pp. 149-177.
[174] F.A. Bovey, P.A. Mirau, H. Gutowsky, Nuclear magnetic resonance spectroscopy, Elsevier, 1988.
[175] G. Engelhardt, Chapter 9 Solid state NMR spectroscopy applied to zeolites, in: H. van Bekkum, E.M. Flanigen, P.A. Jacobs, J.C. Jansen (Eds.) Stud. Surf. Sci. Catal., Elsevier, 2001, pp. 387-418.
[176] G. Paul, C. Bisio, I. Braschi, M. Cossi, G. Gatti, E. Gianotti, L. Marchese, Combined solid-state NMR, FT-IR and computational studies on layered and porous materials, Chem. Soc. Rev., 47 (2018) 5684-5739.
[177] F.C. A., G.G. C., M.W. J., O.R. S., S.D. A., Investigation of the factors affecting the 29si mas NMR linewidths of zeolites, Chem. Lett., 12 (1983) 1547-1550.
[178] R.G. Peter, A.d.H. James, Introduction to Vibrational Spectroscopy, in: Fourier Transform Infrared Spectrometry, John Wiley & Sons, Inc., 2006, pp. 1-18.
[179] K.I. Hadjiivanov, Chapter 10 - Application of Isotopically Labelled IR Probe Molecules for Characterization of Porous Materials, in: V. Valtchev, S. Mintova, M. Tsapatsis (Eds.) Ordered Porous Solids, Elsevier, Amsterdam, 2009, pp. 263-281.
[180] B.C. Smith, Fundamentals of Fourier transform infrared spectroscopy, CRC press, 2011.
[181] S.A. Bradley, R.W. Broach, T.M. Mezza, S. Prabhakar, W. Sinkler, Zeolite Characterization, in: S. Kulprathipanja (Ed.) Zeolites in Industrial Separation and Catalysis, Wiley‐VCH Verlag GmbH & Co. KGaA, 2010, pp. 85-171.
[182] P.A. Jacobs, W.J. Mortier, An attempt to rationalize stretching frequencies of lattice hydroxyl groups in hydrogen-zeolites, Zeolites, 2 (1982) 226-230.
[183] S. Van Donk, A.H. Janssen, J.H. Bitter, K.P. de Jong, Generation, characterization, and impact of mesopores in zeolite catalysts, Catalysis Reviews, 45 (2003) 297-319.
[184] C.H. Christensen, K. Johannsen, E. Törnqvist, I. Schmidt, H. Topsøe, C.H. Christensen, Mesoporous zeolite single crystal catalysts: Diffusion and catalysis in hierarchical zeolites, Catal. Today, 128 (2007) 117-122.
[185] R. Chal, C. Gerardin, M. Bulut, S. Van Donk, Overview and industrial assessment of synthesis strategies towards zeolites with mesopores, ChemCatChem, 3 (2011) 67-81.
[186] M.S. Holm, E. Taarning, K. Egeblad, C.H. Christensen, Catalysis with hierarchical zeolites, Catal. Today, 168 (2011) 3-16.
[187] J. Zhao, Y. Yin, Y. Li, W. Chen, B. Liu, Synthesis and characterization of mesoporous zeolite Y by using block copolymers as templates, Chem. Eng. J., 284 (2016) 405-411.
[188] Z.A.J.M. ALOthman, A review: fundamental aspects of silicate mesoporous materials, Materials, 5 (2012) 2874-2902.
[189] M. Choi, H.S. Cho, R. Srivastava, C. Venkatesan, D.-H. Choi, R. Ryoo, Amphiphilic organosilane-directed synthesis of crystalline zeolite with tunable mesoporosity, Nature materials, 5 (2006) 718.
[190] C.J. Jacobsen, J. Houzvicka, I. Schmidt, C. Madsen, A. Carlsson, Method of preparing zeolite single crystals, in, Google Patents, 2003.
[191] W. Lutz, R. Kurzhals, G. Kryukova, D. Enke, M. Weber, D. Heidemann, Formation of Mesopores in USY Zeolites: A Case Revisited, 636 (2010) 1497-1505.
[192] W. Lutz, Engineering, Zeolite Y: Synthesis, modification, and properties—A case revisited, Advances in Materials Science, 2014 (2014).
[193] M.J. Remy, D. Stanica, G. Poncelet, E.J.P. Feijen, P.J. Grobet, J.A. Martens, P.A. Jacobs, Dealuminated H-Y Zeolites: Relation between Physicochemical Properties and Catalytic Activity in Heptane and Decane Isomerization, The Journal of Physical Chemistry, 100 (1996) 12440-12447.
[194] J. Jae, G.A. Tompsett, A.J. Foster, K.D. Hammond, S.M. Auerbach, R.F. Lobo, G.W. Huber, Investigation into the shape selectivity of zeolite catalysts for biomass conversion, J. Catal., 279 (2011) 257-268.
[195] A. Osatiashtiani, B. Puértolas, C.C.S. Oliveira, J.C. Manayil, B. Barbero, M. Isaacs, C. Michailof, E. Heracleous, J. Pérez-Ramírez, A.F. Lee, K. Wilson, On the influence of Si:Al ratio and hierarchical porosity of FAU zeolites in solid acid catalysed esterification pretreatment of bio-oil, Biomass Conversion and Biorefinery, 7 (2017) 331-342.

[196] M.J. Climent, A. Corma, R. Guil-López, S. Iborra, J. Primo, Use of Mesoporous MCM-41 Aluminosilicates as Catalysts in the Preparation of Fine Chemicals: A New Route for the Preparation of Jasminaldehyde with High Selectivity, J. Catal., 175 (1998) 70-79.
[197] M. Climent, A. Corma, H. Garcia, R. Guil-Lopez, S. Iborra, V. Fornés, Acid-base bifunctional catalysts for the preparation of fine chemicals: synthesis of jasminaldehyde, J. Catal., 197 (2001) 385-393.
[198] V.N. Shetti, J. Kim, R. Srivastava, M. Choi, R. Ryoo, Assessment of the mesopore wall catalytic activities of MFI zeolite with mesoporous/microporous hierarchical structures, J. Catal., 254 (2008) 296-303.
[199] J.C. Manayil, A. Osatiashtiani, A. Mendoza, C.M.A. Parlett, M.A. Isaacs, L.J. Durndell, C. Michailof, E. Heracleous, A. Lappas, A.F. Lee, K. Wilson, Impact of Macroporosity on Catalytic Upgrading of Fast Pyrolysis Bio-Oil by Esterification over Silica Sulfonic Acids, ChemSusChem, 10 (2017) 3506-3511.
[200] X. Fan, X. Ou, F. Xing, G.A. Turley, P. Denissenko, M.A. Williams, N. Batail, C. Pham, A.A. Lapkin, Microtomography-based numerical simulations of heat transfer and fluid flow through β-SiC open-cell foams for catalysis, Catal. Today, 278 (2016) 350-360.
[201] Y. Jiao, X. Fan, M. Perdjon, Z. Yang, J. Zhang, Vapor-phase transport (VPT) modification of ZSM-5/SiC foam catalyst using TPAOH vapor to improve the methanol-to-propylene (MTP) reaction, Appl. Catal., A, 545 (2017) 104-112.
[202] Y. Jiao, C. Jiang, Z. Yang, J. Liu, J. Zhang, Synthesis of highly accessible ZSM-5 coatings on SiC foam support for MTP reaction, Microporous Mesoporous Mater., 181 (2013) 201-207.
[203] X. Ou, S. Xu, J.M. Warnett, S.M. Holmes, A. Zaheer, A.A. Garforth, M.A. Williams, Y. Jiao, X. Fan, Creating hierarchies promptly: Microwave-accelerated synthesis of ZSM-5 zeolites on macrocellular silicon carbide (SiC) foams, Chem. Eng. J., 312 (2017) 1-9.
[204] ASTM D3906-03(2013), Standard Test Method for Determination of Relative X-ray Diffraction Intensities of Faujasite-Type Zeolite-Containing Materials, ASTM International, West Conshohocken, PA, 2013
[205] Q. Tan, X. Bao, T. Song, Y. Fan, G. Shi, B. Shen, C. Liu, X. Gao, Synthesis, characterization, and catalytic properties of hydrothermally stable macro–meso–micro-porous composite materials synthesized via in situ assembly of preformed zeolite Y nanoclusters on kaolin, J. Catal., 251 (2007) 69-79.
[206] R. Xu, W. Pang, J. Yu, Q. Huo, J. Chen, Chemistry of zeolites and related porous materials: synthesis and structure, 2008.
[207] E.M. Flanigen, H. Khatami, H.A. SZYMANSKI, Infrared structural studies of zeolite frameworks, in, ACS Publications, 1971.
[208] W. Baur, Silicon-oxygen bond lengths, bridging angles Si-O-Si and synthetic low tridymite, Acta Crystallographica Section B, 33 (1977) 2615-2619.
[209] R.F. Lobo, Introduction to the structural chemistry of zeolites, in: Handbook of zeolite science and technology, CRC Press, 2003, pp. 92-124.
[210] S.J. Gregg, K.S.W. Sing, Adsorption, surface area, and porosity, Academic Press, London; New York, 1967.
[211] X. Ou, X. Zhang, T. Lowe, R. Blanc, M.N. Rad, Y. Wang, N. Batail, C. Pham, N. Shokri, A.A. Garforth, P.J. Withers, X. Fan, X-ray micro computed tomography characterization of cellular SiC foams for their applications in chemical engineering, Mater. Charact., 123 (2017) 20-28.
[212] S. P. Rigby, R. S. Fletcher, S. N. Riley, Characterisation of porous solids using integrated nitrogen sorption and mercury porosimetry, Chem. Eng. Sci., 59 (2004) 41-51.
[213] J.C. Groen, S. Brouwer, L.A.A. Peffer, J. Pérez-Ramírez, Application of Mercury Intrusion Porosimetry for Characterization of Combined Micro- and Mesoporous Zeolites, 23 (2006) 101-106.
[214] J. Kenvin, J. Jagiello, S. Mitchell, J. Pérez-Ramírez, Unified Method for the Total Pore Volume and Pore Size Distribution of Hierarchical Zeolites from Argon Adsorption and Mercury Intrusion, Langmuir, 31 (2015) 1242-1247.
[215] Y. Jiao, A.-L. Adedigba, Q. He, P. Miedziak, G. Brett, N.F. Dummer, M. Perdjon, J. Liu, G.J. Hutchings, Inter-connected and open pore hierarchical TS-1 with controlled framework titanium for catalytic cyclohexene epoxidation, Catal. Sci. Technol., 8 (2018) 2211-2217.

[216] F. Wakabayashi, J.N. Kondo, K. Domen, C. Hirose, FT-IR study of the interaction of oxygen, argon, helium, nitrogen and xenon with hydroxyl groups in H-Y zeolite at low temperatures, Microporous Mater., 8 (1997) 29-37.
[217] Y. Matsunaga, H. Yamazaki, T. Yokoi, T. Tatsumi, J.N. Kondo, IR Characterization of Homogeneously Mixed Silica–Alumina Samples and Dealuminated Y Zeolites by Using Pyridine, CO, and Propene Probe Molecules, The Journal of Physical Chemistry C, 117 (2013) 14043-14050.
[218] G. Busca, Acidity and basicity of zeolites: A fundamental approach, Microporous Mesoporous Mater., 254 (2017) 3-16.
[219] J.N. Kondo, R. Nishitani, E. Yoda, T. Yokoi, T. Tatsumi, K. Domen, A comparative IR characterization of acidic sites on HY zeolite by pyridine and CO probes with silica–alumina and γ-alumina references, PCCP, 12 (2010) 11576-11586.
[220] C.A. Emeis, Determination of Integrated Molar Extinction Coefficients for Infrared Absorption Bands of Pyridine Adsorbed on Solid Acid Catalysts, J. Catal., 141 (1993) 347-354.
[221] J. Weitkamp, Zeolites and catalysis, Solid State Ionics, 131 (2000) 175-188.
[222] W. Vermeiren, J.P. Gilson, Impact of Zeolites on the Petroleum and Petrochemical Industry, Top. Catal., 52 (2009) 1131-1161.
[223] R. Buzzoni, S. Bordiga, G. Ricchiardi, C. Lamberti, A. Zecchina, G. Bellussi, Interaction of Pyridine with Acidic (H-ZSM5, H-β, H-MORD Zeolites) and Superacidic (H-Nafion Membrane) Systems: An IR Investigation, Langmuir, 12 (1996) 930-940.
[224] H. Wang, M. Frenklach, Transport properties of polycyclic aromatic hydrocarbons for flame modeling, Combust. Flame, 96 (1994) 163-170.
[225] S. Blagov, S. Parada, O. Bailer, P. Moritz, D. Lam, R. Weinand, H. Hasse, Influence of ion-exchange resin catalysts on side reactions of the esterification of n-Butanol with acetic acid, Chem. Eng. Sci., 61 (2006) 753-765.
[226] J. Pérez-Ramírez, D. Verboekend, A. Bonilla, S. Abelló, Zeolite Catalysts with Tunable Hierarchy Factor by Pore-Growth Moderators, Adv. Funct. Mater., 19 (2009) 3972-3979.
[227] X. Zhou, H. Chen, Y. Zhu, Y. Song, Y. Chen, Y. Wang, Y. Gong, G. Zhang, Z. Shu, X. Cui, J. Zhao, J. Shi, Dual-Mesoporous ZSM-5 Zeolite with Highly b-Axis-Oriented Large Mesopore Channels for the Production of Benzoin Ethyl Ether, 19 (2013) 10017-10023.
[228] W. Li, J. Zheng, Y. Luo, Z. Da, Effect of hierarchical porosity and phosphorus modification on the catalytic properties of zeolite Y, Appl. Surf. Sci., 382 (2016) 302-308.
[229] B. Paweewan, P.J. Barrie, L.F. Gladden, Coking and deactivation during n-hexane cracking in ultrastable zeolite Y, Appl. Catal., A, 185 (1999) 259-268.
[230] K. Li, J. Valla, J. Garcia‐Martinez, Realizing the commercial potential of hierarchical zeolites: new opportunities in catalytic cracking, ChemCatChem, 6 (2014) 46-66.
[231] A. Inayat, I. Knoke, E. Spiecker, W. Schwieger, Assemblies of mesoporous FAU‐type zeolite nanosheets, Angew. Chem. Int. Ed., 51 (2012) 1962-1965.
[232] J. Jin, C. Peng, J. Wang, H. Liu, X. Gao, H. Liu, C. Xu, Facile synthesis of mesoporous zeolite Y with improved catalytic performance for heavy oil fluid catalytic cracking, Ind. Eng. Chem. Res., 53 (2014) 3406-3411.
[233] C.S. Triantafillidis, A.G. Vlessidis, N.P. Evmiridis, Dealuminated H-Y zeolites: influence of the degree and the type of dealumination method on the structural and acidic characteristics of H-Y zeolites, Ind. Eng. Chem. Res., 39 (2000) 307-319.
[234] L. Xiao, J. Mao, J. Zhou, X. Guo, S. Zhang, Enhanced performance of HY zeolites by acid wash for glycerol etherification with isobutene, Appl. Catal., A, 393 (2011) 88-95.
[235] A.N.C. van laak, R.W. Gosselink, S.L. Sagala, J.D. Meeldijk, P.E. de Jongh, K.P. de Jong, Alkaline treatment on commercially available aluminum rich mordenite, Appl. Catal., A, 382 (2010) 65-72.
[236] Z. Qin, B. Shen, X. Gao, F. Lin, B. Wang, C. Xu, Mesoporous Y zeolite with homogeneous aluminum distribution obtained by sequential desilication–dealumination and its performance in the catalytic cracking of cumene and 1,3,5-triisopropylbenzene, J. Catal., 278 (2011) 266-275.
[237] E.F.T. Lee, L.V.C. Rees, Dealumination of sodium Y zeolite with hydrochloric acid, Journal of the Chemical Society, Faraday Transactions 1: Physical Chemistry in Condensed Phases, 83 (1987) 1531-1537.

[238] J. Garcia-Martinez, M. Johnson, J. Valla, K. Li, J.Y. Ying, Mesostructured zeolite Y-high hydrothermal stability and superior FCC catalytic performance, Catal. Sci. Technol., 2 (2012) 987-994.
[239] M.R. Apelian, A.S. Fung, G.J. Kennedy, T.F. Degnan, Dealumination of zeolite β via dicarboxylic acid treatment, The Journal of Physical Chemistry, 100 (1996) 16577-16583.
[240] D. Verboekend, S. Mitchell, M. Milina, J.C. Groen, J. Pérez-Ramírez, Full Compositional Flexibility in the Preparation of Mesoporous MFI Zeolites by Desilication, The Journal of Physical Chemistry C, 115 (2011) 14193-14203.
[241] S. Abelló, A. Bonilla, J. Pérez-Ramírez, Mesoporous ZSM-5 zeolite catalysts prepared by desilication with organic hydroxides and comparison with NaOH leaching, Appl. Catal., A, 364 (2009) 191-198.
[242] X. Fan, M.G.Manchon, K. Wilson, S. Tennison, O. Kozynchenko, A.A.Lapkin, P. Plucinski, Coupling of Heck and hydrogenation reactions in a continuous compact reactor, J. Catal., 267 (2009) 114.
[243] R.N. Baig, R.S. Varma, Alternative energy input: mechanochemical, microwave and ultrasound-assisted organic synthesis, Chem. Soc. Rev., 41 (2012) 1559-1584.
[244] S. Askari, S.M. Alipour, R. Halladj, M.H.D.A. Farahani, Effects of ultrasound on the synthesis of zeolites: a review, J. Porous Mater., 20 (2013) 285-302.
[245] S. Oruji, R. Khoshbin, R. Karimzadeh, Preparation of hierarchical structure of Y zeolite with ultrasonic-assisted alkaline treatment method used in catalytic cracking of middle distillate cut: The effect of irradiation time, Fuel Process. Technol., 176 (2018) 283-295.
[246] M.M. Treacy, J.B. Higgins, Collection of simulated XRD powder patterns for zeolites fifth (5th) revised edition, Elsevier, 2007.
[247] C. Pagis, A.R.M. Prates, N. Bats, A. Tuel, D. Farrusseng, High-silica hollow Y zeolite by selective desilication of dealuminated NaY crystals in the presence of protective Al species, CrystEngComm, 20 (2018) 1564-1572.
[248] G.T. Kerr, G.F. Shipman, Reaction of hydrogen Zeolite Y with ammonia at elevated temperatures, The Journal of Physical Chemistry, 72 (1968) 3071-3072.
[249] S. Svelle, L. Sommer, K. Barbera, P.N. Vennestrøm, U. Olsbye, K.P. Lillerud, S. Bordiga, Y.-H. Pan, P. Beato, How defects and crystal morphology control the effects of desilication, Catal. Today, 168 (2011) 38-47.
[250] Y. Fan, X. Bao, X. Lin, G. Shi, H. Liu, Acidity Adjustment of HZSM-5 Zeolites by Dealumination and Realumination with Steaming and Citric Acid Treatments, The Journal of Physical Chemistry B, 110 (2006) 15411-15416.
[251] S.S. Vieira, Z.M. Magriotis, M.F. Ribeiro, I. Graça, A. Fernandes, J.M.F.M. Lopes, S.M. Coelho, N.A.V. Santos, A.A. Saczk, Use of HZSM-5 modified with citric acid as acid heterogeneous catalyst for biodiesel production via esterification of oleic acid, Microporous Mesoporous Mater., 201 (2015) 160-168.
[252] R. Feng, X. Yan, X. Hu, Y. Wang, Z. Li, K. Hou, J. Lin, Hierarchical ZSM-5 zeolite designed by combining desilication and dealumination with related study of n-heptane cracking performance, J. Porous Mater., (2018) 1-14.
[253] Z. Xie, Q. Chen, C. Zhang, J. Bao, Y. Cao, Influence of Citric Acid Treatment on the Surface Acid Properties of Zeolite Beta, The Journal of Physical Chemistry B, 104 (2000) 2853-2859.
[254] Z. Lingjuan, L. Min, D. Xiangmei, S. Chunshan, G. Xinwen, Dehydration of 2-(4′-ethylbenzoyl)-benzoic acid to 2-ethylanthraquinone over Hβ zeolite modified with organic acids, Chinese Journal of Catalysis, 30 (2009) 9-13.
[255] G. Bai, J. Han, H. Zhang, C. Liu, X. Lan, F. Tian, Z. Zhao, H. Jin, Friedel-Crafts acylation of anisole with octanoic acid over acid modified zeolites, RSC Advances, 4 (2014) 27116-27121.
[256] C. Xing, G. Yang, M. Wu, R. Yang, L. Tan, P. Zhu, Q. Wei, J. Li, J. Mao, Y. Yoneyama, N. Tsubaki, Hierarchical zeolite Y supported cobalt bifunctional catalyst for facilely tuning the product distribution of Fischer–Tropsch synthesis, Fuel, 148 (2015) 48-57.
[257] A. Al-Ani, R.J. Darton, S. Sneddon, V. Zholobenko, Nanostructured Zeolites: The Introduction of Intracrystalline Mesoporosity in Basic Faujasite-type Catalysts, ACS Applied Nano Materials, 1 (2018) 310-318.

[258] J.L. Agudelo, E.J.M. Hensen, S.A. Giraldo, L.J. Hoyos, Effect of USY Zeolite Chemical Treatment with Ammonium Nitrate on Its VGO Hydrocracking Performance, Energy & Fuels, 30 (2016) 616-625.
[259] U.J. Etim, B. Xu, Z. Zhang, Z. Zhong, P. Bai, K. Qiao, Z. Yan, Improved catalytic cracking performance of USY in the presence of metal contaminants by post-synthesis modification, Fuel, 178 (2016) 243-252.
[260] A.N. van Laak, S.L. Sagala, J. Zečević, H. Friedrich, P.E. de Jongh, K.P. de Jong, Mesoporous mordenites obtained by sequential acid and alkaline treatments–Catalysts for cumene production with enhanced accessibility, J. Catal., 276 (2010) 170-180.
[261] T. Ennaert, J. Van Aelst, J. Dijkmans, R. De Clercq, W. Schutyser, M. Dusselier, D. Verboekend, B.F. Sels, Potential and challenges of zeolite chemistry in the catalytic conversion of biomass, Chem. Soc. Rev., 45 (2016) 584-611.
[262] G. Szekely, A.G. Livingston, Sustainable Nanoscale Engineering: From Materials Design to Chemical Processing, Elsevier, 2019.
[263] Y. Tao, H. Kanoh, L. Abrams, K. Kaneko, Mesopore-modified zeolites: preparation, characterization, and applications, Chem. Rev., 106 (2006) 896-910.
[264] C. Li, L. Guo, P. Liu, K. Gong, W. Jin, L. Li, X. Zhu, X. Liu, B. Shen, Defects in AHFS-dealuminated Y zeolite: A crucial factor for mesopores formation in the following base treatment procedure, Microporous Mesoporous Mater., 255 (2018) 242-252.
[265] J.S. Beck, J. Vartuli, W.J. Roth, M. Leonowicz, C. Kresge, K. Schmitt, C. Chu, D.H. Olson, E. Sheppard, S. McCullen, A new family of mesoporous molecular sieves prepared with liquid crystal templates, J. Am. Chem. Soc., 114 (1992) 10834-10843.
[266] Y. Jiao, L. Forster, S. Xu, H. Chen, J. Han, X. Liu, Y. Zhou, J. Liu, J. Zhang, J. Yu, C. D'Agostino, X. Fan, Creation of Al-Enriched Mesoporous ZSM-5 Nanoboxes with High Catalytic Activity: Converting Tetrahedral Extra-Framework Al into Framework Sites via Post Treatment, Angew. Chem. Int. Ed., n/a (2020).
[267] J. Čejka, S. Mintova, Perspectives of Micro/Mesoporous Composites in Catalysis, Catalysis Reviews, 49 (2007) 457-509.
[268] A. Corma, V. Fornes, S. Pergher, T.L. Maesen, J. Buglass, Delaminated zeolite precursors as selective acidic catalysts, Nature, 396 (1998) 353.
[269] J. Scherzer, The preparation and characterization of aluminium-deficient zeolites, in: ACS Symp. Ser., Oxford University Press, 1984, pp. 157-200.
[270] J. Garcia-Martinez, M.M. Johnson, I. Valla, Introduction of mesoporosity in low Si/Al zeolites, in, Google Patents, 2013.
[271] C.S. Cundy, Microwave techniques in the synthesis and modification of zeolite catalysts. A review, Collect. Czech. Chem. Commun., 63 (1998) 1699-1723.
[272] X. Meng, F.-S. Xiao, Green routes for synthesis of zeolites, Chem. Rev., 114 (2013) 1521-1543.
[273] R. Vakili, S. Xu, N. Al-Janabi, P. Gorgojo, S.M. Holmes, X. Fan, Microwave-assisted synthesis of zirconium-based metal organic frameworks (MOFs): Optimization and gas adsorption, Microporous Mesoporous Mater., 260 (2018) 45-53.
[274] Fan X, Jiao Y (2018) A microwave-assisted chelation protocol to create mesoporosity in zeolites. U.K. Patent application No. GB 1814932.8.
[275] A. International, Standard Test Method for Determination of the Unit Cell Dimension of a Faujasite-Type Zeolite, in, ASTM International, West Conshohocken, 2019.
[276] H. Liu, X. Liu, X. Li, X. Xu, Study of Dealumination of NaY Zeolite with Different Acids, Petrochemical Technology, 27 (1998) 880-885.
[277] G.M. Gadd, Fungal Production of Citric and Oxalic Acid: Importance in Metal Speciation, Physiology and Biogeochemical Processes, in: R.K. Poole (Ed.) Advances in Microbial Physiology, Academic Press, 1999, pp. 47-92.
[278] J.V. Smith, S.W. Bailey, Second review of Al-O and Si-O tetrahedral distances, Acta Crystallographica, 16 (1963) 801-811.
[279] G. Coudurier, C. Naccache, J.C. Vedrine, Uses of IR spectroscopy in identifying ZSM zeolite structure, J. Chem. Soc., Chem. Commun., (1982) 1413-1415.
[280] B.A. Holmberg, H. Wang, J.M. Norbeck, Y. Yan, Controlling size and yield of zeolite Y nanocrystals using tetramethylammonium bromide, Microporous Mesoporous Mater., 59 (2003) 13-28.

[281] R. Zhang, S. Xu, D. Raja, N.B. Khusni, J. Liu, J. Zhang, S. Abdulridha, H. Xiang, S. Jiang, Y. Guan, On the effect of mesoporosity of FAU Y zeolites in the liquid-phase catalysis, Microporous Mesoporous Mater., 278 (2019) 297-306.
[282] D. Li, Y. Chen, J. Hu, B. Deng, X. Cheng, Y. Zhang, Synthesis of Hierarchical Chabazite Zeolite via Interzeolite Transformation of Coke-containing Spent MFI, Appl. Catal., B, 270 (2020) 118881.
[283] C. Wang, L. Zhang, X. Huang, Y. Zhu, G. Li, Q. Gu, J. Chen, L. Ma, X. Li, Q. He, J. Xu, Q. Sun, C. Song, M. Peng, J. Sun, D. Ma, Maximizing sinusoidal channels of HZSM-5 for high shape-selectivity to p-xylene, Nature Communications, 10 (2019) 4348.
[284] L. Lin, A.M. Sheveleva, I. da Silva, C.M.A. Parlett, Z. Tang, Y. Liu, M. Fan, X. Han, J.H. Carter, F. Tuna, E.J.L. McInnes, Y. Cheng, L.L. Daemen, S. Rudić, A.J. Ramirez-Cuesta, C.C. Tang, S. Yang, Quantitative production of butenes from biomass-derived γ-valerolactone catalysed by hetero-atomic MFI zeolite, Nature Materials, 19 (2020) 86-93.
[285] Z. Guo, X. Li, S. Hu, G. Ye, X. Zhou, M.O.J.A.C. Coppens, Understanding the Role of Internal Diffusion Barriers in Pt/Beta Zeolite Catalyzed Isomerization of n‐Heptane, Angew. Chem. Int. Ed., (2019).
[286] N. Wang, Y. Zhi, Y. Wei, W. Zhang, Z. Liu, J. Huang, T. Sun, S. Xu, S. Lin, Y. He, A. Zheng, Z. Liu, Molecular elucidating of an unusual growth mechanism for polycyclic aromatic hydrocarbons in confined space, Nature Communications, 11 (2020) 1079.
[287] S. Tao, X. Li, X. Wang, Y. Wei, Y. Jia, J. Ju, Y. Cheng, H. Wang, S. Gong, X. Yao, H. Gao, C. Zhang, Q. Zang, Z. Tian, Facile Synthesis of Hierarchical Nanosized Single-Crystal Aluminophosphate Molecular Sieves from Highly Homogeneous and Concentrated Precursors, Angew. Chem. Int. Ed., 59 (2020) 3455-3459.
[288] J. Čejka, R. Millini, M. Opanasenko, D.P. Serrano, W.J. Roth, Advances and challenges in zeolite synthesis and catalysis, Catal. Today, 345 (2020) 2-13.
[289] A. Pande, P. Niphadkar, K. Pandare, V. Bokade, Acid Modified H-USY Zeolite for Efficient Catalytic Transformation of Fructose to 5-Hydroxymethyl Furfural (Biofuel Precursor) in Methyl Isobutyl Ketone–Water Biphasic System, Energy & Fuels, 32 (2018) 3783-3791.
[290] J.R. García, M. Falco, U. Sedran, Impact of the Desilication Treatment of Y Zeolite on the Catalytic Cracking of Bulky Hydrocarbon Molecules, Top. Catal., 59 (2016) 268-277.
[291] A. Sachse, J. García-Martínez, Surfactant-Templating of Zeolites: From Design to Application, Chem. Mater., 29 (2017) 3827-3853.
[292] D. Verboekend, R. Caicedo-Realpe, A. Bonilla, M. Santiago, J. Perez-Ramirez, Properties and functions of hierarchical ferrierite zeolites obtained by sequential post-synthesis treatments, Chem. Mater., 22 (2010) 4679-4689.
[293] D.L. Bhering, A. Ramírez-Solís, C.J.A. Mota, A Density Functional Theory Based Approach to Extraframework Aluminum Species in Zeolites, The Journal of Physical Chemistry B, 107 (2003) 4342-4347.
[294] Z. Yu, A. Zheng, Q. Wang, L. Chen, J. Xu, J.-P. Amoureux, F. Deng, Insights into the Dealumination of Zeolite HY Revealed by Sensitivity-Enhanced 27Al DQ-MAS NMR Spectroscopy at High Field, Angew. Chem. Int. Ed., 49 (2010) 8657-8661.
[295] M.-C. Silaghi, C. Chizallet, J. Sauer, P. Raybaud, Dealumination mechanisms of zeolites and extra-framework aluminum confinement, J. Catal., 339 (2016) 242-255.
[296] K. Valdiviés-Cruz, A. Lam, C.M. Zicovich-Wilson, Full Mechanism of Zeolite Dealumination in Aqueous Strong Acid Medium: Ab Initio Periodic Study on H-Clinoptilolite, The Journal of Physical Chemistry C, 121 (2017) 2652-2660.
[297] J. Sun, H. Fang, P.I. Ravikovitch, D.S. Sholl, Understanding Dealumination Mechanisms in Protonic and Cationic Zeolites, The Journal of Physical Chemistry C, 124 (2020) 668-676.
[298] S. Abdulridha, Y. Jiao, S. Xu, R. Zhang, A.A. Garforth, X. Fan, Mesoporous Zeolitic Materials (MZMs) Derived From Zeolite Y Using a Microwave Method for Catalysis, Frontiers in Chemistry, 8 (2020).
[299] Standard Test Method for Determination of Relative X-ray Diffraction Intensities of Faujasite-Type Zeolite-Containing Materials, ASTM D3906-19 (2019).
[300] H. Maki, G. Sakata, M. Mizuhata, Quantitative NMR of quadrupolar nucleus as a novel analytical method: hydrolysis behaviour analysis of aluminum ion, Analyst, 142 (2017) 1790-1799.

[301] M.B. Yue, T. Xue, W.Q. Jiao, Y.M. Wang, M.-Y. He, Dealumination, silicon insertion and H-proton exchange of NaY in one step with acid ethanol solution, Microporous Mesoporous Mater., 159 (2012) 50-56.
[302] R.K. Iyer, S.B. Karweer, V.K. Jain, Complexes of aluminium with aminopolycarboxylic acids: 27Al NMR and potentiometric studies, Magn. Reson. Chem., 27 (1989) 328-334.
[303] C.C. Perry, K.L. Shafran, The systematic study of aluminium speciation in medium concentrated aqueous solutions, J. Inorg. Biochem., 87 (2001) 115-124.
[304] W. Loewenstein, The distribution of aluminum in the tetrahedra of silicates and aluminates, Am. Mineral., 39 (1954) 92-96.
[305] A. Samoson, E. Lippmaa, G. Engelhardt, U. Lohse, H.G. Jerschkewitz, Quantitative high-resolution 27Al NMR: tetrahedral non-framework aluminium in hydrothermally treated zeolites, Chem. Phys. Lett., 134 (1987) 589-592.
[306] J. Sanz, V. Fornés, A. Corma, Extraframework aluminium in steam- and SiCl4-dealuminated Y zeolite. A 27Al and 29Si nuclear magnetic resonance study, Journal of the Chemical Society, Faraday Transactions 1: Physical Chemistry in Condensed Phases, 84 (1988) 3113-3119.
[307] P. Morales-Pacheco, F. Alvarez, L. Bucio, J.M. Domínguez, Synthesis and Structural Properties of Zeolitic Nanocrystals II: FAU-Type Zeolites, The Journal of Physical Chemistry C, 113 (2009) 2247-2255.
[308] A. Peters, C.C. Wu, Selectivity effects of a new aluminum species in strongly dealuminated USY containing FCC catalysts, Catal. Lett., 30 (1994) 171-179.
[309] C.A. Fyfe, J.L. Bretherton, L.Y. Lam, Detection of the 'invisible aluminium' and characterisation of the multiple aluminium environments in zeolite USY by high-field solid-state NMR, Chem. Commun., (2000) 1575-1576.
[310] A. Gola, B. Rebours, E. Milazzo, J. Lynch, E. Benazzi, S. Lacombe, L. Delevoye, C. Fernandez, Effect of leaching agent in the dealumination of stabilized Y zeolites, Microporous and Mesoporous Materials, 40 (2000) 73-83.
[311] K.U. Gore, A. Abraham, S.G. Hegde, R. Kumar, J.-P. Amoureux, S. Ganapathy, 29Si and 27Al MAS/3Q-MAS NMR studies of high silica USY zeolites, The Journal of Physical Chemistry B, 106 (2002) 6115-6120.
[312] J. Zhuang, D. Ma, G. Yang, Z. Yan, X. Liu, X. Liu, X. Han, X. Bao, P. Xie, Z. Liu, Solid-state MAS NMR studies on the hydrothermal stability of the zeolite catalysts for residual oil selective catalytic cracking, J. Catal., 228 (2004) 234-242.
[313] C. Liu, G. Li, E.J.M. Hensen, E.A. Pidko, Relationship between acidity and catalytic reactivity of faujasite zeolite: A periodic DFT study, J. Catal., 344 (2016) 570-577.
[314] Z. Yan, D. Ma, J. Zhuang, X. Liu, X. Liu, X. Han, X. Bao, F. Chang, L. Xu, Z. Liu, On the acid-dealumination of USY zeolite: a solid state NMR investigation, J. Mol. Catal. A: Chem., 194 (2003) 153-167.
[315] J.A. van Bokhoven, A. Roest, D. Koningsberger, J. Miller, G. Nachtegaal, A. Kentgens, Changes in structural and electronic properties of the zeolite framework induced by extraframework Al and La in H-USY and La (x) NaY: A 29Si and 27Al MAS NMR and 27Al MQ MAS NMR study, The Journal of Physical Chemistry B, 104 (2000) 6743-6754.
[316] M. Ravi, V.L. Sushkevich, J.A. van Bokhoven, Towards a better understanding of Lewis acidic aluminium in zeolites, Nature Materials, 19 (2020) 1047-1056.
[317] H.K. Beyer, Dealumination techniques for zeolites, in: Post-Synthesis Modification I, Springer, 2002, pp. 203-255.
[318] G.T. Kerr, A.W. Chester, D.H. Olson, Dealumination of zeolite Y by H4EDTA, Catal. Lett., 25 (1994) 401-402.
[319] S. Malola, S. Svelle, F.L. Bleken, O. Swang, Detailed reaction paths for zeolite dealumination and desilication from density functional calculations, Angew. Chem. Int. Ed., 51 (2012) 652-655.
[320] J. Datka, B. Sulikowski, B. Gil, IR Spectroscopic Studies of Dealuminated and Realuminated Zeolite HY, The Journal of Physical Chemistry, 100 (1996) 11242-11245.
[321] B. Sulikowski, J. Datka, B. Gil, J. Ptaszynski, J. Klinowski, Acidity and Catalytic Properties of Realuminated Zeolite Y, The Journal of Physical Chemistry B, 101 (1997) 6929-6932.

[322] D. Verboekend, G. Vilé, J. Pérez-Ramírez, Mesopore Formation in USY and Beta Zeolites by Base Leaching: Selection Criteria and Optimization of Pore-Directing Agents, Crystal Growth & Design, 12 (2012) 3123-3132.
[323] M.S. Holm, S. Svelle, F. Joensen, P. Beato, C.H. Christensen, S. Bordiga, M. Bjørgen, Assessing the acid properties of desilicated ZSM-5 by FTIR using CO and 2,4,6-trimethylpyridine (collidine) as molecular probes, Appl. Catal., A, 356 (2009) 23-30.
[324] D. Liu, S. Bao, Q. Xu, Structural evolution of dealuminated Y zeolites during KOH solution treatment, Zeolites, 18 (1997) 162-170.
[325] Z. Zhang, X. Liu, Y. Xu, R. Xu, Realumination of dealuminated zeolites Y, Zeolites, 11 (1991) 232-238.

Chapter 9 Appendix

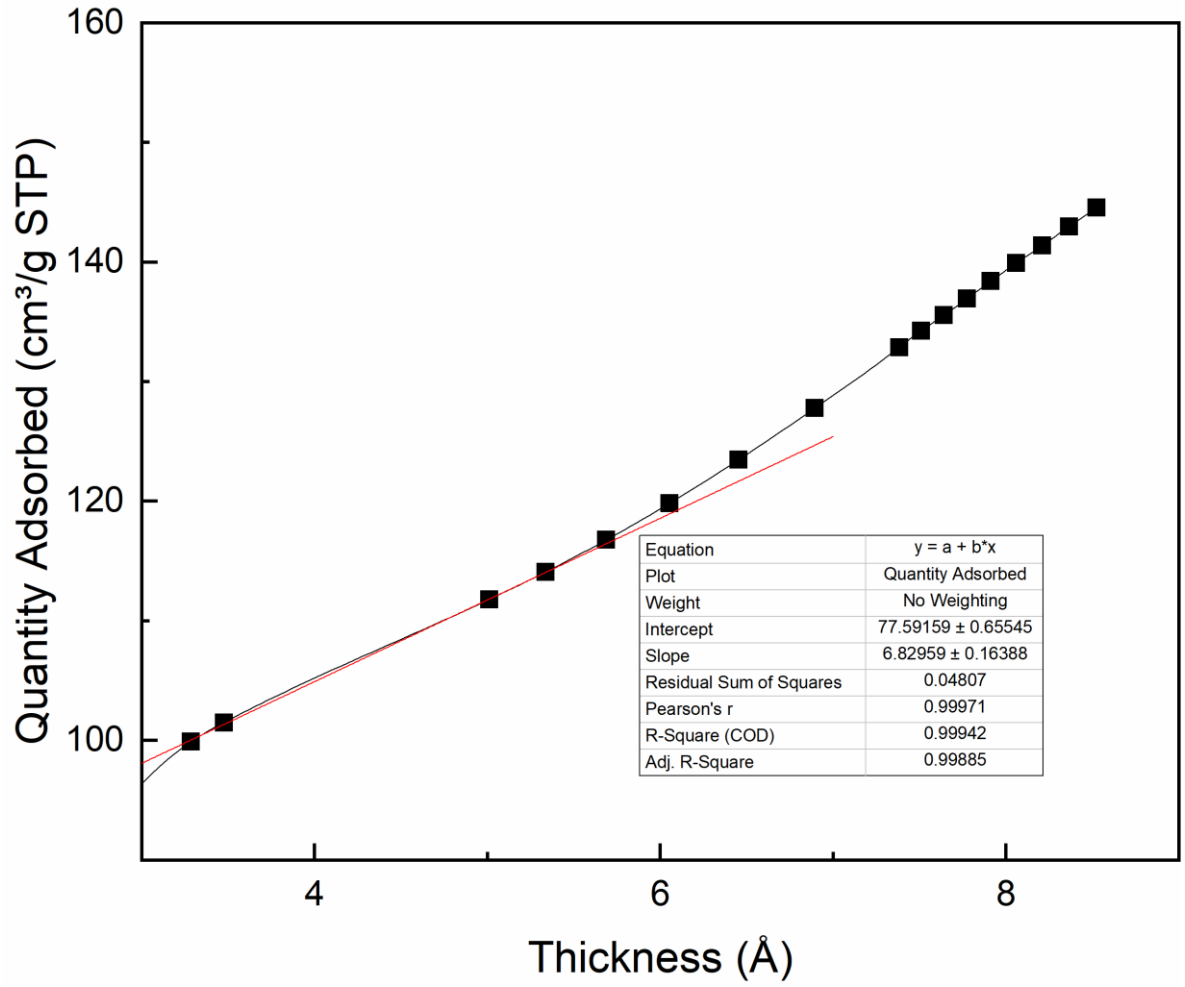

Figure 9.1 *t*-plot linear fitting for micropore volume calculation of sample CAY-*0.16-1h-S* as listed in Table 4.4.

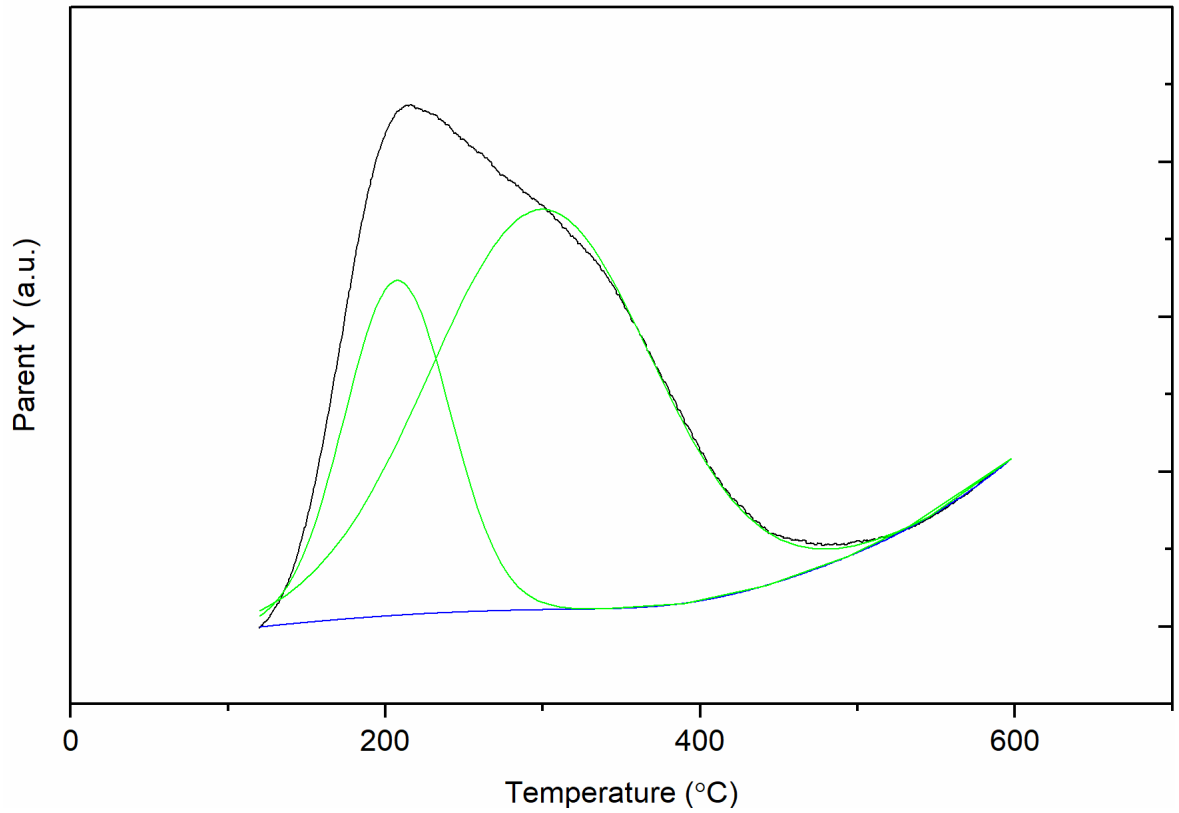

Figure 9.2 NH_3-TPD deconvolution of Parent Y zeolite in Figure 5.4.

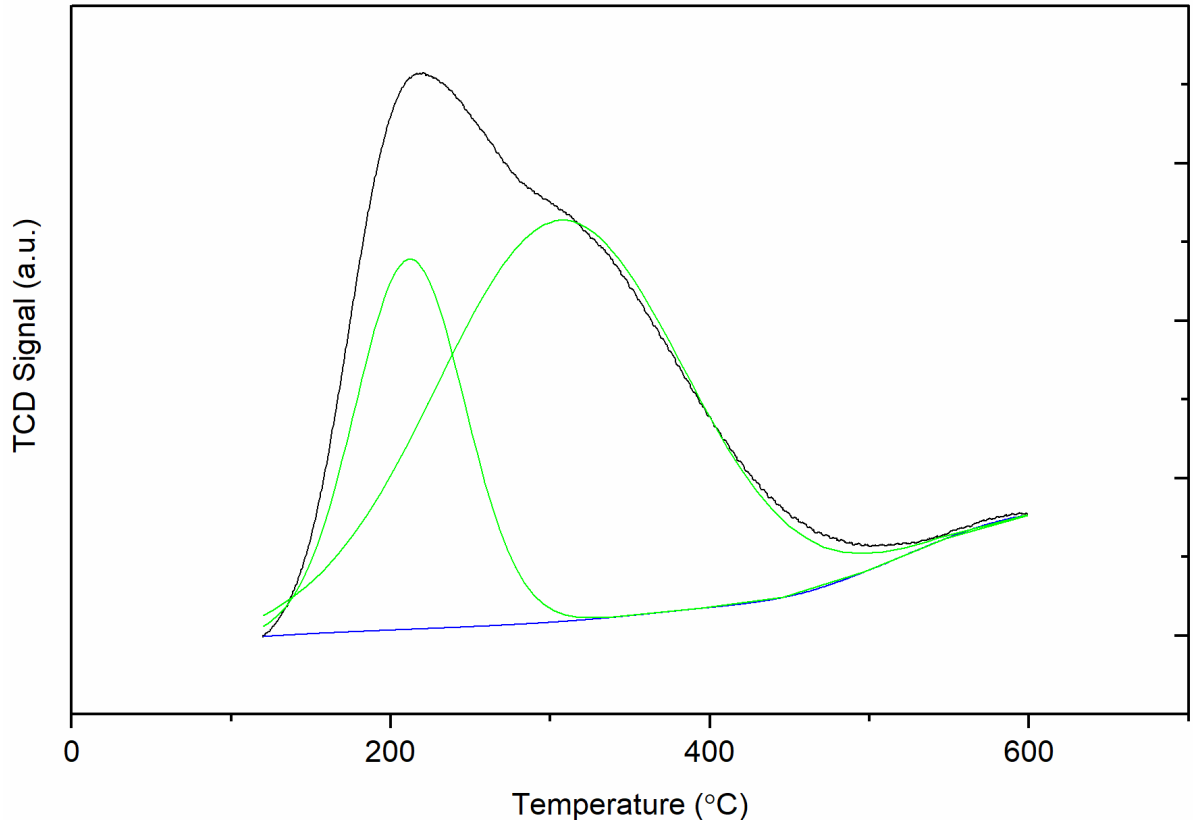

Figure 9.3 NH_3-TPD deconvolution of TA-0.16-Y zeolite in Figure 5.4.